A UNIFIED COMPUTATIONAL FRAMEWORK FOR PROCESS MODELING AND PERFORMANCE MODELING OF MULTI-CONSTITUENT MATERIALS

BY

HARISHANKER GAJENDRAN

DISSERTATION

Submittal in partial fulfillment of the requirements
for the degree of Doctor of Philosophy in Civil Engineering
in the Graduate College of the
University of Illinois at Urbana-Champaign, 2016

Urbana, Illinois

Doctoral Committee:

Professor Arif Masud, Chair and Director of Research
Professor C. Armando Duarte
Assistant Professor Ahmed E. Elbanna
Professor Rizwan Uddin

Abstract

This thesis presents new theoretical and computational developments and an integrated approach for interface and interphase mechanics in the process and performance modeling of fibrous composite materials. A new class of stabilized finite element methods is developed for the coupled-field problems that arise due to curing and chemical reactions at the bi-material interfaces at the time of the manufacturing of the fiber-matrix systems. An accurate modeling of the degree of curing, because of its effects on the evolving properties of the interphase material, is critical to determining the coupled chemo-mechanical interphase stresses that influence the structural integrity of the composite and its fatigue life.

A thermodynamically consistent theory of mixtures for multi-constituent materials is adopted to model curing and interphase evolution during the processing of the composites. The mixture theory model combines the composite constituent behaviors in an effective medium, thereby reducing the computational cost of modeling chemically reacting multi-constituent mixtures, while retaining information involving the kinematic and kinetic responses of the individual constituents. The effective medium and individual constituent behaviors are each constrained to mutually satisfy the balance principles of mechanics. Even though each constituent is governed by its own balance laws and constitutive equations, interactive forces between constituents that emanate from maximization of entropy production inequality provide the coupling between constituent specific balance laws and constitutive models. The mixture model is cast in a finite strain finite element framework that finds roots in the Variational Multiscale (VMS) method.

The deformation of multi-constituent mixtures at the Neumann boundaries requires imposing constraint conditions such that the constituents deform in a self-consistent fashion. A set of boundary conditions is presented that accounts for the non-zero applied tractions, and a variationally consistent method is developed to enforce inter constituent constraints at Neumann boundaries in the finite deformation context. The new method finds roots in a local multiscale decomposition of the deformation map at the Neumann boundary. Locally satisfying the Lagrange multiplier field and subsequent modeling of the fine scales via edge bubble functions results in closed-form expressions for a generalized penalty tensor and a weighted numerical flux

that are free from tunable parameters. The key novelty is that the consistently derived constituent coupling parameters evolve with material and geometric nonlinearity, thereby resulting in optimal enforcement of inter-constituent constraints. A class of coupled field problems for process modeling and for performance molding of fibrous composites is presented that provides insight into the theoretical models and multiscale stabilized formulations for computational modeling of multi-constituent materials.

Acknowledgements

I would like to express my sincere gratitude to my advisor, Prof. Arif Masud for giving me the opportunity to work with him and for all the support during my stay at UIUC. I am very grateful to him for his patience and encouragement to be better in technical and soft skills.

I am also grateful to Prof. Armando Duarte, Prof. Martin Starzeewski, Prof. Ahmed Elbanna and Prof. Rizwan Uddin for being part of my committee and for their insightful comments and continuous support.

I would also like to acknowledge the financial support of Kinra fellowship, CSE fellowship and research assistantship by Air Force Research Laboratory. I would like to thank the Computational Science and Engineering department for providing the parallel computing resource which was an integral part of my research.

I would also like to thank my labmates, Dr. Raguraman Kannan, Dr. JaeHyuk Kwack, Dr. Ramon Calderer, Dr. Tim Truster, Pinlei Chen, Lixing Zhu, Soonpil Kang, Marcelino Anguiano and Ahmad Alnaseem for creating a friendly environment and helpful discussions.

Table of Contents

Chapter 1

Introduction

1.1 Motivation

In the manufacturing of fibrous composites, the fiber-resin mixture is subjected to a cure cycle that initiates cross-linking polymerization in resin to produce a structurally hard material. The properties of the final product as well as its performance characteristics depend on the properties of constituents as well as the properties of the interphase zone formed in the constituent interface region. Theoretical models and numerical methods employed to model material evolution at the microscale level need to capture the behavior of the individual constituents as well as their coupled interactions in an integrated fashion.

From the materials perspective the fabrication of fiber-reinforced polymer matrix composites involves a number of complex interdependent processes, which preclude the resulting materials from achieving chemical or mechanical homogeneity. Firstly, the mixing of thermoset polymer ingredients, resin and hardener, is achieved via a stochastic but finite sequence of folding, stretching, and cutting events. Despite best efforts to achieve spatial dispersion, at some scale this blend consists of pockets, layers, or veins of resin-rich material alternating with cross-linker-rich ones. Secondly, selective chemical affinity of the embedded phase towards these constituents may enhance their separation. The curing process therefore not only involves cross-linking reactions, but also inter-diffusion of reacting species. As the cure progresses, molecular transport slows due to the obstruction imposed by the increasing number of cross-links. The final degree of cure never reaches 100% and most often it varies from location to location. Thirdly, the cross-linking reactions are exothermic, and consequently self-catalyzing. Even autoclave treatment does not prevent the development of temperature gradients due to the difference between the thermal conductivities of polymer matrix and embedded phase. This in turn results in differential chemical reaction along the interface and development of a composite with spatially inhomogeneous physical properties.

Finally, upon extraction from autoclave, due to material mismatch, differential residual stresses are developed that can cause local debonding and crack propagation along this interface. The properties of the interphase region are especially difficult to predict, unless their detailed constitutional history is known. Since interphases play a dominant role in the response of the composite when subjected to mechanical loads, an accurate modeling of the effects of chemo-mechanical heterogeneities and interphase stresses is critical to determine the structural integrity of the composite and its fatigue life.

With the objective of developing a comprehensive theoretical framework we employ mixture theory for a representative infinitesimal volume element of dense mixture of multi-constituent solids where each constituent is governed by its own balance laws and constitutive equations. A literature review reveals that mixture theory as proposed by Truesdell [1] has been widely employed in the modeling of fluid-fluid and solid-fluid mixtures. Comprehensive review articles by Atkin and Craine [2], Green and Naghdi [3,4] and the book by Rajagopal and Tao [5] provide a good exposition to the mixture theory and associated constitutive relations. Mixture theory ideas have also been used to model various phenomena such as classical viscoelasticity [6], swelling of polymers [7], thermo-oxidative degradation of polymer composites [8,9], growth of biological materials [10] and crystallization of polymers [11], to name a few. Mixture theories have also been employed to model the multi-constituent elastic solids, e.g., Bowen et al. [29] presented a thermomechanical theory for diffusion in mixtures of elastic materials. Bedford et al. [30] proposed a multi-continuum theory for composite materials, where the material particles of different constituents are grouped together at reference configuration to define a composite particle. Though these constituent particles occupy different spatial points as the material deforms, the interactions between constituents are evaluated in the reference configuration using the composite particle. Hall and Rajagopal [13] proposed a mixture model for diffusion of chemically reacting fluid through an anisotropic solid based on the maximization of the rate of entropy production constraint, considering anisotropic effective reaction rates and the limits of diffusion-dominated (diffusion of the reactants is far more rapid than the reaction) and reaction-dominated (the reaction is far more rapid than the diffusion of the reactants) processes. In the present work the theory by Hall and Rajagopal [13] is enhanced to the case of mixture of two interacting solid constituents, and an edge-stabilized method is developed to model fibrous composite systems.

The theoretical basis of this work is a mixture based approach for multi-constituent materials that is locally homogeneous but globally heterogeneous and is built on satisfying the full set of balance equations of coupled chemo-mechanics wherein one can treat a range of physics/constitutive laws for the separate constituents. Furthermore, the constitutive laws are based not only on the individual components but also on the interactive forces between them. The latter can be thought of as providing the internal reaction force at the constituent level obtained by slicing through a representative volume element/cell which is acted on at its exterior surfaces by tractions /stresses, and reduces the constituent interactions, which are in reality very geometrically complex, to a force felt by (each) constituent due to its interactions with the others. It can handle fluid drag, solid-solid relative displacement, and high strains across the constituent interfaces, and can facilitate the modeling and analysis of interface and interphase strength in laminates.

In the mixture theory model a thermodynamic framework that appeals to the maximization of the rate of entropy production is adopted. A Gibbs potential–based formulation is proposed to study problems involving chemical reactions and it also leads to implicit constitutive equations for the stress tensor. The assumption of maximization of the rate of entropy production due to dissipation, heat conduction, and chemical reactions is invoked to determine an equation for the evolution of the natural configuration. It helps in the determination (and selection) of admissible entropy production functions and helps identify physically relevant processes. The mixture model combines the composite constituent behaviors in an effective medium sense, reducing the computational cost of modeling chemically reacting multi-constituent mixtures, while retaining information involving the kinematic and kinetic responses of the individual constituents. The effective medium and individual constituent behaviors are each constrained to mutually satisfy the balance principles of mechanics. Interactive forces between constituents that emanate from maximization of entropy production inequality provide the necessary coupling between the balance laws and constitutive models and therefore between the concurrent and overlapping constituents.

Another objective of this thesis is the development of variational formulations with enhanced stability properties for application to multiphysics problems that involve coupled interaction of mechanical, chemical and thermal fields. Enhanced stability properties help develop robust models and associated numerical schemes that can serve as a simulation-based material modeling and design platform. The resulting numerical solution scheme is based on Variational Multiscale (VMS)

method wherein decomposition of the deformation map into an elastic-component and another component that is associated with damage evolution and phase change is assumed. This compositional mapping between referential, intermediate and spatial configurations is integrated with the mixture theory thereby resulting in a novel method that is computationally efficient, and mathematically robust.

1.2 Dissertation Outline

The stabilized computational framework for mixture theory and its application to process modeling and performance modeling of multi-constituent materials are organized as follows:

Chapter 2 starts with the discussion on mixture models for the diffusion of a chemically reacting fluid through a nonlinear elastic solid. Such processes arise in, as examples, the curing of composites using vacuum assisted resin transfer molding (VARTM), in the prediction of oxidation layer growth in composites, and in slurry infiltration in the manufacturing of composites. A residual-based stabilized mixed finite element formulation involving the balance of mass equation for the fluid that is written in an ALE form is presented. This 1-D development sets the stage for extending the stabilized method to full three dimensional contexts in the rest of the chapters. Numerical simulations for Fick's diffusion problem, oxidation of PMR-15 resin and slurry infiltration problem were conducted to verify the method.

Chapter 3 focuses on modeling the composite manufacturing process wherein the fiber-resin mixture is subjected to a cure cycle under high temperature, initiating cross-linking polymerization in resin to produce a structurally hard composite. We employ a modification to the Hall and Rajagopal model [13] for the formation and evolution of interphase in two-constituent materials where both constituents are in the solid phase. In this model, the properties of the matrix at the fiber-matrix interface evolve during the cure cycle and the isotropic reaction resulting from maximization of entropy production is associated with an anisotropic tensor that provides coupling of chemical reaction and mechanical stresses. Representative numerical simulations are presented for matrix curing and interphase formation by employing Ruiz [54,55] model and Yang [56-58] model respectively.

Chapter 4 extends the mixture model and numerical method to three dimensions and special emphasis is laid on the issue of Neumann boundary conditions that are considered a bottleneck in the application of higher order mixture theories to physical systems. The deformation of multi-constituent mixtures at the Neumann boundaries requires imposing constraint conditions such that the constituents deform in a self-consistent fashion. A set of boundary conditions are presented to account for the non-zero applied tractions. A numerical method is developed that draws from the stabilized Discontinuous Galerkin method for finite strain kinematics with an underlying Lagrange multiplier interface formulation. Closed-form expressions are derived for the stabilization tensor and the weighted numerical flux that are free from tunable stability parameters. The key novelty is that the consistently derived stability tensors automatically evolve with evolving material and geometric nonlinearity at the boundaries.

In Chapter 5, a hierarchical Variational multiscale method is developed to model the higher order mixture constitutive relations using lower order Lagrange elements. The fine scale fields are allowed to evolve as a function of the residual of governing equation and are employed in the interactive force field to model the lost physics. Numerical examples both in one dimension and three dimension are presented that showcases the capability of the method. Finally, a comprehensive capstone problem is presented for process and performance modeling of a lamina which includes all the features presented in previous chapters.

Chapter 6 presents the summary and significant contribution of this thesis and possible future research for extending the presented computational famework to model damage and predicting the fatigue life of multi-constituent materials.

Chapter 2

A Stabilized Finite Element Method for Diffusion of a Chemically Reacting Fluid through a Nonlinear Elastic Solid

2.1 Introduction

In this chapter, a stabilized mixed finite element method is presented for the diffusion of a chemically reacting fluid through a nonlinear elastic solid using a mixture theory based model. For a detailed introduction to mixture theory, interested readers are referred to comprehensive review articles by Atkin and Craine [2], Green and Naghdi [3,4] and the book by Rajagopal and Tao [5]. Mixture theory ideas have been used to model various phenomena such as classical viscoelasticity [6], swelling of polymers [7], thermo-oxidative degradation of polymer composites [8,9], and growth of biological materials [10] and crystallization of polymers [11]. Malek and Rajagopal [12] proposed that processes for fluid mixtures are governed by the maximization of the rate of dissipation constraint. Karra and Rajagopal [8] developed a mixture theory model and its constitutive relations based on this constraint for diffusion of a fluid through a viscoelastic solid. Karra and Rajagopal [9] also developed a mixture theory model for degradation of polyimides due to oxidation. A limitation of their model is that it cannot predict the oxidation layer thickness growth. Hall and Rajagopal [13] proposed a mixture theory model for diffusion of chemically reacting fluid through an anisotropic solid based on the maximization of the rate of entropy production constraint, considering anisotropic effective reaction rates and the limits of diffusion-dominated (diffusion of the reactants is far more rapid than the reaction)

---

* This Chapter is has been adapted from "Hall R, Gajendran H, Masud A. Diffusion of chemically reacting fluids through nonlinear elastic solids: mixture model and stabilized methods. Mathematics and Mechanics of Solids. 2014" .

and reaction-dominated (the reaction is far more rapid than the diffusion of the reactants) processes. This model in general can be applied to a variety of processes involving directionality of flow, of the reaction process and of the solid medium, such as curing of composites using vacuum assisted resin transfer molding (VARTM), prediction of oxidation layer growth in composites and slurry infiltration in manufacturing of composites.

One of the applications of interest in this work is the oxidation of polymer matrix composites. Tandon et al. [14] conducted experiments to study oxidation processes in a high-temperature polyimide resin used in aerospace composites, and developed an oxidation reaction rate model that conforms to the observed experimental data. In this work, we implement this oxidation model in the context of mixture theory. Schoeppner et al. [15] and Whitcomb et al. [16,17] developed finite element algorithms for the diffusion reaction equation to model the oxidation in PMR-15 resin and polymer matrix composites. In their work, the fibers and matrix were modeled in a discrete sense and thus their algorithm was computationally intensive. Whitcomb [16] proposed an adaptive mesh strategy and decoupled subdomain strategy to reduce the computational cost of their algorithm. Their adaptive mesh strategy requires a prior knowledge of oxidation layer growth to constrain the unoxidized region, thus reducing the number of unknowns in the problem.

A significant feature of the mixture theory is the modeling of the constituents of the composite in an effective medium sense to reduce the computational cost of modeling chemically reacting multi-constituent mixtures while retaining information involving the kinematic and kinetic responses of the individual constituents. In this work, a stabilized mixed finite element formulation is employed for the conservation equations in the mixture theory and the performance of the model and the numerical algorithm is showcased for various applications.

The outline of the paper is as follows. In section 2.2, we present the governing equations and the constitutive relations derived from the mixture theory for a chemically reacting fluid diffusing through a nonlinear elastic solid in a general three dimensional context. The modeling assumptions and the one-dimensional form of the general mixture theory are presented in section 2.3. In section 2.4, we present the weak form of the mixture theory governing equations and develop the VMS based stabilized method. Section 2.5 presents the finite element results of the

mixture theory for Fick's diffusion problem, in the context of matching an analytical solution for demonstration of accuracy and stability of the numerical approach; oxidation of PMR-15 resin; and slurry infiltration in polymer matrix composites. Conclusions are drawn in section 2.6.

2.2 Mixture Theory

In this section, we first present the mixture theory based model for diffusion of an anisotropic non-linear viscoelastic fluid through an anisotropic elastic solid with mutual chemical reaction, as proposed by Hall and Rajagopal [13]. A basic assumption in the mixture theory is that the constituents of the mixture co-occupy the domain and as the mixture deforms, these co-existing continua deform with respect to each other. A set of appropriate constitutive relations that are based on the constraint of maximum rate of entropy production are also presented in [13]. In the present work, we consider the constitutive relations associated with unconstrained constituent volumes. Detailed derivation is available in [13].

The equations of mass and linear momentum balance for the diffusion of a chemically reacting fluid through a finitely deforming thermoelastic solid are given as follows [13]:

$$\frac{D^{\alpha}\rho^{\alpha}}{dt} + \rho^{\alpha}\mathrm{div}\boldsymbol{v}^{\alpha} = \frac{\partial\rho^{\alpha}}{\partial t} + \mathrm{div}(\rho^{\alpha}\boldsymbol{v}^{\alpha}) = m^{\alpha} \tag{2.1}$$

$$\rho^{\alpha}\frac{D^{\alpha}\boldsymbol{v}^{\alpha}}{dt} = \mathrm{div}(\boldsymbol{T}^{\alpha})^{T} + \rho^{\alpha}\boldsymbol{b} + \boldsymbol{I}^{\alpha} \tag{2.2}$$

where, ρ^{α} is the mass concentration and m^{α} is the rate of mass transferred by chemical reaction, to constituent α, per unit mixture volume; $\boldsymbol{v}^{\alpha}$ is the velocity of constituent α and $\boldsymbol{T}^{\alpha}$ is its partial Cauchy stress, while $\boldsymbol{I}^{\alpha}$ and $\boldsymbol{b}$ are the interactive force on constituent α and the overall body force, per unit mixture volume.

The balance of energy and assumption of maximized rate of entropy production, together with Newton's third law lead to the following relations for the partial stresses on the solid and fluid, $\boldsymbol{T}^{s}$ and $\boldsymbol{T}^{f}$; the interactive force $\boldsymbol{I}^{f}$ on the fluid, the constituent entropy η^{α}, and the rate of fluid mass conversion, m^{f}, all per unit mixture volume; and the heat flux $\boldsymbol{q}$, per unit mixture area:

$$\boldsymbol{I}^f = g^f \frac{\rho^s}{\rho}\nabla\rho^f - g^s \frac{\rho^f}{\rho}\nabla\rho^s - \nabla\left[\frac{\rho^s\rho^f}{\rho}(\psi^f - \psi^s)\right] - (\nabla\theta)\frac{\rho^s\rho^f}{\rho}(\eta^f - \eta^s) - m^f(\boldsymbol{v}^f - \boldsymbol{v}^s) - \mu\,\boldsymbol{A}^v(\boldsymbol{v}^f - \boldsymbol{v}^s) \tag{2.3}$$

$$\boldsymbol{T}^s = \rho\boldsymbol{F}^s\left(\frac{\partial\psi}{\partial\boldsymbol{F}^s}\right)^T - \rho^s\left(g^s + \frac{\rho^f}{\rho}(\psi^f - \psi^s)\right)\boldsymbol{I} \tag{2.4}$$

$$\boldsymbol{T}^f = -\rho^f\left(g^f + \frac{\rho^s}{\rho}(\psi^s - \psi^f)\right)\boldsymbol{I} + \mu\,\boldsymbol{A}^L\cdot\boldsymbol{D}^f \tag{2.5}$$

$$\eta^\alpha = -\frac{\partial\psi^\alpha}{\partial\theta} - \frac{\mu}{\rho}c_\theta^\alpha\dot{\theta} \tag{2.6}$$

$$\frac{\boldsymbol{q}}{\theta} = -\mu\,\boldsymbol{l}\nabla\theta + \frac{\rho^s\rho^f}{\rho}(\eta^f - \eta^s)(\boldsymbol{v}^f - \boldsymbol{v}^s) \tag{2.7}$$

$$m^f = \frac{1}{\mu c_{\mathrm{m}}}\left[-(g^f - g^s) - \frac{1}{2}(\boldsymbol{v}^f - \boldsymbol{v}^s)\cdot(\boldsymbol{v}^f - \boldsymbol{v}^s)\right] \tag{2.8}$$

where the chemical potential g^α of constituent α is defined through

$$g^\alpha \equiv \rho\frac{\partial\psi}{\partial\rho^\alpha} \tag{2.9}$$

ρ, ψ and θ are the mixture density, mixture Helmholtz energy and temperature; while ψ^α are the constituent Helmholtz energies; Material parameters c_θ^α and c_{m} are respectively associated with the constituent entropies, and with mass transfer, while $\boldsymbol{l}$ is the mixture thermal conductivity tensor; $\boldsymbol{F}^s$ is the solid deformation gradient; $\boldsymbol{A}^v$ and $\boldsymbol{A}^L$ are drag and viscosity coefficient tensors and $\boldsymbol{D}^f$ is the fluid rate of deformation tensor.

The rate of mass transfer to the fluid m^f, is determined in coordination with the orientation average of the rate of reaction tensor $\dot{\Gamma}$. Because of the presence of only two constituents, the mass balance provides that the rate of mass converted to the solid is the one lost from the fluid:

$$m^s = -m^f \tag{2.10}$$

In the diffusion-dominated approximation (diffusion of the reactants is far more rapid than the reaction), the operator $\dot{\Pi}\{\boldsymbol{n}, \boldsymbol{X}^s, t\}$ provides the directional solid mass conversion rate in the direction **-*n***, per unit mixture volume, such that:

$$m^s = \frac{1}{4\pi} \int_{\alpha=0}^{4\pi} \dot{\Pi}\{\boldsymbol{n}[\alpha], \boldsymbol{X}^s, t\}\, d\alpha \tag{2.11}$$

where, $\boldsymbol{n}$ is the outward unit normal, $\boldsymbol{X}^s$ is the reference coordinate of the solid, α is the solid angle, and a second-order representation is assumed for the operator $\dot{\Pi}\{\boldsymbol{n}, \boldsymbol{X}^s, t\}$

$$\dot{\Pi}\{\boldsymbol{n}, \boldsymbol{X}^s, t\} \approx \boldsymbol{n} \cdot \dot{\boldsymbol{\Gamma}}[\boldsymbol{X}^s, t]\boldsymbol{n} \tag{2.12}$$

with the tensor

$$\boldsymbol{\Gamma}[\boldsymbol{X}^s, t] = \int_0^t \dot{\boldsymbol{\Gamma}}[\boldsymbol{X}^s, \bar{t}]\, d\bar{t} \tag{2.13}$$

thus, providing an anisotropic measure of the extent of reaction of the solid.

Employing in the present work the Lagrangian solid strain measure $\boldsymbol{E}^s$ and referring $\boldsymbol{\Gamma}$ to material coordinates, the Lagrange multiplier arising from the constraint of maximized rate of entropy production is given by, in the general case, cf. [13]:

$$\mu = \frac{1}{2} + \frac{\left\{ \frac{1}{4} \dot{\Gamma}^0_{IJ} \Gamma^0_{KL} \Gamma^0_{MN} E^s_{OP} K^0_{IJKLMNOP} - \nabla\theta \cdot \frac{\rho^s \rho^f}{\rho} (\eta^f - \eta^s)(\boldsymbol{v}^f - \boldsymbol{v}^s) - m^f (\boldsymbol{v}^f - \boldsymbol{v}^s) \cdot (\boldsymbol{v}^f - \boldsymbol{v}^s) \right\}}{\left\{ \begin{array}{l} \boldsymbol{D}^f \cdot \boldsymbol{A}^{\boldsymbol{L}} \cdot \boldsymbol{D}^f + c_\theta \dot{\theta}^2 + (\boldsymbol{v}^f - \boldsymbol{v}^s) \cdot \boldsymbol{A}^{\boldsymbol{v}} (\boldsymbol{v}^f - \boldsymbol{v}^s) + \dot{\boldsymbol{\Gamma}}^0 \cdot \boldsymbol{A}^{0\boldsymbol{\Gamma}} \cdot \dot{\boldsymbol{\Gamma}}^0 + \nabla\theta \cdot \boldsymbol{l} \nabla\theta + c_{\mathrm{m}} (m^f)^2 \\ + \frac{1}{2} \dot{\Gamma}^0_{AB} \Gamma^0_{CD} \Gamma^0_{EF} E^s_{GH} K^0_{ABCDEFGH} \end{array} \right\}} \tag{2.14}$$

where $K^0_{IJKLMNOP}$ is a tensor which couples the mechanical and chemically-influenced attributes of the model, in a way that is compatible with the results of the maximization of the rate of entropy production as described in [13]. Because η^α and m^f depend on μ, eq. (2.14) is a cubic equation in μ. To obtain a single-valued relation for μ, the following approximations are made:

1. We assume that the attributes of the Helmholtz free energy functions of the constituents and the mixture can be represented in terms of suitably condensed forms, $\psi^s = \psi^f = \psi$, $\eta^s = \eta^f = \eta$.
2. Slow diffusion permits neglect of the squared relative kinetic energy terms $((\boldsymbol{v}^f - \boldsymbol{v}^s)\cdot(\boldsymbol{v}^f - \boldsymbol{v}^s))^2$, which are assumed also negligible relative to the drag force.
3. We assume that the reaction is near enough to equilibrium to neglect the squared difference in the chemical potentials of the constituents, and the product of the chemical potential difference with the relative kinetic energy.

The Lagrange multiplier is thus reduced to the following single-valued function:

$$\mu = \frac{1}{2} + \frac{\frac{1}{4}\dot{\Gamma}^0_{IJ}\Gamma^0_{KL}\Gamma^0_{MN}E^s_{OP}K^0_{IJKLMNOP}}{\left\{\begin{array}{l}\boldsymbol{D}^f\cdot\boldsymbol{A}^{\boldsymbol{L}}\cdot\boldsymbol{D}^f + c_\theta\dot{\theta}^2 + (\boldsymbol{v}^f - \boldsymbol{v}^s)\cdot\boldsymbol{A}^{\boldsymbol{v}}(\boldsymbol{v}^f - \boldsymbol{v}^s) + \\ \dot{\boldsymbol{\Gamma}}^0\cdot\boldsymbol{A}^{0\boldsymbol{\Gamma}}\cdot\dot{\boldsymbol{\Gamma}}^0 + \nabla\theta\cdot\boldsymbol{l}\nabla\theta + \frac{1}{2}\dot{\Gamma}^0_{AB}\Gamma^0_{CD}\Gamma^0_{EF}E^s_{GH}K^0_{ABCDEFGH}\end{array}\right\}} \tag{2.15}$$

It can be noted that the tensor $\boldsymbol{K^0}$ will have mostly zero-valued components. If reaction processes such as oxidation are considered, in which the reaction is several times faster in the fiber direction than the transverse directions thus promoting a unidirectional reaction assumption, and assuming transversely isotropic coupling to the strains, the term involving $\boldsymbol{K^0}$ reduces to the following expression, involving 4 independent constants:

$$\dot{\Gamma}^0_{IJ}\Gamma^0_{KL}\Gamma^0_{MN}E^s_{OP}K^0_{IJKLMNOP} = \dot{\Gamma}^0_{11}(\Gamma^0_{11})^2\left[K^0_1 E^s{}_{11} + K^0_2(E^s{}_{22} + E^s{}_{33}) + K^0_3(E^s{}_{12} + E^s{}_{31}) + K^0_4 E^s{}_{23}\right] \tag{2.16}$$

In the present work, the influence of the energy and entropy production relations are retained through the presence of the Lagrange multiplier, which is obtained via invoking the constraint of maximized rate of entropy production. The equations explicitly retained are the constituent momentum balances and the mass balance equation, which can be considered most strongly enforced. In accordance with the present study being isothermal, the traditional heat capacity measures of the constituents are lost through the assumption above that the constituent entropy functions can be replaced by an overall entropy function. In general, for anisothermal processes, the Helmholtz and entropy functions of each constituent would be retained. It is interesting to

note, however, that the present system of equations incorporates the rate of temperature in combination with a non-traditional overall material property c_θ (the density average of the c_θ^α properties), which may provide a simplified approach to accounting for a class of homogenized anisothermal effects. The present paper however considers only isothermal conditions.

2.3 One Dimensional Mixture Theory

Consider a one dimensional mixture domain Ω of length L with boundary $\partial\Omega = \left\{ x \middle| x \in \{0, L\} \right\}$. The governing equations for the one-dimensional case under isothermal conditions are as follows:

$$\frac{\partial \rho^\alpha}{\partial t} + \frac{\partial \rho^\alpha}{\partial x} v_1^\alpha + \rho^\alpha \frac{\partial v_1^\alpha}{\partial x} - m^\alpha = 0 \tag{2.17}$$

$$\frac{\partial T_{11}^\alpha}{\partial x} + \rho^\alpha b_1 + I_1^\alpha - \rho^\alpha \frac{D v_1^\alpha}{D t} = 0 \tag{2.18}$$

The corresponding stresses and interactive force on the constituents can be written as follows:

$$T_{11}^s = \rho F_{11} \frac{\partial \psi}{\partial F_{11}} - \rho^s \left(\rho \frac{\partial \psi}{\partial \rho^s} + \frac{\rho^f}{\rho} (\psi^f - \psi^s) \right) \tag{2.19}$$

$$T_{11}^f = -\rho^f \left(\rho \frac{\partial \psi}{\partial \rho^f} + \frac{\rho^s}{\rho} (\psi^s - \psi^f) \right) + \mu \mathrm{A}^L \frac{\partial v_1^f}{\partial x} \tag{2.20}$$

$$\begin{aligned} I_1^f = {} & \frac{\partial \psi}{\partial \rho^f} \rho^s \frac{\partial \rho^f}{\partial x} - \frac{\partial \psi}{\partial \rho^s} \rho^f \frac{\partial \rho^s}{\partial x} - \frac{\partial}{\partial x} \left[\frac{\rho^s \rho^f}{\rho} (\psi^f - \psi^s) \right] - \\ & \frac{\partial \theta}{\partial x} \frac{\rho^s \rho^f}{\rho} (\eta^f - \eta^s) - m^f (v_1^f - v_1^s) - \mu \mathrm{A}^v (v_1^f - v_1^s) \end{aligned} \tag{2.21}$$

We consider the following Helmholtz free energy function that corresponds to the 1-D representation of a transversely isotropic thermoelastic solid permeated by a chemically reacting Newtonian fluid.

$$\psi = A^s + (B^s + c^s)(\theta - \theta^s) - \frac{c_1^s}{2}(\theta - \theta^s)^2 - c_2^s \theta \ln(\frac{\theta}{\theta^s}) + \frac{1}{\rho_T}\left\{\bar{R}\theta\rho^f + k_2^f \rho^f\right\} + \frac{\rho^s}{\rho}\frac{1}{\rho_T^s}\left\{\frac{1}{2}\lambda^s + \mu_T^s + \alpha^s + 2(\mu_L^s - \mu_T^s) + \frac{1}{2}\beta^s\right\}(E_{11}^s)^2 + \Lambda \tag{2.22}$$

$$\Lambda = \int \frac{\mu}{2}\left\{(\Gamma_{11}^0)^2 \bar{K}_1 E_{11}^s + 2\dot{\Gamma}_{11}^0 \bar{A}^{0\Gamma}\right\} d\Gamma_{11}^0 \tag{2.23}$$

where Λ describes the coupling between the solid strain and the extent of reaction, consistent with the developments of [13]; $\lambda^s, \alpha^s, \mu_L^s, \mu_T^s, \beta^s$ are the transversely isotropic material constants, which in one dimension reduce to the elastic moduli of the solid. ρ_T^s, ρ_T are the true solid density and the true mixture density respectively. $\bar{R}$ is the ratio of the universal gas constant to the molecular weight of the fluid. $K_1^0 = -\rho\bar{K}_1$ and $A^{0\Gamma} = -\rho\bar{A}^{0\Gamma}$ are defined for convenient manipulations involving Λ.

Remark: *For the case of slurry deposition process that is presented in the section 2.5.3,* Γ_{11}^0 *represents the extent of material deposition. For this case, the term* Λ *provides coupling between the solid strain and the extent of deposition of the suspended particles. We assume that this deposition function* Γ_{11}^0 *is in fact a function of the volume fraction of particles, which is considered a process parameter.*

The one dimensional representation of the *Lagrange multiplier* μ is given as:

$$\mu = \frac{1}{2} - \frac{\frac{1}{4}\dot{\Gamma}_{11}^0(\Gamma_{11}^0)^2 \rho\bar{K}_1 E_{11}^s}{\mathrm{A}^L(\frac{\partial v_1^f}{\partial x})^2 + c_\theta\dot{\theta}^2 + \mathrm{A}^v(v_1^f - v_1^s)^2 - \rho\bar{\mathrm{A}}^{0\Gamma}(\dot{\Gamma}_{11}^0)^2 + I_{11}(\frac{\partial\theta}{\partial x})^2 - \frac{1}{2}\dot{\Gamma}_{11}^0(\Gamma_{11}^0)^2 \rho\bar{K}_1 E_{11}^s} \tag{2.24}$$

Also, from mass balance law and Newton's third law we see that the solid and the fluid interactive forces have the following relationship:

$$I_1^s + m^s v_1^s = -(I_1^f + m^f v_1^s) \tag{2.25}$$

2.3.1 Modeling assumptions and methodology

In mixture theory where both solid and fluid co-occupy the domain and fluid moves relative to the deforming solid, it is natural to write the fluid balance laws in an Arbitrary Lagrangian Eulerian (ALE) framework [18-20]. For the class of problems considered in this work, the inertial effects on the solid are assumed to be negligible. Based on these modeling assumptions, the balance laws eqs. (2.17) and (2.18) can be rewritten as follows.

$$\frac{\partial \rho^s}{\partial t} + \frac{\partial \rho^s}{\partial x} v_1^s + \rho^s \frac{\partial v_1^s}{\partial x} - m^s = 0 \tag{2.26}$$

$$\frac{\partial T_{11}^s}{\partial x} + \rho^s b_1 + I_1^s = 0 \tag{2.27}$$

$$\left.\frac{\partial \rho^f}{\partial t}\right|_Y + \frac{\partial \rho^f}{\partial x}(v_1^f - v_1^m) + \rho^f \frac{\partial v_1^f}{\partial x} - m^f = 0 \tag{2.28}$$

$$\frac{\partial T_{11}^f}{\partial x} + \rho^f b_1 + I_1^f - \rho^f \left.\frac{\partial v_1^f}{\partial t}\right|_Y - \rho^f (v_1^f - v_1^m)\frac{\partial v_1^f}{\partial x} = 0 \tag{2.29}$$

where, $\left.\frac{\partial (\cdot)}{\partial t}\right|_Y$ represents the time derivative in the ALE frame [19,20] and v_1^m is the fluid mesh velocity. It is important to note that as the solid domain deforms, the Lagrangian mesh that is tied to material points deforms together with it. Consequently, the mesh velocity v_1^m is set equal to v_1^s where, v_1^s is the velocity of the solid domain. Accordingly, the constitutive relations can be rewritten as,

$$T_{11}^s = \rho F_{11} \frac{\partial \psi}{\partial F_{11}} - \rho^s \rho \frac{\partial \psi}{\partial \rho^s} \tag{2.30}$$

$$T_{11}^f = -\rho^f \rho \frac{\partial \psi}{\partial \rho^f} + \mu \mathrm{A}^L \frac{\partial v^f}{\partial x} \tag{2.31}$$

$$I_1^f = -m^f (v_1^f - v_1^s) - \mu \mathrm{A}^v (v_1^f - v_1^s) \tag{2.32}$$

$$m^f = \dot{\Gamma}_{11}^0 \tag{2.33}$$

Remark: *In [13] an expression for the rate of mass conversion for fluid m^f is derived via maximization of the rate of dissipation constraint. However, in the present work we prescribe an oxidation rate given in [14] that is developed based on physical measurements. Likewise, in the slurry infiltration model we prescribe a rate of particle deposition as is given in [28]. Because of these postulated rates, the physics involved in the consistent derivation of mass conversion given in [13] is circumvented.*

2.4 Weak Form and Development of Stabilized Method

The initial conditions for the density and velocity fields of the two constituents, and the displacement field of the solid are:

$$\rho^\alpha(x,0) = \rho_0^\alpha; \quad v_1^\alpha(x,0) = v_0^\alpha; \quad u_1^s(x,0) = u_0^s \quad \forall\, x \in \Omega \tag{2.34}$$

The boundary $\partial\Omega$ admits decomposition into $\partial\Omega_g$ and $\partial\Omega_h$, where $\partial\Omega_g \bigcap \partial\Omega_h = \phi$, and we denote the unit normal to the boundary $\partial\Omega$ by n_1. The boundary conditions for the problem are:

$$\begin{aligned}
&\rho^f = \rho_0^f \quad \text{on} \quad \partial\Omega_g^{\rho^f} \times]0,\mathrm{T}[\\
&v_1^f = v_0^f \quad \text{on} \quad \partial\Omega_g^f \times]0,\mathrm{T}[\\
&u_1^s = u_0^s \quad \text{on} \quad \partial\Omega_g^s \times]0,\mathrm{T}[\\
&T_{11}^f n_1 = t_0^f \quad \text{on} \quad \partial\Omega_h^f \times]0,\mathrm{T}[\\
&T_{11}^s n_1 = t_0^s \quad \text{on} \quad \partial\Omega_h^s \times]0,\mathrm{T}[
\end{aligned} \tag{2.35}$$

where ρ_0^f, v_0^f are the prescribed fluid density and velocity, and u_0^s is the prescribed solid displacement. t_0^f and t_0^s represent the prescribed fluid and solid boundary tractions, respectively.

Let g^α and w_1^α denote the weighting functions for the balance of mass and linear momentum for the corresponding constituent, respectively. The appropriate spaces for these weighting functions are:

$$\mathcal{V} = \left\{ g^\alpha \,\middle|\, g^\alpha \in H^1(\Omega), g^\alpha = 0 \ \text{ on } \ \partial\Omega_g^{\rho^\alpha} \right\} \tag{2.36}$$

$$\mathcal{Q} = \left\{ w_1^\alpha \,\middle|\, w_1^\alpha \in H^1(\Omega), w_1^\alpha = 0 \ \text{ on } \ \partial\Omega_g^\alpha \right\} \tag{2.37}$$

The corresponding trial solution spaces for the fluid and solid density, fluid velocity and solid displacement are:

$$\mathcal{S}^{\rho^\alpha} = \left\{ \rho^\alpha(\bullet,t) \middle| \rho^\alpha(\bullet,t) \in H^1(\Omega), \rho^\alpha(\bullet,t) = \rho_0^\alpha \ \text{ on } \partial\Omega_g^{\rho^\alpha} \times]0,T[\right\} \tag{2.38}$$

$$\mathcal{S}^f = \left\{ v_1^f(\bullet,t) \middle| v_1^f(\bullet,t) \in H^1(\Omega), v_1^f(\bullet,t) = v_0^f \ \text{ on } \partial\Omega_g^f \times]0,T[\right\} \tag{2.39}$$

$$\mathcal{S}^s = \left\{ u_1^s(\bullet,t) \middle| u_1^s(\bullet,t) \in H^1(\Omega), u_1^s(\bullet,t) = u_0^s \ \text{ on } \partial\Omega_g^s \times]0,T[\right\} \tag{2.40}$$

The weak form of governing equations for the solid-fluid system can be stated as follows: For all constituents $\alpha \in \{s, f\}$, $\forall\, t \in (0,T)$, $\forall g^\alpha \in \mathcal{V}$ and $\forall w_1^\alpha \in \mathcal{Q}$, solve $\rho^\alpha \in \mathcal{S}^{\rho^\alpha}$, $v_1^f \in \mathcal{S}^f$ and $u_1^s \in \mathcal{S}^s$ such that the following system holds.

Weak form of equations for the fluid

$$(g^f, \frac{\partial \rho^f}{\partial t}\Big|_Y) + (g^f, (v_1^f - v_1^s)\frac{\partial \rho^f}{\partial x}) + (g^f, \rho^f \frac{\partial v_1^f}{\partial x}) - (g^f, m^f) = 0 \tag{2.41}$$

$$\begin{aligned}(\frac{\partial w_1^f}{\partial x}, T_{11}^f) - (w_1^f, \rho^f b_1) - (w_1^f, I_1^f) + (w_1^f, \rho^f \frac{\partial v_1^f}{\partial t}\Big|_Y) + \\ (w_1^f, \rho^f (v_1^f - v_1^s)\frac{\partial v_1^f}{\partial x}) - (w_1^f, T_{11}^f n_1)_{\partial\Omega_h^f} = 0\end{aligned} \tag{2.42}$$

Weak form of equations for the solid:

$$(g^s, \frac{\partial \rho^s}{\partial t}) + (g^s, \rho^s \frac{\partial v_1^s}{\partial x}) + (g^s, v_1^s \frac{\partial \rho^s}{\partial x}) - (g^s, m^s) = 0 \tag{2.43}$$

$$(\frac{\partial w_1^s}{\partial x}, T_{11}^s) - (w_1^s, \rho^s b_1) - (w_1^s, I_1^s) - (w_1^s, T_{11}^s n_1)_{\partial\Omega_h^s} = 0 \tag{2.44}$$

where, $(\bullet,\bullet) = \int_\Omega (\bullet)\, d\Omega$ is the $L_2(\Omega)$ inner product.

2.4.1 Fluid Sub-System: Residual-based Stabilization

Our objective is to model the diffusion of a chemically reacting fluid through a nonlinear elastic solid, a phenomenon that is observed in the process modeling of composites, oxidation of resin/composites, and slurry infiltration in porous media, to name a few. In the modeling of these

processes, fluid mass concentration is invariably specified at the inlet boundary. Since the strong form of mass balance of fluid given in eq. (2.17) is a first order hyperbolic equation, any specified mass concentration boundary condition at the inlet that is different from the initial condition results in a discontinuous fluid concentration field. This discontinuity introduces spurious oscillations in the computed solution right at the beginning of the nonlinear iterative process that can lead to non-convergent and therefore non-physical solutions.

To address this issue, we consider the weak form of the balance of mass equation for the fluid that is written in an ALE form. We employ Variational Multiscale (VMS) ideas [22-25] and develop a stabilized weak form for eq. (2.41). Underlying idea of VMS is an additive decomposition of the solution field into coarse and fine scale components as given below.

$$\rho^f = \hat{\rho}^f + \tilde{\rho}^f \tag{2.45}$$

$$g^f = \hat{g}^f + \tilde{g}^f \tag{2.46}$$

where, $\hat{\rho}^f, \tilde{\rho}^f$ represents the coarse-scale and fine-scale components of the density field and $\hat{g}^f, \tilde{g}^f$ represents the coarse-scale and fine-scale counterpart of the weighting function respectively. Various scale separations of ρ^f are possible in eq. (2.46). However, they are subject to the restriction imposed by the stability of the formulation that requires the spaces for the coarse-scale and fine-scale functions to be linearly independent. In the development presented here, the space of coarse-scale weighting functions is identified with the standard finite element spaces, while the fine-scale weighting functions can contain various finite dimensional approximations, e.g., bubble functions or p-refinements or higher order NURBS functions.

Substituting eqs. (2.45) and (2.46) in eq. (2.41) and employing the linearity of the weighting function slot in eq. (2.41), we obtain the coarse-scale problem and the fine-scale problem as given in eqs. (2.47) and (2.48) respectively.

$$\hat{\mathcal{W}}^{\rho^f} = (\hat{g}^f, \frac{\partial(\hat{\rho}^f + \tilde{\rho}^f)}{\partial t}\Big|_Y) + (\hat{g}^f, \frac{\partial(\hat{\rho}^f + \tilde{\rho}^f)v_1^f}{\partial x}) - (\hat{g}^f, v_1^s \frac{\partial(\hat{\rho}^f + \tilde{\rho}^f)}{\partial x}) - (\hat{g}^f, m^f) = 0 \tag{2.47}$$

$$\tilde{\mathcal{W}}^{\rho^f} = (\tilde{g}^f, \frac{\partial(\hat{\rho}^f + \tilde{\rho}^f)}{\partial t}\Big|_Y) + (\tilde{g}^f, \frac{\partial(\hat{\rho}^f + \tilde{\rho}^f)v_1^f}{\partial x}) - (\tilde{g}^f, v_1^s \frac{\partial(\hat{\rho}^f + \tilde{\rho}^f)}{\partial x}) - (\tilde{g}^f, m^f) = 0 \tag{2.48}$$

It is important to note that both systems are nonlinear, and are also fully coupled in terms of the scales. The key idea at this point is to solve the fine-scale problem eq. (2.48) locally, using analytical methods or numerical methods, and extract the fine-scale component, $\tilde{\rho}^f$. This can then be substituted in the corresponding coarse-scale problem given in eq. (2.47), thereby eliminating the fine-scales, yet modeling their effects.

Solution of the Fine Scale Problem:

We segregate the terms into coarse-scale and fine-scale terms and group all the terms containing coarse-scale density field

$$\tilde{\mathcal{W}}^{\rho^f} = (\tilde{g}^f, \left.\frac{\partial \tilde{\rho}^f}{\partial t}\right|_Y) + (\tilde{g}^f, \frac{\partial \tilde{\rho}^f v_1^f}{\partial x}) - (\tilde{g}^f, v_1^s \frac{\partial \tilde{\rho}^f}{\partial x}) + (\tilde{g}^f, \hat{R}) = 0 \tag{2.49}$$

where, $\hat{R}$ is the residual of the Euler-Lagrange equations of the coarse-scales over element interiors and is given as,

$$\hat{R} = \left.\frac{\partial \hat{\rho}^f}{\partial t}\right|_Y + \frac{\partial \hat{\rho}^f v_1^f}{\partial x} - v_1^s \frac{\partial \hat{\rho}^f}{\partial x} - m^f(\hat{\rho}^f) \tag{2.50}$$

In obtaining the above form of the fine scale problem, we have assumed that the fluid mass conversion rate is a function of the coarse-scale fluid density field only, $m^f(\hat{\rho}^f, \tilde{\rho}^f) \approx m^f(\hat{\rho}^f)$. To reduce the complexity of the fine-scale problem and also to reduce the computational cost for evaluating the fine-scale solution field, we assume that the fine-scale field vanishes at the element boundaries.

$$\tilde{g}^f = 0, \;\; \tilde{\rho}^f = 0 \quad \text{on} \quad \Gamma^e \tag{2.51}$$

Remark: *The assumption that fine-scales vanish at the inter-element boundaries helps in keeping the presentation of the ideas simple and concise. Relaxing this assumption in fact leads to a more general framework. This however requires Lagrange multipliers to enforce the continuity of the fine-scales fields across inter element boundaries. It is important to note that Lagrange multiplies can be accommodated in the present hierarchical framework as well.*

Using Backward Euler time integration scheme and assuming that the fine-scale fluid density field at *n*-th time step is zero, $\tilde{\rho}_n^f = 0$, we can obtain the time discretized form of the eq. (2.49) as given below,

$$\tilde{\mathcal{W}}^{\rho^f} = (\tilde{g}^f, \frac{\tilde{\rho}^f}{\Delta t}\Big|_Y) + (\tilde{g}^f, \frac{\partial \tilde{\rho}^f v_1^f}{\partial x}) - (\tilde{g}^f, v_1^s \frac{\partial \tilde{\rho}^f}{\partial x}) + (\tilde{g}^f, \hat{R}) = 0 \tag{2.52}$$

The fine-scale fields are represented by bubble functions within each element and are given as,

$$\tilde{g}_{n+1}^f = b_2^e \bar{g}_{n+1}^f, \quad \tilde{\rho}_{n+1}^f = b_1^e \bar{\rho}_{n+1}^f \tag{2.53}$$

where, b_1^e, b_2^e are bubble functions and $\bar{g}_{n+1}^f$, $\bar{\rho}_{n+1}^f$ are the coefficients associated with the fine-scale fields over the element, as shown schematically in Figure 2.1.

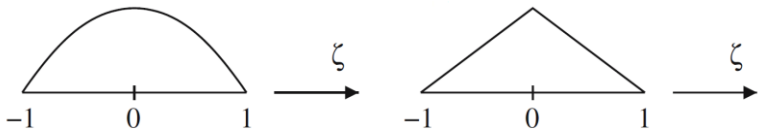

Figure 2.1. Schematic representation of quadratic and linear-hat bubbles

Substituting eq. (2.53) in eq. (2.52), we can obtain the fine-scale density field via solution of eq. (2.52) as follows,

$$\tilde{\rho}^f = \tau \hat{R} \tag{2.54}$$

where, $\hat{R}$ is the residual of the Euler-Lagrange equations of the coarse-scales for eq. (2.47). The stabilization parameter, τ is given as,

$$\tau = \frac{-b_1^e (b_2^e, 1)_{\Omega_e}}{(b_2^e, \frac{1}{\Delta t} b_1^e)_{\Omega_e} + (b_2^e, \frac{\partial v_1^f}{\partial x} b_1^e)_{\Omega_e} + (b_2^e, v_1^f \frac{\partial b_1^e}{\partial x})_{\Omega_e} - (b_2^e, v_1^s \frac{\partial b_1^e}{\partial x})_{\Omega_e}} \tag{2.55}$$

We now substitute the fine-scale solution given in the eq. (54) into the coarse-scale problem, eq. (2.47).

$$\hat{\mathcal{W}}^{\rho^f} = (\hat{g}^f, \frac{\partial \hat{\rho}^f}{\partial t}\bigg|_Y) + (\hat{g}^f, \frac{\partial \hat{\rho}^f v_1^f}{\partial x}) - (\hat{g}^f, v_1^s \frac{\partial \hat{\rho}^f}{\partial x}) - (\hat{g}^f, m^f) + (\hat{g}^f, \left(\frac{1}{\Delta t} + \frac{\partial v_1^s}{\partial x}\right)\tau \hat{R}) - (\frac{\partial \hat{g}^f}{\partial x}, \left(v_1^f - v_1^s\right)\tau \hat{R}) = 0 \tag{2.56}$$

Equation (2.56) represents the modified coarse-scale problem with the fine-scale effects embedded implicitly via the coarse-scale residual terms. The first four integral terms in eq. (2.56) correspond to the standard Galerkin method for the balance of mass for the fluid. The last two terms in the eq. (2.56) have appeared because of the fine-scale density field. It is important to note that the fine-scale density does not explicitly appear in eq. (2.56), rather the fine-scale effects are implicitly reflected in this form via the modeling terms.

Equations (2.56), (2.42), (2.43) and (2.44) are linearized and solved simultaneously using Newton-Raphson solution procedure. This coupled system of equations is discretized-in-time using backward Euler scheme, while linear and quadratic Lagrange elements with equal order fields are employed. The resulting stiffness matrix for the full system is non-symmetric.

2.5 Numerical Results

We present three test cases that investigate the stability and accuracy of the numerical method developed for the mixture theory model described in section 2.3. In section 2.5.1, we solve a reduced mixture model that is equivalent to the Fick's diffusion problem. A system comprising a first order hyperbolic equation and an algebraic equation is solved and the results are compared with the exact solution. Section 2.5.2 presents the oxidation problem of PMR-15 resin wherein full system of mixture theory equations is solved and the results are compared with the experimental and numerical results reported in Tandon et al. [14]. Section 2.5.3 simulates slurry infiltration process that is involved in the manufacturing of composites, and a parametric study of the reduction in the porosity of the solid as a function of slurry particle fraction and initial solid porosity are presented.

2.5.1 Fick's diffusion problem

In this section we employ a reduced mixture model to solve Fick's diffusion problem. The transient Fick's diffusion equation can be derived from the mixture theory balance laws, eqs.

(2.17) and (2.18) based on the following simplifications: (a) solid is assumed to be rigid, (b) fluid is assumed ideal, (c) fluid inertial effects are neglected, and (d) fluid is assumed non-reactive. The constitutive relations for an ideal fluid and the interactive force between the fluid and rigid solid can be given as [26],

$$T_{11}^{f} = -\rho^{f}\bar{R}\theta \tag{2.57}$$

$$I_{1}^{f} = -A^{v}\rho^{f}v_{1}^{f} \tag{2.58}$$

where, A^{v} is the drag coefficient. The governing eqs. (2.17) and (2.18) can be reduced to the following system of equations,

$$\frac{\partial\rho^{f}}{\partial t} + \frac{\partial(\rho^{f}v_{1}^{f})}{\partial x} = 0 \tag{2.59}$$

$$-\frac{\partial\rho^{f}}{\partial x}\bar{R}\theta - A^{v}\rho^{f}v_{1}^{f} = 0 \tag{2.60}$$

Since the coupled system of eqs. (2.59) and (2.60) serves as a reduced order model for the mixture theory, we solve this first order system to investigate the underlying characteristics of the mixture model wherein the conservation of mass equation for the fluid is hyperbolic. The diffusivity of the solid can be written in terms of the drag coefficient of the solid as

$$D = \frac{\bar{R}\theta}{A^{v}} \tag{2.61}$$

The derivation of the eq. (2.61) is provided in Appendix A.

Remark: *Solving for fluid velocity from eq.* (2.60) *and substituting back in eq.* (2.59)*, one can obtain Fick's diffusion equation. Since our full mixture model results in a first order system, in this work we have opted to solve the reduced system also in its first order form to help serve as a test case to evaluate our numerical method.*

The unknown fields in this problem are the fluid concentration and fluid velocity and are solved with zero initial conditions. The one-dimensional domain of length 0.001 m is exposed to air at the left end of the domain where the fluid concentration is assigned a value of 22.8863E-3

kg/m^3 and fluid velocity is constrained to be zero at the right end of the domain. The gas constant $\bar{R}$ and the drag coefficient A^v are assigned values of 286.987 J/kg-K and 1.63E17 s^{-1} respectively. The problem is discretized in time with the first order Backward Euler scheme and the simulation is run for a total time of 30,000 seconds. A variable time step increment is used: the time steps employed during the first second is $\Delta t = 1\text{E-}4$, and it is increased to $\Delta t = 0.1$ for the remaining steps.

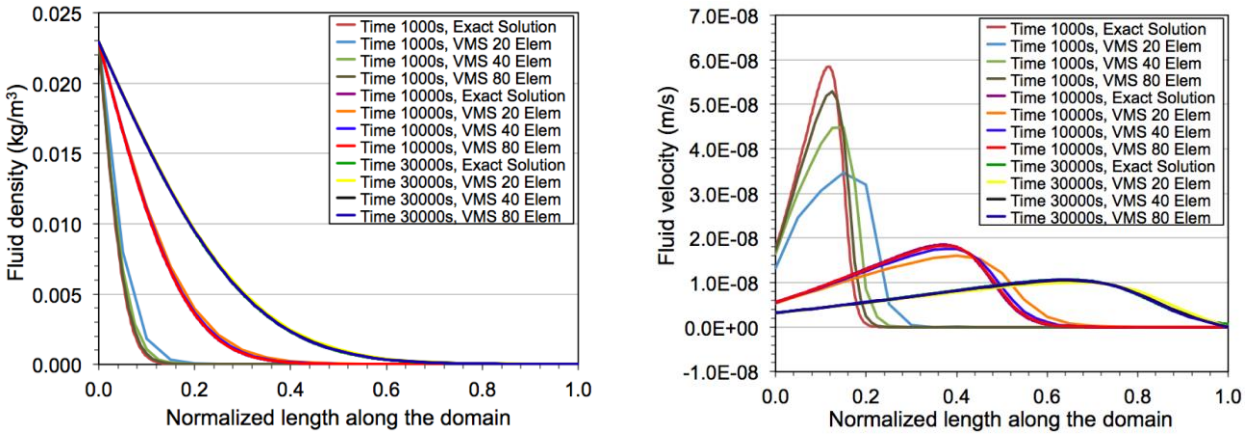

a) Fluid density: Linear Lagrange *h*-refinement b) Fluid velocity: Linear Lagrange *h*-refinement

Figure 2.2. Mesh refinement study at various time levels

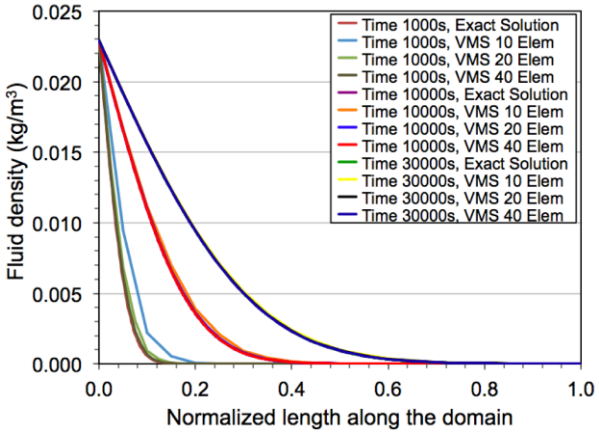

Figure 2.3. Mesh refinement study using quadratic Lagrange elements

It should be noted that eq. (2.59) is a first order hyperbolic equation for fluid concentration. For a non-zero fluid concentration boundary condition applied at the inflow, the

standard Galerkin finite element method results in oscillations around the steep front thereby causing numerical instability. We employ the variational multiscale method as described in section 4 to stabilize the formulation, and provide a comparison between of the stabilized numerical result with the exact solution. Figure 2.2a and Figure 2.2b show performance of the new method for *h*-refinement wherein we have used linear Lagrange interpolation functions. These plots show the spatial profiles of the fluid concentration and velocity fields at 1000, 10,000 and 30,000 seconds. It can be seen that as the number of elements is increased, computed solution converges to the exact solution which is a numerical validation of the consistency of the formulation. Likewise Figure 2.3 shows the convergence of the fluid density field for quadratic elements. Figure 2.4 shows the variation of L_2 norm of the error in fluid density field with mesh refinement for linear and quadratic VMS elements. A sub-optimal convergence rate of 1.54 for linear VMS element and 1.88 for quadratic VMS element is obtained for the nonlinear first order problem. Figure 2.5a and Figure 2.5b show that numerical results compare well with the exact solution at 1000, 10,000 and 30,000 seconds wherein domain is discretized with 400 elements.

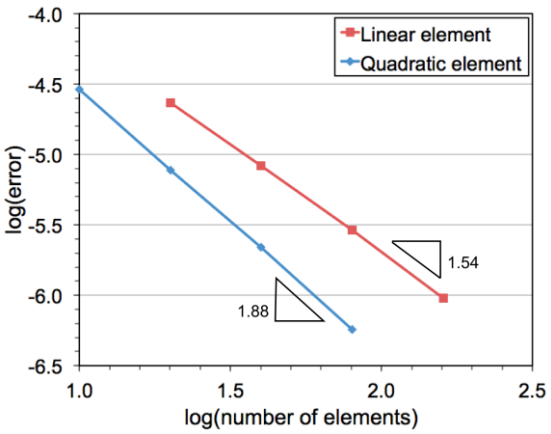

Figure 2.4. Convergence plot of L_2 norm of fluid density

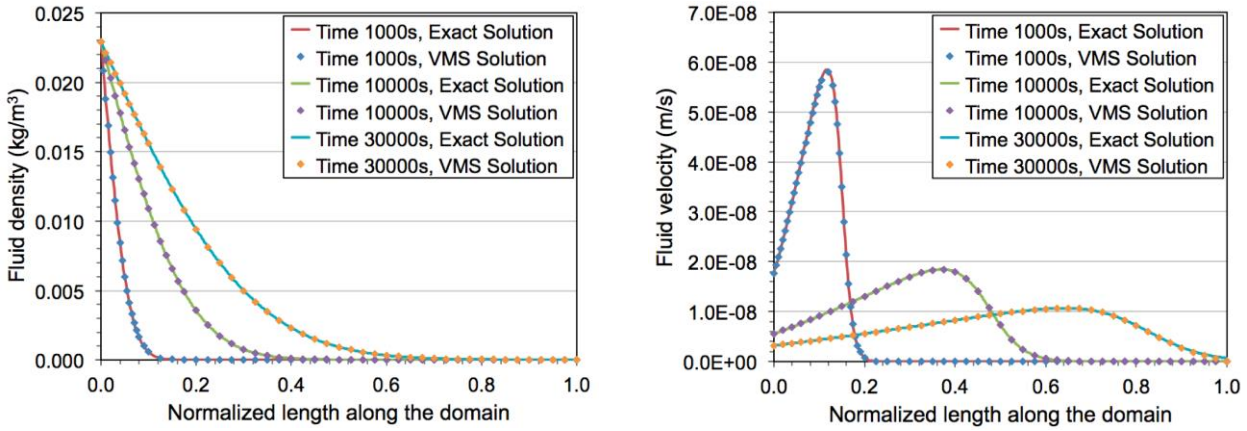

a) Fluid density along the domain b) Fluid velocity along the domain

Figure 2.5. Comparison between exact and finite element solution

In Figure 2.6a and Figure 2.6b, we show the spatial distributions of fluid density and fluid velocity for three different values of the drag coefficient for a domain of length 1 m. It can be seen that for lower drag coefficient that corresponds to higher diffusivity, fluid propagates further down in the porous solid as compared to the cases of higher drag coefficients.

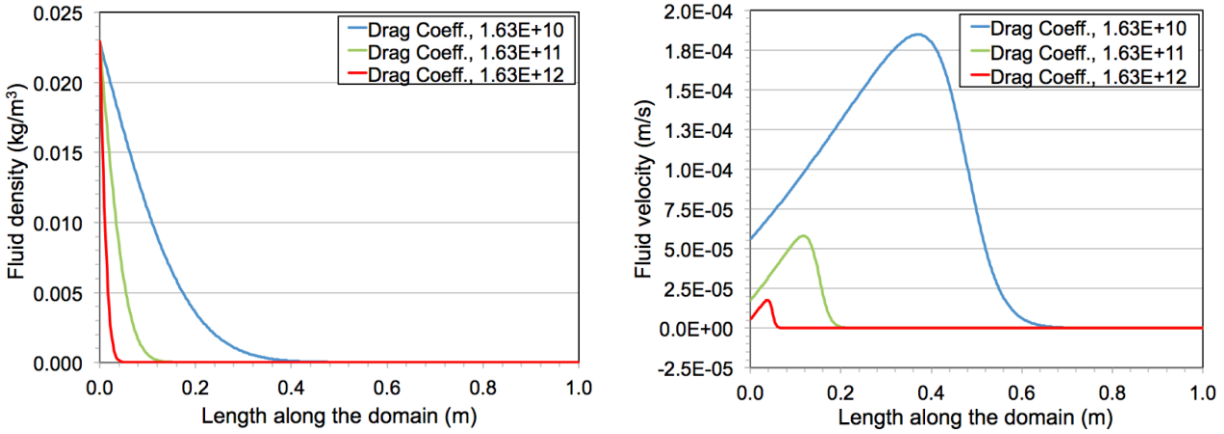

a) Fluid concentration along the domain b) Fluid velocity along the domain

Figure 2.6. Fluid quantities for three different drag coefficients

2.5.2 Oxidation of PMR-15 resin

Thermo-oxidative aging of polymer matrix composites (PMC's) in high temperature applications influences the life and performance of these materials. In this section, we present numerical results for the oxidation behavior of polyimide PMR-15 resin based on the oxidation reaction model developed in the works of Tandon et al. [14]. For the sake of completeness, we provide a brief description of the oxidation process in polymer. However, for a detailed description of the oxidation process and the reaction kinetics model, refer to [14,15]. Oxidation front in polymer materials advances through a combination of diffusion and reaction mechanism. The exposed surface reacts with the diffusing air that depletes the amount of polymer available in that region. Once this region is fully oxidized, it acts as a medium through which air/oxygen diffuses through and an active oxidation zone is formed ahead of the fully oxidized zone. Thus, at any instant of time, the oxidation process in polymers comprises of a fully oxidized zone, an active oxidation zone and a neat resin zone as shown in Figure 2.7.

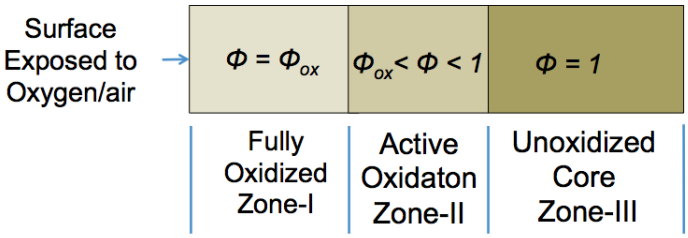

Figure 2.7. Schematic representation of thermo-oxidation process

The oxidation reaction rate implemented in this work is given in [14] as,

$$\dot{\Gamma}_{11}^{0} = \left(\frac{\phi - \phi_{ox}}{1 - \phi_{ox}}\right) R(\rho^f) \tag{2.62}$$

$$R(\rho^f) = \begin{cases} -R_0 2\xi(1 - 0.5\xi) & \phi > \phi_{ox} \\ 0 & \phi \le \phi_{ox} \end{cases} \tag{2.63}$$

$$\xi = \frac{\bar{\beta}\rho^f}{1 + \bar{\beta}\rho^f} \tag{2.64}$$

where, $\dot{\Gamma}_{11}^{0}$ is the rate of reaction, ϕ is the oxidation state variable which indicates the availability of polymer for oxidation, ϕ_{ox} specifies the fully oxidized state of the material (Zone I), R_0 is the saturated rate of reaction, and $\bar{\beta}$ is the inverse of the saturation air/Oxygen concentration. The evolution equation for the oxidation state variable ϕ is given as,

$$\frac{d\phi}{dt} = \alpha m^f \tag{2.65}$$

where, α is the constant of proportionality. ϕ varies in the active oxidation region while it assumes a value of ϕ_{ox} in the fully oxidized region and a value of 1.0 in the unoxidized region. Accordingly, oxidation front lies in the active oxidation region and for plotting purposes, it can be defined via a given, but otherwise arbitrary value of $\phi_c \in [\phi_{ox}, 1]$.

In the numerical test presented below, we consider a one-dimensional domain of length 1 mm. The left end of the domain is exposed to air, and the simulation is run under isothermal conditions at a uniform temperature of 288 ^{0}C. Material parameters used in the simulation are given as follows: (i) the true air density at 288 ^{0}C, $\rho_T^f = 0.6273 \ \text{kg/m}^3$, (ii) viscosity of air, $A^L = 29.5\text{E-}6 \ \text{kg/ms}$, (iii) Gas constant, $\bar{R} = 286.987 \ \text{J/kg-K}$, (iv) body force, $b_f = 0$, (v) molecular weight of air is $MW_{air} = 0.02897 \ \text{kg/mol}$, (vi) $\bar{\beta} = 32.4412 \ \text{m}^3/\text{kg}$, (vii) oxidation state, $\phi_{ox} = 0.187$, (viii) reaction rate, $R_0 = 1.69\text{E-}2 \ \text{kg/m}^3\text{s}$, (ix) true solid density, $\rho_T^s = 1320 \ \text{kg/m}^3$, (x) porosity of solid, $\phi^s = 0.1$, (xi) Diffusivity of the solid, $D = 8.933\text{E-}13 \ \text{m}^2/\text{s}$, (xii) Young's modulus, $E^s = 2.6 \ \text{GPa}$, (xiii) $k_2^f = 0$, (xiv) $\alpha = 0.35 \ \text{m}^3/\text{kg}$, (xv) $\bar{A}^{0\Gamma} = -0.25\text{E12}$ and (xvi) $\bar{K}_1 = -1.0\text{E9}$. It is noted that the only new parameters that are not constrained by direct measurements are the last two parameters, i.e., $\bar{A}^{0\Gamma}$ and $\bar{K}_1$. The remaining parameters are either specified in the original work [13], or are standard reported values (limited to the viscosity of air $A^L = 29.5\text{E-}6 \ \text{kg/ms}$ and Youngs modulus of PMR-15 $E^s = 2.6 \ \text{GPa}$).

The one-dimensional domain is discretized non-uniformly with linear Lagrange elements. The subset of the domain, [0, 0.0012] m is discretized with 100 elements and the rest of the domain also with 100 elements. The fluid and the solid constituents coexist over this domain. A fluid concentration of 22.8863E-3 kg/m^3 is specified as boundary condition for the fluid and a load of 1 atm is applied on the solid at the left end of the domain. The problem is run with time steps of 1E-5 seconds for 1000 steps, followed by a time step of 1E-3 seconds for 10000 steps and with a time step of 0.1 seconds for a total time of 100 hours. The drag coefficient A^v for the oxidation problem is defined in terms of diffusivity of the solid, as $A^v = \rho^f(\rho+\rho^f)\bar{R}\theta/\rho_T\mu D$ where, μ is the Lagrange multiplier. For the derivation of this expression, refer to Appendix A.

Remark: *In our model, the fluid properties and its initial/boundary conditions are defined in mass concentration units. Since, fluid properties in Tandon et al. [14] are provided in molar concentration units, they have been converted to appropriate units for the present system of equations using the standard conversion relations.*

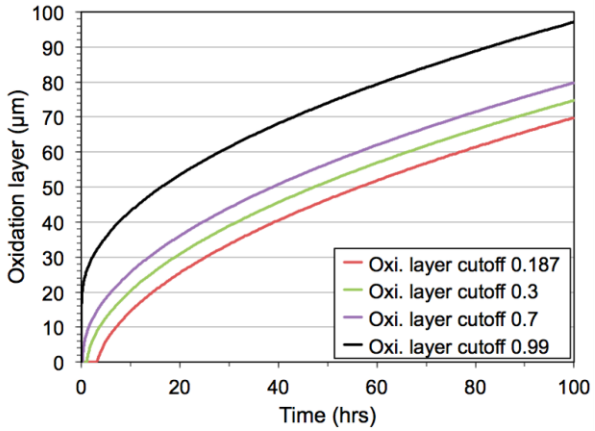

Figure 2.8. Oxidation layer growth with time for various values of oxidation state cutoff variable

The active oxidation zone that lies between the fully oxidized zone and the unoxidized core has a continuous variation of ϕ from ϕ_{ox} to 1, respectively. Specifically, it can be seen from Figure 2.7 that for a value of $\phi_c = 1.0$, the oxidation front is the boundary between the active oxidation region and the neat resin region. Similarly, for a value of $\phi_c = \phi_{ox}$, which in the current

case is $\phi_{ox} = 0.187$, the oxidation front is the boundary between the fully oxidized region and the active oxidation region. In Figure 2.8, we plot the oxidation layer for various values of the post processing parameter ϕ_c that represents the location of the front in the active oxidation zone, for a reaction rate of 1.69E-3 kg/m^3-s and a solid diffusivity of 8.93E-13 m^2/s. The oxidation layer growth results shown in Figure 2.9-Figure 2.11 are plotted for $\phi_c = 0.3$.

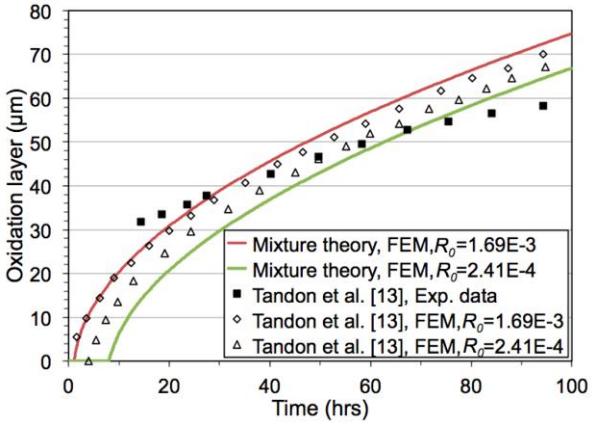

Figure 2.9. Oxidation layer growth with time for various values of reaction rate

A parametric study was done for the oxidation layer growth with time and results are presented as shown in Figure 2.9-Figure 2.11. Figure 2.9 shows the variation in oxidation layer growth for different reaction rate parameters for a duration of 100 hours. The solid line shows the results from the mixture theory, where it can be seen that the reaction rate of 2.41E-4 kg/m^3-s produces an oxidation layer growth of 66.9 μm as compared to 74.7 μm for the reaction rate of

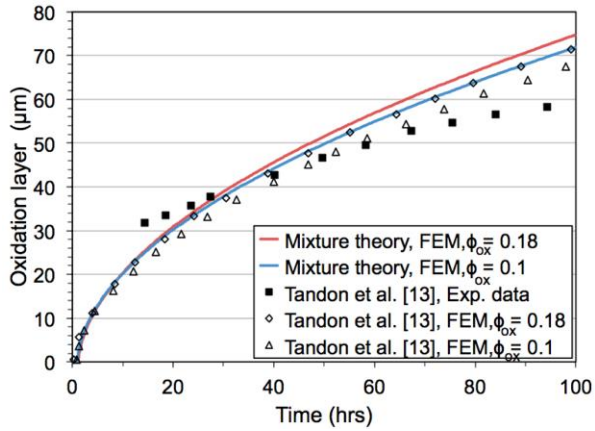

Figure 2.10. Oxidation layer growth with time for various values of oxidation state

1.69E-3 kg/m^3-s at the end of 100 hours. The mixture theory results follow a similar trend in comparison with the Tandon et al. [14] numerical results.

Figure 2.10 shows the growth of oxidation layer for 0.1 and 0.187 oxidation state values. Since $\phi \in [\phi_{ox}, 1]$, the local value of ϕ indicates the amount of polymer that is available for oxidation. An oxidation state value of 0.1 indicates the spatial location where almost 90% of the polymer is available for oxidation, as compared to a value of 0.187 that indicates that only 81.3% of the polymer can be oxidized. For a constant oxidation rate, a lower value of ϕ_{ox} indicates that the oxidation front will stay at that spatial point longer, and therefore the rate of growth of the oxidation layer will be slower, as can be seen in Figure 2.10. Figure 2.11 shows the influence of the diffusivity of the solid on oxidation layer growth in PMR-15 resin. It can be observed that a diffusivity value of 1.667E-12 m^2/s advances the oxidation layer at a higher rate in comparison to the lower diffusivity values of 1.3E-12 and 8.933E-13 m^2/s. The oxidation layer depth of 74.7, 90.1 and 100.1 μm are observed for solid diffusivity values of 8.933E-13, 1.3E-12 and 1.667E-12 m^2/s at the end of 100 hours, respectively.

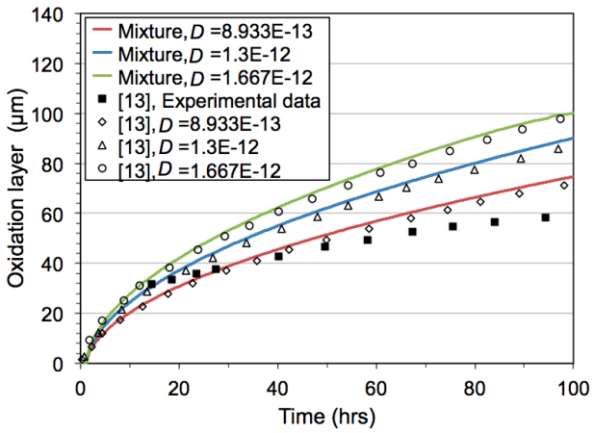

Figure 2.11. Oxidation layer growth with time for various values of drag coefficient

Tandon et al. [14] studied the oxidation layer growth via diffusion reaction equation assuming an ideal fluid permeating through a rigid solid. Accordingly, in their model the deformation of the solid and viscous effects in the fluid are neglected. In the present work where we employ the mixture theory, a Newtonian fluid and an elastic solid are considered. Since the unknown fields in the mixture model are fluid density, fluid velocity, solid displacement and solid density, therefore kinematic and the force measures can be readily obtained from the simulations. Figure

2.12 shows the variation of the fluid and the solid kinematic and force quantities for solid diffusivity values of 8.93E-13, 1.30E-12 and 1.67E-12 m^2/s. The plots shown are obtained for an oxidation state value of 0.187 and a reaction rate of 1.69E-3 kg/m^3-s. Figure 2.12a and Figure 2.12b show the variation of solid density and fluid density along the domain at the end of 100 hours. Equation (2.65) provides the evolving oxidation state variable ϕ that defines the fully oxidized region that has reached its saturation point. This can be observed in Figure 2.12a where solid density reaches a plateau and further oxidation in this region ceases.

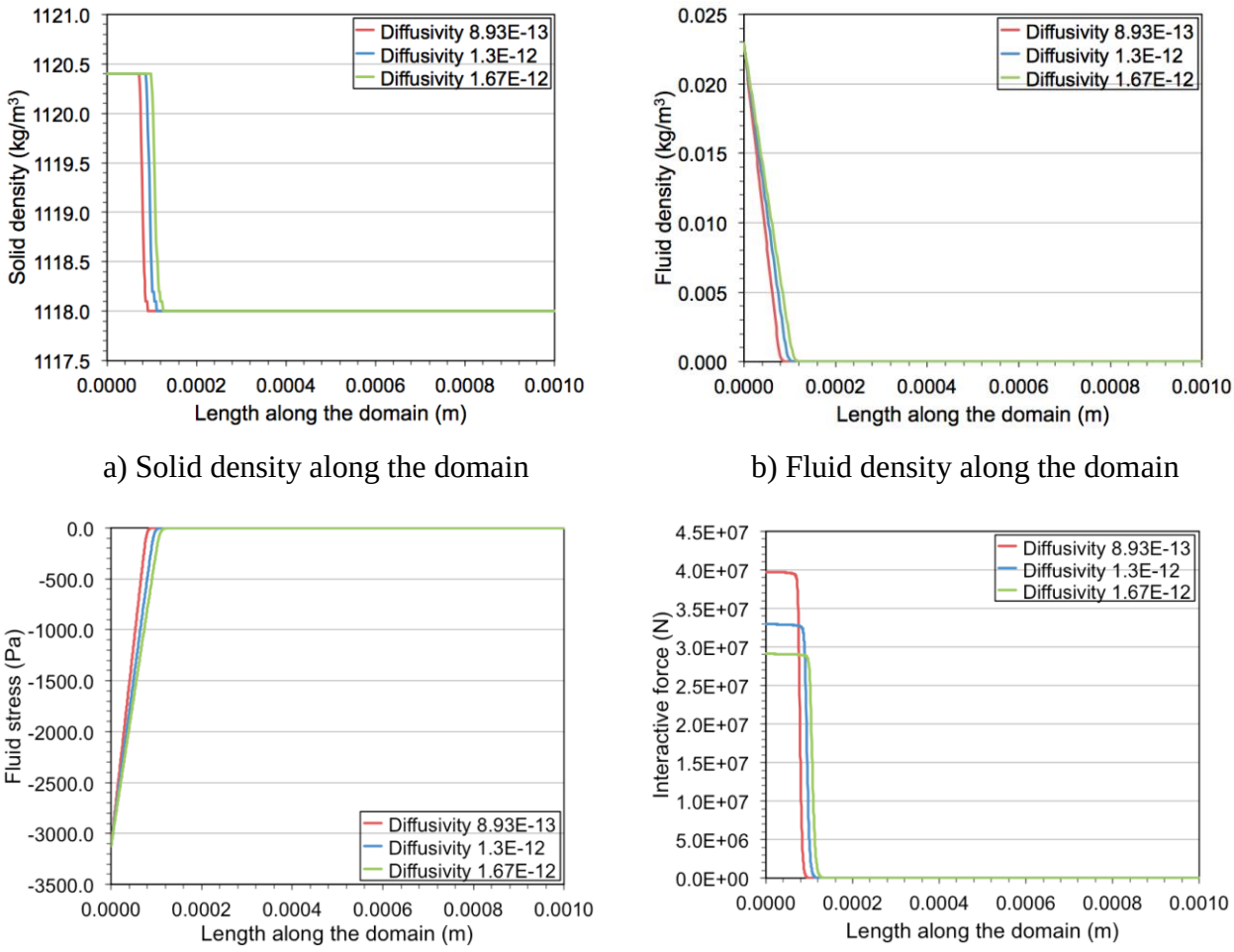

a) Solid density along the domain

b) Fluid density along the domain

c) Fluid stress along the domain

d) Interactive force along the domain

Figure 2.12. Fluid and solid kinematic and force quantities along the domain at the end of 100 hours

Since there are only two constituents in the present model, loss of mass from one is the gain in mass of the other. Consequently, the density of the solid increases as shown in Figure 2.12a

wherein the apparent solid density has a higher value as compared to the neat resin region. This is rather contradictory to the experimental observations as the density of the PMR-15 resin is expected to decrease with increased levels of oxidation. If the two-constituent mixture model is extended to three-constituent model where the third constituent is allowed to evolve and also leave the domain, it can account for the experimentally observed weight loss in solid due to the oxidation process. Figure 2.12c shows that the variation in fluid stress is dominated by the hydrostatic pressure. Figure 2.12d shows the distribution of interactive force between the diffusing fluid and deforming solid. It can be seen that the interactive force becomes zero in the neat resin region where the fluid has not reached yet.

2.5.3 Slurry Infiltration Problem

Slurry infiltration is an important step in the processing of ceramic matrix composites (CMC). In the slurry infiltration process, a viscous fluid that is laden with particles of various sizes, composition, and volume fraction is injected into a fiber preform. In this process, fluid serves as a medium that carries the suspended particles to the preform. This cycle is repeated several times till the density of the preform increases and its porosity reduces to some desired design value. Once slurry infiltration process is complete, a second process called melt infiltration is carried out with a viscous fluid that can chemically react with the preform as well as the deposited particles to make a composite with desired strength and density distribution [27].

In this section, we consider the slurry infiltration process wherein we employ properties of a porous PMC as a surrogate model for CMC material. We assume that water based slurry has permeated the porous elastic solid and we model the process of deposition of suspension onto the fiber preform. Youngs modulus of the porous PMC is obtained via rule of mixtures as given below,

$$E_L = E_f V_f + E_m V_m \tag{2.66}$$

where E_f, E_m are the fiber and epoxy Youngs moduli, respectively, and are assigned values of 380 GPa and 3.45 GPa. V_f, V_m are the volume fractions of the fiber and the matrix in the porous composite. For a 50% porous PMC, we evaluate the properties based on 40% fiber and 10%

matrix composition. The carbon fiber density and the matrix density are 1950 kg/m^3 and 1200 kg/m^3, respectively. The water-based slurry is assumed to contain SiO_2 particles of dimension 2-15 μm with 50% volume fraction. The viscosity of the slurry can be computed from Einstein's equation as follows.

$$\mu^{sl} = \mu^{w}(1+2.5\phi_{SiO_2}) \tag{2.67}$$

where μ^{sl} is the viscosity of slurry, μ^{w} is the viscosity of water, and ϕ_{SiO_2} is the volume fraction of SiO_2 particles in the slurry. Assuming 50% volume fraction of SiO_2 particles, the slurry viscosity turns out to be 1.793E-3 kg/m-s. Given that the density of the SiO_2 particles is 2650 kg/m^3 and the density of water is 1000 kg/m^3, slurry density can be computed as,

$$\begin{aligned}\rho^{sl} &= 0.5\times\rho^{w} + 0.5\times\rho^{SiO_2} \\ &= 1825 \ \ \mathrm{kg/m^3}\end{aligned} \tag{2.68}$$

where ρ^{sl}, ρ^{w} and ρ^{SiO_2} are the density of the slurry, water and the SiO_2 particles, respectively. In the present model, it is assumed that the particle laden fluid is uniformly present in the domain and the dependence of the rate of deposition on the flow velocity is ignored. Accordingly, the mass deposition rate of particles from the slurry onto the porous composite, as given in [28], is modified for the present case as follows,

$$\dot{m}^{f} = -k\rho^{f} w \tag{2.69}$$

where k is the filtration constant, and w is the apparent mass fraction of the particles in the slurry. The filtration rate of the solid medium is assumed to be 83.8341E-3 s^{-1}. The initial apparent mass fraction of particles in the slurry can be computed as,

$$w_0 = \phi_s V_{sl}^{p} \frac{\rho^{p}}{\rho^{sl}} \tag{2.70}$$

where ϕ_s is the solid porosity, and ρ^{p}, V_{sl}^{p} are the density and volume fraction of particles in the slurry, respectively. The drag coefficient A^{v} for the slurry infiltration (permeation) problem is defined in terms of permeability of the solid K and the viscosity of the fluid A^{L} as $A^{v} = A^{L}/K$.

(For the derivation of this expression, see Appendix A). The permeability of the solid is taken to be 4.935E-17 m^2. The chemical reaction and solid strain coupling parameters are assigned to be $\bar{A}^{0\Gamma} = -0.25E3, \bar{K}_1 = -1.0E0$.

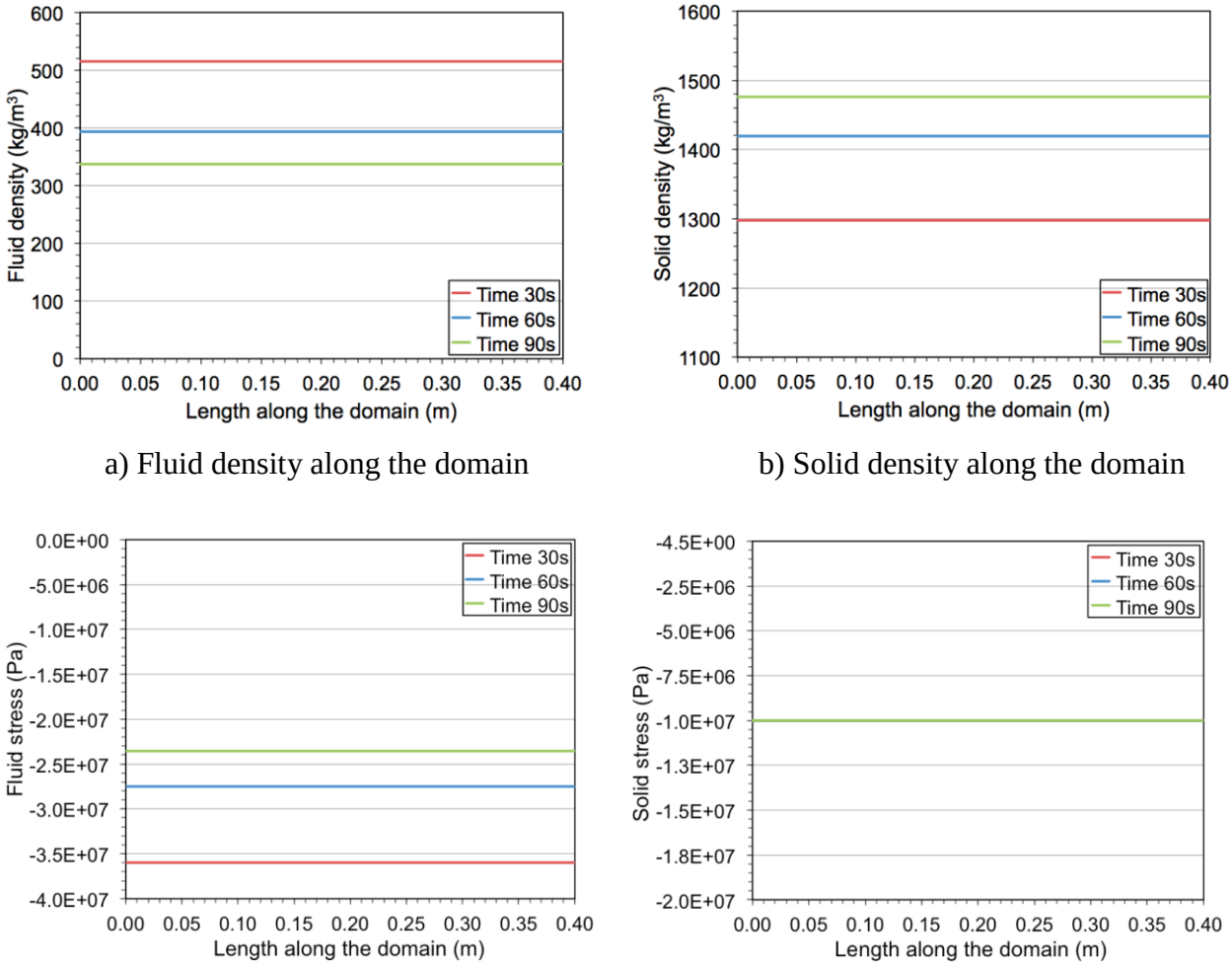

a) Fluid density along the domain

b) Solid density along the domain

c) Fluid stress along the domain

d) Solid stress along the domain

Figure 2.13. Mixture constituents kinematic and stress measures along the domain at 30, 60 and 90 seconds

In this problem, one-dimensional domain of length 0.4 m is considered that contains both solid and fluid constituents uniformly present everywhere. We assume uniform material properties and temperature distribution. In addition, we assume that deposition of the suspended particles is occurring throughout the domain. The problem is run for 90 seconds with a time step of 5E-4

seconds. The solid displacement and fluid velocity is constrained at the left end of the domain. A load of 1E7 N is applied at the right end of the domain.

Figure 2.13a and Figure 2.13b show the reduction in apparent fluid density and increase in apparent solid density along the domain at the end of 30, 60 and 90 seconds. The initial apparent fluid density of 912.5 kg/m^3 drops to 514.9 kg/m^3 at the end of 30 seconds and further drops to 393.4 and 337.1 kg/m^3 at the end of 60 and 90 seconds, respectively. This drop in fluid density is due to particle deposition on to the porous solid that results in an apparent solid density increase (see Figure 2.13b) from 900 kg/m^3 to 1297.7, 1419.1 and 1475.5 kg/m^3 at the end of 30, 60 and 90 seconds, respectively. In order to evaluate the evolution in the stress carrying capacity of the solid, an external load is applied to the solid which is held constant in time, i.e., the solid is under constant compressive stress of 10 MPa throughout the process. Figure 2.13c and Figure 2.13d show the solid and fluid stress profiles along the domain. As deposition of particles are uniform along the length of the domain, the fluid and solid stresses remain constant along the domain.

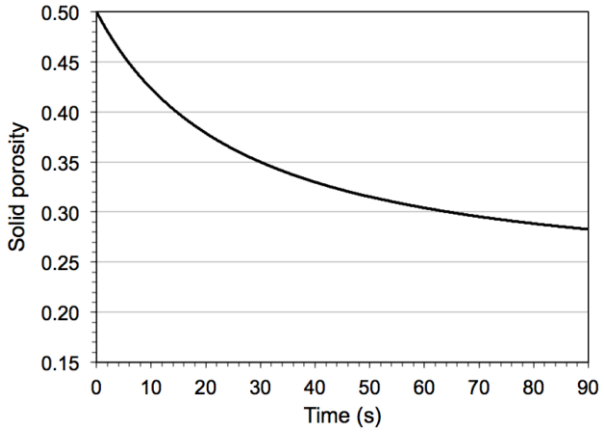

Figure 2.14. Reduction in solid porosity with time

Figure 2.14 shows the decrease in solid porosity as a function of time. For a 50% initial solid porosity and with a 50% particle slurry, the maximum reduction in porosity is bounded by 0.25. As can be seen from the Figure 2.14, the solid porosity asymptotes to 0.25 with time.

Next, we present the results for the case where the porous solid is subjected to three infiltration cycles of 30 seconds each, for a total of 90 seconds. At the end of each cycle, the particle mass fraction W is reset to the initial particle mass fraction in the slurry W_0. Figure 2.15

shows the variation of the solid porosity with time for 50% porous solid and 30%, 40% and 50% SiO_2 particle volume fraction in the slurry. We see that as the particles get deposited, the porosity of the solid decreases. For all three different particle volume fractions in the slurry, this decrease in porosity is nonlinear, wherein the rate of reduction in porosity seems to be slowing down with time that is indicated by the relatively flatter portion of the curve at the end of each cycle. From the perspective of the physics of the problem this means that while there is more relative reduction in porosity during early infiltration cycles, due to closure of pores due to the solid mass buildup, the relative reduction in porosity in subsequent cycles slows down. Figure 2.16 shows a similar trend in reduction in porosity with time for three different initial solid porosities that are infiltrated with 50% particle slurry.

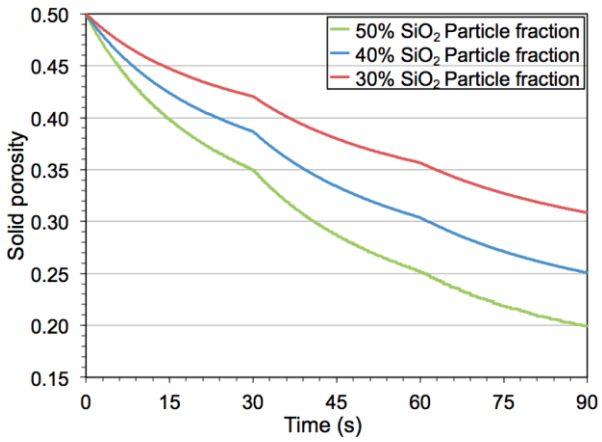

Figure 2.15. Reduction in solid porosity with time for 30%, 40% and 50% SiO_2 particles in the slurry

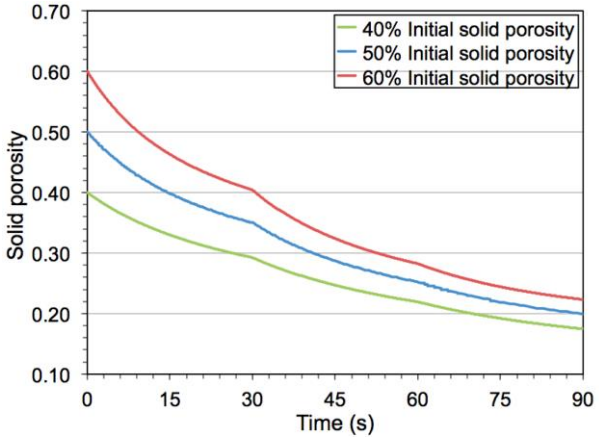

Figure 2.16. Reduction in solid porosity with time for 40%, 50% and 60% initial solid porosity

2.6 Conclusions

We have presented a VMS based finite element method [22,24,25] for the fluid-solid mixture theory model of Hall and Rajagopal [13] that is based on the constituent equations of motion and mass balance. The model addresses the energy and entropy production equations through an equation for Lagrange multiplier that results from consideration of the full set of balance equations as a constraint during the process of maximization of entropy production. The present system of equations is applied to isothermal processes in the one-dimensional context. Employing VMS ideas, a multiscale decomposition of the fluid density field into coarse and fine scales and a-priori unique decomposition of the admissible spaces of functions leads to two coupled nonlinear problems termed as the coarse-scale and the fine-scale sub-problems. The fine-scale solution is extracted from the nonlinear fine-scale sub-problem which is then variationally projected onto the coarse-scale space, leading to a formulation that is expressed entirely in terms of the coarse-scales. Although the final formulation does not depend explicitly on the fine-scale density field for the fluid, the effects of fine-scales are consistently represented via the additional residual based terms, and they add to the stability of the numerical method. The resulting stabilized method for the mixture model is applied to hyperbolic propagation while recovering Fickian diffusion, anisotropic oxidation in composite materials recovering the data of Tandon et al. [14], and mass deposition. Results of the oxidation modeling of Tandon et al. [14] are recovered by employing the reaction kinetics model and properties assumed there; the only additional assumed properties are two constants describing coupled chemomechanical and purely chemical dissipation. In all of these cases the mixture provides rich detail concerning the kinematic and kinetic behaviors of the constituents, in contrast to standard effective media approaches. The proposed solution scheme based on a single Helmholtz energy reveals the importance of an effective material property related to the temperature rate; further investigation is 3D context needed to determine applicability to general anisotropic and anisothermal problems.

Chapter 3

A Mixture Model for Curing and Interphase Evolution in Multi-Constituent Materials

3.1 Introduction

The fabrication of fiber-reinforced polymer matrix composites involves a number of complex interdependent processes, which preclude the resulting materials from achieving chemical or mechanical homogeneity. Firstly, the mixing of thermoset polymer ingredients, resin and hardener, is achieved via a stochastic but finite sequence of folding, stretching, and cutting events. Despite best efforts to achieve spatial dispersion, at some scale this blend consists of pockets, layers, or veins of resin-rich material alternating with cross-linker-rich ones. Secondly, selective chemical affinity of the embedded phase towards these constituents may enhance their separation. The curing process therefore not only involves cross-linking reactions, but also interdiffusion of reacting species. As the cure progresses, molecular transport slows due to the obstruction imposed by the increasing number of cross-links. The final degree of cure never reaches 100% and it likely varies from location to location. Thirdly, the cross-linking reactions are exothermic, and consequently self-catalyzing. Even autoclave treatment does not prevent the development of temperature gradients due to the difference between the thermal conductivities of polymer matric and embedded phase. This in turn results in differential chemical reaction along the interface and development of a composite with spatially inhomogeneous physical properties. Finally, upon extraction from autoclave, due to material mismatch, differential residual stresses are developed that can cause local debonding and crack propagation along this interface. The properties of the interphase region are especially difficult to predict, unless their detailed constitutional history is known. Since interphases play a dominant role in the response of the composite when subjected to mechanical loads, an accurate modeling of the effects of chemo-mechanical heterogeneities and interphase stresses is critical to determine the structural integrity of the composite and its fatigue life.

While many theoretical models and associated numerical schemes have been developed for structure-functional modeling and analysis of components made of composites, numerical methods that can adequately model process modeling of these engineered materials are scarce. For example, in composite manufacturing, the fiber-resin mixture is subjected to a cure cycle under high temperature, initiating cross-linking polymerization in resin to produce a structurally hard composite. The properties of the final product as well as its performance characteristics depend on the properties of constituents, processing parameters such as cure time, cure temperature, cure pressure and the chemical reaction in the resin. Due to the preferential adsorption of fibers, the chemical composition of resin near the fiber surface is different in comparison to the bulk resin. During curing, due to this change in constituent composition an interphase material is formed near the fiber surface. The interphase material plays a significant role in the effective properties of the composite, as the load carrying capacity of the composite is determined by the capability of the matrix to transfer load to the fiber. To tailor a composite with optimum properties for optimal performance, modeling and understanding the mechanism in the formation of interphase is very important. Theoretical models and numerical methods that can be applied to understand the processes modeling of multi-constituent materials need to adopt systems based approach. Consequently, in this class of problems, there is a sequence of constitutive equations that are applicable at the appropriate levels of the physical processes.

Numerical methods which involve explicit modeling and individual tracking of fiber/matrix/interphase system result in high cost of computation. Mixture theory on the other hand provides a locally homogeneous but globally heterogeneous model for multi-constituent materials and allows co-occupancy, i.e., each spatial point in the mixture is occupied by all phases simultaneously. This assumption avoids the need to track/follow individual spatial points corresponding to individual phases by capturing the mixture response macroscopically through constitutive models. These locally homogeneous but globally heterogeneous models reduce the cost of computation when compared to discrete modeling of individual components. Mixture theory ideas have been used to model various phenomena such as classical viscoelasticity [6], swelling of polymers [7], thermo-oxidative degradation of polymer composites [8,9], growth of biological materials [10] and crystallization of polymers [11]. Mixture theory has also been employed to model the mixture of two elastic solids. Bowen et al. [29] presented a thermomechanical theory for diffusion in mixtures of elastic materials. Bedford et al. [30]

proposed a multi-continuum theory for composite materials, where the material particles of different constituents are grouped together at reference configuration to define a composite particle. Though these constituent particles occupy different spatial points as the material deforms, the interactions between constituents are evaluated in the reference configuration using the composite particle. This concept is employed in this work to model the interaction force fields.

In [13] Hall and Rajagopal proposed a mixture theory model for diffusion of chemically reacting fluid through an anisotropic solid. Model is based on the maximization of the rate of entropy production constraint, considering anisotropic effective reaction rates and the limits of diffusion-dominated (diffusion of the reactants is far more rapid than the reaction) and reaction-dominated (the reaction is far more rapid than the diffusion of the reactants) processes. A modification to the Hall and Rajagopal model [13] is employed in the present work for the formation and evolution of interphase material in two-constituent materials where both constituents are in the solid phase. In this model, the properties of the matrix at the fiber-matrix interface evolve during a cure cycle and the isotropic reaction resulting from maximization of entropy production is associated with an anisotropic tensor that provides coupling of chemical reaction and mechanical stresses.

The outline of the paper is as follows: In section 3.2, we present two-constituent mixture theory model for interphase evolution and curing. Section 3.3 presents the weak form of the governing equations with embedded constitutive relations along with linearization of the nonlinear system for finite element implementation. Section 3.4 discusses some representative curing and interphase evolution models that are then integrated in the mixture theory model from Section 2. Numerical test of curing and interphase evolution for some benchmark problems are presented in Section 3.5, and conclusions are drawn in Section 3.6.

3.2 Two-constituent Mixture Theory Model for Interphase Evolution and Curing

A two-constituent solid model that is developed in the context of mixture theory is employed for curing and interphase formation in a continuum sense. The model is embedded with solid-solid phase change wherein due to chemical reactions the matrix material transforms into interphase

material at the solid-solid interface. It is assumed that there is no mass exchange between the fiber and the matrix and that the interphase is formed in the matrix material along the contact surface with fibers. It is also assumed that the reaction is affected by the reinforcement spacing that results in a potentially transversely isotropic interphase.

As there is no interconversion of mass between matrix and fiber material, conservation of mass for the matrix and reinforcement can be given as,

$$\rho^m J^m = \rho_R^m \tag{3.1}$$

$$\rho^r J^r = \rho_R^r \tag{3.2}$$

where the superscript, *m*, *r* refers to matrix and fiber/reinforcement respectively. ρ_R^m, ρ_R^r are the apparent reference densities of matrix and fiber with respect to the reference mixture volume, respectively. Conservation of linear momentum can be written as,

$$\text{DIV}\,\boldsymbol{T}^m + \rho^m \boldsymbol{b}^m + \boldsymbol{I}^m = \rho^m \frac{D\boldsymbol{v}^m}{Dt} \tag{3.3}$$

$$\text{DIV}\,\boldsymbol{T}^r + \rho^r \boldsymbol{b}^r + \boldsymbol{I}^r = \rho^r \frac{D\boldsymbol{v}^r}{Dt} \tag{3.4}$$

where $\boldsymbol{T}^\alpha$ is the Cauchy stress, $\boldsymbol{b}^\alpha$ is the body force and $\boldsymbol{I}^\alpha$ is the interactive force acting on the α^{th} component in the mixture. To keep the presentation concise, the superscript α is used to represent both matrix (*m*) and reinforcement (*r*). According to Newton's third law, the interactive force acting between the matrix and fiber follow the relation,

$$\boldsymbol{I}^r = -\boldsymbol{I}^m \tag{3.5}$$

3.2.1 Constitutive relations based on maximization of rate of dissipation

The thermodynamic system of the mixture comprised of two-solid constituents is assumed to be defined by the following set of state variables,

$$s[t] = s\left\{\boldsymbol{F}^m, \boldsymbol{F}^r, \rho^m, \rho^r, \theta, \Gamma\right\}[t] \tag{3.6}$$

where $\boldsymbol{F}^\alpha$ is the deformation gradient of the α^{th} component, Γ is the extent of chemical reaction in current configuration and θ is the temperature of the mixture. It is assumed that the temperature of mixture and its components are equal and constant with respect to space and time. The Helmholtz free energy function of the mixture is defined as,

$$\psi = \psi\left[s(t)\right] = \psi\left\{\boldsymbol{F}^m, \boldsymbol{F}^r, \rho^m, \rho^r, \theta, \Gamma\right\} \tag{3.7}$$

In the component form, the mixture Helmholtz free energy function is given as,

$$\begin{aligned} \rho\psi &= \rho^m\psi^m + \rho^r\psi^r \\ \rho &= \rho^m + \rho^r \end{aligned} \tag{3.8}$$

where, ψ^α is the Helmholtz free energy function of the α^{th} component and ρ is the mixture density.

From a set of admissible class of constitutive relations, the following relations were obtained [13] by enforcing the maximum rate of dissipation constraint. These relations also correspond to the case where the volume additivity constraint is not required.

$$\boldsymbol{T}^m = \rho\boldsymbol{F}^m\left(\frac{\partial\psi}{\partial\boldsymbol{F}^m}\right)^T - \rho^m\left(g^m + \frac{\rho^r}{\rho}\left(\psi^r - \psi^m\right)\right)\boldsymbol{I} + \mu\frac{\partial\xi}{\partial\boldsymbol{L}^m} \tag{3.9}$$

$$\boldsymbol{T}^r = \rho\boldsymbol{F}^r\left(\frac{\partial\psi}{\partial\boldsymbol{F}^r}\right)^T - \rho^r\left(g^r + \frac{\rho^m}{\rho}\left(\psi^m - \psi^r\right)\right)\boldsymbol{I} \tag{3.10}$$

$$\begin{aligned} \boldsymbol{I}^r = \frac{\partial\psi}{\partial\rho^r}\rho^m\nabla\rho^r - \frac{\partial\psi}{\partial\rho^m}\rho^r\nabla\rho^m - \nabla\left[\frac{\rho^r\rho^m}{\rho}\left(\psi^r - \psi^m\right)\right] \\ - \nabla\theta\frac{\rho^r\rho^m}{\rho}\left(\eta^r - \eta^m\right) - \mu\frac{\partial\xi}{\partial\left(\boldsymbol{v}^r - \boldsymbol{v}^m\right)} \end{aligned} \tag{3.11}$$

$$\mu\frac{\partial\xi}{\partial\dot{\theta}} = -\rho\left(\frac{\partial\psi}{\partial\theta} + \eta\right) \tag{3.12}$$

$$-\rho\left(\frac{\partial\psi}{\partial\Gamma^0}\right)=\mu\frac{\partial\xi}{\partial\dot{\Gamma}^0} \tag{3.13}$$

where, $\dot{\Gamma}^0$ is the reaction rate, ξ is the rate of dissipation, μ is the Lagrange multiplier enforcing the maximum rate of dissipation constraint, η^α and g^α are the entropy and chemical potential of the α^{th} component of the mixture.

The chemical potential of the matrix in (3.9) is given as,

$$g^m=\rho\frac{\partial\psi}{\partial\rho^m} \tag{3.14}$$

Using (3.7)-(3.8), the above equation can be modified as,

$$\begin{aligned} g^m &= \rho\left(\frac{\psi^m}{\rho}+\frac{\rho^m}{\rho}\frac{\partial\psi}{\partial\rho^m}-\frac{\rho^m\psi^m}{\rho^2}-\frac{\rho^r\psi^r}{\rho^2}\right) \\ &= \frac{\rho^r}{\rho}\left(\psi^m-\psi^r\right)+\rho^m\frac{\partial\psi}{\partial\rho^m} \end{aligned} \tag{3.15}$$

$$g^m+\frac{\rho^r}{\rho}\left(\psi^r-\psi^m\right)=\rho^m\frac{\partial\psi^m}{\partial\rho^m} \tag{3.16}$$

Similarly, the chemical potential of the reinforcement in (3.10) can be written as,

$$\begin{aligned} g^r &= \rho\frac{\partial\psi}{\partial\rho^r}=\rho\left(\frac{\psi^r}{\rho}-\frac{\rho^r\psi^r}{\rho}-\frac{\rho^m\psi^m}{\rho^2}\right) \\ &= \frac{\rho^m}{\rho}\left(\psi^r-\psi^m\right) \end{aligned} \tag{3.17}$$

$$g^r+\frac{\rho^m}{\rho}\left(\psi^m-\psi^r\right)=0 \tag{3.18}$$

3.2.2 Constitutive model for the mixture theory

In this section we consider a constitutive model wherein thermal field has pronounced effect on the evolving mechanical field, while the reserve coupling of the mechanical field with the thermal field is considered weak. The constitutive relations (3.9)-(3.11) are modified based on

the specified constitutive equations and the interphase model. The reduced form of Helmholtz functionals for the matrix and fiber are:

$$\psi^m\left[\boldsymbol{E}^m,t\right]=\frac{1}{\rho_T^m}\left\{\frac{1}{2}\lambda^m\left(tr\left[\boldsymbol{E}^m\right]\right)^2+\mu^m tr\left[\left(\boldsymbol{E}^m\right)^2\right]\right\}+\Lambda^m \tag{3.19}$$

$$\psi^r\left[\boldsymbol{E}^r,t\right]=\frac{1}{\rho_T^r}\begin{Bmatrix}\frac{1}{2}\lambda^r\left(tr\left[\boldsymbol{E}^r\right]\right)^2+\mu_T^r tr\left[\left(\boldsymbol{E}^r\right)^2\right]+\alpha^r\left(\boldsymbol{m}^0\cdot\left[\boldsymbol{E}^r\right]\boldsymbol{m}^0\right)tr\left[\boldsymbol{E}^r\right]\\+2\left(\mu_L^r-\mu_T^r\right)\boldsymbol{m}^0\cdot\left[\boldsymbol{E}^r\right]^2\boldsymbol{m}^0+\frac{1}{2}\beta^r\left(\boldsymbol{m}^0\cdot\left[\boldsymbol{E}^r\right]\boldsymbol{m}^0\right)^2\end{Bmatrix} \tag{3.20}$$

Using (3.19) in (3.9), the matrix stress can be rewritten as,

$$\boldsymbol{T}^m=F^m\left(\frac{\partial\left(\rho\psi\right)}{\partial\boldsymbol{E}^m}\right)^T\left(\boldsymbol{F}^m\right)^T-\left(\rho^m\right)^2\frac{\partial\psi^m}{\partial\rho^m}\boldsymbol{I}+\mu\frac{\partial\xi}{\partial\boldsymbol{L}^m} \tag{3.21}$$

where assuming major and minor symmetries for the interphase modulus $\tilde{K}$ we get

$$\begin{aligned}\frac{\partial\left(\rho\psi\right)}{\partial\boldsymbol{E}^m}&=\rho^m\frac{\partial\psi^m}{\partial\boldsymbol{E}^m}\\&=\frac{\rho^m}{\rho_T^m}\left\{\lambda^m tr\left[\boldsymbol{E}^m-a^{m0}\boldsymbol{I}\left(\theta-\theta_R\right)\right]\boldsymbol{I}+2\mu^m\left[\boldsymbol{E}^m-a^{m0}\boldsymbol{I}\left(\theta-\theta_R\right)\right]\right\}+\rho^m\frac{\partial\Lambda^m}{\partial\boldsymbol{E}^m}\end{aligned} \tag{3.22}$$

where Λ^m is the coupling term between the matrix strain and the extent of chemical reaction, . θ_R is the reference temperature, ρ_T^m is the matrix true density and a^{m0},λ^m,μ^m are matrix material constants.

$$\rho^m\frac{\partial\Lambda^m}{\partial E_{IJ}^m}=-\frac{1}{\rho_T^m}\left\{E_{OP}^m\int k\left[\rho^c,\Gamma^0\right]\tilde{K}_{IJOP}\left[\Gamma^0\right]d\Gamma^0+\int\int m^c\left[\rho^c,\Gamma^0\right]\tilde{\alpha}_{IJ}^c\left[\theta\right]d\theta d\Gamma^0\right\} \tag{3.23}$$

In (3.23) $k\left[\rho^c,\Gamma^0\right]$ is the bulk modulus of the composite which is a function of the composite density and the chemical reaction and is defined as $k\left[\rho^c,\Gamma^0\right]=c_1\rho^c$ and c_1 is constant of proportionality, $\tilde{K}_{OPQR}\left[\Gamma^0\right]$ is the stiffness of the interphase material $m^c\left[\rho^c,\Gamma^0\right]$ is the mass of the composite that is a function of the density of composite as well as the mass conversion due to

chemical reactions, and $\tilde{\alpha}_{OP}\left[\theta\right]$ is the coefficient of thermal expansion. In the current implementation of the model, the second term in (3.23) is neglected.

The rate of dissipation due to chemical reaction and viscous effects is given as,

$$\begin{aligned}\xi \equiv \xi_v = \frac{\rho}{\rho_R}\xi_v^0 = \frac{1}{\rho_R}\left\{\frac{1}{2}\left(\dot{\Gamma}^0\right)^2 g\left[\rho^c,\Gamma^0\right] + \dot{\Gamma}^0 n^c\left[\rho^c,\Gamma^0\right]\dot{\theta}^2\right\} \\ + \frac{1}{2}\frac{1}{\rho_R}\left\{\rho^m \dot{E}_{ij}^m A_{ijkl}^{L0}\dot{E}_{kl}^m + \rho c_\theta^0 \dot{\theta}^2\right\}\end{aligned} \tag{3.24}$$

where A_{ijkl}^{L0} is the fourth order tensor representing viscous effects and the terms $g\left[\rho^c,\Gamma^0\right]$, $n^c\left[\rho^c,\Gamma^0\right]$ represent the chemo-thermal dissipative energy during the curing and interphase formation of the matrix material.

Likewise, the Helmholtz free energy function of the reinforcement in reference coordinates accounts for the effect of thermal field on the mechanical properties of the fibrous constituent. Using (3.20) in (3.10), the reinforcement stress can be rewritten as:

$$\boldsymbol{T}^r = \boldsymbol{F}^r\left(\frac{\partial\left(\rho\psi\right)}{\partial \boldsymbol{E}^r}\right)^T\left(\boldsymbol{F}^r\right)^T \tag{3.25}$$

where,

$$\begin{aligned}\frac{\partial\left(\rho\psi\right)}{\partial \boldsymbol{E}^r} &= \rho^r\frac{\partial\psi^r}{\partial \boldsymbol{E}^r} \\ &= \frac{\rho^r}{\rho_T^r}\begin{Bmatrix}\left(\lambda^r tr\left[\boldsymbol{E}^r\right] + \alpha^r \boldsymbol{m}^0\cdot\left[\boldsymbol{E}^r\right]\boldsymbol{m}^0\right)\boldsymbol{I} + 2\mu_T^r\left[\boldsymbol{E}^r\right] + \\ \left(\alpha^r tr\left[\boldsymbol{E}^r\right] + \beta^r \boldsymbol{m}^0\cdot\left[\boldsymbol{E}^r\right]\boldsymbol{m}^0\right)\boldsymbol{m}^0\otimes\boldsymbol{m}^0 \\ +2\left(\mu_L^r - \mu_T^r\right)\left(\boldsymbol{m}^0\otimes\left[\boldsymbol{E}^r\right]\boldsymbol{m}^0 + \boldsymbol{m}^0\cdot\left[\boldsymbol{E}^r\right]\otimes\boldsymbol{m}^0\right)\end{Bmatrix}\end{aligned} \tag{3.26}$$

Where $\boldsymbol{m}^0$ is the fiber direction in reference coordinates, ρ_T^r is the fiber true density and $\boldsymbol{a}^{r0}, \lambda^r, \alpha^r, \mu_L^r, \mu_T^r, \beta^r$ are fiber material constants.

In the absence of drag force between solid constituents and under isothermal conditions the interactive force acting on the fiber (3.11) can be further simplified as:

$$\boldsymbol{I}^r = \frac{\partial \psi}{\partial \rho^r}\rho^m \nabla \rho^r - \frac{\partial \psi}{\partial \rho^m}\rho^r \nabla \rho^m - \nabla\left[\frac{\rho^r \rho^m}{\rho}\left(\psi^r - \psi^m\right)\right] \tag{3.27}$$

Using (3.16)-(3.18), the interactive force in (3.27) can be rewritten as,

$$\boldsymbol{I}^r = \frac{\rho^r \rho^m}{\rho}\left(\nabla \psi^m - \nabla \psi^r\right) - \frac{\rho^r \rho^m}{\rho}\frac{\partial \psi^m}{\partial \rho^m}\nabla \rho^m \tag{3.28}$$

From (3.7) the spatial gradient of the Helmholtz free energy function is:

$$\begin{aligned}
\nabla \psi^m &= \frac{\partial \psi^m}{\partial \boldsymbol{F}^m}\nabla \boldsymbol{F}^m + \frac{\partial \psi^m}{\partial \rho^m}\nabla \rho^m + \frac{\partial \psi^m}{\partial \theta}\nabla \theta + \frac{\partial \psi^m}{\partial \Gamma^0}\nabla \Gamma^0 \\
&\approx \frac{\partial \psi^m}{\partial \boldsymbol{F}^m}\nabla \boldsymbol{F}^m + \frac{\partial \psi^m}{\partial \rho^m}\nabla \rho^m \\
\nabla \psi^r &= \frac{\partial \psi^r}{\partial \boldsymbol{F}^r}\nabla \boldsymbol{F}^r + \frac{\partial \psi^r}{\partial \theta}\nabla \theta \\
&\approx \frac{\partial \psi^r}{\partial \boldsymbol{F}^r}\nabla \boldsymbol{F}^r
\end{aligned} \tag{3.29}$$

Substituing (3.29) in (3.28), the expression for the interactive force becomes

$$\boldsymbol{I}^r \approx \frac{\rho^r \rho^m}{\rho}\left(\frac{\partial \psi^m}{\partial \boldsymbol{F}^m}\nabla \boldsymbol{F}^m - \frac{\partial \psi^r}{\partial \boldsymbol{F}^r}\nabla \boldsymbol{F}^r\right) \tag{3.30}$$

Remark: *From the above equation, it is observed that the interactive force is a function of the gradient of deformation gradient. Hence, for a linear displacement field, there will be no interactive force between the matrix and the reinforcement. To model the interactive force in a finite element discretization, the shape functions should be at least quadratic in order.*

As the interphase is formed from the matrix material, the matrix density is defined by the following additive split,

$$\rho^u\left(\boldsymbol{F}^m, \Gamma^0\right) = \rho^m\left(\boldsymbol{F}^m\right) - \rho^c\left(\Gamma^0\right) \tag{3.31}$$

Where ρ^u is the unconverted matrix density and ρ^c is the converted matrix density.

Remark: *Though portion of matrix material adjoining the reinforcement gets converted in to an interphase material, the density of the untransformed matrix material* $\rho^m\left(\boldsymbol{F}^m\right)$ *is a function of matrix mechanical deformation alone. The converted matrix material density* $\rho^c\left(\Gamma^0\right)$ *is a function of the chemical reaction alone and is independent of mechanical deformation.*

3.3 Weak Form and Linearization of Governing Equations

This section presents the variational form of the quasi-static version of governing equations described in Section 3.2.1. Since it is a nonlinear system of equations, we also present the linearization of the nonlinear weak form for finite element implementation.

The space of trial solutions for the matrix and reinforcement are:

$$\mathcal{S}_t^m = \left\{\boldsymbol{\varphi}_t^m : \Omega \to \mathbb{R}^{nsd} \mid \boldsymbol{\varphi}_t^m \in H^1(\Omega),\ \boldsymbol{\varphi}_t^m = \bar{\boldsymbol{\varphi}}_t^m \ \text{ on } \ \partial\Omega_u\right\} \tag{3.32}$$

$$\mathcal{S}_t^r = \left\{\boldsymbol{\varphi}_t^r : \Omega \to \mathbb{R}^{nsd} \mid \boldsymbol{\varphi}_t^r \in H^1(\Omega),\ \boldsymbol{\varphi}_t^r = \bar{\boldsymbol{\varphi}}_t^r \ \text{ on } \ \partial\Omega_u\right\} \tag{3.33}$$

The space of weighting functions for the matrix $\mathcal{V}^m$ and reinforcement $\mathcal{V}^r$ are the homogeneous and time independent counterparts of the corresponding spaces of trial solutions $\mathcal{S}_t^m$ and $\mathcal{S}_t^r$, respectively.

Taking the inner product of (3.3) and (3.4) with the corresponding weighting functions and integrating over the domain leads to the weighted residual form:

$$\int_\Omega w_i^\alpha \left(T_{ij,j}^\alpha + \rho^\alpha b_i^\alpha + I_i^\alpha\right) d\Omega = 0 \tag{3.34}$$

where α represents both matrix and fiber. Integrating (3.34)by parts and using divergence theorem we develop the weak form for the mixture model which is stated as: Given the boundary conditions $\bar{\boldsymbol{\varphi}}^m = \bar{\boldsymbol{\varphi}}^r$ on $\boldsymbol{\varphi}^\alpha\left(\partial\Omega_u\right)$ and the initial conditions, find $\boldsymbol{\varphi}^m \in \mathcal{S}_t^m$ and $\boldsymbol{\varphi}^r \in \mathcal{S}_t^r$ for $\forall\ t \in \mathbb{I}$, such that

$$\int_\Omega w_{i,j}^\alpha T_{ij}^\alpha d\Omega - \int_\Omega w_i^\alpha \rho^\alpha b_i^\alpha d\Omega - \int_\Omega w_i^\alpha I_i^\alpha d\Omega = 0, \qquad \alpha \in \{m, r\} \tag{3.35}$$

An important issue in mixture theory based models is the Neumann boundary conditions where the constituents need to be tied in a self-consistent fashion to simulate the response a material where constituents are fully bonded. In this work we have employed a finite strain finite element method for the consistent tying of the constituents at the boundaries via a variational formulation that finds roots in the VMS method presented in Chapter 4.

To keep the discussion simple and without loss of generality, we present linearization of (3.35) in the 1-D context.

$$\mathcal{R}^{\alpha} = \int_{\Omega} w_{1,1}^{\alpha} T_{11}^{\alpha} d\Omega - \int_{\Omega} w_1^{\alpha} \rho^{\alpha} b_1^{\alpha} d\Omega - \int_{\Omega} w_1^{\alpha} I_1^{\alpha} d\Omega \tag{3.36}$$

$$\mathcal{R}^{\alpha} + \mathrm{D}\mathcal{R}^{\alpha}\left(\varphi_1^{\alpha}\right) \cdot \Delta u_1^{\alpha} = 0 \tag{3.37}$$

where the directional derivative of the residual is defined as,

$$\mathrm{D}\mathcal{R}^{\alpha}\left(\varphi_1^{\alpha}\right) \cdot \Delta u_1^{\alpha} = \left. \frac{d}{d\varepsilon} \right|_{\varepsilon=0} \mathcal{R}^{\alpha}\left(\varphi_1^{\alpha} + \varepsilon\, \Delta u_1^{\alpha}\right) \tag{3.38}$$

The consistent tangent for the matrix constituent is:

$$\begin{aligned}
\mathrm{D}\mathcal{R}^{m}\left(\varphi_1^{m}\right) \cdot \Delta u_1^{m} &= \int_{\Omega} \frac{\partial w_1^{m}}{\partial x} a_{1111} \frac{\partial \Delta u_1^{m}}{\partial x} dx \\
&- \int_{\Omega} w_1^{m} \left(\frac{\rho^{m}}{\rho} \right)^2 \rho^{r} \left[\frac{\partial \psi^{r}}{\partial F_{11}^{r}} \frac{\partial F_{11}^{r}}{\partial x} - \frac{\partial \psi^{m}}{\partial F_{11}^{m}} \frac{\partial F_{11}^{m}}{\partial x} \right] \frac{\partial \Delta u_1^{m}}{\partial x} dx \\
&+ \int_{\Omega} w_1^{m} \frac{\rho^{m} \rho^{r}}{\rho} \frac{\partial \psi^{m}}{\partial F_{11}^{m}} F_{11}^{m} \frac{\partial^2 \Delta u_1^{m}}{\partial x^2} dx \\
&+ \int_{\Omega} w_1^{m} \frac{\rho^{m} \rho^{r}}{\rho} \frac{\partial}{\partial F_{11}^{m}} \left(\frac{\partial \psi^{m}}{\partial F_{11}^{m}} \right) F_{11}^{m} \frac{\partial F_{11}^{m}}{\partial x} \frac{\partial \Delta u_1^{m}}{\partial x} dx
\end{aligned} \tag{3.39}$$

where, the matrix tangent moduli is given as,

$$a_{1111}^{m} = \frac{\partial T_{11}^{m}}{\partial F_{11}^{m}} F_{11}^{m} \tag{3.40}$$

Similarly, the directional derivative for the reinforcement is given as:

$$
\begin{aligned}
&\mathrm{D}\mathcal{R}^r\left(\varphi_1^r\right)\cdot\Delta u_1^r = \int_\Omega \frac{\partial w_1^r}{\partial x}\, a_{1111}^r \frac{\partial \Delta u_1^r}{\partial x}\, dx \\
&-\int_\Omega w_1^r \left(\frac{\rho^r}{\rho}\right)^2 \rho^m \left[\frac{\partial \psi^m}{\partial F_{11}^m}\frac{\partial F_{11}^m}{\partial x} - \frac{\partial \psi^r}{\partial F_{11}^r}\frac{\partial F_{11}^r}{\partial x}\right]\frac{\partial \Delta u_1^r}{\partial x}\, dx \\
&+\int_\Omega w_1^r \frac{\rho^r \rho^m}{\rho}\frac{\partial \psi^r}{\partial F_{11}^r} F_{11}^r \frac{\partial^2 \Delta u_1^r}{\partial x^2}\, dx \\
&+\int_\Omega w_1^r \frac{\rho^m \rho^r}{\rho}\frac{\partial}{\partial F_{11}^r}\left(\frac{\partial \psi^r}{\partial F_{11}^r}\right) F_{11}^r \frac{\partial F_{11}^r}{\partial x}\frac{\partial \Delta u_1^r}{\partial x}\, dx
\end{aligned}
\tag{3.41}
$$

where the fiber tangent moduli is given as,

$$
a_{1111}^r = \frac{\partial T_{11}^r}{\partial F_{11}^r} F_{11}^r \tag{3.42}
$$

The one-dimensional quasi-static version of the discretized residual vector and its directional derivative are summarized in Box. 3.1. For ease of numerical implementation, various terms in the above relations are presented in Appendix-A.

Box 3.1. One-dimensional form of linearized finite element equations

$$
D_\varphi F_{\text{int}}^\alpha \cdot \Delta d^\alpha - D_\varphi F_I^\alpha \cdot \Delta d^\alpha = F_B^\alpha + F_I^\alpha - F_{\text{int}}^\alpha
$$

$$
D_\varphi F_{\text{int}}^\alpha \cdot \Delta d^\alpha = \mathop{\mathbf{A}}_{e=1}^{nel} \int_{\Omega^e} \frac{\partial N_a}{\partial x} a^\alpha \frac{\partial N_b}{\partial x}\, d\Omega \quad \Delta d^\alpha
$$

$$
D_\varphi F_I^\alpha \cdot \Delta d^\alpha = \mathop{\mathbf{A}}_{e=1}^{nel} \int_{\Omega^e} N_a I^\alpha \frac{\partial N_b}{\partial x}\, d\Omega \quad \Delta d^\alpha + \int_{\Omega^e} N_a \frac{\partial I^\alpha}{\partial F^\alpha} F^\alpha \frac{\partial N_b}{\partial x}\, d\Omega \quad \Delta d^\alpha
$$

$$
F_I^\alpha = \mathop{\mathbf{A}}_{e=1}^{nel} \int_{\Omega^e} N_a I^\alpha d\Omega \ , \ F_B^\alpha = \mathop{\mathbf{A}}_{e=1}^{nel} \int_{\Omega^e} N_a \rho^\alpha b^\alpha d\Omega \ , \ F_{\text{int}}^\alpha = \mathop{\mathbf{A}}_{e=1}^{nel} \int_{\Omega^e} \frac{\partial N_a}{\partial x} T^\alpha d\Omega
$$

$$
a^\alpha = \frac{\partial T^\alpha}{\partial F^\alpha} F^\alpha
$$

where N_a represents the shape function associated with a generic node.

3.4 Curing and Interphase Evolution Models

During the curing process, chemical reactions that are triggered by the temperature field result in evolving natural configurations of matrix as shown in Figure 3.1. These reactions result in an overall curing of the matrix material in addition to the formation of interphase material along the fiber-matrix interface. In this work we have employed the Ruiz and Trochu [54,55] model for curing, and Yang and Pitchumani [56-58] model for interphase evolution. Both models have been cast in the context of mixture theory presented in Section 3.2 and have been implemented in the context of finite-strain finite element method discussed in Section 3.3.

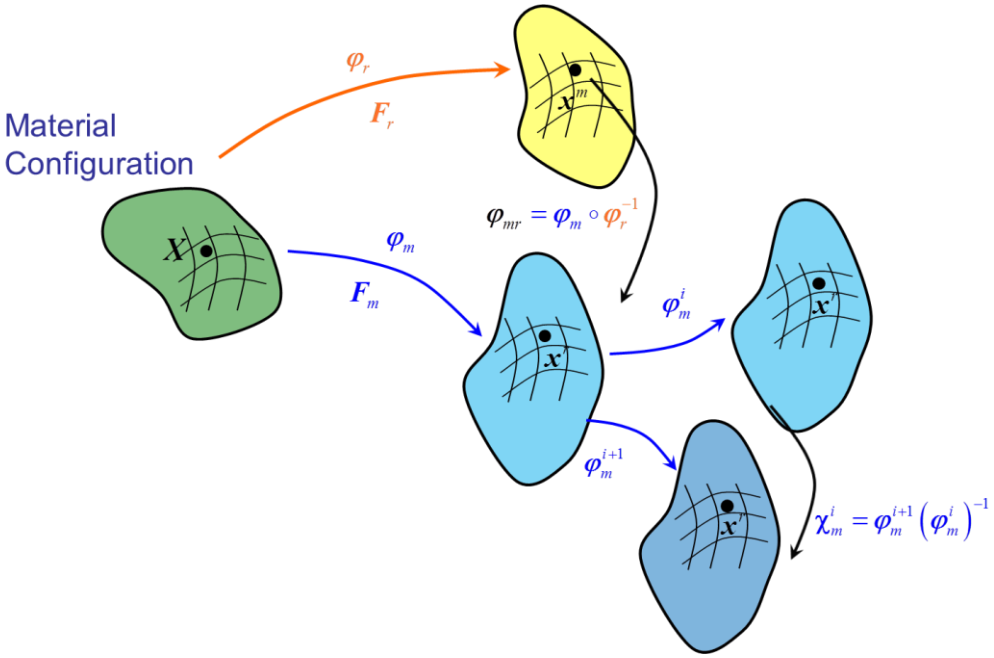

Figure 3.1. Evolving natural configurations of the matrix material due to chemical reaction

3.4.1 Curing model

In fiber reinforced polymeric composites, fiber materials are often oriented to provide the designed structural properties in the desired direction. These fiber materials are interlocked with a weaker material (a thermoset resin) and allowed to cure through a polymerization process. The matrix material is comprised of resin and hardener and catalysts are usually present in the

hardener to accelerate cure. Because of chemical reactions, the viscosity of the thermoset increases and ultimately cross linking occurs due to growth and branching of chains, leading to an increase in the molecular mass. A model for resin kinetics and evolution of composite properties during curing for glass-polyester composites is presented in Ruiz and Trochu [54,55].

$$E_r\left(T,\Gamma\right)=E_{agp}\left(T\right)+\left[E_c\left(T\right)-E_{agp}\left(T\right)\right]F_r\left(\Gamma\right)W_r\left(T_g\right) \tag{3.43}$$

where

$$\begin{aligned}
&E_c\left(T\right)=\frac{E_c^{'}}{\cosh\left(a_1T\right)^{b_1}},\quad E_{agp}\left(T\right)=\frac{E_{agp}^{'}}{\cosh\left(a_2T\right)^{b_2}}\\
&F_r\left(\Gamma\right)=c\exp\left(d\hat{\alpha}\right)+e\ \hat{\alpha}\\
&W_r\left(T_g\right)=h\exp\left(\hat{T}\right),\quad T_g\left(\Gamma\right)=a_g\exp\left(\frac{b_g}{1-\hat{\alpha}}\right)
\end{aligned} \tag{3.44}$$

In (3.43) $E_r\left(T,\Gamma\right)$ is the resin Young's modulus which is a function of the temperature field, α is the degree of cure, and T is the glass transition temperature. $a_1,a_2,c,d,b_g\hat{\alpha},E_c^{'},E_{agp}^{'}$ are constitutive parameters and are given in [54,55]. We embed this model within the mixture theory framework in the context of finite strain finite element method. The parametric values employed for the numerical implementation of the model are obtained from [54,55].

For the mixture theory described in Section 3.2, the evolution of matrix properties is given by the interphase evolution function $\tilde{K}\left(\Gamma^0\right)$. In the mixture model presented in Section 3.2, this function is defined as the derivative of the Ruiz model for evolution of Young's modulus with respect to the cure parameter. Accordingly, by taking the functional form of $\tilde{K}\left(\Gamma^0\right)$ to be the first derivative of $E_r\left(T,\Gamma\right)$ given in (3.43), we embed the Ruiz and Trochu [54,55]. model in the mixture theory presented in Section 3.2.

$$\tilde{K}\left(\Gamma^0\right)=\frac{\partial E_r}{\partial\Gamma}=\left(E_c\left(T\right)-E_{agp}\left(T\right)\right)\left(\frac{\partial F_r}{\partial\Gamma}W+\frac{\partial W_r}{\partial\Gamma}F_r\right) \tag{3.45}$$

where

$$\frac{\partial F_r}{\partial \Gamma} = c\exp\left(d\hat{\alpha}\right)d\frac{1}{\alpha_{ult}-\alpha_{agp}} + \frac{e}{\alpha_{ult}-\alpha_{agp}}$$

$$\frac{\partial W_r}{\partial \Gamma} = h\exp\left(\hat{T}\right)\left[\frac{1}{T_g\left(\Gamma\right)-T_{ref}} - \frac{T_g\left(\Gamma\right)-T}{\left(T_g\left(\Gamma\right)-T_{ref}\right)^2}\right]\frac{\partial T_g}{\partial \Gamma} \tag{3.46}$$

$$\frac{\partial T_g}{\partial \Gamma} = a_g\exp\left(\frac{b_g}{1-\hat{\alpha}}\right)\frac{b_g}{\left(1-\hat{\alpha}\right)^2}\frac{1}{\alpha_{ult}-\alpha_{agp}}$$

We have employed the Kamal-Sourour kinetic model [54] for the evolution of matrix stress.

$$\dot{\Gamma}^0 = \left(K_1 + K_2\Gamma^0\right)\left(1-\Gamma^0\right)^2 \tag{3.47}$$

where K_1 and K_2 are the rate constants.

3.4.2 Interphase evolution model

In the manufacturing of fibrous composites, the fibers are aligned in a mold and injected with a polymer matrix. This impregnation of the fiber layout with epoxy-amine resin mixture initiates a curing reaction at the fiber-matrix interface. Because of the selective adsorption of the fiber, a concentration gradient of amine species is formed near the fiber surface. During the curing cycle, adsorption, desorption, diffusion, reaction mechanisms take place simultaneously in the resin. An interphase model that links the process parameters to the interphase structure and properties for an inorganic fiber/epoxy-amine thermosetting system is proposed by Yang and Pitchumani in [56-58]. The reaction in the resin is written as:

$$n_1 E + n_2 A \rightarrow P \tag{3.48}$$

where n_1, n_2 are molar number of epoxy and amine respectively and E, A, P are epoxy, amine and product respectively.

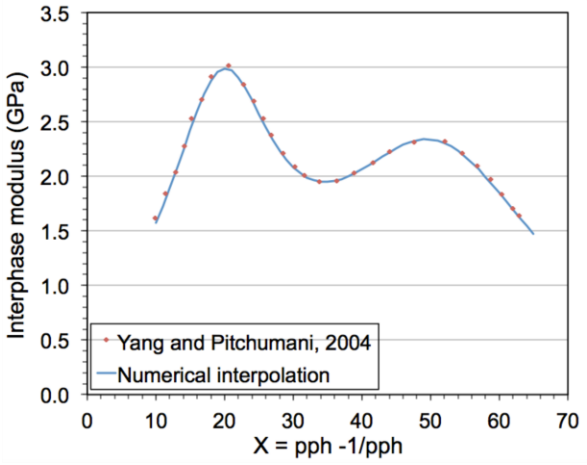

(a) Interphase modulus vs Amine conc.

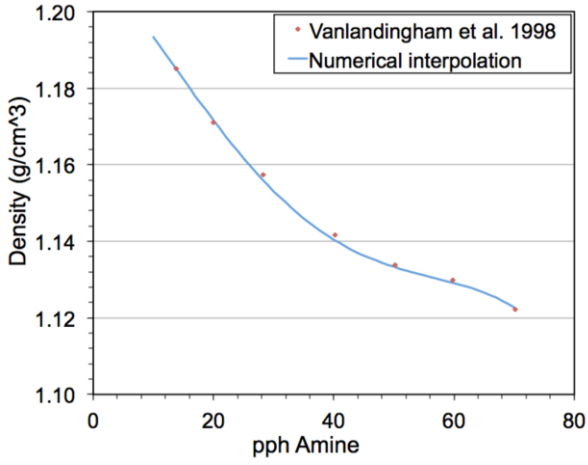

(b) Interphase density vs amine conc.

Figure 3.2. Interphase properties evolution for epoxy-amine resin

Figure 3.2a represents the variation in experimental values of interphase modulus of the neat resin with amine content. A numerical fit for this variation is given by eq. (3.49)

$$E(X)=\tilde{K}_{1111}(X)=\frac{1}{(X-19.57)^2/214.42+0.42}+\frac{1}{(X-50.59)^2/803.09+0.47} \tag{3.49}$$

where $X=(pph^2-1)/pph$. In the mixture model we express the evolution of composite density as a function of the reaction Γ. This function can be developed based on the experimentally obtained density versus amine concentration plot, and in our work we have developed this function based on data from Vanlandingham et al. [59] as presented in Figure 3.2b. Accordingly, the converted density $\rho^c\left[\Gamma^0\right]$ function is defined as

$$\begin{aligned}\rho_c(pph)=1.21373-0.0017357\,pph-4.3204\times10^{-5}\,pph^2\\+1.4373\times10^{-6}\,pph^2-1.04455\times10^{-8}\,pph^4\end{aligned} \tag{3.50}$$

Remark: *Experimental data for the evolution of density as a function of amine concentration as given in Vanlandingham et al. [59] is shown in Figure 3.2b. Employing least-squares fit to the experimental data we extracted equation* (3.50) *for the evolving density of the interphase material.*

Given that the stoichiometric ratio for epoxy amine reaction is 2:1, *pph* amine concentration can be given as follows [56-58].

$$\Gamma^0 = \frac{c_{E0} - c_E}{c_{E0}} = 2\frac{c_{A0} - c_A}{c_{E0}} \tag{3.51}$$

$$pph = \frac{c_A}{c_E} \times \frac{210}{382} \times 100 = \frac{c_{A0} - 0.5\Gamma^0 c_{A0}}{c_{E0}\left(1-\Gamma^0\right)} \times \frac{210}{382} \times 100 \tag{3.52}$$

where c_E, c_A is the concentration of epoxy and amine in the system at time *t*, molecular weight of epoxy and amine are 382 and 210 g/mol, respectively. For a value of *pph*=28 epoxy-amine system, the mass of epoxy and amine are 97.21g and 27.31g, respectively.

For present implementation a simple phenomenological model as presented in (3.53) was used for the evolution of the chemical reaction.

$$\dot{\Gamma}^0 = \alpha\left(1-\Gamma^0\right)^n \tag{3.53}$$

where α is the reaction rate coefficient.

Remark: *The reaction rate given in* (3.53) *can be calibrated for the experimentally obtained data for material under investigation such that it results in a good match with the experimentally observed degree of cure.*

3.5 Numerical Results and Model Validation

3.5.1 Numerical test of curing with the Ruiz model

This section presents verification of the model and the computational method. We consider a one-dimensional domain of glass-epoxy composite of length 1m. The composite is assumed to be under isothermal conditions at a temperature of 393K. The matrix material is allowed to achieve 96% curing at this temperature, while the fiber is assumed to be chemically inert. The domain in subjected to a body force of 10 m/sec^2 and the displacement is constrained at x=0. The problem is run for 600 seconds with a time step of 5 seconds in order to achieve 96% curing. The right

end of the domain x=1, is subjected to a compressive displacement of 0.01m which is applied at the first time step and maintained constant through the remaining time steps.

The evolution of matrix density ρ^c is assumed to occur all over the matrix domain, and not just at the matrix/fiber interface. Figure 3.3 shows the degree of cure of the resin as a function of time up to a point where reaction is approximately 96% complete in around 600 seconds. Evolution of matrix modulus is presented in Figure 3.4a and shows a delayed response. The matrix modulus in Figure 3.4a is obtained by evaluating the ratio of the average matrix stress over the average matrix strain. The matrix stress obtained from mixture model is shown in Figure 3.4b and it compares well with the stress obtained from the Ruiz and Trochu [54-55] model. Both models predict a rapid increase in matrix stress once the degree of cure reaches 0.88 and higher, and this increase in stress can be attributed to the increase in Young's modulus of resin with an increase in the degree of cure. The fiber interactive force varies linearly along the domain at 600 sec as shown in Figure 3.5. The interactive force is less towards the right end of the domain due to the applied body force, which subjects the domain to higher strain at the left end of the domain.

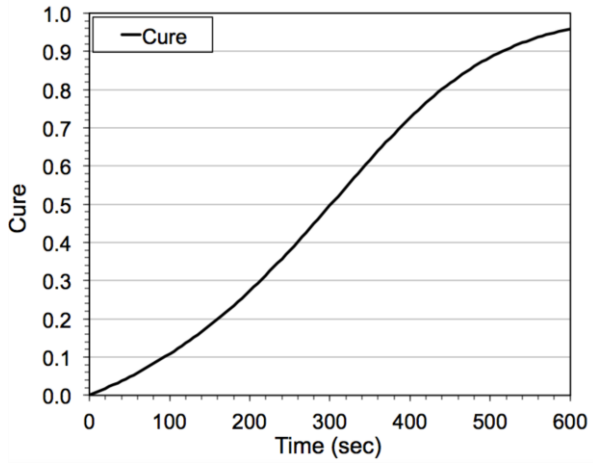

Figure 3.3. Degree of cure as a function of time

Figure 3.6 shows a comparison between the elastic modulus obtained from the Ruiz model and from the mixture theory model for a cure of 0.93 at various temperatures. For the mixture theory model, results are plotted for compressive displacement boundary condition of

0.01m. It can be seen from the plots that the elastic modulus obtained at the end of cure cycle compares well with that predicted by the Ruiz model (3.43).

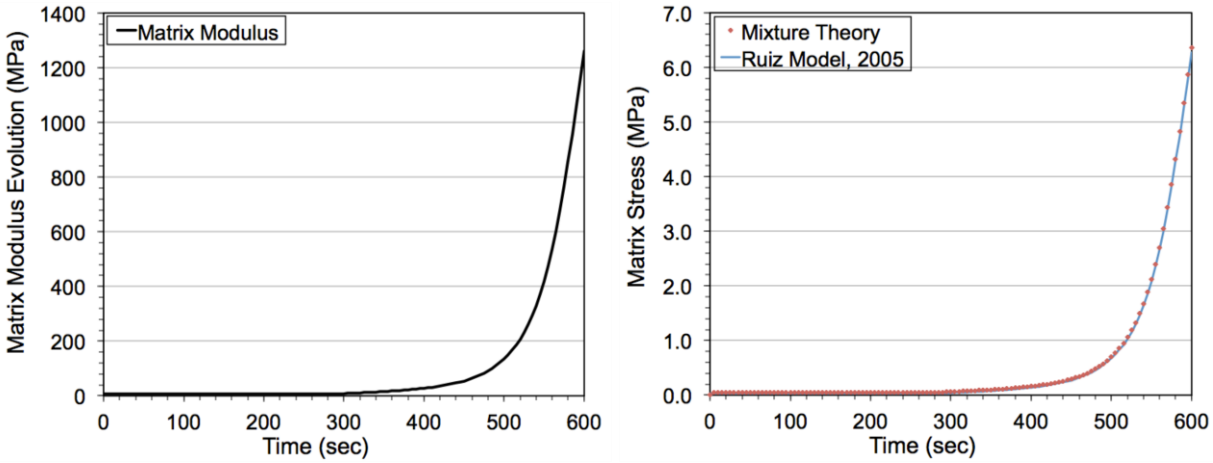

(a) Matrix modulus vs time (b) Matrix stress vs time

Figure 3.4. Evolution of matrix modulus and matrix stress with progressive curing of the resin

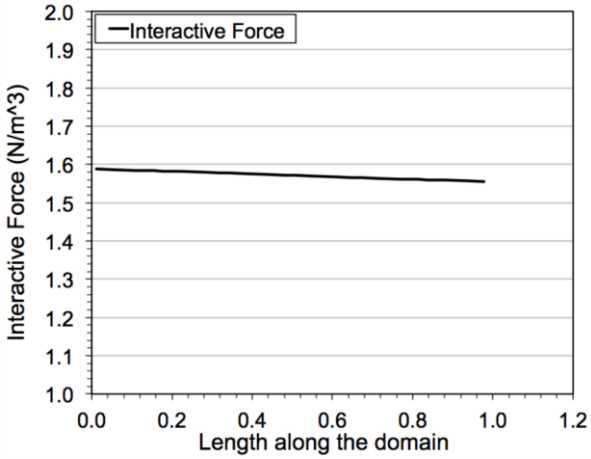

Figure 3.5. Fiber interactive force along the domain at t=600 seconds

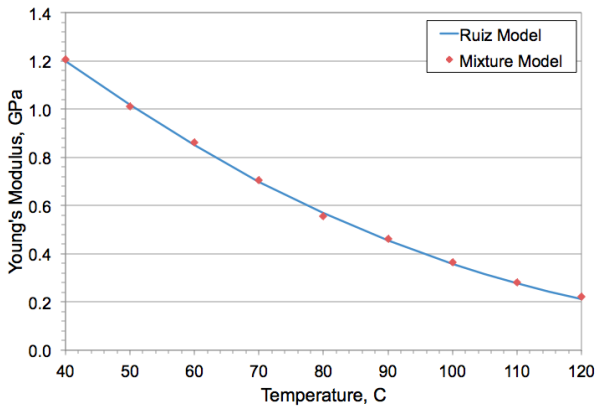

Figure 3.6. Evolution of elastic modulus as a function of temperature

3.5.2 Numerical test of interphase evolution

This test case investigates interphase formation between matrix and fiber for a given reaction rate. We consider a domain of unit length, fixed at x=0 and subjected to a specified displacement of 0.01 applied at x=L to induce compressive stress that develops in the autoclave during the cure cycle. The domain is discretized with 40 one-dimensional cubic elements. A temperature field of 600K, which is otherwise arbitrary, is prescribed, and it is constant and uniform with respect to space and time. Material constants for the reinforcement (i.e., fiber) are: $\rho_T^r = 1740,\ \alpha^r = 8.595\times10^8,\ \beta^r = 3.6113\times10^{11},$ and the bulk and shear moduli are $\lambda^r = 7.0590\times10^9,\ \mu_L^r = 6.4573\times10^9,\ \mu_T^r = 5.349\times10^9$, respectively. Material constants for the matrix material are: $\rho_T^m = 1200,\ \lambda^m = 1.99\times10^9,\ \mu^m = 1.33\times10^9$.

Figure 3.7 shows the evolution of the cure in the interphase material for n = 1.4, 1.6 and 1.8 in (3.53). It can be observed that the cure of the interphase material reaches a value of 0.99, 0.97 and 0.95 for n = 1.4, 1.6 and 1.8 at 1200 seconds, respectively. For these reaction rates, the interphase modulus and interphase density varies with time as shown in Figure 3.8a and Figure 3.8b, respectively. Interphase modulus is a function of amine concentration and is an inherent property of the material. As the reaction proceeds the amine concentration decreases and the interphase modulus follows a curve shown in Figure 3.2a. Likewise, due to the reduction in amine concentration, interphase density also decreases as in shown in Figure 3.2b.

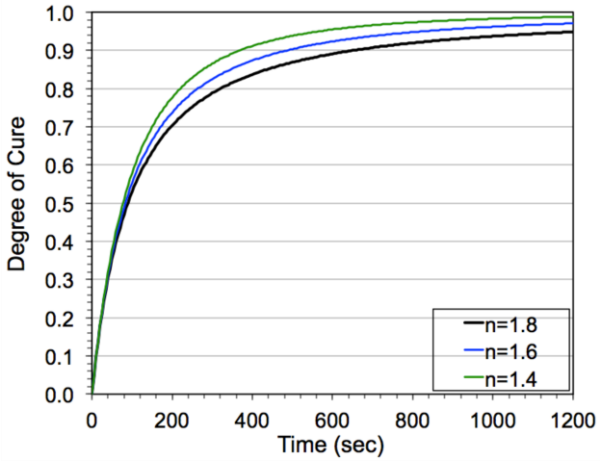

Figure 3.7. Degree of cure vs time

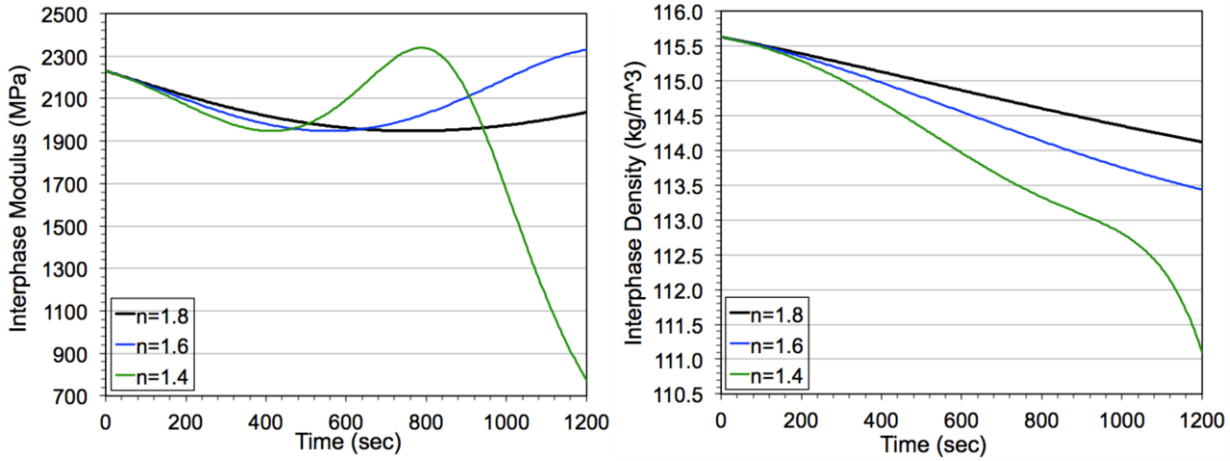

a). Interphase modulus vs time b). Interphase density vs time

Figure 3.8. Interphase property evolution with time

Figure 3.9a shows the average matrix stress variation with respect to time. As the interphase properties evolves, the epoxy-amine system shows nearly a linear variation in stress in the initial stages and reaches plateau after 400 seconds. In order to segregate the effects of stress evolution due to chemical evolution from evolving mechanical stretching, we ran the problem with a prescribed stretched at time zero. Though only the interphase material evolves (the matrix is assumed to be inert), the effect of the curing in interphase on the overall matrix strength is shown in Figure 3.9b. It can be observed that the overall matrix modulus evolves similar to the matrix stress for a reaction constant of n = 1.8.

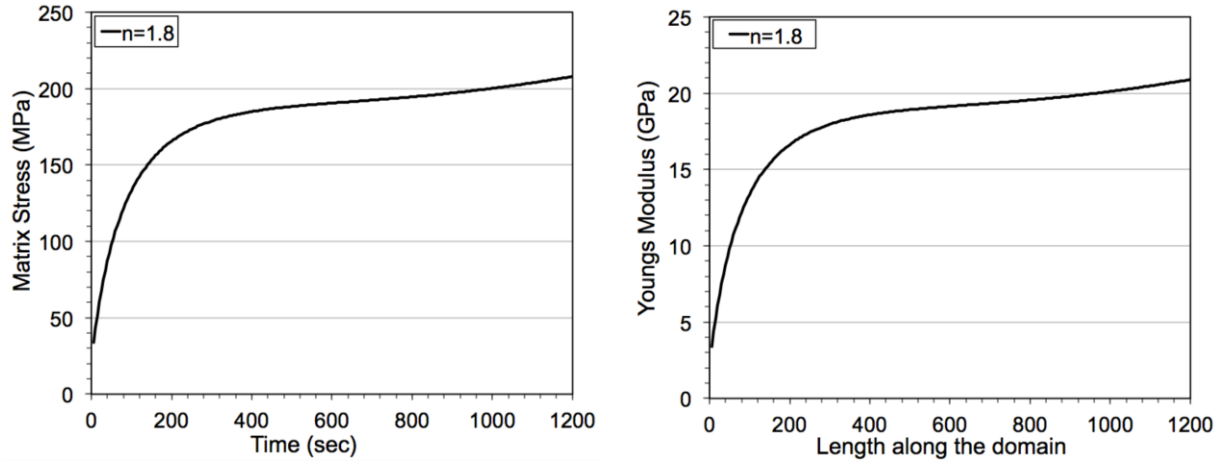

(a) Matrix stress vs time (b) Youngs modulus vs time

Figure 3.9. Interphase properties evolution for epoxy-amine resin

3.5.3 Interphase formation in zones with different reaction rates

This test case models interphase evolution for variable reaction rates along the length of the rod and showcases that while the mixture model is locally homogeneous, it retains the global heterogeneity property. The spatial dimension, boundary conditions and mesh resolution are same as in the previous case. The reference and the current uniform temperatures are 580K and 600K, respectively. The rod is divided into subdomains $A \cup B$ as shown in Figure 3.10 and it is assumed that the reaction rate in $A \cup B$ is 100 times faster than in $\Omega / A \cup B$ subdomain, i.e., $\dot{\Gamma}^0_A = \dot{\Gamma}^0_B, \quad \dot{\Gamma}^0_{\Omega/\mathrm{A}\cup\mathrm{B}} = 0.01\,\dot{\Gamma}^0_B$. This gives rise to a sharp interface between material zones with variable curing rates. The problem was run for 400, 800 and 1200 seconds with a time step of 5 seconds. Material constants for the reinforcement (i.e., fiber) are: $\rho^r = 1590,\ \alpha^r = -0.566\times10^4,\ \beta^r = 111\times10^4$, and the bulk and shear moduli are $\lambda^r = 5.71\times10^4,\ \mu^r_L = 3.81\times10^4,\ \mu^r_T = 2.51\times10^4$, respectively. Material constants for the matrix material are: $\rho^m = 559,\ \lambda^m = 5.71\times10^2,\ \mu^m = 3.81\times10^2$.

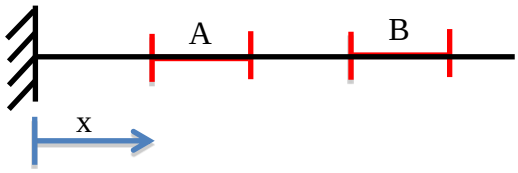

Figure 3.10. Reaction zones in 1D mixture domain

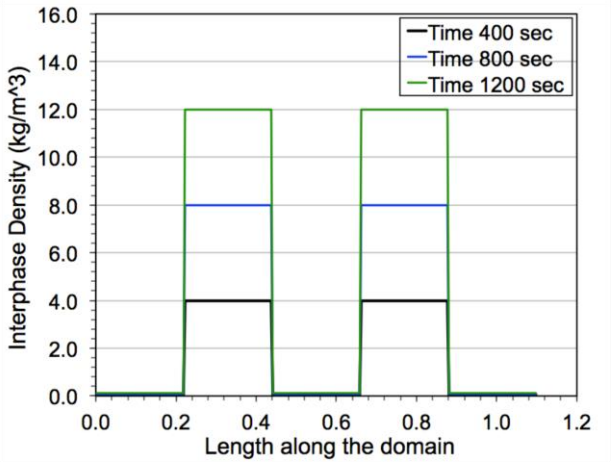

(a) Interphase density vs time

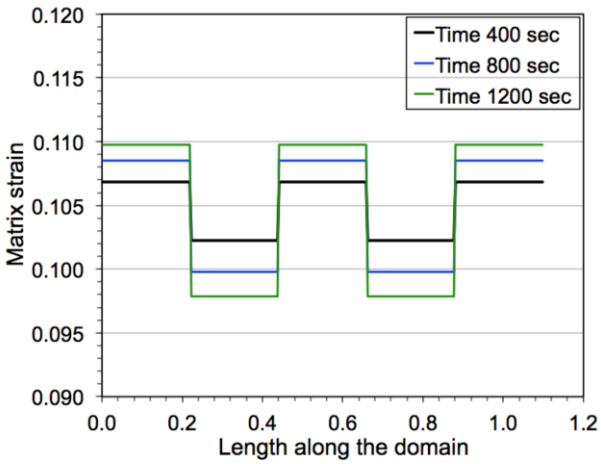

(b) Matrix strain along the domain

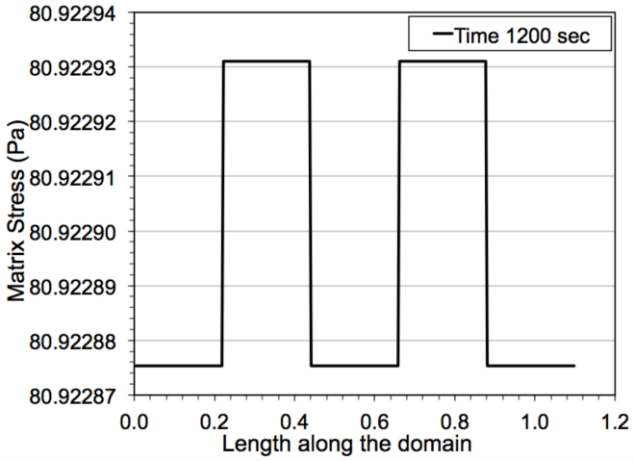

(c) Matrix stress along the domain

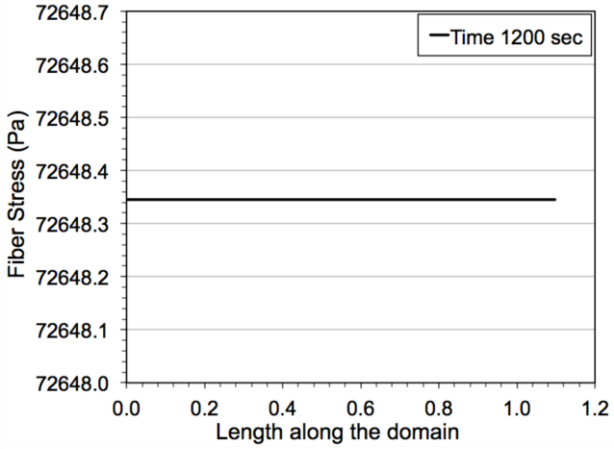

(d) Fiber stress along the domain

Figure 3.11. Interphase properties evolution for epoxy-amine resin

Figure 3.11a shows the spatial distribution of the density of the interphase material r^c (density of converted matrix) along the domain for 400, 800 and 1200 seconds. This sharp variation in the density of the interphase matrix material results in rapid variation in the stiffness of the system

that manifests itself in terms of sharp variation in the axial strain as shown in Figure 3.11b. Figure 3.11c shows the matrix stress variation along the domain at 1200 seconds. It can be observed that the matrix stress is higher in the faster reaction zone, as they reach maximum cure faster and hence higher interphase modulus. Since the fiber is assumed to be inert and is subjected to a constant mechanical loading, Figure 3.11d shows a constant fiber stress at 1200 seconds as expected.

3.5.4 Interphase evolution and interactive force field

This problem is an extension of the previous test case with an applied body force of 0.5 m/s^2 that produces a nonlinear displacement field. Figure 3.12a shows the spatial distribution of ρ^c (density of converted matrix). As seen in (3.31), the converted matrix density is only a function of the degree of cure and independent of the mechanical deformation. Hence, we see a similar variation in the converted density in comparison to the previous case with no body force. Since the displacement field is non-linear, the gradient of the deformation gradient does not vanish in equation (3.30). Figure 3.12b shows the spatial distribution of the interactive force field between the two constituents, that also shows sharp variation across the zones of fast and slow chemical reactions.

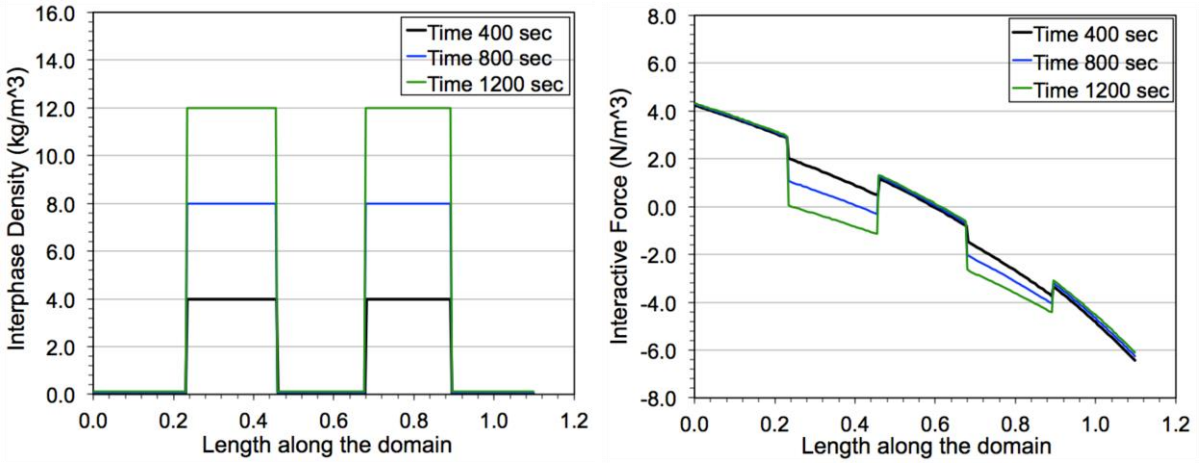

(a) Interphase density along the domain (b) Fiber interactive force along the domain

Figure 3.12. Converted matrix density along the domain

3.5.5 Tri-axial model with curing and coupled chemo-mechanical evolution

This test case is three dimensional implementation of the cure and interphase evolution model. The constitutive model is tri-axial, however it is implemented in a three dimensional kinematic context. Since the underlying displacement formulation is based on variational multiscale ideas that give rise to a multiscale/stabilized displacement field which inherits the properties of the classical $\bar{\boldsymbol{F}}(\boldsymbol{X},t)$ type methods as shown in Masud and Truster [42], introduction of the temperature field leads to an additional mapping that accounts for thermal evolution of the problem, however the thermal field is not split into coarse and fine scales. In the finite deformation context, it leads to a split of the total deformation map $\boldsymbol{\varphi}^{\alpha}$ of each constituent into thermal $\boldsymbol{\varphi}^{th}$ and mechanical mappings $\boldsymbol{\varphi}^{mech}\left(\boldsymbol{X}^{\alpha},t\right)$, where mechanical mapping is further split into fine scale deformation map $\tilde{\boldsymbol{\varphi}}^{\alpha}$ over the coarse scale deformation map $\bar{\boldsymbol{\varphi}}^{\alpha}\left(\boldsymbol{X}^{\alpha},t\right)$:

$$\begin{aligned}\boldsymbol{\varphi}^{\alpha} &= \boldsymbol{\varphi}^{th}\left(\boldsymbol{X}^{\alpha},t\right)\circ\boldsymbol{\varphi}^{mech}\left(\boldsymbol{X}^{\alpha},t\right)\\ &= \boldsymbol{\varphi}^{th}\left(\boldsymbol{X}^{\alpha},t\right)\circ\left[\tilde{\boldsymbol{\varphi}}^{\alpha}\circ\bar{\boldsymbol{\varphi}}^{\alpha}\left(\boldsymbol{X}^{\alpha},t\right)\right]\\ &= \boldsymbol{X}^{\alpha}+\boldsymbol{u}^{th}+(\bar{\boldsymbol{u}}^{\alpha}+\tilde{\boldsymbol{u}}^{\alpha})\end{aligned} \tag{3.54}$$

where $\boldsymbol{u}^{th}$ is the displacement component associated with the thermal field, $\bar{\boldsymbol{u}}^{a}$ is the coarse scale displacement field and $\tilde{\boldsymbol{u}}^{a}$ is the fine scale displacement field. Accordingly, the deformation gradient can be written as follows,

$$\boldsymbol{F}^{\alpha} = \boldsymbol{F}^{th}\cdot\left(\tilde{\boldsymbol{F}}^{\alpha}\cdot\bar{\boldsymbol{F}}^{\alpha}\right) \tag{3.55}$$

where $\boldsymbol{F}^{th}$ is the thermal part of the deformation gradient, $\tilde{\boldsymbol{F}}^{a}$ is the fine scale deformation gradient and $\bar{\boldsymbol{F}}^{\alpha}$ is the coarse scale deformation gradient.

Table 3.1. Material properties of the lamina

	λ (MPa)	α (MPa)	β (MPa)	μ_L (MPa)	μ_T (MPa)	ρ (kg/mm^3)	Volume Fraction
Fiber	4.424E+03	1.2028E+3	2.467E+05	1.039E+04	1.039E+04	1550E-09	0.5
Matrix	3.4315	-	-	2.2877	-	1200E-09	0.5

Consider a Graphite-Epoxy composite rod of 1x0.1x0.1 mm as shown in Figure 3.14. The domain is discretized using 27 noded Lagrange elements with 8x2x2 elements. The mechanical material coefficients for the fiber and the matrix constituents are given in Table 3.1. The coefficient of thermal expansion of the matrix is 45e-6 1/K. The coefficient of thermal expansion of the fiber in longitudinal and transverse direction are -1.8e-6 and 21.6e-6 1/K respectively. A compressive displacement of -0.001 is applied at x=1.0, y = 0.1 and z=0.1 plane to simulate the pressure loading in the autoclave. The domain is also subjected to temperature field as shown in Figure 3.13a. It can be observed that the temperature varies axially in X direction, where the temperature is maximum at the boundaries and minimum at the center of the domain. This problem is run for 300 seconds, where the displacement boundary conditions is applied at the first time step and help constant until 300 seconds.

Figure 3.13b shows the evolution of curing at 100, 200 and 300 seconds in the domain. It can be seen that the cure at the boundary region reaches a value of 0.99 faster in comparison to the middle region of the domain. This is due to the prescribed temperature variation along the domain. Figure 3.13c shows the variation in the Youngs modulus in the matrix material at 100, 200 and 300 seconds. An uneven variation in the Youngs modulus can be observed along the length of the domain. The reason for this variation can be attributed to two factors: degree of cure and temperature. As the Youngs modulus decrease with increase in temperature even for fully cured material and time required to achieve complete curing is a function of temperature, we see uneven but symmetric variation in matrix Youngs modulus along the domain. The matrix stress shows in Figure 3.13d follows a similar trend.

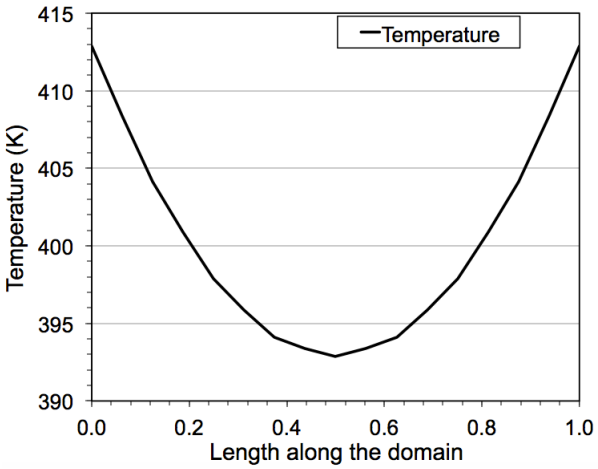

(a) Temperature along the domain

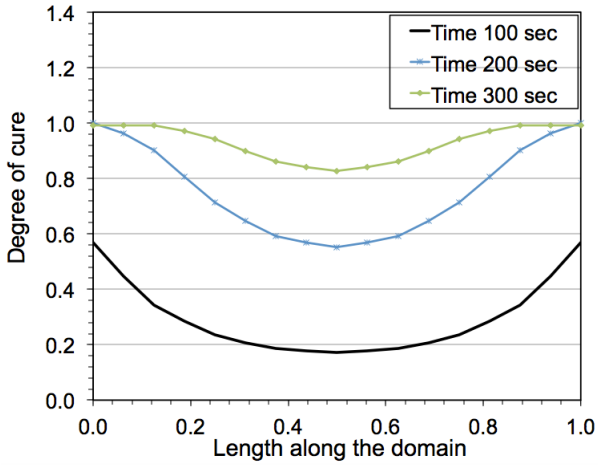

(b) Cure along the domain

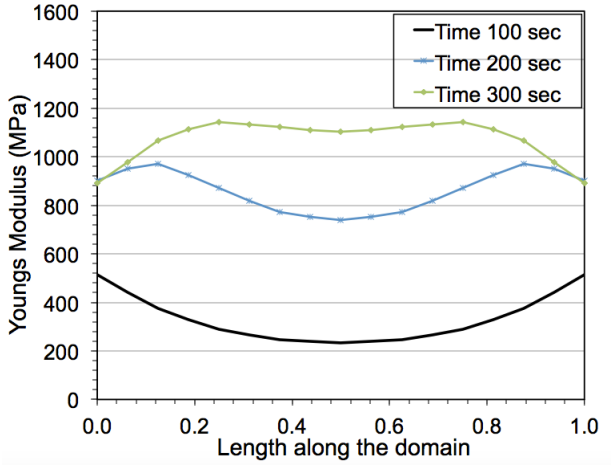

(c) Youngs Modulus along the domain

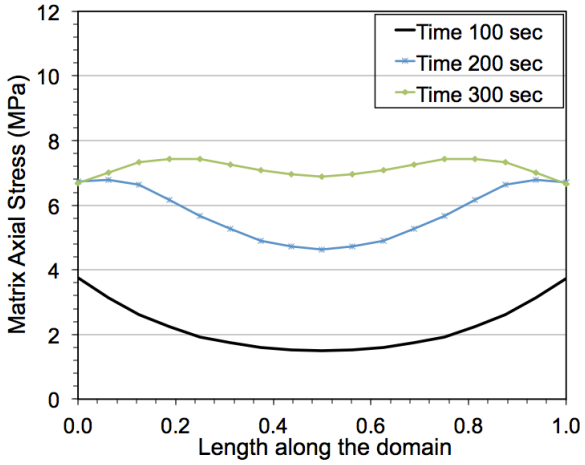

(d) Matrix axial stress along the domain

Figure 3.13. Chemically evolving variables at time = 100, 200 and 300 seconds

Figure 3.14a shows the matrix stress variation at 300 seconds for the whole domain. The matrix stress is symmetric along the x-axis and varies between 6.62 MPa and 7.45 MPa. Though the applied displacement is compressive, the matrix stress is tensile due to the thermal effects. Figure 3.14b shows the composite axial stress variation which is dominated by the fiber stress. As the coefficient of thermal expansion of the fiber is negative, we observe a compressive stress for the composite. To the contrary, as the coefficient of thermal expansion of the fiber is positive in transverse direction we observe a tensile transverse stress field of the composite in Figure 3.14c. The fiber interactive force field in X and Y direction are shown in Figure 3.14d and Figure 3.14e,

which accounts for the interaction in the fiber and matrix in a homogenized sense due to the differential expansion and curing of the matrix material.

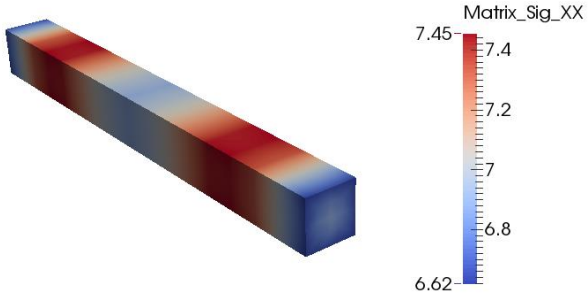

(a) Matrix axial stress

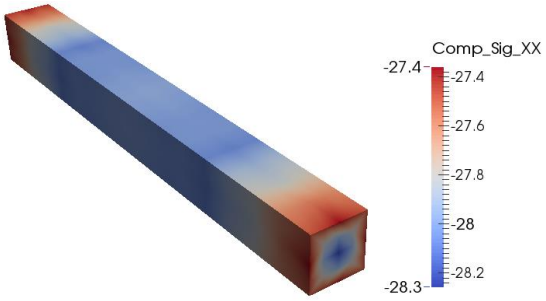

(b) Composite axial stress

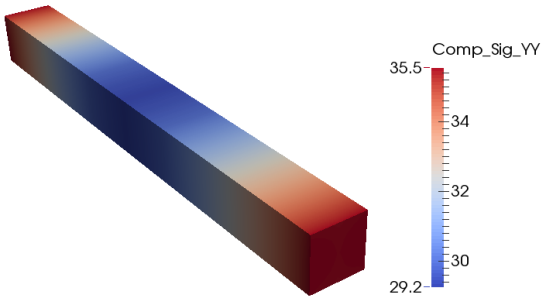

(c) Composite transverse stress

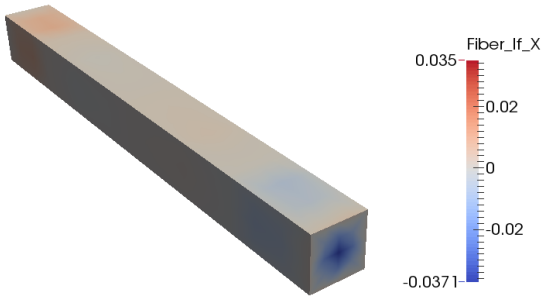

(d) Fiber interactive force in X direction

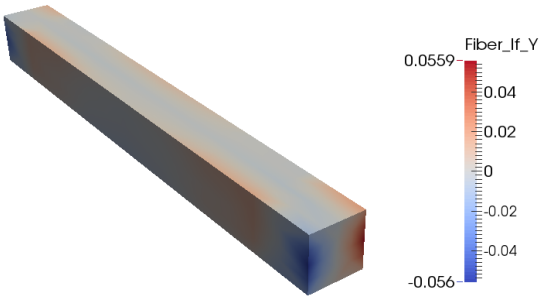

(e) Fiber interactive force in Y direction

Figure 3.14. Kinematic and kinetic quantities of the constituents and composite at 300 seconds

3.6 Conclusions

In this paper we have presented a model for interphase formation during the curing process of composite materials in the context of mixture theory and cast in a finite strain framework. The model is based on the maximization of the rate of entropy production constraint and accommodates anisotropic effective reaction rates accompanied with an anisotropic tensor that provides coupling of chemical reaction and mechanical stresses. In this multi-continuum theory for composites, the material particles of different constituents are grouped together at reference configuration to define a composite particle. Though these constituent particles occupy different spatial points as the material deforms, the interactions between constituents are evaluated in the reference configuration using the composite particle. A significant feature of the mixture model is the interactive force field that is generated due to the interplay of the constituents. Even though in the homogenized mixture element an explicit discrete representation of the constituents is suppressed, the interplay of the constituents is fully accounted for via interactive force fields and the corresponding coupling terms that emanate from the mixture modeling ideas. It is important to realize that the standard single continuum homogenization theories do not possess this feature and while they can model kinematics of deformation, they cannot provide an insight into the interplay of the constituents. As such they are not able to identify the regions in the composite where interactive force fields can exceed the load transfer capability between fiber and matrix which can lead to the initiation of localized damage.

Chapter 4

Edge Stabilization and Consistent Tying of Constituents at Neumann Boundaries in Multi-Constituent Mixture Models*

4.1 Introduction

In the manufacturing of fibrous composites, the fiber-resin mixture is subjected to a cure cycle that initiates cross-linking polymerization in resin to produce a structurally hard material. The properties of the final product as well as its performance characteristics depend on the properties of constituents as well as the properties of the interphase zone formed in the constituent interface region. Theoretical models and numerical methods employed to model material evolution at the microscale level need to capture the behavior of the individual constituents as well as their coupled interactions in an integrated fashion. This chapter employs a mixture theory based model for a representative infinitesimal volume element of dense mixture of multi-constituent solids where each constituent is governed by its own balance laws and constitutive equations. Interactive forces between constituents that emanate from maximization of entropy production inequality provide the necessary coupling between the balance laws and constitutive models and therefore between the concurrent and overlapping constituents.

A literature review reveals that mixture theory as proposed by Truesdell [1] has been widely employed in the modeling of fluid-fluid and solid-fluid mixtures. Comprehensive review articles by Atkin and Craine [2], Green and Naghdi [3,4] and the book by Rajagopal and Tao [5] provide

* This Chapter has been submitted for publication in IJNME

a good exposition to the mixture theory and associated constitutive relations. Mixture theory ideas have been used to model various phenomena such as classical viscoelasticity [6], swelling of polymers [7], thermo-oxidative degradation of polymer composites [8,9], growth of biological materials [10] and crystallization of polymers [11], to name a few. Mixture theories have also been employed to model the multi-constituent elastic solids, e.g., Bowen et al. [29] presented a thermomechanical theory for diffusion in mixtures of elastic materials. Bedford et al. [30] proposed a multi-continuum theory for composite materials, where the material particles of different constituents are grouped together at reference configuration to define a composite particle. Though these constituent particles occupy different spatial points as the material deforms, the interactions between constituents are evaluated in the reference configuration using the composite particle. Hall and Rajagopal [13,31] proposed a mixture model for diffusion of chemically reacting fluid through an anisotropic solid based on the maximization of the rate of entropy production constraint, considering anisotropic effective reaction rates and the limits of diffusion-dominated (diffusion of the reactants is far more rapid than the reaction) and reaction-dominated (the reaction is far more rapid than the diffusion of the reactants) processes. In the present work the theory by Hall and Rajagopal [13,31] is enhanced to the case of mixture of two interacting solid constituents, and a edge-stabilized method is developed to model fibrous composite systems.

A general preface of the mixture theory is that the constituents are assumed to coexist over each other at every point in the domain, a condition that arises due to the volumetric homogenization of each constituent over the composite/mixture domain. As the constituents deform over each other, the domain boundary of the mixture has to be constrained through continuity conditions. Enforcing continuity between constituents at the boundary is analogous to the interface treatment in domain decomposition methods, contact problems and material interfaces. Amongst the various numerical techniques that enforce continuity conditions and traction equilibrium at the interface, a classical approach is the unconstrained optimization problem a Lagrange multiplier field is employed to enforce continuity at the interface. The stability issues that arise in this dual field formulation in its discretized form are well known [32], where the interpolation functions for the primary field and Lagrange multipliers need to be chosen such that the celebrated Babuska-Brezzi condition is not violated. In addition, the computational cost increases because of the introduction of additional variables associated with

the Lagrange multipliers. This however can be addressed via a primal field formulation that can be derived by defining the Lagrange multipliers through penalty parameter and the continuity conditions. The disadvantage of the penalty method is that it attains optimal convergence only as the penalty parameter approaches infinity, which however leads to ill conditioning of the matrix systems. A consistent penalty formulation was introduced by Nitsche [33] to enforce Dirichlet boundary condition weakly on the boundaries. This primal formulation is consistent and symmetric, wherein the Lagrange multiplier fields are approximated by the numerical fluxes at the boundary. Nitsche method was then extended to handle interfaces that arise in domain decomposition methods, embedded finite element methods and physical interfaces. The penalty parameter in Nitsche method needs to be defined to ensure the coercivity of the method and there have been many works to define this parameter through an *a-priori* analysis, solving a global or local eigenvalue problem, and through bubble function approach [34-38]. Masud and coworkers [39-44] have developed a unified formulation for interface coupling and frictional contact modeling where the penalty parameter is derived through variational multiscale framework and Lagrange multiplier field is approximated as simple average of fluxes. Truster and Masud [45] extended this framework in finite deformation context where the stabilization tensor is consistently derived and is a function of both material and geometric nonlinearity.

The deformation of multi-constituent mixtures at the Neumann boundaries requires imposing constraint conditions such that the constituents deform in a self-consistent fashion. In the present work, a set of boundary conditions are presented that are modified to account for the non-zero applied tractions. Following the line of thought in [39-44] a numerical method is developed that draws from the stabilized Discontinuous Galerkin method for finite strain kinematics with an underlying Lagrange multiplier interface formulation. The derivation of the new method hinges upon a multiscale decomposition of the deformation map locally at the Neumann boundary and subsequent modeling of the fine scales via edge bubble functions. The resulting terms enable the condensation of the multiplier field from the formulation in addition to providing an edge based stabilization of the method. Closed-form expressions are derived for the stabilization tensor and the weighted numerical flux that are free from tunable stability parameters. The key novelty is that the consistently derived stability tensors automatically evolve with evolving material and geometric nonlinearity at the boundaries.

The outline of thid chapter is as follows. In section 4.2, we present the governing equations and the constitutive relations for two-solid constituent mixtures for the modeling of composites. Boundary conditions and a procedure to determine the material properties of the constituents is presented in Section 4.3. The stabilized formulation for the imposition of continuity and traction equilibrium conditions is derived in Section 4.4. Section 4.5 presents a series of numerical test cases and results are compared with analytical solutions and results available in literature. Conclusions are drawn in section 4.6.

4.2 Mixture Theory Governing Equations

Although mixture theory provides a general framework for modeling an N constituent mixture, we present mixture equations in the context of two-constituents, namely matrix and fiber, where both constituents are assumed to be in the solid phase. The underlying idea in mixture theory for the modeling of composites is that the constituents are assumed to coexist concurrently at every point in the domain. This assumption arises due to the volumetric homogenization of each constituent over the composite/mixture domain.

Let us consider a microstructure of a composite as shown in Figure 4.1a. A macroscopic point in the mixture domain represents an average behavior of the constituents at the microscale. Thus, assuming certain periodicity in the microstructure, the macroscopic point can be represented by a unit cell as shown in Figure 4.1b. The unit cell comprises of fibers with given orientation embedded in the matrix material. These constituents are segregated and homogenized over the mixture volume (as shown in Figure 4.1c and Figure 4.1d) and are assigned an apparent density property which is defined as ratio of the mass of the constituent over the mixture volume. Thus the composite density is the sum addition of the constituent apparent densities.

$$\rho = \rho^m + \rho^r \tag{4.1}$$

where ρ^m, ρ^r are the matrix and fiber apparent density, respectively and ρ^c is the composite density.

Remark: *The effective properties of a composite are orthotropic due to fiber orientation and fiber-matrix interaction even when the constituents are isotropic. In mixture theory, as the*

constituents are homogenized at the individual level in a volumetric sense over the mixture volume, in order to obtain the effective orthotropic properties of the composite, the domain of homogenized fibers is modeled as an orthotropic material.

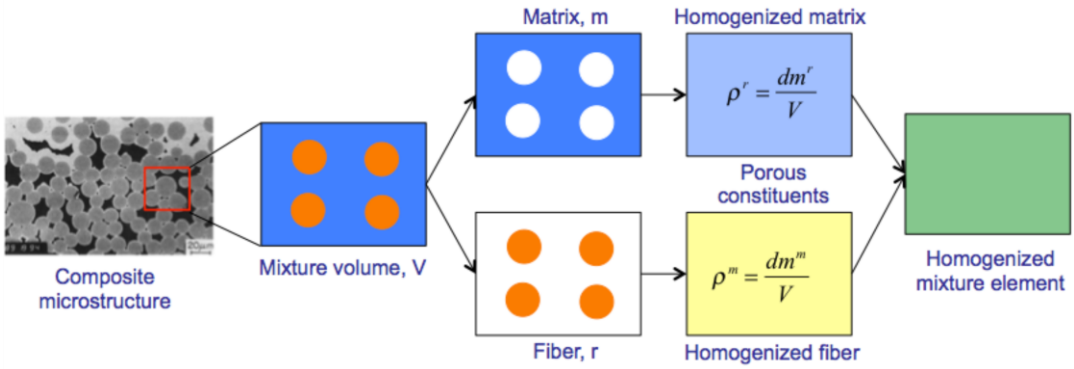

Figure 4.1. Mixture theory homogenization

Consider an open bounded region of the mixture Ω^c in the reference configuration as shown in Figure 4.2, where a matrix reference domain Ω^m and a fiber reference domain Ω^m coexist over each other. It should be noted that in the reference configuration, $\Omega^c = \Omega^r = \Omega^m$. The boundaries of the fiber, matrix and the composite domains are denoted by Γ^r, Γ^m and Γ^c, respectively, where, $\Gamma^c = \Gamma^r = \Gamma^m$ because every point on the boundary is concurrently occupied by fiber and matrix. For compact presentation of ideas, the kinematic and kinetic quantities of the matrix, fiber and the composite will be denoted by a superscript α, where $\alpha \in \{m, r, c\}$. For a given point $\boldsymbol{X}$ in the material configuration of the composite, there exists a particle of matrix, $\boldsymbol{X}^m$ and that of fiber, $\boldsymbol{X}^r$ with same material coordinates. Although $X^r = X^m = X^c$, these constituent material points are shown in two separate domain in Figure 4.2 for the sake of clarity. As explained earlier, the fiber domain W and the matrix domain W^m coexist over each other in the composite domain, W. When the mixture domain is subjected to external loadings, the reference configuration of the constituent α, Ω^α deforms to the current configuration Ω^α_φ under the deformation map, $\boldsymbol{\varphi}^\alpha\left(\boldsymbol{X}^\alpha, t\right)$. Thus the deformation gradient of each constituent α, is given as,

$$\boldsymbol{F}^{\alpha} = \frac{\partial \boldsymbol{\varphi}^{\alpha}\left(\boldsymbol{X}^{\alpha}, t\right)}{\partial \boldsymbol{X}} \tag{4.2}$$

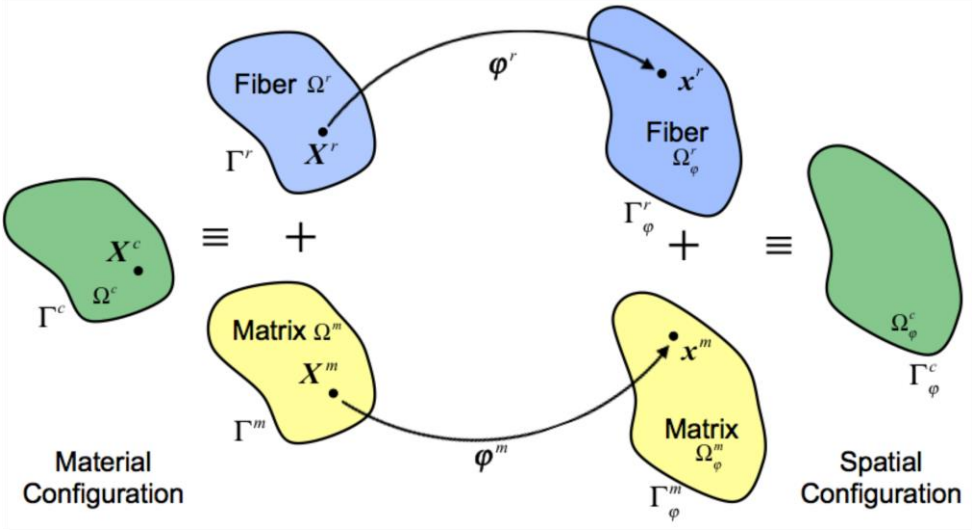

Figure 4.2. Mixture kinematics

From Figure 4.2, it can be seen that the coexisting material points $\boldsymbol{X}^r, \boldsymbol{X}^m$ of the constituents in material configuration maps to two different spatial points in the current configuration. The interaction between these homogenized constituents as they deform with respect to each other is a function of the relative stretch and rotation of these two spatial points. For any point in one of the constituent spatial configurations, the corresponding spatial point from the other constituent can be obtained via a pull back and push forward mapping as given below.

$$\boldsymbol{x}^r = \boldsymbol{\varphi}^r\left(X^r, t\right) = \boldsymbol{\varphi}^r\left(X^m, t\right) = \boldsymbol{\varphi}^r\left(\boldsymbol{\varphi}^{m^{-1}}\left(\boldsymbol{x}^m, t\right), t\right) \tag{4.3}$$

The balance of mass and balance of linear momentum of the constituents in the current configuration are given as follows:

$$\frac{\partial \rho^{\alpha}}{\partial t} + \nabla \cdot \left(\rho^{\alpha} \boldsymbol{v}^{\alpha}\right) = m^{\alpha} \tag{4.4}$$

$$\nabla \cdot \left(\boldsymbol{T}^{\alpha}\right)^{T} + \rho^{\alpha} \boldsymbol{b}^{\alpha} + \boldsymbol{I}^{\alpha} = \boldsymbol{0} \tag{4.5}$$

where ρ^{α} is the apparent density in the current configuration, and m^{α} is the rate of mass transferred by chemical reaction to constituent α; $\boldsymbol{T}^{\alpha}$ is the partial Cauchy stress, $\boldsymbol{b}^{\alpha}$ is the body force per unit mass and $\boldsymbol{I}^{\alpha}$ is the interactive force per unit mixture volume of the constituent in the reference configuration as the constituents deforms over each other. Newton's third law requires that

$$\boldsymbol{I}^{r} + \boldsymbol{I}^{m} = \boldsymbol{0} \tag{4.6}$$

Remark: *Interactive force is a unique feature of mixture theory that models the interaction between the constituents as they deform with respect to each other. This volumetric force is a homogenized quantity that captures the interactions at the fiber-matrix interface through constitutive relations. A failure model based on the interactive force between fiber and matrix can be developed to model the damage at the fiber-matrix interface in a macroscopic sense.*

In the absence of mass exchange between the constituents, the balance of mass equations reduce to algebraic form,

$$\rho^{\alpha} J^{\alpha} = \rho_{R}^{\alpha} \tag{4.7}$$

where ρ_{R}^{α} is the apparent density in the reference configuration.

Remark: *Though it has been assumed that there is no mass transfer between the matrix and fiber, the theory still allows the modeling of the interphase evolution in the composite, by postulating that the interphase evolves in the boundary layer of the matrix domain at the fiber-matrix interface.*

The constitutive relations for the mixture theory are obtained through the maximization of the rate of dissipation constraint. Details for this derivation can be seen in [13] and [31]. Here we present the summary of the constitutive relations, where the volume additivity constraint is not imposed.

Constitutive relations:

$$\boldsymbol{T}^m = \rho \boldsymbol{F}^m \left(\frac{\partial \psi}{\partial \boldsymbol{F}^m} \right)^T - \rho^m g^m \mathbf{I} + \mu \frac{\partial \xi}{\partial \boldsymbol{L}^m} \tag{4.8}$$

$$\boldsymbol{T}^r = \rho \boldsymbol{F}^r \left(\frac{\partial \psi}{\partial \boldsymbol{F}^r} \right)^T - \rho^r g^r \mathbf{I} \tag{4.9}$$

$$\begin{aligned} \boldsymbol{I}^m = {} & g^m \frac{\rho^r}{\rho} \nabla \rho^m - g^r \frac{\rho^m}{\rho} \nabla \rho^r + \frac{\rho^r \rho^m}{\rho} \left(\frac{\partial \phi^m}{\partial \boldsymbol{F}^m} : \nabla \boldsymbol{F}^m - \frac{\partial \phi^r}{\partial \boldsymbol{F}^r} : \nabla \boldsymbol{F}^r \right) \\ & - m^m (\mathbf{v}^m - \mathbf{v}^r) - (\nabla \theta) \frac{\rho^m \rho^r}{\rho} (\eta^m - \eta^r) - \mu \mathbf{A}^v (\mathbf{v}^m - \mathbf{v}^r) \end{aligned} \tag{4.10}$$

$$\mu \frac{\partial \xi}{\partial \dot{\theta}} = -\rho \left(\frac{\partial \psi}{\partial \theta} + \eta \right) \tag{4.11}$$

$$-\rho \left(\frac{\partial \psi}{\partial \Gamma^0} \right) = \mu \frac{\partial \xi}{\partial \dot{\Gamma}^0} \tag{4.12}$$

where $\dot{\Gamma}^0$ is the reaction rate, ξ is the rate of dissipation, μ is the Lagrange multiplier enforcing the maximum rate of dissipation constraint, h^a are the entropy and g^a chemical potential of the a^{th} component of the mixture.

Assuming isothermal conditions and chemically non-reactive nonlinear elastic constituents, the constitutive relations for the matrix stress, fiber stress and the fiber interactive force given in (4.8)-(4.10) can be reduced to

$$\boldsymbol{T}^m = \boldsymbol{F}^m \left(\frac{\partial (\rho \psi)}{\partial \boldsymbol{E}^m} \right) (\boldsymbol{F}^m)^T \tag{4.13}$$

$$\boldsymbol{T}^r = \boldsymbol{F}^r \left(\frac{\partial (\rho \psi)}{\partial \boldsymbol{E}^r} \right) (\boldsymbol{F}^r)^T \tag{4.14}$$

$$\boldsymbol{I}^m = \frac{\rho^r \rho^m}{\rho} \left(\frac{\partial \phi^m}{\partial \boldsymbol{F}^m} : \nabla \boldsymbol{F}^m - \frac{\partial \phi^r}{\partial \boldsymbol{F}^r} : \nabla \boldsymbol{F}^r \right) \tag{4.15}$$

Remark: *Interactive force in the fiber under isothermal conditions is given by* (4.15)*. It should be noted that the interactive force is a function of both matrix and fiber displacement field and in fact involves the second order derivative of the displacement fields. Thus the constitutive relation*

for the interactive force is a higher order relation and requires at least a quadratic piecewise polynomial as the shape function. As indicated by Hall [31], the components of the interactive forces relevant here are related to the expression for the force on a defect. The interactive force is required for force balance of a given constituent as obtained from both the surface tractions on a representative element and the interacting constituents within the element.

4.3 Boundary Conditions and Material Properties for the Mixture Model

In this section, we specify the boundary conditions and the material properties of the constituents to complete the definition of the mixture boundary value problem. In single continuum theories for solid mechanics problems, the definition of the Dirichlet or Neumann boundary conditions are well posed. But in mixture theory, as the constituents are allowed to deform with respect to each other, the definitions of the boundary conditions are unclear for two reasons. First, given a composite traction field, one needs an equivalent matrix and fiber traction boundary condition to complete the matrix and fiber boundary value problem. Second, due to finite deformation kinematics, the constituent boundaries can have different spatial maps, thus making it difficult to impose consistent boundary conditions.

4.3.1 Consistent split of traction fields

In mixture theory literature, a volumetric split of the traction fields is usually proposed, which however has the drawback of inconsistent deformation of the constituent boundaries. Following along the lines of the strategy adopted in interface problems, where continuity in the traction and displacement fields are weakly imposed, we propose a set of equations that ensures displacement continuity and traction equilibrium at the constituent boundary, that can be written in the spatial configuration as:

$$\begin{aligned} \boldsymbol{T}^r\boldsymbol{n}^r + \boldsymbol{T}^m\boldsymbol{n}^m &= \boldsymbol{h}^c \ \text{ on } \ \Gamma_\varphi \\ \boldsymbol{\varphi}^m - \boldsymbol{\varphi}^r &= \boldsymbol{0} \quad \text{ on } \ \Gamma_\varphi^h \\ \boldsymbol{\varphi}^r = \boldsymbol{\varphi}^m &= \bar{\boldsymbol{\varphi}}^c \ \text{ on } \ \Gamma_\varphi^g \end{aligned} \tag{4.16}$$

where, $\boldsymbol{h}^c$ is the composite traction field on the boundary Γ^{φ} and $\bar{\boldsymbol{\varphi}}^c$ is the specified composite displacement field, respectively.

4.3.2 Modeling of homogeneous fiber constituent

In mixture theories the constituents are homogenized over the mixture volume. While each of the constituents, i.e. matrix and the fiber material may be homogenous and isotropic, the structural layout of the fibers makes the homogenized fiber material as being transversely isotropic. The material constants of the homogenized fiber and matrix material can be obtained from experiments that capture the effective composite behavior. There are several material models for composites that are based on single continuum homogenization theories [46-48]. In this work, we employ these models from the literature to obtain the material constants for the homogenized constituents.

The total Helmholtz free energy function of the composite mixture can be written as,

$$\begin{aligned}\psi^c = &\frac{\rho^m}{\rho_T^m}\left\{\frac{1}{2}\lambda^m\left(tr\left[\boldsymbol{E}^m\right]\right)^2+\mu^m tr\left[\left(\boldsymbol{E}^m\right)^2\right]\right\}\\ &+\frac{\rho^r}{\rho_T^r}\left\{\begin{aligned}&\frac{1}{2}\lambda^r\left(tr\left[\boldsymbol{E}^r\right]\right)^2+\mu_T^r tr\left[\left(\boldsymbol{E}^r\right)^2\right]+\alpha^r\left(m^0\cdot\left[\boldsymbol{E}^r\right]m^0\right)tr\left[\boldsymbol{E}^r\right]\\ &+2\left(\mu_L^r-\mu_T^r\right)\boldsymbol{m}^0\cdot\left[\boldsymbol{E}^r\right]^2\boldsymbol{m}^0+\frac{1}{2}\beta^r\left(\boldsymbol{m}^0\cdot\boldsymbol{E}^r\boldsymbol{m}^0\right)^2\end{aligned}\right\}\end{aligned} \tag{4.17}$$

where ρ_T^m and ρ_T^r are the matrix and fiber true density, λ^m, μ^m are matrix material constants, $\lambda^r, \alpha^r, \mu_L^r, \mu_T^r, \beta^r$ are fiber material constants and $\boldsymbol{m}^0$ is the fiber direction in reference coordinates. For a transversely isotropic composite, the Helmholtz free energy of the composite based on single continuum homogenization (sch) can be written as follows,

$$\psi^{sch}\left[\boldsymbol{X},t\right]=\left\{\begin{aligned}&\frac{1}{2}\lambda^{sch}\left(tr\left[\boldsymbol{E}^{sch}\right]\right)^2+\mu_T^{sch}tr\left[\left(\boldsymbol{E}^{sch}\right)^2\right]+\alpha^{sch}\left(\boldsymbol{m}^0\cdot\left[\boldsymbol{E}^{sch}\right]\boldsymbol{m}^0\right)tr\left[\boldsymbol{E}^{sch}\right]\\ &+2\left(\mu_L^{sch}-\mu_T^{sch}\right)\boldsymbol{m}^0\cdot\left[\boldsymbol{E}^{sch}\right]^2\boldsymbol{m}^0+\frac{1}{2}\beta^{sch}\left(\boldsymbol{m}^0\cdot\boldsymbol{E}^{sch}\boldsymbol{m}^0\right)^2\end{aligned}\right\} \tag{4.18}$$

where, $\lambda^{sch}, \alpha^{sch}, \mu_L^{sch}, \mu_T^{sch}, \beta^{sch}$ are single continuum homogenization composite material constants and $\boldsymbol{m}^0$ is the fiber direction in reference coordinates. For the homogenized composite, the five independent material constants in (4.18) can be obtained from the literature for various material classes. The material constants associated with the homogenized matrix in (4.17) are modeled using the true matrix material parameters, also available in literature. Then, for the case of equally strained composite and its constituents, the material constants of the homogenized fiber material in (4.17) can be obtained by comparing the coefficients of the five strain invariants in (4.17) and (4.18).

4.4 Variational Multiscale Framework for Mixture Theory

This section presents a Lagrange multiplier formulation for imposing continuity constraints given in equation (4.16) on the constituent boundaries. Employing the Variational Multiscale (VMS) framework, we transform the Lagrange multiplier formulation to a stabilized primal formulation in the finite deformation context, where the closed-form approximation for numerical flux and stabilization parameter are consistently derived. This derivation is a generalization of the primal formulation for the interfaces that arise due to material discontinuity and possible non-conforming meshes [39-45]. We consider the balance of linear momentum equations of the constituents and its boundary conditions in reference configuration,

$$\text{DIV}\,\boldsymbol{P}^a + r_R^a \boldsymbol{b}^a + J^a \boldsymbol{I}^a = \boldsymbol{0} \quad \text{in} \quad \Omega^a, \;\; a \in \{r, m\} \tag{4.19}$$

$$\begin{aligned} \boldsymbol{P}^r \boldsymbol{N}^r + \boldsymbol{P}^m \boldsymbol{N}^m &= \boldsymbol{H}^c \quad \text{on} \;\; \Gamma \\ \boldsymbol{\varphi}^m - \boldsymbol{\varphi}^r &= \boldsymbol{0} \quad \text{on} \;\; \Gamma^h \\ \boldsymbol{\varphi}^r = \boldsymbol{\varphi}^m &= \bar{\boldsymbol{\varphi}}^c \quad \text{on} \;\; \Gamma^g \end{aligned} \tag{4.20}$$

where $\boldsymbol{P}^\alpha$ is the first Piola-Kirchhoff stress tensor, $\boldsymbol{N}^\alpha$ is the unit outward normal to the constituent boundary Γ^α, $\boldsymbol{b}^\alpha$ is the body force, $\boldsymbol{I}^\alpha$ is the interactive force field and $\boldsymbol{\varphi}^\alpha$ is the deformation map of constituent α. We write this boundary value problem as an unconstrained minimization problem via the use of Lagrange multiplier method as,

$$\Pi\left(\boldsymbol{\varphi}^r,\boldsymbol{\varphi}^m,\boldsymbol{\lambda}\right)=\sum_{\alpha=r,m}\left[\int_{\Omega^\alpha}\psi^\alpha\left(\boldsymbol{F}^\alpha\right)\mathrm{d}\Omega-\int_{\Omega^\alpha}\rho_R^\alpha\boldsymbol{b}^\alpha\bullet\boldsymbol{\varphi}^\alpha\,\mathrm{d}\Omega-\int_{\Omega^\alpha}J^\alpha\boldsymbol{I}^\alpha\bullet\boldsymbol{\varphi}^\alpha\,\mathrm{d}\Omega\right]$$
$$-\int_{\Gamma^c}\boldsymbol{H}^c\bullet\boldsymbol{\varphi}^c\,\mathrm{d}\Gamma-\int_{\Gamma^c}\boldsymbol{\lambda}\bullet\left[\!\left[\boldsymbol{\varphi}^r-\boldsymbol{\varphi}^m\right]\!\right]\mathrm{d}\Gamma=0 \tag{4.21}$$

where ψ^α is the Helmholtz free energy function of the constituent α and $\boldsymbol{\lambda}$ is the Lagrange multiplier field defined on the boundary to enforce the continuity constraints. Employing the continuity conditions (4.20) in the work done by the surface traction term in (4.21) and also considering the fact that the sum of the volume fraction of the constituents is unity, the above equation can be rewritten as,

$$\Pi\left(\boldsymbol{\varphi}^r,\boldsymbol{\varphi}^m,\boldsymbol{\lambda}\right)=\sum_{\alpha=r,m}\left[\int_{\Omega^\alpha}\psi^\alpha\left(\boldsymbol{F}^\alpha\right)\mathrm{d}\Omega-\int_{\Omega^\alpha}\rho_R^\alpha\boldsymbol{b}^\alpha\bullet\boldsymbol{\varphi}^\alpha\,\mathrm{d}\Omega-\int_{\Omega^\alpha}J^\alpha\boldsymbol{I}^\alpha\bullet\boldsymbol{\varphi}^\alpha\,\mathrm{d}\Omega\right]$$
$$-\int_{\Gamma^c}\boldsymbol{H}^c\bullet\left(V^r\boldsymbol{\varphi}^r+V^m\boldsymbol{\varphi}^m\right)\mathrm{d}\Gamma-\int_{\Gamma^c}\boldsymbol{\lambda}\bullet\left[\!\left[\boldsymbol{\varphi}^r-\boldsymbol{\varphi}^m\right]\!\right]\mathrm{d}\Gamma=0 \tag{4.22}$$

The associated weak form is obtained by taking variational derivative of (4.22) with respect to $\left(\boldsymbol{\varphi}^r,\boldsymbol{\varphi}^m,\boldsymbol{\lambda}\right)$ and is stated as follows: For all $\left\{\boldsymbol{\eta}_o^r,\boldsymbol{\eta}_o^m,\boldsymbol{\mu}\right\}\in\mathcal{V}^r\times\mathcal{V}^m\times\mathcal{Q}$, find $\left\{\boldsymbol{\varphi}^r,\boldsymbol{\varphi}^m,\boldsymbol{\lambda}\right\}\in\mathcal{S}^r\times\mathcal{S}^m\times\mathcal{Q}$, such that

$$\mathcal{W}_{\boldsymbol{\varphi}}=\sum_{\alpha=r,m}\left[\int_{\Omega^\alpha}\nabla_X\boldsymbol{\eta}_o^\alpha\bullet\boldsymbol{P}^\alpha\,\mathrm{d}\Omega-\int_{\Omega^\alpha}\boldsymbol{\eta}_o^\alpha\bullet\rho_R^\alpha\boldsymbol{b}^\alpha\,\mathrm{d}\Omega-\int_{\Omega^\alpha}\boldsymbol{\eta}_o^\alpha\bullet J^\alpha\boldsymbol{I}^\alpha\,\mathrm{d}\Omega\right]$$
$$-\int_{\Gamma^c}\left(V^r\boldsymbol{\eta}_o^r+V^m\boldsymbol{\eta}_o^m\right)\bullet\boldsymbol{H}^c\,\mathrm{d}\Gamma-\int_{\Gamma^c}\boldsymbol{\lambda}\bullet\left[\!\left[\boldsymbol{\eta}_o^r-\boldsymbol{\eta}_o^m\right]\!\right]\mathrm{d}\Gamma=0 \tag{4.23}$$
$$\mathcal{W}_{\boldsymbol{\lambda}}=\int_{\Gamma^c}\boldsymbol{\mu}\bullet\left[\!\left[\boldsymbol{\varphi}^r-\boldsymbol{\varphi}^m\right]\!\right]\mathrm{d}\Gamma=0$$

where the functional spaces are defined as follows:

$$
\begin{aligned}
\mathcal{S}^{\alpha} &= \left\{ \boldsymbol{\varphi}^{\alpha} \middle| \boldsymbol{\varphi}^{\alpha} \in \left[H^{2}\left(\Omega^{\alpha}\right) \right]^{nsd},\ \det\left(\boldsymbol{F}^{\alpha}\left(\boldsymbol{\varphi}^{\alpha}\right) \right) > 0,\ \boldsymbol{\varphi}^{\alpha}\big|_{\Gamma^{g}} = \bar{\boldsymbol{\varphi}}^{c} \right\} \\
\mathcal{V}^{\alpha} &= \left\{ \boldsymbol{\eta}_{o}^{\alpha} \middle| \boldsymbol{\eta}_{o}^{\alpha} \in \left[H^{2}\left(\Omega^{\alpha}\right) \right]^{nsd},\ \boldsymbol{\eta}_{o}^{\alpha}\big|_{\Gamma^{g}} = \mathbf{0} \right\} \\
\mathcal{Q}^{\alpha} &= \left\{ \boldsymbol{\lambda} \middle| \boldsymbol{\lambda} \in \left[H^{-\frac{1}{2}}\left(\Gamma^{c}\right) \right]^{nsd} \right\}
\end{aligned}
\tag{4.24}
$$

The functional spaces for the kinematically admissible constituent deformation field and the corresponding variational field lie in the $H^{2}\left(\Omega^{\alpha}\right)$ Sobolev space. This requirement arises due to the constitutive relation obtained for the interactive force through the maximization of rate of dissipation constraint. As seen in the equation (4.15), the interactive force is a function of spatial gradient of deformation gradient and thus we require the non-standard definition of the admissible spaces for mixture theory as compared to single continuum theories.

4.4.1 Multiscale decomposition

Although the Lagrange multiplier formulation consistently enforces the constraint at the constituent boundary, it leads to a mixed form for which the admissible spaces of functions for the displacement field and the Lagrange multiplier field must satisfy the Babuska-Brezzi condition [32]. In this section, we present a synopsis of the stabilized DG formulation that has been extended to the case of two-constituent mixture by employing the VMS framework presented in [45].

In the VMS framework, the underlying field is decomposed into a coarse scale field and a fine scale field. The coarse scale field represents the part of the solution that is represented by the given numerical discretization and the fine scale field represents the unresolved part of the solution. In the finite deformation context, it leads to a split of the total deformation map $\boldsymbol{\varphi}^{\alpha}$ of each constituent, which is written as a composition of fine scale deformation map $\tilde{\boldsymbol{\varphi}}^{\alpha}$ over the coarse scale deformation map $\bar{\boldsymbol{\varphi}}^{\alpha}$,

$$
\begin{aligned}
\boldsymbol{\varphi}^{\alpha} &= \tilde{\boldsymbol{\varphi}}^{\alpha} \circ \bar{\boldsymbol{\varphi}}^{\alpha}\left(\boldsymbol{X}^{\alpha}, t \right) \\
&= \boldsymbol{X}^{\alpha} + \bar{\boldsymbol{u}}^{\alpha} + \tilde{\boldsymbol{u}}^{\alpha}
\end{aligned}
\tag{4.25}
$$

where $\bar{\boldsymbol{u}}^a$ is the coarse scale displacement field and $\tilde{\boldsymbol{u}}^a$ is the fine scale displacement field. By substituting (4.25) in (4.2), we obtain the multiplicative split of the total deformation gradient as follows,

$$\boldsymbol{F}^\alpha = \tilde{\boldsymbol{F}}^\alpha \cdot \bar{\boldsymbol{F}}^\alpha \tag{4.26}$$

where $\tilde{\boldsymbol{F}}^a$ is the fine scale deformation gradient and $\bar{\boldsymbol{F}}^\alpha$ is the coarse scale deformation gradient. Substituting the multiscale decomposition of the solution field and weighting field into the weak form (4.23) and by employing the standard arguments regarding the linearity of the weighting function field, we obtain the coarse-scale problem and fine-scale problem as follows:

Coarse scale sub-problem

$$\begin{aligned}\bar{\mathcal{W}}_{\boldsymbol{\varphi}} = \sum_{\alpha=r,m}\Bigg[&\int_{\Omega^\alpha} \nabla_X \bar{\boldsymbol{\eta}}_o^\alpha \bullet \boldsymbol{P}^\alpha \,\mathrm{d}\Omega - \int_{\Omega^\alpha} \bar{\boldsymbol{\eta}}_o^\alpha \bullet \rho_R^\alpha \boldsymbol{b}^\alpha \,\mathrm{d}\Omega - \int_{\Omega^\alpha} \bar{\boldsymbol{\eta}}_o^\alpha \bullet J^\alpha \boldsymbol{I}^\alpha \,\mathrm{d}\Omega \Bigg] \\ &- \int_{\Gamma^c} \left(V^r \bar{\boldsymbol{\eta}}_o^r + V^m \bar{\boldsymbol{\eta}}_o^m \right) \bullet \boldsymbol{H}^c \,\mathrm{d}\Gamma - \int_{\Gamma^c} \boldsymbol{\lambda} \bullet \left[\!\left[\bar{\boldsymbol{\eta}}_o^r - \bar{\boldsymbol{\eta}}_o^m \right]\!\right] \mathrm{d}\Gamma = 0 \\ \mathcal{W}_{\boldsymbol{\lambda}} = &\int_{\Gamma^c} \boldsymbol{\mu} \bullet \left[\!\left[\boldsymbol{\varphi}^r - \boldsymbol{\varphi}^m \right]\!\right] \mathrm{d}\Gamma = 0\end{aligned} \tag{4.27}$$

Fine scale sub-problem

$$\begin{aligned}\tilde{\mathcal{W}}_{\boldsymbol{\varphi}} = \sum_{\alpha=r,m}\Bigg[&\int_{\Omega^\alpha} \nabla_X \tilde{\boldsymbol{\eta}}_o^\alpha \bullet \boldsymbol{P}^\alpha \,\mathrm{d}\Omega - \int_{\Omega^\alpha} \tilde{\boldsymbol{\eta}}_o^\alpha \bullet \rho_R^\alpha \boldsymbol{b}^\alpha \,\mathrm{d}\Omega - \int_{\Omega^\alpha} \tilde{\boldsymbol{\eta}}_o^\alpha \bullet J^\alpha \boldsymbol{I}^\alpha \,\mathrm{d}\Omega \Bigg] \\ &- \int_{\Gamma^c} \left(V^r \tilde{\boldsymbol{\eta}}_o^r + V^m \tilde{\boldsymbol{\eta}}_o^m \right) \bullet \boldsymbol{H}^c \,\mathrm{d}\Gamma - \int_{\Gamma^c} \boldsymbol{\lambda} \bullet \left[\!\left[\tilde{\boldsymbol{\eta}}_o^r - \tilde{\boldsymbol{\eta}}_o^m \right]\!\right] \mathrm{d}\Gamma = 0\end{aligned} \tag{4.28}$$

To obtain a primal formulation, we follow along the derivations presented in [45], and first solve the fine scale problem to obtain a closed form approximation of the incremental fine scale field. Consider a finite element discretization of the constituent domain, where the union of all disjoint elements represent the domain, $\bigcup_{e=1}^{n_{elem}} \Omega_e^\alpha = \Omega^\alpha$. Though the formulation allows the modeling of non-conforming meshes between the constituents, for the sake of clarity and ease of implementation of the mixture theory, we assume a conforming mesh between the matrix and the fiber, $\forall\ e,\ \Omega_e^r = \Omega_e^m$. Similarly, the boundary of the constituent domain can be written as,

$\bigcup_{s=1}^{n_{seg}} \Gamma_e^\alpha = \Gamma^\alpha$, where n_{seg} is the total number of boundary segments. The union of the elements attached to these boundary segments is denoted as, $\bigcup_{e=1}^{n_{seg}} \omega_e^\alpha = \omega^\alpha$. As a modeling step, the fine scales are assumed to exist close to the boundary and asymptote to zero beyond the elements attached to the boundary and in the direction of unit normal to the boundary. Thus, the nonlinear fine scale problem can be written as a series of local problems defined in the elements across the interface. The fine scales are modeled using edge bubble functions and can be written as,

$$\tilde{\boldsymbol{\varphi}}^\alpha = b_s^\alpha\left(\boldsymbol{X}\right)\boldsymbol{\beta}^\alpha \qquad \tilde{\boldsymbol{\eta}}_o^\alpha = b_s^\alpha\left(\boldsymbol{X}\right)\boldsymbol{\gamma}^\alpha \tag{4.29}$$

where $b_s^a\left(\boldsymbol{X}\right)$ is the edge bubble function that is non-zero on the boundary segment and vanish along the remaining boundaries of the element, $\boldsymbol{\beta}^\alpha$ is the unknown fine scale degree of freedom of the a^{th} constituent. Thus, the fine scale problem (4.28) can be rewritten as a local problem over the matching pair of boundary elements:

$$\begin{aligned}\tilde{R}_{\boldsymbol{\varphi}}\left(\bar{\boldsymbol{\varphi}}^\alpha,\tilde{\boldsymbol{\varphi}}^\alpha,\boldsymbol{\lambda};\tilde{\boldsymbol{\eta}}_o^\alpha\right) = \sum_{\alpha=r,m}\left[\int_{\omega_e^\alpha}\nabla_X\tilde{\boldsymbol{\eta}}_o^\alpha\bullet\boldsymbol{P}^\alpha\,\mathrm{d}\Omega-\int_{\omega_e^\alpha}\tilde{\boldsymbol{\eta}}_o^\alpha\bullet\rho_R^\alpha\boldsymbol{b}^\alpha\,\mathrm{d}\Omega-\int_{\omega_e^\alpha}\tilde{\boldsymbol{\eta}}_o^\alpha\bullet J^\alpha\boldsymbol{I}^\alpha\,\mathrm{d}\Omega\right]\\ -\int_{\Gamma_e^\alpha}\left(V^r\tilde{\boldsymbol{\eta}}_o^r+V^m\tilde{\boldsymbol{\eta}}_o^m\right)\bullet\boldsymbol{H}^c\,\mathrm{d}\Gamma-\int_{\Gamma_e^\alpha}\boldsymbol{\lambda}\bullet\left[\!\left[\tilde{\boldsymbol{\eta}}_o^r-\tilde{\boldsymbol{\eta}}_o^m\right]\!\right]\mathrm{d}\Gamma=0\end{aligned} \tag{4.30}$$

As equation (4.30) is a nonlinear problem, we first linearize this equation about the fine scale solution field,

$$\tilde{R}_{\boldsymbol{\varphi}}\left(\bar{\boldsymbol{\varphi}}^\alpha,\boldsymbol{0},\boldsymbol{\lambda};\tilde{\boldsymbol{\eta}}_o^\alpha\right)+\mathrm{D}\tilde{R}_{\boldsymbol{\varphi}}\left(\bar{\boldsymbol{\varphi}}^\alpha,\boldsymbol{0},\boldsymbol{\lambda};\tilde{\boldsymbol{\eta}}_o^\alpha\right)\bullet\Delta\tilde{\boldsymbol{u}}^\alpha=0 \tag{4.31}$$

$$\sum_{\alpha=r,m}\left[\int_{\omega_e^\alpha}\nabla_X\tilde{\boldsymbol{\eta}}_o^\alpha:\mathbf{A}^\alpha:\nabla_X\Delta\tilde{\boldsymbol{u}}^\alpha\,\mathrm{d}\Omega-\int_{\omega_e^\alpha}\tilde{\boldsymbol{\eta}}_o^\alpha\bullet\mathrm{D}\left[J^\alpha\boldsymbol{I}^\alpha\right]\bullet\Delta\tilde{\boldsymbol{u}}^\alpha\,\mathrm{d}\Omega\right]=-\tilde{R}_{\boldsymbol{\varphi}}\left(\bar{\boldsymbol{\varphi}}^\alpha,\boldsymbol{0},\boldsymbol{\lambda};\tilde{\boldsymbol{\eta}}_o^\alpha\right) \tag{4.32}$$

where $\mathrm{D}\tilde{\boldsymbol{u}}^a$ is the incremental fine scale displacement field, $\mathbf{A}^a$ is the acoustic tensor moduli and is given as,

$$\mathsf{A}_{iIaA}^a = S_{AI}^a\delta_{ia}+F_{iJ}^a\mathsf{C}_{IJKA}^aF_{aK}^a \tag{4.33}$$

where $\boldsymbol{S}^{\alpha}$ is the second Piola-Kirchhoff stress tensor and $\mathbf{C}^{\alpha}$ is the material moduli in reference configuration. The second term in (4.32) represents the stiffness contribution from the interactive force and is obtained by taking the variational derivative of (4.15) with respect to fine scale fields. The expressions for the variational derivative of the interactive force with respect to the fine scale fields are given in Appendix B.1.

Now, by substituting the incremental form of the fine scale fields (4.29) and integrating by parts the right hand side of (4.32), we obtain the linearized fine scale problem:

$$\begin{aligned}
&\boldsymbol{\gamma}^{r} \bullet \left[\int_{\omega_e^r} \boldsymbol{\chi}^{r}\left(b^{e}\right) : \mathbf{A}^{r} : \boldsymbol{\chi}^{r}_{aAu}\left(b^{e}\right) \mathrm{d}\Omega - \int_{\omega_e^r} b^{e} \mathbf{B}^{rm} \, \mathrm{d}\Omega \right] \Delta\beta_u^r \\
&+\boldsymbol{\gamma}^{m} \bullet \left[\int_{\omega_e^m} \boldsymbol{\chi}^{m}\left(b^{e}\right) \mathbf{A}^{m} \boldsymbol{\chi}^{m}\left(b^{e}\right) \mathrm{d}\Omega - \int_{\omega_e^m} b^{e} \mathbf{B}^{mr} \, \mathrm{d}\Omega \right] \Delta\beta_u^m \\
&= \boldsymbol{\gamma}^{r} \bullet \left[\int_{\omega_e^r} b^{e}\left(\mathrm{DIV}\boldsymbol{P}^{r} + \rho_R^{r}\boldsymbol{b}^{r} + J^{r}\boldsymbol{I}^{r}\right) \mathrm{d}\Omega + \int_{\Gamma_e^r} b^{e}\left(\boldsymbol{\lambda} - \boldsymbol{P}^{r}\boldsymbol{N}^{r} + V^{r}\boldsymbol{H}^{c}\right) \mathrm{d}\Gamma \right] \\
&+\boldsymbol{\gamma}^{m} \bullet \left[\int_{\omega_e^m} b^{e}\left(\mathrm{DIV}\boldsymbol{P}^{m} + \rho_R^{m}\boldsymbol{b}^{m} + J^{m}\boldsymbol{I}^{m}\right) \mathrm{d}\Omega + \int_{\Gamma_e^m} b^{e}\left(-\boldsymbol{\lambda} - \boldsymbol{P}^{m}\boldsymbol{N}^{m} + V^{m}\boldsymbol{H}^{c}\right) \mathrm{d}\Gamma \right] = 0
\end{aligned} \tag{4.34}$$

where $\boldsymbol{\chi}^{\alpha}\left(b^{e}\right)$ is the third order tensor of the bubble function. $\mathbf{B}^{rm}, \mathbf{B}^{mr}$ are second order stiffness tensors obtained by substituting the fine scale fields given in (4.29) in the variational derivative of the interactive force expressions provided in Appendix B.1. By employing the arbitrariness of the fine scale weighting function field, the incremental fine scale displacement field for both the constituents can be written as,

$$\begin{aligned}
\Delta\beta_u^r &= \overline{\tau}_s^r \bullet \left[\int_{\omega_e^r} b^{e}\left(\mathrm{DIV}\boldsymbol{P}^{r} + \rho_R^{r}\boldsymbol{b}^{r} + J^{r}\boldsymbol{I}^{r}\right) \mathrm{d}\Omega + \int_{\Gamma_e^r} b^{e}\left(\boldsymbol{\lambda} - \boldsymbol{P}^{r}\boldsymbol{N}^{r} + V^{r}\boldsymbol{H}^{c}\right) \mathrm{d}\Gamma \right] \\
\Delta\beta_u^m &= \overline{\tau}_s^m \bullet \left[\int_{\omega_e^m} b^{e}\left(\mathrm{DIV}\boldsymbol{P}^{m} + \rho_R^{m}\boldsymbol{b}^{m} + J^{m}\boldsymbol{I}^{m}\right) \mathrm{d}\Omega + \int_{\Gamma_e^m} b^{e}\left(-\boldsymbol{\lambda} - \boldsymbol{P}^{m}\boldsymbol{N}^{m} + V^{m}\boldsymbol{H}^{c}\right) \mathrm{d}\Gamma \right]
\end{aligned} \tag{4.35}$$

where the stabilization tensor for each constituent is given as,

$$\overline{\tau}_s^r = \left[\int_{\omega_e^r} \boldsymbol{\chi}^r \left(b^e \right) : \mathbf{A}^r : \boldsymbol{\chi}^r \left(b^e \right) \mathrm{d}\Omega - \int_{\omega_e^r} b^e \mathbf{B}^{rm} \, \mathrm{d}\Omega \right]^{-1}$$
$$\overline{\tau}_s^m = \left[\int_{\omega_e^m} \boldsymbol{\chi}^m \left(b^e \right) : \mathbf{A}^m : \boldsymbol{\chi}^m \left(b^e \right) \mathrm{d}\Omega - \int_{\omega_e^m} b^e \mathbf{B}^{mr} \, \mathrm{d}\Omega \right]^{-1} \tag{4.36}$$

In order to simplify calculations, we introduce certain assumptions along the lines of [45]. We ignore the bulk contribution in (4.35) for both the constituents, assuming that the bubble functions are orthogonal to coarse-scale residual. Though this assumption is not strictly enforced by modeling the bubble functions using polynomials, it has been shown in [42] and [45] that we obtain a stable algorithm for wide variety of problems both in small and finite deformation context. Thus, the incremental fine scale displacement fields reduces to,

$$\Delta\beta_u^r = \overline{\tau}_s^r \bullet \int_{\Gamma_e^r} b^e \left(\boldsymbol{\lambda} - \boldsymbol{P}^r \boldsymbol{N}^r + V^r \boldsymbol{H}^c \right) \mathrm{d}\Gamma$$
$$\Delta\beta_u^m = \overline{\tau}_s^m \bullet \int_{\Gamma_e^m} b^e \left(-\boldsymbol{\lambda} - \boldsymbol{P}^m \boldsymbol{N}^m + V^m \boldsymbol{H}^c \right) \mathrm{d}\Gamma \tag{4.37}$$

Further, by employing the mean value theorem, we extract the traction residual out of the integral over boundary and the incremental fine scale displacement fields are written as,

$$\Delta\tilde{\boldsymbol{u}}^r = \tau^r \bullet \left(\boldsymbol{\lambda} - \boldsymbol{P}^r \boldsymbol{N}^r + V^r \boldsymbol{H}^c \right)$$
$$\Delta\tilde{\boldsymbol{u}}^m = \tau^m \bullet \left(-\boldsymbol{\lambda} - \boldsymbol{P}^m \boldsymbol{N}^m + V^m \boldsymbol{H}^c \right) \tag{4.38}$$

The stabilization tensor of each constituent in the above equation is given as,

$$\boldsymbol{\tau}^r = \left[meas\left(\Gamma_e^r \right) \right]^{-1} \left(\int_{\Gamma_e^r} b_s \, \mathrm{d}\Gamma \right)^2 \overline{\tau}^r$$
$$\boldsymbol{\tau}^m = \left[meas\left(\Gamma_e^m \right) \right]^{-1} \left(\int_{\Gamma_e^m} b_s \, \mathrm{d}\Gamma \right)^2 \overline{\tau}^m \tag{4.39}$$

where the average value of the bubble function over the interface is employed.

4.4.2 Variational embedding in coarse scale problem

To obtain a primal stabilized formulation for two solid-constituents mixture theory, we first embed the incremental fine scales into the continuity equation (4.27) with the objective to obtain a closed form expression for the Lagrange multiplier in terms of the coarse scale displacement fields. Accordingly, we first consider the displacement continuity equation,

$$\mathcal{W}_{\lambda} = -\int_{\Gamma^c} \boldsymbol{\mu} \bullet \left[\!\left[\boldsymbol{\varphi}^r - \boldsymbol{\varphi}^m \right]\!\right] \mathrm{d}\Gamma = 0 \tag{4.40}$$

We linearize (4.40) with respect to the fine scale fields and by substituting the incremental fine scales for each constituent as given in equation (4.38), we obtain the linearized continuity problem

$$-\int_{\Gamma^c} \boldsymbol{\mu} \bullet \left[\!\left[\boldsymbol{\varphi}^r - \boldsymbol{\varphi}^m + \tau^r \bullet \left(\boldsymbol{\lambda} - \boldsymbol{P}^r \boldsymbol{N}^r + V^r \boldsymbol{H}^c \right) - \left(-\boldsymbol{\lambda} - \boldsymbol{P}^m \boldsymbol{N}^m + V^m \boldsymbol{H}^c \right) \right]\!\right] \mathrm{d}\Gamma = 0 \tag{4.41}$$

The second and the third terms in (4.41) are the Lagrange multiplier enforcement of the bouondary constraints that are written in terms of normal tractions while accounting for any externally applied forces. Equation (4.42) holds for all μ .

Because of the edge based stabilization facilitated by the fine scale equations we can employ arbitrary combination of interpolation functions for the displacement and Lagrange multiplier fields. Assuming that the Lagrange multipliers belong to the space of discontinuous L_2 functions, we can localize (4.41) to sum of element interiors, and following along the lines of Truster and Masud [45] allows us to obtain a close form expression for the Lagrange multiplier field $\boldsymbol{\lambda}$ on each segment along the Neumann boundary. Accordingly, a pointwise expression for the Lagrange multiplier field at the boundary can be obtained,

$$\boldsymbol{\lambda} = \boldsymbol{\delta}_s^r \bullet \left(\boldsymbol{P}^r \boldsymbol{N}^r - V^r \boldsymbol{H}^c \right) - \boldsymbol{\delta}_s^m \bullet \left(\boldsymbol{P}^m \boldsymbol{N}^m - V^m \boldsymbol{H}^c \right) - \tau_s \bullet \left[\!\left[\boldsymbol{\varphi}^r - \boldsymbol{\varphi}^m \right]\!\right] \tag{4.42}$$

where the flux weighting tensors $\boldsymbol{\delta}_s^{\alpha}$ and the stabilization tensors $\boldsymbol{\tau}_s$ are given as,

$$\boldsymbol{\delta}_s^{\alpha} = \tau_s \bullet \tau_s^{\alpha} \qquad\qquad \tau_s = \left(\tau_s^r + \tau_s^m \right)^{-1} \tag{4.43}$$

By substituting (4.42) into the incremental fine scale displacement fields (4.38), the fine scale fields are written as a function of coarse scale displacement fields:

$$\begin{aligned}\Delta\tilde{\boldsymbol{u}}^r &= -\boldsymbol{\delta}_s \bullet \left(\boldsymbol{P}^r\boldsymbol{N}^r + \boldsymbol{P}^m\boldsymbol{N}^m - \boldsymbol{H}^c\right) - \left(\boldsymbol{\delta}_s^r\right)^T \bullet \left[\!\left[\boldsymbol{\varphi}^r - \boldsymbol{\varphi}^m\right]\!\right] \\ \Delta\tilde{\boldsymbol{u}}^m &= -\boldsymbol{\delta}_s \bullet \left(\boldsymbol{P}^r\boldsymbol{N}^r + \boldsymbol{P}^m\boldsymbol{N}^m - \boldsymbol{H}^c\right) + \left(\boldsymbol{\delta}_s^m\right)^T \bullet \left[\!\left[\boldsymbol{\varphi}^r - \boldsymbol{\varphi}^m\right]\!\right]\end{aligned} \tag{4.44}$$

wherein we have employed the symmetry of the tensors $\boldsymbol{\tau}_s^\alpha$ to enable the substitution $\left(\boldsymbol{\delta}_s^\alpha\right)^T = \boldsymbol{\tau}_s^\alpha \bullet \boldsymbol{\tau}_s$. The additional stability tensor $\boldsymbol{\delta}_s^\alpha$ that arises during the stabilization is defined as follows.

$$\boldsymbol{\delta}_s = \boldsymbol{\tau}_s^r \bullet \boldsymbol{\delta}_s^m = \boldsymbol{\tau}_s^m \bullet \boldsymbol{\delta}_s^r \tag{4.45}$$

Remark: It is important to note that in general $\left(\boldsymbol{\delta}_s^\alpha\right)^T \neq \boldsymbol{\delta}_s^\alpha$.

Now we return to the coarse scale problem to obtain the final multiscale weak form by embedding the expressions obtained for the incremental fine scale fields and Lagrange multiplier field. We first linearize the coarse scale problem in equation (4.27) with respect to the fine scale fields.

$$\bar{R}_{\boldsymbol{\varphi}}\left(\bar{\boldsymbol{\varphi}}^\alpha, \boldsymbol{0}, \boldsymbol{\lambda}; \tilde{\boldsymbol{\eta}}_o^\alpha\right) + \mathrm{D}\bar{R}_{\boldsymbol{\varphi}}\left(\bar{\boldsymbol{\varphi}}^\alpha, \boldsymbol{0}, \boldsymbol{\lambda}; \tilde{\boldsymbol{\eta}}_o^\alpha\right) \bullet \Delta\tilde{\boldsymbol{u}}^\alpha = 0 \tag{4.46}$$

where

$$\begin{aligned}\mathrm{D}\bar{R}_{\boldsymbol{\varphi}}\left(\bar{\boldsymbol{\varphi}}^\alpha, \boldsymbol{0}, \boldsymbol{\lambda}; \tilde{\boldsymbol{\eta}}_o^\alpha\right) \bullet \Delta\tilde{\boldsymbol{u}}^\alpha &= -\int_{\Omega^\alpha} \mathrm{DIV}\left[\nabla_X \bar{\boldsymbol{\eta}}_o^\alpha : \mathbf{A}^\alpha\right] \bullet \Delta\tilde{\boldsymbol{u}}^\alpha \,\mathrm{d}\Omega \\ &\quad + \int_{\Gamma^\alpha} \left[\left(\nabla_X \bar{\boldsymbol{\eta}}_o^\alpha : \mathbf{A}^\alpha\right) \bullet \boldsymbol{N}^\alpha\right] \bullet \Delta\tilde{\boldsymbol{u}}^\alpha \,\mathrm{d}\Omega - \int_{\Omega^\alpha} \bar{\boldsymbol{\eta}}_o^\alpha \bullet \mathrm{D}\left[J^\alpha \boldsymbol{I}^\alpha\right] \bullet \Delta\tilde{\boldsymbol{u}}^\alpha \,\mathrm{d}\Omega\end{aligned} \tag{4.47}$$

Following along the assumptions presented above for the fine-scale problem, we neglect the bulk term and the interactive force contribution for computational expediency in equation (4.46) to obtain the final stabilized form.

$$\begin{aligned}&\sum_{\alpha=r,m}\left[\int_{\Omega^\alpha} \nabla_X \bar{\boldsymbol{\eta}}_o^\alpha \bullet \boldsymbol{P}^\alpha \,\mathrm{d}\Omega - \int_{\Omega^\alpha} \bar{\boldsymbol{\eta}}_o^\alpha \bullet \rho_R^\alpha \boldsymbol{b}^\alpha \,\mathrm{d}\Omega - \int_{\Omega^\alpha} \bar{\boldsymbol{\eta}}_o^\alpha \bullet J^\alpha \boldsymbol{I}^\alpha \,\mathrm{d}\Omega\right] - \int_{\Gamma^\alpha} \left(V^r \bar{\boldsymbol{\eta}}_o^r + V^m \bar{\boldsymbol{\eta}}_o^m\right) \bullet \boldsymbol{H}^c \,\mathrm{d}\Gamma \\ &- \int_{\Gamma^\alpha} \boldsymbol{\lambda} \bullet \left[\!\left[\bar{\boldsymbol{\eta}}_o^r - \bar{\boldsymbol{\eta}}_o^m\right]\!\right] \mathrm{d}\Gamma + \int_{\Gamma^\alpha} \left[\left(\nabla_X \bar{\boldsymbol{\eta}}_o^\alpha : \mathbf{A}^\alpha\right) \bullet \boldsymbol{N}^\alpha\right] \bullet \Delta\tilde{\boldsymbol{u}}^\alpha \,\mathrm{d}\Omega = 0\end{aligned} \tag{4.48}$$

By embedding the expressions for Lagrange multiplier field from equation (4.42) and incremental fine scale displacement field from equation (4.44) into the above equation (4.47), we obtain the final multiscale weak form in the primal variables for self-consistent imposing of the tractions at the Neumann boundaries.

$$
\begin{aligned}
&\sum_{\alpha=r,m}\left[\int_{\Omega^\alpha}\nabla_X\bar{\boldsymbol{\eta}}_o^\alpha\bullet\boldsymbol{P}^\alpha\,\mathrm{d}\Omega-\int_{\Omega^\alpha}\bar{\boldsymbol{\eta}}_o^\alpha\bullet\rho_R^\alpha\boldsymbol{b}^\alpha\,\mathrm{d}\Omega-\int_{\Omega^\alpha}\bar{\boldsymbol{\eta}}_o^\alpha\bullet J^\alpha\boldsymbol{I}^\alpha\,\mathrm{d}\Omega\right]-\int_{\Gamma^\alpha}\left(V^r\bar{\boldsymbol{\eta}}_o^r+V^m\bar{\boldsymbol{\eta}}_o^m\right)\bullet\boldsymbol{H}^c\,\mathrm{d}\Gamma\\
&-\int_{\Gamma^\alpha}\left[\!\left[\bar{\boldsymbol{\eta}}_o^r-\bar{\boldsymbol{\eta}}_o^m\right]\!\right]\bullet\left[\boldsymbol{\delta}_s^r\bullet\left(\boldsymbol{P}^r\boldsymbol{N}^r-V^r\boldsymbol{H}^c\right)-\boldsymbol{\delta}_s^m\bullet\left(\boldsymbol{P}^m\boldsymbol{N}^m-V^m\boldsymbol{H}^c\right)\right]\mathrm{d}\Gamma\\
&+\int_{\Gamma^\alpha}\left[\!\left[\bar{\boldsymbol{\eta}}_o^r-\bar{\boldsymbol{\eta}}_o^m\right]\!\right]\bullet\tau_s\bullet\left[\!\left[\boldsymbol{\varphi}^r-\boldsymbol{\varphi}^m\right]\!\right]\mathrm{d}\Gamma\\
&-\int_{\Gamma^\alpha}\left[\left(\nabla_X\bar{\boldsymbol{\eta}}_o^r:\mathbf{A}^r\right)\bullet\boldsymbol{N}^r\right]\bullet\left(\boldsymbol{\delta}_s^r\right)^T\left[\!\left[\boldsymbol{\varphi}^r-\boldsymbol{\varphi}^m\right]\!\right]\mathrm{d}\Omega\\
&+\int_{\Gamma^\alpha}\left[\left(\nabla_X\bar{\boldsymbol{\eta}}_o^m:\mathbf{A}^m\right)\bullet\boldsymbol{N}^m\right]\bullet\left(\boldsymbol{\delta}_s^m\right)^T\left[\!\left[\boldsymbol{\varphi}^r-\boldsymbol{\varphi}^m\right]\!\right]\mathrm{d}\Omega\\
&-\int_{\Gamma^\alpha}\left[\left(\nabla_X\bar{\boldsymbol{\eta}}_o^r:\mathbf{A}^r\right)\bullet\boldsymbol{N}^r\right]\bullet\boldsymbol{\delta}_s\left[\boldsymbol{P}^r\boldsymbol{N}^r+\boldsymbol{P}^m\boldsymbol{N}^m-V^r\boldsymbol{H}^c\right]\mathrm{d}\Omega\\
&-\int_{\Gamma^\alpha}\left[\left(\nabla_X\bar{\boldsymbol{\eta}}_o^m:\mathbf{A}^m\right)\bullet\boldsymbol{N}^m\right]\bullet\boldsymbol{\delta}_s\left[\boldsymbol{P}^r\boldsymbol{N}^r+\boldsymbol{P}^m\boldsymbol{N}^m-V^r\boldsymbol{H}^c\right]\mathrm{d}\Omega=0
\end{aligned}
\tag{4.49}
$$

The last two terms are the contributions from the stress jump. By employing the standard notations in the DG method literature and by neglecting the last two terms in (4.48) to improve computational efficiency, we simplify the final multiscale form:

$$
\begin{aligned}
&\sum_{\alpha=r,m}\left[\int_{\Omega^\alpha}\nabla_X\bar{\boldsymbol{\eta}}_o^\alpha\square\boldsymbol{P}^\alpha\,\mathrm{d}\Omega-\int_{\Omega^\alpha}\bar{\boldsymbol{\eta}}_o^\alpha\square\rho_R^\alpha\boldsymbol{b}^\alpha\,\mathrm{d}\Omega-\int_{\Omega^\alpha}\bar{\boldsymbol{\eta}}_o^\alpha\square J^\alpha\boldsymbol{I}^\alpha\,\mathrm{d}\Omega\right]-\int_{\Gamma^\alpha}\left(V^r\bar{\boldsymbol{\eta}}_o^r+V^m\bar{\boldsymbol{\eta}}_o^m\right)\square\boldsymbol{H}^c\,\mathrm{d}\Gamma\\
&-\int_{\Gamma^\alpha}\left[\!\left[\bar{\boldsymbol{\eta}}_o^r-\bar{\boldsymbol{\eta}}_o^m\right]\!\right]\square\left\{\boldsymbol{P}\ \ \boldsymbol{N}\right\}\mathrm{d}\Gamma-\int_{\Gamma^\alpha}\left\{\left(\nabla_X\bar{\boldsymbol{\eta}}_o:\mathbf{A}\right)\square\boldsymbol{N}\right\}\square\left[\!\left[\boldsymbol{\varphi}^r-\boldsymbol{\varphi}^m\right]\!\right]\mathrm{d}\Omega\\
&+\int_{\Gamma^\alpha}\left[\!\left[\bar{\boldsymbol{\eta}}_o^r-\bar{\boldsymbol{\eta}}_o^m\right]\!\right]\square\tau_s\square\left[\!\left[\boldsymbol{\varphi}^r-\boldsymbol{\varphi}^m\right]\!\right]\mathrm{d}\Gamma=0
\end{aligned}
\tag{4.50}
$$

where the average flux operators are given as,

$$\begin{aligned}\left\{\boldsymbol{P}\bullet\boldsymbol{N}\right\} &= \boldsymbol{\delta}_s^r\bullet\left(\boldsymbol{P}^r\boldsymbol{N}^r - V^r\boldsymbol{H}^c\right) - \boldsymbol{\delta}_s^m\bullet\left(\boldsymbol{P}^m\boldsymbol{N}^m - V^m\boldsymbol{H}^c\right)\\ \left\{\left(\nabla_X\bar{\boldsymbol{\eta}}_o : \mathbf{A}\right)\bullet\boldsymbol{N}\right\} &= \left[\left(\nabla_X\bar{\boldsymbol{\eta}}_o^r : \mathbf{A}^r\right)\bullet\boldsymbol{N}^r\right]\bullet\left(\boldsymbol{\delta}_s^r\right)^T - \left[\left(\nabla_X\bar{\boldsymbol{\eta}}_o^m : \mathbf{A}^m\right)\bullet\boldsymbol{N}^m\right]\bullet\left(\boldsymbol{\delta}_s^m\right)^T\end{aligned} \tag{4.51}$$

The set of first three bracketed terms are the weak form of momentum balance for the mixture model wherein the third term is contribution to momentum balance from the interactive force field. The fourth term is self-consistent weak form for boundary tractions. Fifth and sixth terms are the stabilization terms that arise due to the variational gap in the weighting function fields of matrix and fiber to enforce the displacement continuity and traction continuity. Similarly, the last integral is the stabilization term that accounts for the variation in material moduli of matrix and fiber to enforce the displacement continuity.

Remark: This derivation follows the general framework developed in [45] wherein starting from an underlying Lagrange multiplier method for weakly imposing the continuity constraints, and employing the fine scale problem facilitated by the variational multiscale split of the boundary problem, we derive closed form expression for the Lagrange multiplier field. Substituting it in the corresponding coarse-scale problem results in a method that is free of explicit representation of the Lagrange multiplier field.

4.5 Numerical Results

This section presents numerical results obtained for several three-dimensional problems by employing the proposed VMS based formulation for mixture theory for the modeling of composites. Our objective is to be able to account for more features at the micromechanics level than are facilitated by the homogenization theories that smear away any local effects in the interest of producing computationally economic models. The present theory brings in the interactive force field that arises due to relative deformation or evolution of the constituents that were related in their corresponding reference configurations. This micromechanics feature is modeled via the interactive force field which serves as a measure of the local interactions between constituents, and can serve as an indicator for the onset of damage in the material.

Section 4.5.1 presents axial stretching of 4-ply symmetric laminate and the results are compared with Pipes and Pagano [49] and Reddy [50]. In Section 4.5.2, we consider a graphite-epoxy lamina plate with a hole which is subjected to a given axial pressure field. In this problem, the

ratio of the hoop stress along the circumference of the hole to the applied pressure at the composite boundary is compared with the analytical solution provided by Lekhnitskii [51]. In Section 4.5.3, we present the solution for the bending of a 4-ply laminate subjected to transverse pressure load and the results are compared with the First Order Shear Deformation (FSDT) theory [52]. We conclude the section with pure bending of the rectangular composite block to highlight the finite deformation capability of the method. As all the numerical problems presented are solved in the context of mixture theory, each lamina consists of overlapping and coexisting matrix and fiber domains. The matrix material is modeled as a homogenous isotropic material and the fiber as a transversely isotropic material. The corresponding constitutive model is given in (4.17)**.**

The matrix and the fiber domain are discretized using structured linear hexahedral meshes that are comprised of 27-noded Lagrange elements. The volume and surface integrals are evaluated with sufficiently high Gauss quadrature rule to integrate all the terms. The significant features of mixture theory are the constituent stresses and the interactive force field that are highlighted throughout.

4.5.1 Four Ply Laminate, $[+45/-45]_s$

Consider the Graphite-Epoxy laminate of dimensions $60\times20\times2.5$ mm with $[+45/-45]_s$ as shown in Figure 4.3. The laminate consists of four plys, where each ply is of 0.625 mm thickness. The top and the bottom ply have a fiber orientation of $+45^0$ and the middle plys have an orientation of -45^0 with respect to the longitudinal axis. As the laminate is modeled using mixture theory, every node has six degrees of freedom, namely the 3-displacements for the matrix and the fiber each. The material properties of the matrix and fiber are given in Table 4.1. The boundary of the laminate, i.e., the matrix and the fiber boundary are tied with the interface formulation as explained in Section 4.4. This ensures the consistent tying of the boundaries.

The laminate is subjected to an axial displacement of 0.3 mm at $x=\pm30$ mm plane. The nodes at $x=0$ plane are appropriately constrained to avoid any rigid body motion. This axial stretching problem is solved with four different meshes and the results are compared with Pipes and Pagano [49] and Reddy [50]. Figure 4.4 shows the axial displacement, composite axial stress, in-plane shear stress and out of plane shear stress at top surface along the width of the

laminate at $x = 0$ plane obtained from mixture theory. It can be seen that the results obtained from mixture theory converge with mesh refinement along the width and the thickness of the laminate and follow the trends of Pipes and Pagano [49]. The in-plane shear stress along the width of the laminate at the interlaminar interface between +45 and -45 at $x = 0$ plane is shown in Figure 4.5. Theoretically, a stress singularity is predicted at $y = \pm 10$ mm in the interlaminar interface plane and the present mixture model produces a good comparison for in-plane shear stress with Reddy [50].

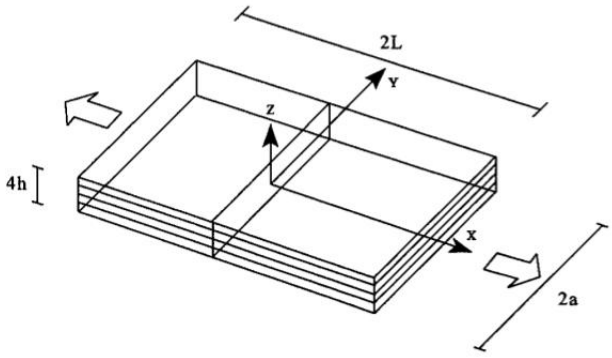

Figure 4.3. 4-ply laminate

Table 4.1. Material properties of the laminate

	λ (MPa)	α (MPa)	β (MPa)	μ_L (MPa)	μ_T (MPa)	ρ (kg/mm^3)	Volume Fraction
Fiber	4.424E+03	1.203E+03	2.467E+05	1.039E+04	1.039E+04	1550E-09	0.5
Matrix	1.990E+03	-	-	1.327E+03	-	1200E-09	0.5

Figure 4.6 shows the axial stress and in-plane shear stress of the composite. As predicted by the classical laminate theory, we observe a uniform state of stress in the middle region of the laminate, while there is distortion in the stress fields close to the boundary due to finite width effects of the laminate. One of the advantages of mixture theory is that kinetic and kinematic response of each constituent is readily available for analysis and for failure prediction in the constituents without resorting to the discrete modeling of the microstructure. Figure 4.7-Figure

4.9shows the axial stress and in-plane shear stress of the fiber and matrix respectively. From Figure 4.7b, it can be observed that the fiber in-plane shear stress in the top and bottom plys is tensile, while it is compressive in the middle plys. This is an artifact of the angle ply laminate configuration. From Figure 4.8, it can be seen that the matrix stress exhibits the effect of the fiber orientation at the boundaries, though matrix is modeled as homogeneous isotropic material. This effect arises due to the tying of the constituent boundaries, where the surface tractions at the boundaries are distributed between the constituents in a consistent fashion.

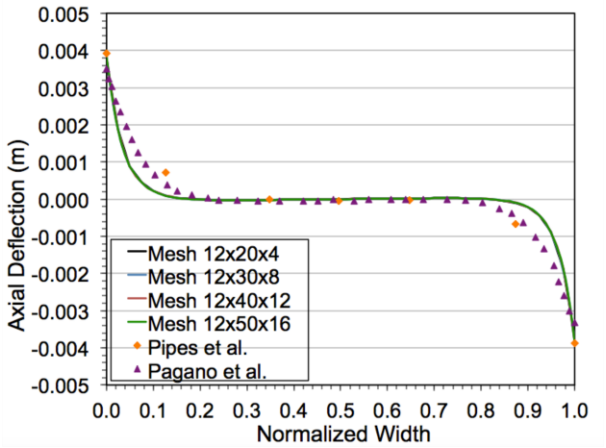

(a) Axial deflection

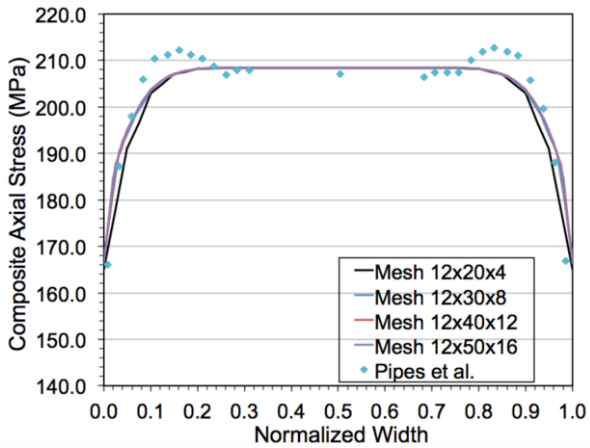

(b) Composite axial stress

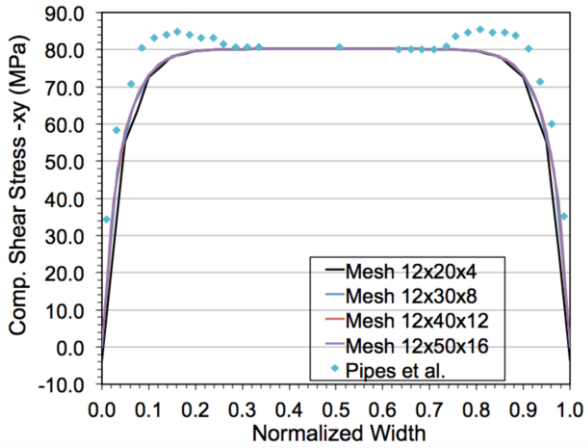

(c) Composite in-plane shear stress

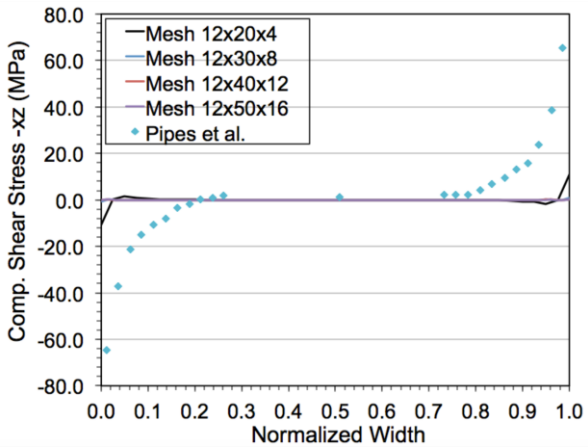

(d) Composite out-of-plane shear stress

Figure 4.4. Comparison with Pipes and Pagano results

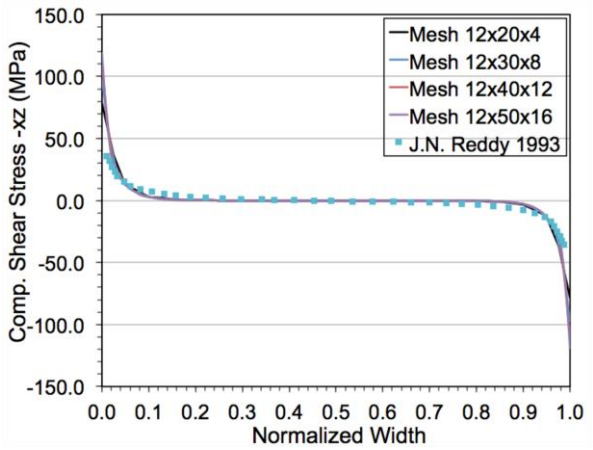

Figure 4.5. Composite shear stress-*xz* along the interlaminar interface (between +45 and -45 lamina)

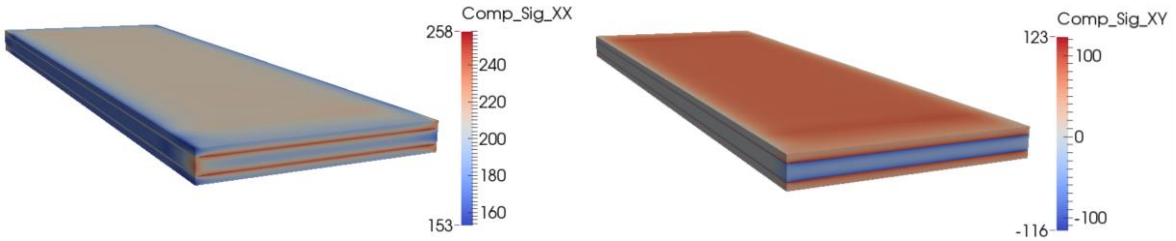

(a) Axial stress (b) In-plane shear stress

Figure 4.6. Composite stress in the domain

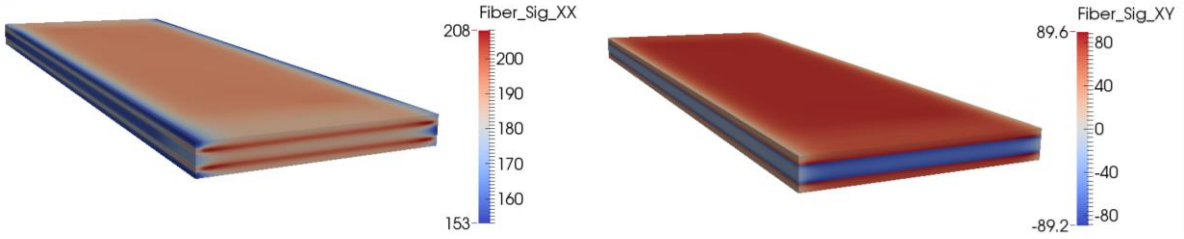

(a) Axial stress (b) In-plane shear stress

Figure 4.7. Fiber stress in the domain

The significant feature of the mixture theory is that apart from obtaining the constituent stress fields, it provides a distribution of the interaction between fiber and matrix, which is a measure of the fiber-matrix interface strength. This interaction produces a volumetric force field that models the interaction between the matrix and the fiber as they deform over each other. While traditional laminate theories for composites can model the overall deformation modes of

the laminate, they do not have the microstructural information to be able to identify the regions in the domain where the fiber-matrix interface is under higher stress.

Remark: *As mixture theory provides matrix, fiber and composite stress fields in addition to interactive force field, a comprehensive failure theory can be developed for modeling failure in matrix and fiber, and at the fiber-matrix interface.*

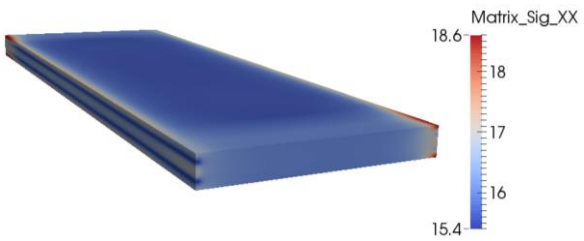

(a) Axial stress

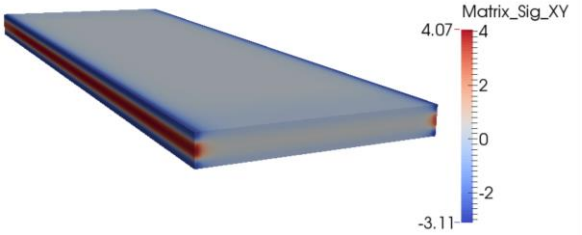

(b) In-plane shear stress

Figure 4.8. Matrix stress in the domain

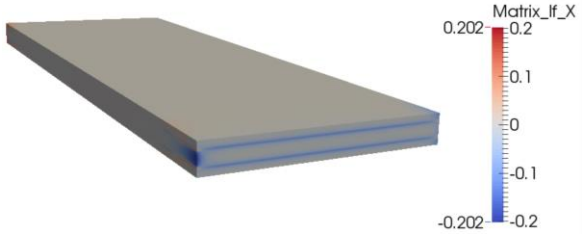

(a) Interactive force in X direction

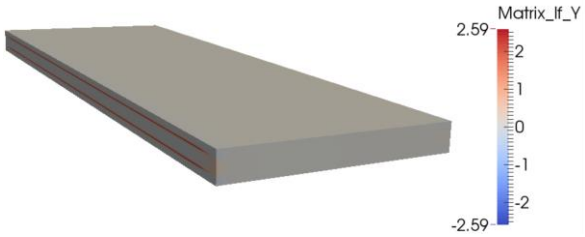

(b) Interactive force in Y direction

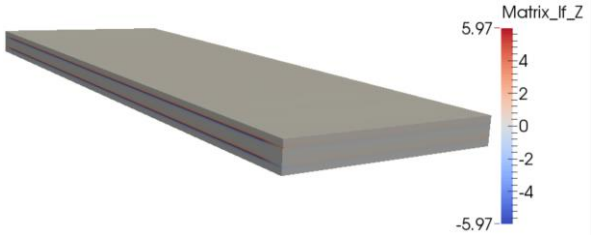

(c) Interactive force in Z direction

Figure 4.9. Matrix interactive force in the domain

Figure 4.9 shows the matrix interactive force field in *X*, *Y* and *Z* direction. Figure 4.9c shows that the interactive force acting on the matrix in the top ply ($+45^o$) and middle ply (-45^o) along the interlaminar surface are in tension and compression, respectively. Similar force distribution is observed in the bottom layer and middle layer along the interlaminar surface.

From Figure 4.9, it can be observed that the matrix interactive force achieves its maximum and minimum along the interlaminar interface close to the boundary. The interactive force in z direction has a maximum value of 5.97 N/mm^3 along y= $\pm$ 10 mm plane at the interlaminar interface for the top ply and achieves a minimum value of -5.97 N/mm^3 at the interlaminar interface for the middle ply. This suggests that the interlaminar peeling is one of the failure mode for symmetric angle ply laminate when subjected to axial loading.

Remark: *Fiber-matrix interaction is a function of the loading, the boundary conditions, the material orientation, as well as the mode of deformation. Therefore, sections with higher interactive force indicate the regions where fiber-matrix debonding can get initiated, thereby providing crucial insight into the potential onset of damage in the material system.*

Remark: *From* (4.6)*, it can be deduced that the fiber interactive force in equal and opposite to the matrix interactive force. Thus, for conciseness, fiber interactive force plots are not shown here.*

4.5.2 Single Ply Lamina with Hole

Next, we consider the axial stretching of single ply lamina with hole at the center. This is a representative simulation of a composite with crack or hole that results in stress concentration leading to failure of the structure. A rectangular prismatic domain of dimensions $60\times 20\times 2.5$ mm is considered with a circular hole of radius of 1.0 mm. The composite is comprised of epoxy matrix and graphite fibers with material properties are provided in Table 4.2. The lamina is subjected to an axial pressure of 200 MPa at $x=\pm 30$ mm plane in the axial direction. The domain is discretized using 27-noded Lagrange elements and the nodes are appropriately constrained at $x=0$ plane to avoid rigid body motion.

The stress concentration, which is defined as the ratio of the hoop stress and the applied pressure, is plotted along the circumference of the hole. A closed form solution for the stress concentration around the hole for an infinite width laminate is derived in Leknitskii [51] for a given axial load and for an arbitrary fiber orientation. Figure 4.10 shows that the stress concentration obtained from the mixture theory compares well with analytical solution for both 0^0 and 45^0 fiber orientation that is considered in the simulations presented here. It can also be

observed that with mesh refinement, the finite element solution variationally converges monotonically to the exact solution which is a numerical validation of the variational consistency of the method. For the fiber orientation of 0^0, the stress concentration reaches a maximum value of 6.8 at 90^0 along the circumference of the hole, while a fiber orientation of 45^0 reduces the stress concentration in the lamina to 4.4. The location of the maximum stress concentration also shifts from 90^0 to 123^0.

Table 4.2. Material properties of the lamina

	λ (MPa)	α (MPa)	β (MPa)	μ_L (MPa)	μ_T (MPa)	ρ (kg/mm^3)	Volume Fraction
Fiber	1.314E+03	-3.86E+03	2.252E+05	9.674E+03	3.531E+03	1550E-09	0.7
Matrix	1.990E+03	-	-	1.327E+03	-	1200E-09	0.3

Figure 4.11 and Figure 4.12 show the composite axial stress and in-plane shear stress for the 45^0 lamina, respectively. From these plots, it can be seen that the stress profile is fairly uniform away from the hole and therefore there is no substantial effect of the finite width of the geometry on the stress variations around the hole. This justifies the comparison of the stress concentration with analytical solution derived for the infinite width lamina. Figure 4.13 and Figure 4.14 present the interactive force profile in *X* and *Y* direction for 45^0 lamina respectively. Interactive force in *X* and *Y* direction reaches a maximum value of 10.1 N/mm^3 and 10.2 N/mm^3, respectively. From Figure 4.11-Figure 4.14, it can be deduced that the constituent stresses and matrix fiber interactions achieve their maximum and minimum values around the hole and thus the failure in the load carrying capacity of the lamina will initiate in the region around the hole.

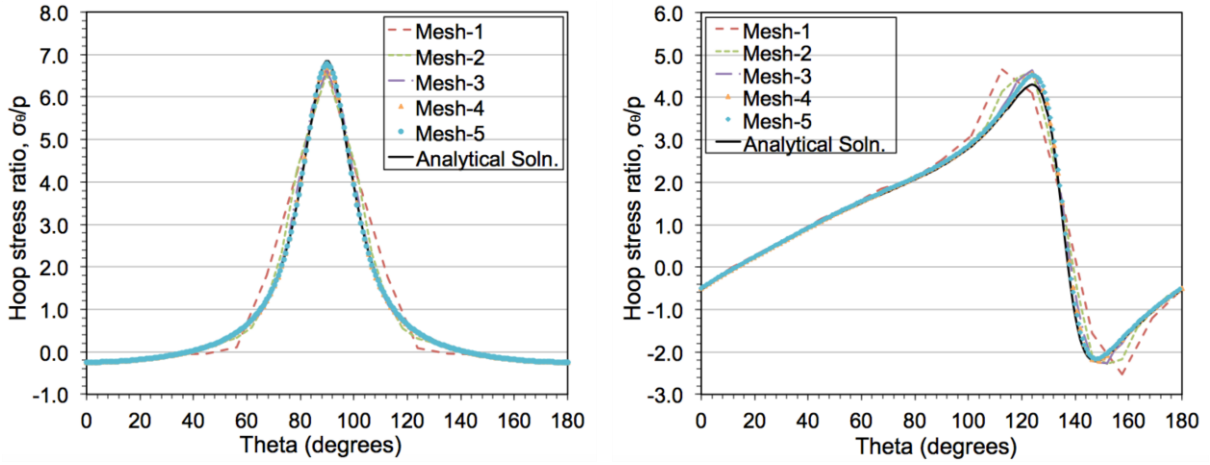

(a) 0^0 fiber orientation (b) 45^0 fiber orientation

Figure 4.10. Hoop stress along the circumference of the hole

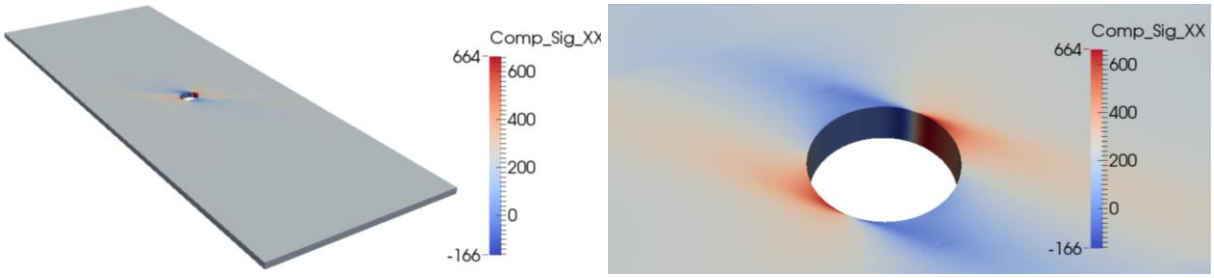

(a) 45^0 fiber orientation (b) Zoomed view

Figure 4.11. Composite axial stress

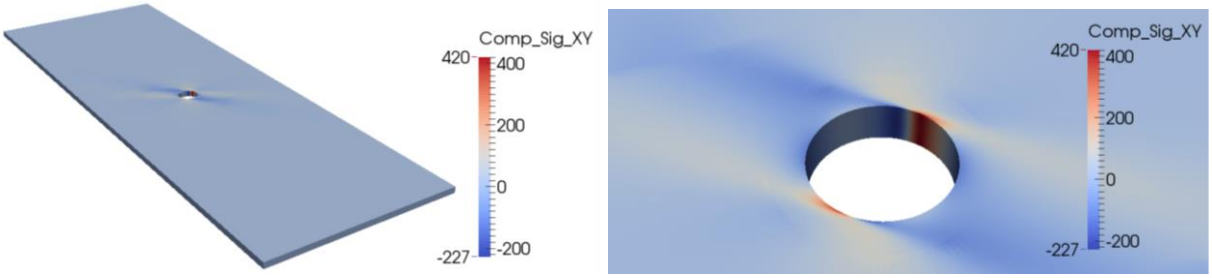

(a) 45^0 fiber orientation (b) Zoomed view

Figure 4.12. Composite in-plane shear stress

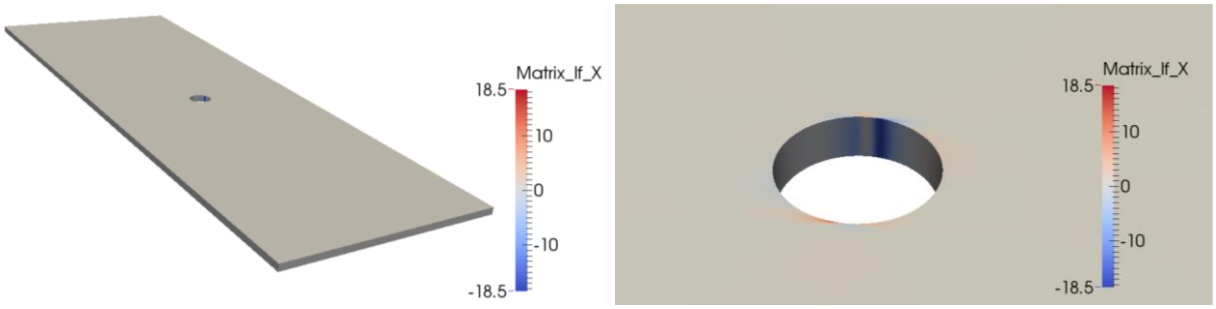

(a) 45^0 fiber orientation (b) Zoomed view

Figure 4.13. Interactive force in X direction

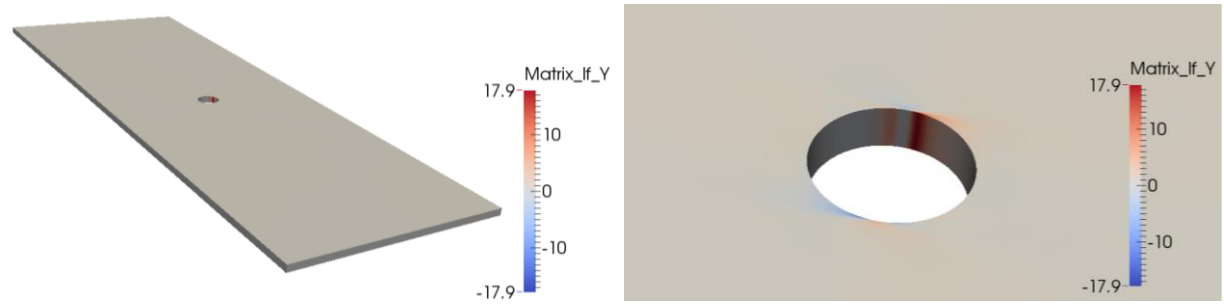

(a) 45^0 fiber orientation (b) Zoomed view

Figure 4.14. Interactive force in Y direction

4.5.3 Laminated Plate Bending Problem

This problem presents bending of four-ply Graphite-Epoxy laminate under uniformly distributed load. We consider a square laminate of dimension, $1\times1\times0.1$ mm subjected to uniformly distributed load $q=-1$ units on the top surface. Simply supported boundary conditions are applied on all four edges at the mid-plane of the laminate. The results are presented for anti-symmetric cross ply [0,90,0,90] configuration and compared with the analytical solution obtained from classical laminate plate theory (CLPT) and first order shear deformation theory (FSDT) for laminated plates [52]. The material properties of the fiber and the matrix are given in Table 1.

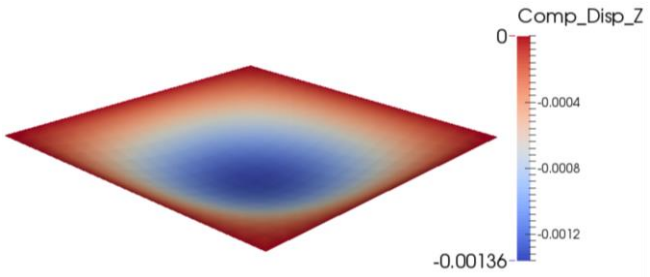

Figure 4.15. Vertical deflection of the mid plane for 8×8×4 mesh

Figure 4.15 shows the vertical displacement contour of the mid-plane for 8×8×4 mesh configuration where the deflection has been magnified 100 times for plotting purposes. It can be observed that the maximum vertical displacement of 0.00136 mm is obtained at the center of the plane. Figure 4.16 provides a comparison between the vertical deflection along the diagonal of the mid plane of the anti-symmetric cross ply laminate obtained for four mesh configurations, namely, 2×2×4, 4×4×4, 8×8×4, 16×16×4 and the analytical results obtained from CLPT and FSDT [52]. It can be observed that the finite element solution of the vertical deflection converges monotonically with mesh refinement. As the CLPT assumes that the transverse normal and shear stresses are negligible, it underpredicts the displacement of the laminate. The vertical deflection compares well with the results obtained with coarse mesh, which corresponds to a stiff behavior. As the FSDT accounts for constant transverse shear stress, we can see from Figure 4.16 that the FSDT solution compares well with 16×16×4 mesh. Figure 4.17 shows the interactive force field through the thickness for 8×8×4 mesh. It can be observed from the plot that the second ply from the bottom which has a 90^0 fiber orientaion has a compressive interactive force in *z* direction while the third ply where the fiber orientation is at 0^0, has a tensile interactive force in *z* direction. As the second and third ply shows opposite interactive force in the z direction, it can be seen that one of the failure modes for antisymmetric cross ply laminate will be delamination along the mid-plane interface at the center of the edges.

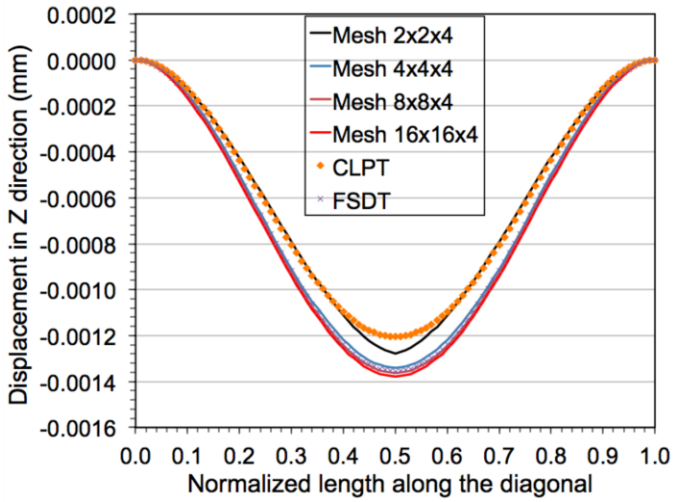

Figure 4.16. Comparison of vertical deflection along the diagonal between mixture theory and plate theory

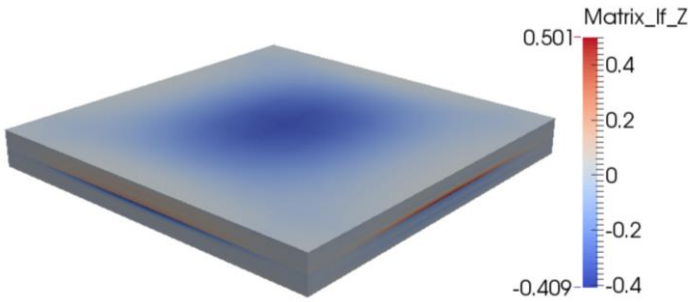

Figure 4.17. Interactive force in Z direction

4.5.4 Large Deformation Bending of a Composite Beam

This section tests the finite deformation capability of the proposed numerical method, under plane strain conditions. A Graphite-Epoxy lamina of dimensions $8\times1\times1$ mm is considered, where the fibers are oriented along the axial direction. This finite deformation pure bending problem is adapted from Ogden [53] and Truster *et al.* [45] where the exact solution and corresponding First Piola-Kirchhoff stress is provided for incompressible and compressible neo-Hookean materials respectively. The deformation map of the matrix and fiber constituents for arbitrary bending angle of ψ is given as,

$$\boldsymbol{x} = \begin{bmatrix} r\cos\theta \\ r\sin\theta \\ Z \end{bmatrix} \quad r(X) = \sqrt{\frac{2LX}{\psi} + R_o^2 - \frac{LH}{\psi}}, \quad \theta(Y) = \frac{Y\psi}{L} \tag{4.52}$$

where R_o is the outer radius, *L* and *H* are the length and the width of the domain, respectively. In Ogden [53], the following equations are employed to impose the incompressibility constraint,

$$\begin{aligned} \psi\left(R_o^2 - R_i^2\right) &= 2HL \\ R_o R_i &= \left(\frac{L}{\psi}\right)^2 \end{aligned} \tag{4.53}$$

where R_i is the inner radius of the deformed domain. Using (4.52) and (4.53), the deformation map can be rewritten as,

$$\boldsymbol{x} = \begin{bmatrix} r\cos\theta \\ r\sin\theta \\ Z \end{bmatrix}, \quad r(\boldsymbol{X}) = \sqrt{\frac{2LX}{\psi} + \sqrt{\frac{L^2H^2}{\psi^2} + \frac{L^4}{\psi^4}}}, \quad \theta(\boldsymbol{Y}) = \frac{Y\psi}{L} \tag{4.54}$$

and the deformation gradient and its inverse are given as,

$$\boldsymbol{F} = \begin{bmatrix} \frac{L}{\psi r}\cos\theta & -\frac{\psi r}{L}\sin\theta & 0 \\ \frac{L}{\psi r}\sin\theta & \frac{\psi r}{L}\cos\theta & 0 \\ 0 & 0 & 1 \end{bmatrix}, \quad \boldsymbol{F}^{-1} = \begin{bmatrix} \frac{\psi r}{L}\cos\theta & \frac{\psi r}{L}\sin\theta & 0 \\ -\frac{L}{\psi r}\sin\theta & \frac{L}{\psi r}\cos\theta & 0 \\ 0 & 0 & 1 \end{bmatrix} \tag{4.55}$$

It can be observed from (4.54) that the deformation map is a function of the bending angle Y only. Now, ignoring the interactive forces, we can solve for the body force in both the constituents based on the material model given in (4.17) that satisfy the equilibrium equations. The expressions for the body force and the first Piola-Kirchhoff stress for the fiber is given in Appendix B.

The domain consists of matrix and fiber and their corresponding material properties are given in Table 1. Using the symmetry conditions, only the upper half of the domain is modeled. The

block is discretized with $16\times128\times2$ mesh and is constrained in thickness direction to simulate plane strain conditions. The mid-plane is constrained in the Y direction to enforce symmetry and is appropriately constrained in X direction to avoid rigid body motion. For a given bending angle, the body force and traction fields are evaluated based on equations (B.11-B.14) given in Appendix B which are employed to drive the simulation The problem is run for a total bending angle of 22.5^0 in increments of 2.5^0. Figure 4.18 compares the discrete bending angle with the applied bending angle for $16\times128\times2$ mesh. It can be seen the discrete bend angle compares well with applied bend angle and has a slope of 0.93. Ideally, the bending angle computed through finite element simulation will be equal to the actual value for a very fine mesh, which corresponds to a slope of unity. Figure 4.19 shows the hoop stress of fiber, matrix and the composite in the deformed configuration for the bend angle of 22.5^0.

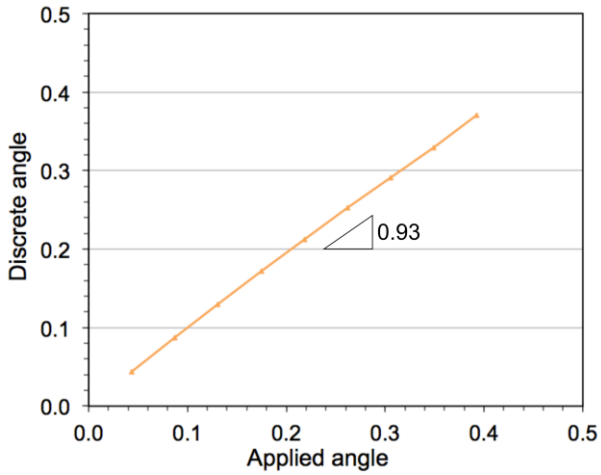

Figure 4.18. Discrete angle vs the applied angle for $16\times128\times2$ mesh

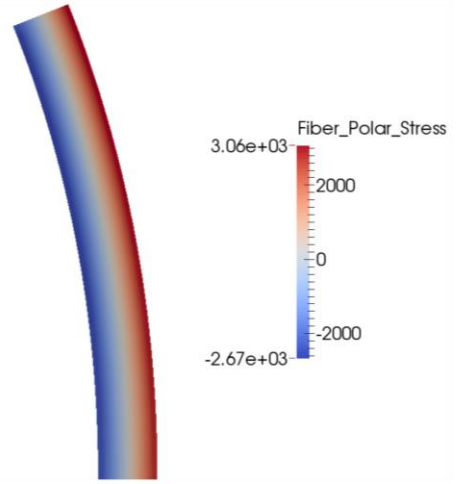

(a) Fiber hoop stress

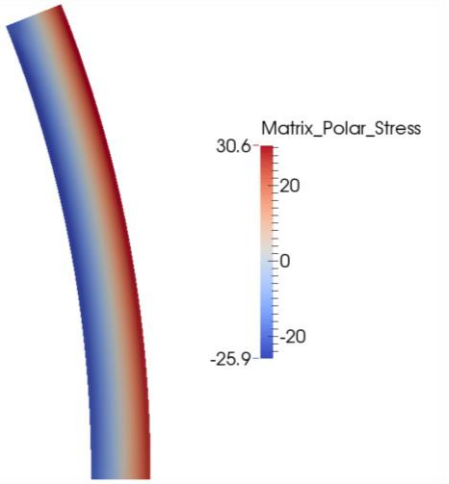

(b) Matrix hoop stress

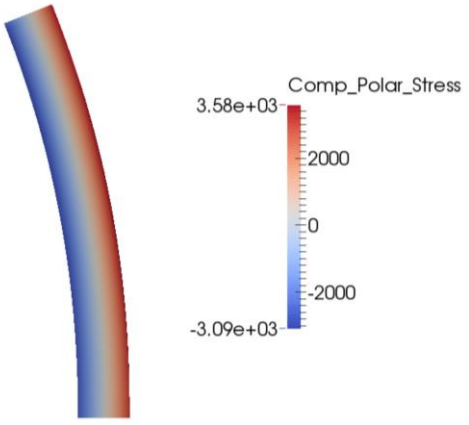

(c) Composite hoop stress

Figure 4.19. Hoop stress in the deformed configuration, $\psi = 22.5^0$

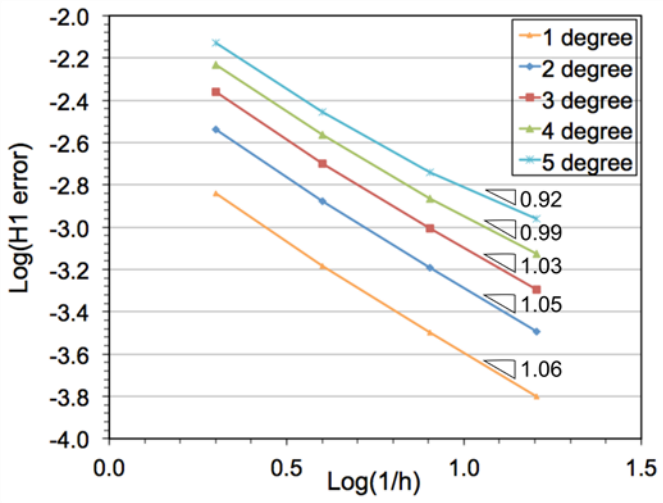

Figure 4.20. Convergence rate plot for H^1 seminorm error in displacement for various bending angle

In this work, we used 27 node Lagrange elements for all numerical test cases because of the gradient of the deformation gradient which leads to second order derivatives in the displacement field that appear in the interactive force constitutive relation. For the current problem the interactive forces were neglected in mixture theory framework to derive an exact solution so that numerical solution can be compared with the exact solution to see variational convergence of the method. This simplification allowed us to model the composite beam with 8 node Lagrange elements for four different meshes with spatial resolution of $2\times16\times1$, $4\times32\times1$, $8\times64\times1$, $16\times128\times1$, and perform a convergence rate study.

The convergence rate study for the nonlinear problem was carried out for various bending angles from 1^0 to 5^0. In each case, the problem was run via Newton-Raphson method to convergence for the given bend angle, with a normalized residual of 10^{-10}. Once the converged solution was obtained, it was used in the calculation of the seminorm of the error field. Figure 4.20 shows the H^1 seminorm of error in the displacement field for various bending angles from 1^0 to 5^0. Computed results show an optimal convergence rate of 1.0. As expected, it can be seen that for higher bend angles that increase the nonlinearity in the problem, though the absolute error increases monotonically with the increase in nonlinearity, the convergence rate from the computed solution in the H^1 seminorm is almost 1.0, as predicted by the finite element theory.

4.6 Conclusions

We have presented a mixture based model for multi-constituent solids where constituents are governed by their individual balance laws and are cognizant of the presence of other coexisting constituents via the interactive forces that emanate from maximizing the entropy production. The model is locally homogeneous while the structural layout of the fiber component introduces directionality as well as heterogeneity at the mesoscale. The coexisting constituents are represented independently inside the domain, weighted by their volume fractions and coupled via the interactive force field. To model the damage-free boundaries of the composite, a method is presented to tie the constituents at the Neumann boundaries. The boundary constraint equations find roots in the interface mechanics literature and they are modified to account for the non-zero applied tractions. The resulting computational method draws from the stabilized Discontinuous Galerkin method for finite strain kinematics where VMS based multiscale decomposition of the deformation map at the Neumann boundary and subsequent elimination of the underlying Lagrange multiplier via local modeling of the edge fine scales via edge bubble functions results in terms that self-consistently tie the multiple constituents. The resulting terms that enable the condensation of the multiplier field from the formulation also provide an edge based stabilization of the method. Closed-form expressions are derived for a generalized penalty tensor and a weighted numerical flux that are free from any tunable stability parameters. Numerical tests verify that the consistently derived constituent coupling parameters automatically evolve with evolving material and geometric nonlinearity at the boundaries.

Several three-dimensional test cases are presented to validate the method via comparison with experimental, numerical and analytical data published in the literature. In all the cases the representative volume element consists of overlapping and coexisting matrix and fiber domains where matrix constituent is considered to be homogenous and isotropic and the fiber constituent is considered to be a transversely isotropic material. The interactive force field plots for the various test cases highlight the region that are susceptible to peeling and debonding of the laminates and this insight can help in developing methods for delamination in composites that is one of the most dominant modes of failure of laminated material systems.

Chapter 5

Variational Multiscale Method for a Comprehensive Two-Constituent Mixture Theory Model

5.1 Introduction

In this chapter we present a numerical scheme that is based on a new variational formulation that possesses enhanced stability properties as well as an ability to account for multiple spatial scales in the solution. We wish to highlight that the development of the multiscale stabilized form that is pursued in this chapter wherein lower-order Lagrange elements can be used to model higher order constitutive theories has not been reported in the literature to date.

In addition, in the theory and the finite element method presented here, we incorporate all the ingredients developed in the earlier chapters for various facets of the mixture constitutive models into one comprehensive mathematical and computational framework. Since the mixture theory is comprised of higher-order constitutive equations, therefore in Chapter 4 we had employed quadratic interpolation functions in 3D that leads to a formulation that works with 27-noded brick element or higher order elements. In Chapter 4 we had focused on the development of variationally consistent method for tying the constituents at the Neumann boundaries employing a methodology that emanated from Lagrange multiplier enforcement of constraints across interfaces in Discontinuous Galerkin method. A literature review reveals that Nitsche method can also been used for this class of problems, however in the finite strain context, finding optimal coefficients for the Nitsche method is non-trivial. Various scaling techniques have been proposed in the literature for the purpose of scaling the coefficients in the Nitsche method [34-38]. Since we are primarily interested in class of problems involving finite strains, in Chapter 4 we developed a variationally consistent method for self-consistent tying of the constituents, wherein VMS ideas were employed but only in a narrow band at the Neumann boundaries.

A major contribution in this Chapter is the derivation and development of a computational formulation wherein linear Lagrange polynomials with quadratic bubble functions, implemented within Heterogeneous Variational Multiscale Framework (HVMF) of Masud and Scovazzi [60] can model the higher order constitutive equations facilitated by the mixture model presented in Chapter 3 and Chapter 4. The importance of this development can be realized via the following example: If cubic Lagrange polynomials are generalized to 3D, they result in 64-noded element with 6 dof per node. Not only do they result in a large element stiffness matrix, they also require 5x5x5 integration rule for accurate numerical integration. However, via HVMF of Masud and coworkers [40-45] if we could get the mixture theory models work with linear brick elements with quadratic bubbles for fine-scales, it can result in substantial computational economy as it would lead to 8-node bricks with 6 dof per node that can be evaluated using 2x2x2 or 3x3x3 numerical integration rules.

Our objective is to develop a numerical method for process modeling of fibrous composite materials. As noted earlier, although there are many theoretical and computational models that are available in the literature that can be used for performance modeling of laminated composite materials and structures, a robust theoretical framework along with computationally efficient algorithms and a scalable code that can be used for process modeling of fibrous composite materials is still not available. The process modeling phase requires (a) consideration of the reactions amongst the constituents, and (b) accounting for the thermal effects during chemical reactions that can then affect the residual stresses in the resulting material. The performance modeling of the fabricated composites needs to be carried out on this resulting material which in fact can have local variations in the mechanical material properties that get reflected in the tensor of material moduli as a function of spatial coordinates. Consequently, in this situation the material tensor is not given by closed form expressions that are typically employed in engineering analysis.

A significant feature of the Mixture Theory model is the Interactive Force field that is generated due to the interplay of the constituents. Although in the homogenized mixture element an explicit discrete representation of the constituents is suppressed, however the interplay of the constituents is fully accounted for via interactive force fields and the corresponding coupling terms that emanate from the mixture modeling ideas. In Section 5.7, via numerical test cases we

try to highlight this unique feature of the method and show how it provides an insight into the material design process. We wish to state that these insightful features are not there in the competing homogenization methods that are available in the literature and can model kinematics of deformation, but cannot provide insight into the interplay of the constituents.

The outline of the chapter is as follows. We first present the governing equations and the constitutive relations for a mixture theory for two-solid constituents with the objective to develop a numerical method for modeling processing and performance of composites. In Section 5.3, we present the variational multiscale method for modeling the higher order constitutive theory with lower order Lagrange elements in 1D context. This formulation is extended to three dimension in Section 5.4. In Section 5.5, the error estimation feature of the proposed framework is presented. Then, the material model employed in the numerical section is stated. The proposed VMS methods capability and feature are showcased in numerical section through curing of composite problem, 3D block problem under gravity. Finally, a comprehensive problem for both process modeling and performance modeling of the composite is presented.

5.2 Mixture Theory for Two Solid-Constituents Material

In Chapter 2 we presented the mixture theory in the context of fluid-solid constituents, and in Chapter 3 we presented a version of the theory that is appropriate for two solid constituent mixtures. The model in Chapter 3 was extended to 3D implementation with the objective to validate the model and simulate the curing process and interphase formation between matrix and fiber. In this model it is assumed that there is no mass exchange between the fiber and the matrix and the interphase material is formed in the matrix material along the contact surface with the fibers in a homogenized sense.

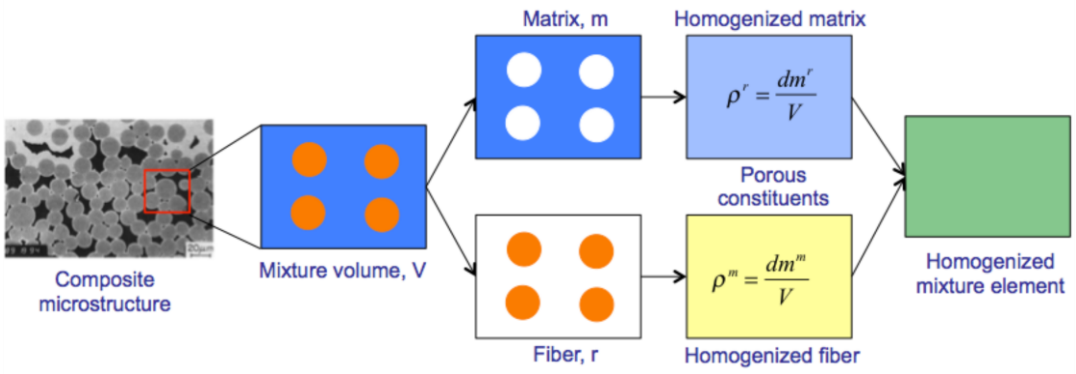

Figure 5.1. Mixture theory homogenization

Figure 5.1 shows the schematics of the underlying mixture modeling idea in which an infinitesimal composite volume is considered that is comprised of fiber (indicated via orange circles) and matrix (represented via blue surrounding material). The constituents of this representative discrete volume element are segregated, and employing the notion of homogenization, some averaged parameters are introduced to describe the attributes of the segregated constituents. One such modeling parameter is the apparent density that is obtained by dividing the mass of the constituent with the total volume of the domain. In the schematic representation in Figure 5.1, this gives rise to the light blue and yellow regions that represent the equivalent matrix and fiber materials. These equivalent materials are also characterized via a second modeling parameter of porosity that is defined as ratios of volumes of the constituents to the volume of the domain. Governing systems of equations for each of the constituents is then developed wherein interaction amongst the constituents is accounted for via interaction and coupling terms. Consequently, these equivalent materials are then made aware of the coexistence of other constituents via the governing equations that bring into play the inter-constituent forces fields and stress fields. This mathematical coupling of the effects of constituents on each other yields an equivalent or homogenized mixture element that is schematically shown with the green block. Although in the homogenized mixture element an explicit discrete representation of the constituents is suppressed, however the interplay of the constituents is fully accounted for via interactive force fields and coupling terms that emanate because of the mixture modeling ideas and the material models on the homogenized constituents.

5.2.1 Governing equations for the mixture theory model

The governing equations for the mixture theory were presented in earlier chapters, and therefore in the interest of brevity they are not being repeated here. However, to develop the variational formulation that goes together with the theoretical model we present the following.

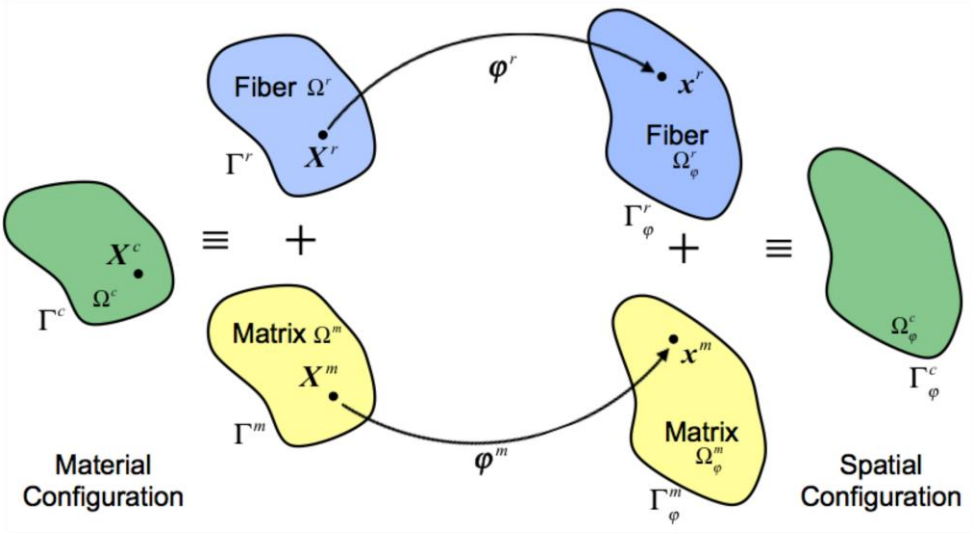

Figure 5.2. Mixture kinematics

Consider the reference, initial and current configuration of the composite as shown in Figure 5.2, where every point in the domain is co-occupied by the constituents. In reference configuration, these coexisting material points of each constituent are paired with each other, i.e., they are assumed to be bonded together. Thus in all the configurations, there exists a homogenized fiber, homogenized matrix and a homogenized composite domain. Ω, Ω^m and Ω^r. And similarly, the current configurations can be written as, Ω_f, Ω_f^m and Ω^r. Let the deformation map of matrix and fiber constituent be given as, $\boldsymbol{\varphi}^r\left(\boldsymbol{X}^r\right)$, $\boldsymbol{\varphi}^m\left(\boldsymbol{X}^m\right)$, where $\boldsymbol{X}^r$, $\boldsymbol{X}^m$ have the same material coordinates. But the deformation map of these material points can map $\boldsymbol{X}^r$, $\boldsymbol{X}^m$ to different spatial points $\boldsymbol{x}^r, \boldsymbol{x}^m$ in the current configuration. Though the material points are paired together and assumed to be perfectly bonded, as it is homogenized volumetrically, it is allowed to deform with respect to each other.

In the reference configuration, as the material points of each constituent are paired with each other, the composite density and second Piola-Kirchhoff stress are given as,

$$\rho_R^c = \rho_R^r + \rho_R^m \tag{5.1}$$

$$\boldsymbol{S}^c = \boldsymbol{S}^r + \boldsymbol{S}^m \tag{5.2}$$

where, $\boldsymbol{S}^r, \boldsymbol{S}^m$ are the partial second Piola-Kirchhoff stress of the matrix and fiber, respectively. The composite deformation map is defined as, $\boldsymbol{\varphi}^c\left(\boldsymbol{X}^c\right) = \boldsymbol{V}^r\boldsymbol{\varphi}^r\left(\boldsymbol{X}^r\right) + \boldsymbol{V}^m\boldsymbol{\varphi}^m\left(\boldsymbol{X}^m\right)$. We denote points in the reference configuration by $\boldsymbol{X}^\alpha \in \Omega^\alpha$ and their corresponding images in the current configuration by $\boldsymbol{x}^\alpha \in \Omega_\varphi^\alpha$, where $\alpha \in [r, m]$ and $\Omega^r = \Omega^m$. The current position of each region Ω^α at time t is given by the image of all points $\boldsymbol{X}^\alpha \in \Omega^\alpha$ under the deformation map $\boldsymbol{\varphi}^\alpha\left(\boldsymbol{X}^\alpha, t\right)$ such that $\boldsymbol{x}^\alpha = \boldsymbol{\varphi}^\alpha\left(\boldsymbol{X}^\alpha, t\right)$. We also define the displacement field associated with the deformation $\boldsymbol{\varphi}^\alpha$ as $\boldsymbol{u}^\alpha = \boldsymbol{x}^\alpha\left(\boldsymbol{X}^\alpha, t\right) - \boldsymbol{X}^\alpha$ $\boldsymbol{u}^{(\alpha)}\left(\boldsymbol{X}, t\right) = \boldsymbol{x}\left(\boldsymbol{X}, t\right) - \boldsymbol{X}$. Finally, the deformation gradient $\boldsymbol{F}^\alpha\left(\boldsymbol{X}^\alpha, t\right)$ emanating from $\boldsymbol{\varphi}^\alpha\left(\boldsymbol{X}^\alpha, t\right)$ is obtained as:

$$\boldsymbol{F}^\alpha\left(\boldsymbol{X}^\alpha, t\right) = \frac{\partial \boldsymbol{x}^\alpha}{\partial \boldsymbol{X}^\alpha} \tag{5.3}$$

Thus, the equilibrium equation and boundary conditions for each region $\Omega^{(\alpha)}$ are combined with the statements of deformation continuity and balance of tractions along Γ_I to yield the following system of equations for the composite domain Ω:

Balance of linear momentum:

$$\operatorname{div}(\boldsymbol{T}^r) + \rho^r \boldsymbol{b}_e + \boldsymbol{I}^r = \boldsymbol{0} \tag{5.4}$$

$$\operatorname{div}(\boldsymbol{T}^m) + \rho^m \boldsymbol{b}_e + \boldsymbol{I}^m = \boldsymbol{0} \tag{5.5}$$

where, $\boldsymbol{T}^\alpha$ is the Cauchy stress, $\boldsymbol{b}^\alpha$ is the body force and $\boldsymbol{I}^\alpha$ is the interactive force acting on the α^{th} component in the mixture. In this work, as we focus only on two consitutent mixture, according to Newton'w third law, the fiber and matrix interactive force satisfies the following equation:

$$\boldsymbol{I}^r + \boldsymbol{I}^r = \mathbf{0} \tag{5.6}$$

In the current mixture theory model we assume that there is no inter-conversion of mass between matrix and fiber material. The interphase is formed in the matrix material along the contact surface with fibers. It is also assumed that the reaction is affected by the reinforcement spacing that results in a potentially transversely isotropic interphase. These assumptions result in reducing the balance of mass equations to an algebraic equation

$$\rho^r J^r = \rho_R^r \tag{5.7}$$

$$\rho^m J^m = \rho_R^m \tag{5.8}$$

5.2.2 Constitutive relations

The constitutive relations for the partial stress in matrix and fiber and the interactive force for mixture theory is obtained by enforcing the constraint of maximization of rate of dissipation:

$$\boldsymbol{T}^m = \boldsymbol{F}^m \left(\frac{\partial(\rho\psi)}{\partial \boldsymbol{E}^m} \right)^T \left(\boldsymbol{F}^m \right)^T - \left(\rho^m \right)^2 \frac{\partial \psi^m}{\partial \rho^m} \boldsymbol{I} \tag{5.9}$$

$$\boldsymbol{T}^r = \boldsymbol{F}^r \left(\frac{\partial(\rho\psi)}{\partial \boldsymbol{E}^r} \right)^T \left(\boldsymbol{F}^r \right)^T \tag{5.10}$$

$$\boldsymbol{I}^r = \frac{\rho^r \rho^m}{\rho} \left(\nabla \psi^m - \nabla \psi^r \right) - \frac{\rho^r \rho^m}{\rho} \frac{\partial \psi^m}{\partial \rho^m} \nabla \rho^m \tag{5.11}$$

By assuming isothermal condition and ignoring the drag force for the solid-solid mixture, the interactive force for the fiber as given in eq. (5.11) can be further simplified and is written as,

$$\boldsymbol{I}^r \approx \frac{\rho^r \rho^m}{\rho} \left(\frac{\partial \psi^m}{\partial \boldsymbol{F}^m} \nabla \boldsymbol{F}^m - \frac{\partial \psi^r}{\partial \boldsymbol{F}^r} \nabla \boldsymbol{F}^r \right) \tag{5.12}$$

The above equation in indicial notation is given as follows,

$$
\begin{aligned}
I_i^r &= \phi^m J^{m^{-1}} \frac{\rho^r}{\rho} S_{PQ}^m F_{aQ}^m \frac{\partial F_{aP}^m}{\partial x_i} - \phi^r J^{r^{-1}} \frac{\rho^m}{\rho} S_{PQ}^r F_{aQ}^r \frac{\partial F_{aP}^r}{\partial x_i} \\
&= \bar{C}_1 S_{PQ}^m F_{aQ}^m \frac{\partial F_{aP}^m}{\partial x_i} - \bar{C}_2 S_{PQ}^r F_{aQ}^r \frac{\partial F_{aP}^r}{\partial x_i} \\
&= \bar{C}_1 D_{Pa}^m \frac{\partial F_{aP}^m}{\partial x_i} - \bar{C}_2 D_{Pa}^r \frac{\partial F_{aP}^r}{\partial x_i}
\end{aligned}
\tag{5.13}
$$

where, $\bar{C}_1 = \phi^m J^{m^{-1}} \dfrac{\rho^r}{\rho}$, $\bar{C}_2 = \phi^r J^{r^{-1}} \dfrac{\rho^m}{\rho}$, $D_{Pa}^m = S_{PQ}^m F_{aQ}^m$, $D_{Pa}^r = S_{PQ}^r F_{aQ}^r$.

5.2.3 Boundary conditions

In mixture theory literature, a volumetric split of the traction fields is usually proposed, which however has the drawback of inconsistent deformation of the constituent boundaries. Following along the lines of the strategy adopted in interface problems, where continuity in the traction and displacement fields are weakly imposed, we propose a set of equations that ensures displacement continuity and traction equilibrium at the constituent boundary, that can be written in the spatial configuration as:

$$
\begin{aligned}
&\boldsymbol{T}^r \boldsymbol{n}^r + \boldsymbol{T}^m \boldsymbol{n}^m = \boldsymbol{h}^c \ \text{ on } \ \Gamma_\varphi \\
&\boldsymbol{\varphi}^m - \boldsymbol{\varphi}^r = \boldsymbol{0} \quad \text{ on } \ \Gamma_\varphi^h \\
&\boldsymbol{\varphi}^r = \boldsymbol{\varphi}^m = \bar{\boldsymbol{\varphi}}^c \ \text{ on } \ \Gamma_\varphi^g
\end{aligned}
\tag{5.14}
$$

where, $\boldsymbol{h}^c$ is the composite traction field on the boundary Γ^φ and $\bar{\boldsymbol{\varphi}}^c$ is the specified composite displacement field, respectively.

5.2.4 Functional spaces for the higher order constitutive models

In the mathematical analysis of boundary-value problems, and consequently in finite element analysis, we need to introduce classes of functions that possess generalized derivatives and, in addition, certain integrability properties. From equation (5.12), it is observed that the interactive force is a function of the gradient of deformation gradient. Therefore, the displacement field needs to be at least quadratic so that gradient of the deformation gradient is non-zero, and this component of the interactive force field can be modeled. Furthermore, this

interactive force field for the matrix $\boldsymbol{I}^m$ and the fiber $\boldsymbol{I}^r$ appears in the equilibrium equations (5.4) and (5.5). From the mathematical theory of BVPs we need the class of functions that are continuous as well as their first derivatives are also continuous. These functions are called C^1 functions and therefore from a Finite Element perspective this mixture theory is a higher order theory that requires C^1 continuity of functions for numerical modeling. This has implications with the continuity and differentiability of the polynomials employed, and therefore this issue in turn feeds into the type of elements that can be developed and the cost of computation associated with these elements.

Based on the discussion presented above, we make two observations.

1. The only terms in the governing equilibrium equations that necessitate the use of C^1 continuity are these terms in the interactive force field.
2. These terms become zero when approximated via linear shape functions.

Generally, finite element functions are smooth on element interiors but possess only low-order continuity across element boundaries. One might characterize them as locally smooth but globally rough. The piecewise linear finite element functions are of class C_b^0, which means these functions are continuous and possess square-integrable first derivatives, but the derivatives are not globally continuous. To calculate derivatives of C^0 functions we need to employ the notion of generalized derivatives. For example, the first derivative of a piecewise linear finite element functions is a generalized step function; second derivative is a Dirac delta function (i.e., Delta functions of various amplitudes, acting at the nodes).

On the other hand Hermite Cubic functions are C_b^1 functions, i.e., these functions are continuous and their first derivatives are also continuous functions, while their second derivative is a generalized step function, and so on. Although, one would need Hermite cubic type functions for this mixture theory [13], one has to consider that generalizing Hermite cubic functions to 2D and 3D is neither easy nor straightforward. A literature review reveals that this C^1 continuity requirement has been the reason for the demise of several theoretical models in solid and fluid mechanics.

At this point we pose a question: To model the interactive force via finite element discretization, the shape functions should be at least quadratic or higher-order. Is it possible that we can employ linear Lagrange shape functions for this otherwise higher-order mixture model? Our objective is to develop a numerical method where we can use C^0 functions and wherein the displacement field is continuous but derivatives may be discontinuous, and still we are able to model the physics in the higher order constitutive equations of the mixture theory model.

To address these issues we have employ the Heterogeneous Variational Multiscale Method of Masud and Scovazzi [60] and develop a multiscale numerical method for the mixture theory. Our new developments that are outlined in Section 4 below possesses two significant mathematical attributes that are uniquely important for the mixture theory model employed here:

1. It helps in effective modeling of scale even when cruder mesh discretizations are employed.
2. It facilitates an algorithmic treatment wherein higher-order Lagrange functions are employed only within the element and not across the inter-element boundaries, thereby reducing the inter-element continuity requirement. These internal nodal contributions can then be statically condensed out, yet retaining the higher order effects.

Consequently, at the coarse-scale level when lower order Lagrange functions are employed and some of the higher-order terms in the constitutive equation are lost, the overall model will still retain their effect, which will get manifested via the fine-scale terms. This aspect of VMS formulation is highlighted in the following sections.

5.3 Development of the Multiscale Finite Element Method

The numerical implementation of the mixture theory requires at least quadratic Lagrange polynomials to accurately capture the interactive force effects between the matrix and reinforcement. In Chapter 4 it was implemented with quadratic brick element in 3D that helped preserve the dominant terms in the interactive force field which is an important tenant of the mixture model and keeps the constituents interact in domain interiors. However, the resulting method is computationally expensive for larger applications. In addition, there are not many mesh generation tools for complex geometries using 27 noded brick elements.

With these two as the bottlenecks for the generalization of the mixture theory for general applications, we embark upon in this Chapter to develop a method that can work with lowest order Lagrange functions even for the higher order constitutive relations facilitated by the mixture theory. In this section, we derive a Variational Multiscale framework for the two-solid mixture theory to capture the fine scale effects through the fine-scale sub-problem that provides us an option to use higher order functions locally, thereby capturing part of physics that is otherwise lost at the coarse-scale level if lower-order Lagrange interpolation functions are used.

In addition, for the class of incompressible or nearly incompressible materials in the finite strain regime, one needs to use enhanced strain formulations that do not lock in the incompressible limit. More advanced versions of enhanced assumed strain formulations have been proposed over the years that exhibit improved performance for both incompressible material behavior as well as for bending-dominated problems, although hourglassing and other instabilities have been concerns for some elements [63,64]. We wish to highlight that the developments presented in this section result in a formulation that successfully overcome volumetric locking. Specifically, one can show that the formulation that we derive in the pure displacement context below has equivalence under simplifying assumptions with the $\bar{\boldsymbol{F}}$ method [42].

The hallmark of the VMS approach is the decomposition of the primary field into overlapping coarse- and fine-scale components. The coarse-scale part corresponds to the portion of the total solution that is resolvable by a given numerical discretization while the fine-scale part is beyond the resolution capacity of the coarse scales system and therefore must be modeled in a variational setting. In the context of finite deformations, this concept yields a decomposition of the deformation mapping $\boldsymbol{\varphi}$ into a coarse-scale mapping $\bar{\boldsymbol{\varphi}}$ corresponding to the deformations representable by the given discretization and a fine-scale mapping $\tilde{\boldsymbol{\varphi}}$ representing the smooth yet higher order effects. We denote the intermediate configuration obtained from the coarse-scale mapping as $\Omega_{\bar{\varphi}} \equiv \bar{\boldsymbol{\varphi}}(\Omega)$. These mappings can be expressed in terms of coarse- and fine-scale components of the displacement field $\bar{\boldsymbol{u}}^{\alpha}$ and $\tilde{\boldsymbol{u}}^{\alpha}$, respectively, as follows:

$$\boldsymbol{u}^{\alpha} = \bar{\boldsymbol{u}}^{\alpha} + \tilde{\boldsymbol{u}}^{\alpha} \tag{5.15}$$

These mappings can be expressed in terms of coarse- and fine-scale components of the displacement field $\bar{\boldsymbol{u}}$ and $\tilde{\boldsymbol{u}}$, respectively, as follows:

$$\bar{\boldsymbol{\varphi}}\left(\boldsymbol{X},t\right)=\boldsymbol{1}_{\bar{\boldsymbol{\varphi}}}\cdot\boldsymbol{X}+\bar{\boldsymbol{u}}\equiv\bar{\boldsymbol{x}} \tag{5.16}$$

$$\tilde{\boldsymbol{\varphi}}\left(\bar{\boldsymbol{x}},t\right)=\boldsymbol{1}_{\tilde{\phi}}\cdot\bar{\boldsymbol{x}}+\tilde{\boldsymbol{u}} \tag{5.17}$$

$$\boldsymbol{\varphi}\left(\boldsymbol{X},t\right)=\tilde{\boldsymbol{\varphi}}\circ\bar{\boldsymbol{\varphi}}\left(\boldsymbol{X},t\right)=\boldsymbol{1}_{\tilde{\boldsymbol{\varphi}}}\cdot\left[\boldsymbol{1}_{\bar{\boldsymbol{\varphi}}}\cdot\boldsymbol{X}+\bar{\boldsymbol{u}}\right]+\tilde{\boldsymbol{u}}=\boldsymbol{1}_{\bar{\boldsymbol{\varphi}}}\cdot\boldsymbol{X}+\boldsymbol{1}_{\phi'}\cdot\bar{\boldsymbol{u}}+\tilde{\boldsymbol{u}} \tag{5.18}$$

Similar to the classical $\bar{\boldsymbol{F}}$ method, the multiscale decomposition of mappings leads to a multiplicative split of the deformation gradient $\boldsymbol{F}\left(\boldsymbol{X},t\right)$. Substituting (5.18)(28) into (5.3)(9), we obtain:

$$\boldsymbol{F}\left(\boldsymbol{X},t\right)=\frac{\partial\boldsymbol{x}}{\partial\boldsymbol{X}}=\frac{\partial\boldsymbol{x}}{\partial\hat{\boldsymbol{x}}}\cdot\frac{\partial\hat{\boldsymbol{x}}}{\partial\boldsymbol{X}}=\left[\boldsymbol{1}_{\phi'}+\mathrm{GRAD}\,\boldsymbol{u}'\right]\cdot\left[\boldsymbol{1}_{\hat{\phi}}+\mathrm{GRAD}\,\hat{\boldsymbol{u}}\right]\equiv\boldsymbol{F}'\cdot\hat{\boldsymbol{F}} \tag{5.19}$$

5.3.1 Development of the multiscale finite element method in 1D context

In order to keep the presentation as clear as possible, we will first present the details of the derivation in the context of 1D finite strain VMS formulation. Once made precise, we will follow in Section 5.4 with a general three dimensional version of the stabilized finite element formulation for finite deformations.

In Variational Multiscale method, as the underlying field is decomposed into a coarse scale field and a fine scale field, the compositional mapping gives rise to a multiplicative split of the deformation gradient that can be written as

$$F_{11}^{\alpha}=\tilde{F}_{11}^{\alpha}\bar{F}_{11}^{\alpha} \tag{5.20}$$

By employing the linearity in the weighting function slot in the weak form of the mixture theory governing equations, the coarse and fine scale residuals in reference configuration of each constituents are given as follows:

Coarse-Scale Problem $\mathcal{C}$

$$\bar{R}^{\alpha} = \int_{V} \frac{\partial \bar{W}_1^{\alpha}}{\partial X} P_{11}^{\alpha} dX - \int_{V} \bar{W}_1^{\alpha} \rho_R^{\alpha} B_1^{\alpha} dX - \int_{V} \bar{W}_1^{\alpha} J^{\alpha} I_1^{\alpha} dX \tag{5.21}$$

Fine-Scale Problem $\mathcal{F}$

$$\tilde{R}^{\alpha} = \int_{V} \frac{\partial \tilde{W}_1^{\alpha}}{\partial X} P_{11}^{\alpha} dX - \int_{V} \tilde{W}_1^{\alpha} \rho_R^{\alpha} B_1^{\alpha} dX - \int_{V} \tilde{W}_1^{\alpha} J^{\alpha} I_1^{\alpha} dX \tag{5.22}$$

The objective at this point is to solve the fine-scale problem (5.22) either via analytical or via computational method and extract an expression for the fine-scale field. This fine-scale field can then be substituted in the corresponding coarse-scale formulation given by (5.21), thereby eliminating the explicit appearance of fine-scales in those equations. Consequently, the additional terms that are thus inducted in (5.21) serve the role of modeling terms for the fine scales.

5.3.1.1 Step A: Modeling of fine scales

As stated earlier, the objective now is to solve the fine-scale problem. Since the problem at hand is nonlinear, therefore a closed form solution of the fine-scale problem may not be possible. As such, we will try to extract a closed-form expression, which in fact may need some coefficients to be determined via numerical techniques. To obtain an explicit expression for the fine scale, equation (5.22) is linearized with respect to fine scale field and is given as,

$$\tilde{R}^{\alpha} + \mathrm{D}\tilde{R}^{\alpha}\left(\varphi_1^{\alpha}\right) \cdot \Delta\tilde{u}_1^{\alpha} = 0 \tag{5.23}$$

For the matrix, the consistent tangent term in equation (5.23) is given as,

$$
\begin{aligned}
&\mathrm{D}R^m\left(\varphi_1^m\right)\cdot\Delta U_1'^m = \int_V \frac{\partial \tilde{W}_1^m}{\partial X}\frac{\partial P_{11}^m}{\partial F_{11}^m}\frac{\partial \Delta \tilde{U}_1^m}{\partial X}dX \\
&-\int_V \tilde{W}_1^m \frac{\rho_R^m \rho^m \rho^r}{\rho^2}\frac{1}{F_{11}^m}\left[\frac{\partial \psi^r}{\partial F_{11}^r}\frac{\partial F_{11}^r}{\partial x} - \frac{\partial \psi^m}{\partial F_{11}^m}\frac{\partial F_{11}^m}{\partial x}\right]\frac{\partial \Delta \tilde{U}_1^m}{\partial X}dX \\
&+\int_V \tilde{W}_1^m \frac{\rho_R^m \rho^r}{\rho}\frac{\partial \psi^m}{\partial F_{11}^m}\frac{1}{F_{11}^m}\frac{\partial^2 \Delta \tilde{U}_1^m}{\partial X^2}dX \\
&-\int_V \tilde{W}_1^m \frac{\rho_R^m \rho^r}{\rho}\frac{\partial \psi^m}{\partial F_{11}^m}\frac{\partial F_{11}^m}{\partial X}\frac{1}{\left(F_{11}^m\right)^2}\frac{\partial \Delta \tilde{U}_1^m}{\partial X}dX \\
&-\int_V \tilde{W}_1^m \frac{\rho_R^m \rho^r}{\rho}\frac{\partial}{\partial F_{11}^m}\left(\frac{\partial \psi^m}{\partial F_{11}^m}\right)\frac{1}{F_{11}^m}\frac{\partial F_{11}^m}{\partial X}\frac{\partial \Delta U_1^m}{\partial X}dX
\end{aligned}
\tag{5.24}
$$

where, the first term is the tangent moduli that arises due to the stress term and the rest of the terms are the contributions from interactive force term.

5.3.1.2 Hierarchical bubbles for fine scale field

Unlike the conventional application of VMS for the development of stabilized methods for the PDEs, in the present case fine scales are not just the corrections terms to the coarse scale fields. Rather, they are also part of the physics that is otherwise not accounted for in the coarse scales system due to the use of lower order Lagrange polynomials employed to expand the coarse field. Consequently, these fine scales are nonlinear and history dependent, and therefore need to be stored and transferred forward. In order to model the higher order terms in the interactive force field, the displacement field is not just the coarse scale field as modeled conventionally, but it is a sum decomposition of the coarse scale field and fine scale field. The incremental fine scale solution given by equation (5.23) is added to the previously converged fine scale field at the last load step. Thus, in this formulation, the fine scale fields are not independent of the previous load step and iteration, but it is a continuously evolving field that captures the physics that is lost by linear Lagrange function employed to model the coarse scale field. Hence, the total displacement field in the interactive force term is summation of coarse scale field and fine scale field, where the coarse scale field is discretized using linear Lagrange function and fine scale field is modeled using quadratic bubble function. Thus, though the second derivative of the coarse scale displacement field is zero, due to the evolving fine scale field, the interactive force field is non-zero.

To present the development of the method where fine scales are modeled using bubble functions, we employ a representative bubble function for linear Lagrange elements as shown in Figure 5.3. Observe that (5.23) is defined over the entire domain Ω. In view of computational expediency, we assume that the fine scales vanish over the boundaries Γ_e^α of the subdomains in the reference configuration. This is done by employing bubble functions that are polynomial functions, non-zero within the element and are assumed to vanish at element boundaries. Accordingly, fine scales are given as, $\tilde{U}_1^\alpha = 0,\ \tilde{W}_1^\alpha = 0$ on Γ_e^α and

$$\tilde{U}_1^\alpha\big|_{\Omega_e} = b^e(\xi)\beta_1^\alpha \tag{5.25}$$

$$\tilde{W}_1^\alpha\big|_{\Omega_e} = b^e(\xi)\gamma_1^\alpha \tag{5.26}$$

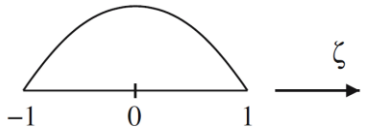

Figure 5.3. 1D bubble function

Substituting the assumed form of fine scales in (5.23) we obtain,

$$\begin{aligned}
&\int_{V^e} \frac{\partial b^e}{\partial X}\frac{\partial P_{11}^m}{\partial F_{11}^m}\frac{\partial b^e}{\partial X}dX\beta_1 - \int_{V^e} b^e \frac{\rho_R^m \rho^m \rho^r}{\rho^2}\frac{1}{F_{11}^m}\left[\frac{\partial \psi^r}{\partial F_{11}^r}\frac{\partial F_{11}^r}{\partial x} - \frac{\partial \psi^m}{\partial F_{11}^m}\frac{\partial F_{11}^m}{\partial x}\right]\frac{\partial b^e}{\partial X}dX\beta_1 \\
&+\int_{V^e} b^e \frac{\rho_R^m \rho^r}{\rho}\frac{\partial \psi^m}{\partial F_{11}^m}\frac{1}{F_{11}^m}\frac{\partial^2 b^e}{\partial X^2}dX\beta_1 - \int_{V^e} b^e \frac{\rho_R^m \rho^r}{\rho}\frac{\partial \psi^m}{\partial F_{11}^m}\frac{\partial F_{11}^m}{\partial X}\frac{1}{\left(F_{11}^m\right)^2}\frac{\partial b^e}{\partial X}dX\beta_1 \\
&+\int_{V^e} b^e \frac{\rho_R^m \rho^r}{\rho}\frac{\partial}{\partial F_{11}^m}\left(\frac{\partial \psi^m}{\partial F_{11}^m}\right)\frac{1}{F_{11}^m}\frac{\partial F_{11}^m}{\partial X}\frac{\partial b^e}{\partial X}dX\beta_1 \\
&= -\left(\int_{V^e}\frac{\partial b^e}{\partial X}P_{11}^m dX - \int_{V^e} b^e \rho_R^m B_1^m dX - \int_{V^e} b^e J^m I_1^m dX\right)
\end{aligned} \tag{5.27}$$

Equation (5.27) can be resolved locally, and the fine scales can be written as,

$$\Delta U_1'^m = b^e\beta_1 = b^e Y_1\left[Y_2\right]^{-1} \tag{5.28}$$

wherein various quantities are defined as follows:

$$\begin{aligned}\left[Y_2\right] &= \int_{V^e} \frac{\partial b^e}{\partial X}\frac{\partial P_{11}^m}{\partial F_{11}^m}\frac{\partial b^e}{\partial X}\,dX - \int_{V^e} b^e\,\frac{\rho_R^m\rho^m\rho^r}{\rho^2}\frac{1}{F_{11}^m}\left[\frac{\partial \psi^r}{\partial F_{11}^r}\frac{\partial F_{11}^r}{\partial x} - \frac{\partial \psi^m}{\partial F_{11}^m}\frac{\partial F_{11}^m}{\partial x}\right]\frac{\partial b^e}{\partial X}\,dX \\ &+ \int_{V^e} b^e\,\frac{\rho_R^m\rho^r}{\rho}\frac{\partial \psi^m}{\partial F_{11}^m}\frac{1}{F_{11}^m}\frac{\partial^2 b^e}{\partial X^2}\,dX - \int_{V^e} b^e\,\frac{\rho_R^m\rho^r}{\rho}\frac{\partial \psi^m}{\partial F_{11}^m}\frac{\partial F_{11}^m}{\partial X}\frac{1}{\left(F_{11}^m\right)^2}\frac{\partial b^e}{\partial X}\,dX \\ &+ \int_{V^e} b^e\,\frac{\rho_R^m\rho^r}{\rho}\frac{\partial}{\partial F_{11}^m}\left(\frac{\partial \psi^m}{\partial F_{11}^m}\right)\frac{1}{F_{11}^m}\frac{\partial F_{11}^m}{\partial X}\frac{\partial b^e}{\partial X}\,dX\end{aligned} \tag{5.29}$$

$$\left[Y_1\right] = -\int_{V^e}\frac{\partial b^e}{\partial X}P_{11}^m\,dX + \int_{V^e} b^e\rho_R^m B_1^m\,dX + \int_{V^e} b^e J^m I_1^m\,dX \tag{5.30}$$

Equation (5.30) shows an important relation that fine scale displacement field is proportional to the residual of the Euler-Lagrange equations over the sum of element interiors. Consequently, fine scales are residual based, and therefore the formulation emanating from embedding the fine scale solution into the coarse scales will be a variationally consistent formulation.

$$\bar{\tau}\left(x\right) = Y_1\left[Y_2\right]^{-1} \tag{5.31}$$

At this point we wish to emphasize that an important aspect of this derivation is that the stabilization tensor τ that is given in equation (5.31) does not contain any approximation and for the case of finite deformation kinematics it evolves together with the solution. Since it incorporates equations (5.29) and (5.30), one can see that the mechanical parameters are represented in the expression of this tensor. In addition, this tensor evolves as the problem evolves, which is considered an important aspect of the formulation so that it is able to provide a stabilized response in the entire range of deformation.

5.3.1.3 Step B: Variational embedding in coarse-scale problem

With the fine-scale solution in hand, we return to the coarse-scale problem (5.21) to derive the stabilized multiscale formulation. Since (5.21) is a nonlinear function of $\tilde{U}_1^\alpha$, we first linearize it with respect to $\tilde{U}_1^\alpha$ so that the relationship (5.28) may be substituted. Accordingly, equation (5.21) is linearized with respect to fine scales,

$$
\begin{aligned}
&\mathrm{D}R^m\left(\varphi_1^m\right)\cdot\Delta\tilde{U}_1^m=\int_V\frac{\partial\bar{W}_1^m}{\partial X}\frac{\partial P_{11}^m}{\partial F_{11}^m}\frac{\partial\Delta\tilde{U}_1^m}{\partial X}dX\\
&-\int_V\bar{W}_1^m\frac{\rho_R^m\rho^m\rho^r}{\rho^2}\frac{1}{F_{11}^m}\left[\frac{\partial\psi^r}{\partial F_{11}^r}\frac{\partial F_{11}^r}{\partial x}-\frac{\partial\psi^m}{\partial F_{11}^m}\frac{\partial F_{11}^m}{\partial x}\right]\frac{\partial\Delta\tilde{U}_1^m}{\partial X}dX\\
&+\int_V\bar{W}_1^m\frac{\rho_R^m\rho^r}{\rho}\frac{\partial\psi^m}{\partial F_{11}^m}\frac{1}{F_{11}^m}\frac{\partial^2\Delta\tilde{U}_1^m}{\partial X^2}dX-\int_V\bar{W}_1^m\frac{\rho_R^m\rho^r}{\rho}\frac{\partial\psi^m}{\partial F_{11}^m}\frac{\partial F_{11}^m}{\partial X}\frac{1}{\left(F_{11}^m\right)^2}\frac{\partial\Delta\tilde{U}_1^m}{\partial X}dX\\
&+\int_V\bar{W}_1^m\frac{\rho_R^m\rho^r}{\rho}\frac{\partial}{\partial F_{11}^m}\left(\frac{\partial\psi^m}{\partial F_{11}^m}\right)\frac{1}{F_{11}^m}\frac{\partial F_{11}^m}{\partial X}\frac{\partial\Delta\tilde{U}_1^m}{\partial X}dX
\end{aligned}
\tag{5.32}
$$

Substituting (5.28) for the fine scales in the above equation, we obtain the multi-scale stabilized coarse-scale form, which is written here for the matrix constituent, in its residual form.

$$
\begin{aligned}
&\bar{R}^m=\int_V\frac{\partial\bar{W}_1^m}{\partial X}P_{11}^m dX-\int_V\bar{W}_1^m\rho_R^m B_1^m dX-\int_V\bar{W}_1^m J^m I_1^m dX\\
&+\int_V\frac{\partial\bar{W}_1^m}{\partial X}\frac{\partial P_{11}^m}{\partial F_{11}^m}\frac{\partial b^e}{\partial X}\tau\left(X\right)dX\\
&-\int_V\bar{W}_1^m\frac{\rho_R^m\rho^m\rho^r}{\rho^2}\frac{1}{F_{11}^m}\left[\frac{\partial\psi^r}{\partial F_{11}^r}\frac{\partial F_{11}^r}{\partial x}-\frac{\partial\psi^m}{\partial F_{11}^m}\frac{\partial F_{11}^m}{\partial x}\right]\frac{\partial b^e}{\partial X}\tau\left(X\right)dX\\
&+\int_V\bar{W}_1^m\frac{\rho_R^m\rho^r}{\rho}\frac{\partial\psi^m}{\partial F_{11}^m}\frac{1}{F_{11}^m}\frac{\partial^2 b^e}{\partial X^2}\tau\left(X\right)dX-\int_V\bar{W}_1^m\frac{\rho_R^m\rho^r}{\rho}\frac{\partial\psi^m}{\partial F_{11}^m}\frac{\partial F_{11}^m}{\partial X}\frac{1}{\left(F_{11}^m\right)^2}\frac{\partial b^e}{\partial X}\tau\left(X\right)dX\\
&+\int_V\bar{W}_1^m\frac{\rho_R^m\rho^r}{\rho}\frac{\partial}{\partial F_{11}^m}\left(\frac{\partial\psi^m}{\partial F_{11}^m}\right)\frac{1}{F_{11}^m}\frac{\partial F_{11}^m}{\partial X}\frac{\partial b^e}{\partial X}\tau\left(X\right)dX=0
\end{aligned}
\tag{5.33}
$$

A simiar expression can be obtained for the fiber constituent.

5.3.1.4 Spatial description of the formulation

At this point coarse scales can be solved by linearizing the above equation (5.33). The corresponding spatial form of the multiscale weak form of the matrix constituent can be obtained by pushing forward to the current configuration.

$$
\bar{R}^m+\mathrm{D}\bar{R}^m\left(\varphi_1^m\right)\cdot\Delta\tilde{u}_1^m=0 \tag{5.34}
$$

Therefore,

$$
\begin{aligned}
\bar{R}^m &= \int_\Omega \frac{\partial \bar{w}_1^m}{\partial x} T_{11}^m dx - \int_\Omega \bar{w}_1^m \rho^m b_1^m dx - \int_\Omega \bar{w}_1^m I_1^m dx \\
&+ \int_\Omega \frac{\partial \bar{w}_1^m}{\partial x} F_{11}^m \frac{\partial T_{11}^m}{\partial F_{11}^m} \frac{\partial b^e}{\partial x} \bar{\tau}(x) dx \\
&- \int_\Omega \bar{w}_1^m \frac{\rho_R^m \rho^m \rho^r}{\rho^2} \frac{1}{F_{11}^m} \left[\frac{\partial \psi^r}{\partial F_{11}^r} \frac{\partial F_{11}^r}{\partial x} - \frac{\partial \psi^m}{\partial F_{11}^m} \frac{\partial F_{11}^m}{\partial x} \right] \frac{\partial b^e}{\partial x} \bar{\tau}(x) dx \\
&+ \int_\Omega \bar{w}_1^m \frac{\rho_R^m \rho^r}{\rho} \frac{\partial \psi^m}{\partial F_{11}^m} \frac{1}{\left(F_{11}^m\right)^2} \left[\frac{\partial^2 b^e}{\partial x^2} \left(F_{11}^m\right)^2 + \frac{\partial b^e}{\partial x} \frac{\partial F_{11}^m}{\partial X} \right] \bar{\tau}(x) dx \\
&- \int_\Omega \bar{w}_1^m \frac{\rho_R^m \rho^r}{\rho} \frac{\partial \psi^m}{\partial F_{11}^m} \frac{\partial F_{11}^m}{\partial X} \frac{1}{\left(F_{11}^m\right)^2} \frac{\partial b^e}{\partial x} \bar{\tau}(x) dx \\
&+ \int_\Omega \bar{w}_1^m \frac{\rho_R^m \rho^r}{\rho} \frac{\partial}{\partial F_{11}^m} \left(\frac{\partial \psi^m}{\partial F_{11}^m} \right) \frac{1}{F_{11}^m} \frac{\partial F_{11}^m}{\partial X} \frac{\partial b^e}{\partial x} \bar{\tau}(x) dx
\end{aligned}
\tag{5.35}
$$

where, the matrix stabilization tensor is given as,

$$
\begin{aligned}
&\bar{\tau}(x) = Y_1 \left[Y_2 \right]^{-1}, \\
&Y_1 = -\int_{\Omega^e} \frac{\partial b^e}{\partial x} T_{11}^m dx + \int_{\Omega^e} b^e \rho^m b_1^m dx + \int_{\Omega^e} b^e I_1^m dx \\
&Y_2 = \int_{\Omega^e} \frac{\partial b^e}{\partial x} F_{11}^m \frac{\partial T_{11}^m}{\partial F_{11}^m} \frac{\partial b^e}{\partial x} dx - \int_{\Omega^e} b^e \frac{\rho_R^m \rho^m \rho^r}{\rho^2} \frac{1}{F_{11}^m} \left[\frac{\partial \psi^r}{\partial F_{11}^r} \frac{\partial F_{11}^r}{\partial x} - \frac{\partial \psi^m}{\partial F_{11}^m} \frac{\partial F_{11}^m}{\partial x} \right] \frac{\partial b^e}{\partial x} dx \\
&+ \int_{\Omega^e} b^e \frac{\rho_R^m \rho^r}{\rho} \frac{\partial \psi^m}{\partial F_{11}^m} \frac{1}{\left(F_{11}^m\right)^2} \left[\frac{\partial^2 b^e}{\partial x^2} \left(F_{11}^m\right)^2 + \frac{\partial b^e}{\partial x} \frac{\partial F_{11}^m}{\partial X} \right] dx \\
&- \int_{\Omega^e} b^e \frac{\rho_R^m \rho^r}{\rho} \frac{\partial \psi^m}{\partial F_{11}^m} \frac{\partial F_{11}^m}{\partial X} \frac{1}{\left(F_{11}^m\right)^2} \frac{\partial b^e}{\partial x} dx + \int_\Omega b^e \frac{\rho_R^m \rho^r}{\rho} \frac{\partial}{\partial F_{11}^m} \left(\frac{\partial \psi^m}{\partial F_{11}^m} \right) \frac{1}{F_{11}^m} \frac{\partial F_{11}^m}{\partial X} \frac{\partial b^e}{\partial x} dx
\end{aligned}
\tag{5.36}
$$

Since the multiscale formulation (5.35) is nonlinear, we need to linearize it in order to use nonlinear solution strategies such as the Newton-Raphson method. We perform linearization in the reference configuration and then push forward the results to the current configuration.

Remark: *Similar procedure can be used in deriving the corresponding equations for reinforcement and for the sake of brevity these equations are not shown here.*

5.3.1.5 Important feature of the VMS stabilized formulation

There are several important features in the modified weak-form presented above.

1. The first line in (5.33) corresponds to the standard Galerkin method, and therefore this method is fully backward compatible with the standard Galerkin finite element techniques.
2. The next four lines appear because of the assumption of fine-scales in the solution field. Accordingly, these terms are the fine-scale modeling terms, as they are representing the effects of the fine-scales that would otherwise be missed in the standard formulations.
3. It is important to note that this formulation, by design, is a residual based formulation. This has important implications from a mathematical perspective. If the mesh generated to solve the problem is fine enough to resolve all the scales, as is done in direct numerical simulations, then the residual of the Euler-Lagrange equations for the coarse-scales are zero over sum of element interiors. As such, the driving term for the fine-scale problem becomes zero, and therefore fine-scales automatically disappear.
4. Due to item 3 listed above, the formulation is mathematically consistent as it is fully capable to accommodate exact solution to the problem wherever the solution lies in the admissible space of functions employed in the finite element calculations.
5. As the fine scale are allowed to evolve and kept track at every load step, the second order derivative of the displacement field in the interactive force term is non-zero. Thus, the lost physics due to the discretization of the coarse scale field using linear Lagrange element is captured through the evolving fine scale field.

5.4 Three Dimensional Extension of the Stabilized Finite Element Formulation for Finite Deformations

Following along the lines of the 1D case, we perform additive scale decomposition of the displacement field as follows:

$$\boldsymbol{u}^{\alpha} = \bar{\boldsymbol{u}}^{\alpha} + \tilde{\boldsymbol{u}}^{\alpha} \tag{5.37}$$

$$\boldsymbol{\eta}^{\alpha} = \bar{\boldsymbol{\eta}}^{\alpha} + \tilde{\boldsymbol{\eta}}^{\alpha} \tag{5.38}$$

where, $\boldsymbol{u}^{\alpha}$ is displacement field and $\boldsymbol{\eta}^{\alpha}$ is the weighting function field of the α^{th} constituent. By substituting the additive decomposition of the fields into the weak form associated with each of

the constituents and employing linearity of the weighting function slots in these system, we recover the set of coarse and fine scale problem for each of the constituents. Since the procedure for multiscale form for each constituent is same, we present it in the generic form in reference configuration.

Coarse-scale problem $\mathcal{C}$:

$$\bar{R}^{\alpha}\left(\bar{\boldsymbol{\eta}}^{\alpha};\boldsymbol{u}^{\alpha}\right)\equiv\int_{\Omega}\nabla_{X}\bar{\boldsymbol{\eta}}^{\alpha}:\boldsymbol{P}^{\alpha}\mathrm{d}\Omega-\int_{\Omega}\bar{\boldsymbol{\eta}}^{\alpha}\cdot\rho_{R}^{\alpha}\boldsymbol{b}^{\alpha}\mathrm{d}\Omega-\int_{\Omega}\bar{\boldsymbol{\eta}}^{\alpha}\cdot J^{\alpha}\boldsymbol{I}^{\alpha}\mathrm{d}\Omega=0 \tag{5.39}$$

Fine-scale problem $\mathcal{F}$:

$$\tilde{R}^{\alpha}\left(\tilde{\boldsymbol{\eta}}^{\alpha};\boldsymbol{u}^{\alpha}\right)\equiv\int_{\Omega}\nabla_{X}\tilde{\boldsymbol{\eta}}^{\alpha}:\boldsymbol{P}^{\alpha}\mathrm{d}\Omega-\int_{\Omega}\tilde{\boldsymbol{\eta}}^{\alpha}\cdot\rho_{R}^{\alpha}\boldsymbol{b}^{\alpha}\mathrm{d}\Omega-\int_{\Omega}\tilde{\boldsymbol{\eta}}^{\alpha}\cdot J^{\alpha}\boldsymbol{I}^{\alpha}\mathrm{d}\Omega=0 \tag{5.40}$$

In order to solve the fine scale problem (5.40), we first linearize the above equation with respect to the fine scale field. The linearized fine scale problem is given as,

$$\left\{\begin{array}{c}\int_{\Omega}\left[\nabla_{X}\left(\Delta\tilde{\boldsymbol{u}}^{\alpha}\right)\phi^{\alpha}\boldsymbol{S}^{\alpha}\right]:\nabla_{X}\tilde{\boldsymbol{\eta}}^{\alpha}\mathrm{d}\Omega+\\ \int_{\Omega}\Delta\boldsymbol{E}\left(\tilde{\boldsymbol{\eta}}^{\alpha}\right):\left[\phi^{\alpha}\boldsymbol{C}^{\alpha}:\Delta\boldsymbol{E}\left(\Delta\tilde{\boldsymbol{u}}^{\alpha}\right)\right]\mathrm{d}\Omega-\int_{\Omega}\tilde{\boldsymbol{\eta}}^{\alpha}\cdot\mathrm{D}\left[J^{\alpha}\boldsymbol{I}^{\alpha}\right]\cdot\Delta\tilde{\boldsymbol{u}}^{\alpha}\mathrm{d}\Omega\end{array}\right\}=-\tilde{R}^{\alpha}\left(\tilde{\boldsymbol{\eta}}^{\alpha};\boldsymbol{u}^{\alpha}\right) \tag{5.41}$$

In order to obtain a closed form approximation of the incremental fine scale fields, we impose the following conditions on the fine scale space,

$$\tilde{\boldsymbol{u}}^{\alpha}=\boldsymbol{0};\quad\tilde{\boldsymbol{\eta}}^{\alpha}=\boldsymbol{0}\qquad\text{on}\quad\Gamma_{e}^{\alpha} \tag{5.42}$$

This reduces the linearized fine scale problem to be defined over each element and can be written as,

$$\left\{\begin{array}{c}\int_{\Omega_{e}}\left[\nabla_{X}\left(\Delta\tilde{\boldsymbol{u}}^{\alpha}\right)\phi^{\alpha}\boldsymbol{S}^{\alpha}\right]:\nabla_{X}\tilde{\boldsymbol{\eta}}^{\alpha}\mathrm{d}\Omega+\\ \int_{\Omega_{e}}\Delta\boldsymbol{E}\left(\tilde{\boldsymbol{\eta}}^{\alpha}\right):\left[\phi^{\alpha}\boldsymbol{C}^{\alpha}:\Delta\boldsymbol{E}\left(\Delta\tilde{\boldsymbol{u}}^{\alpha}\right)\right]\mathrm{d}\Omega-\int_{\Omega_{e}}\tilde{\boldsymbol{\eta}}^{\alpha}\cdot\mathrm{D}\left[J^{\alpha}\boldsymbol{I}^{\alpha}\right]\cdot\Delta\tilde{\boldsymbol{u}}^{\alpha}\mathrm{d}\Omega\end{array}\right\}=-\tilde{R}^{\alpha}\left(\tilde{\boldsymbol{\eta}}^{\alpha};\boldsymbol{u}^{\alpha}\right) \tag{5.43}$$

In the stabilized finite element literature, it is customary to discretize the fine scale space with a single bubble function, which has been found sufficient for stability of mixed field problems, interface problem and diffusion-advection equations. The objective of this chapter is to develop a method where the fine scales are employed to model the lost physics in the higher order mixture

constitutive theory when modeling using linear Lagrange elements. In order to achieve this goal, we approximate the fine scale using multiple bubble functions as given below

$$\Delta\tilde{\boldsymbol{u}}^{\alpha} = \sum b_e \boldsymbol{\beta}^{\alpha}; \quad \tilde{\boldsymbol{\eta}}^{\alpha} = \sum b_e \boldsymbol{\gamma}^{\alpha} \tag{5.44}$$

Substituting the above discretization of the fine scale field into (5.43), the closed form approximation of the incremental fine scale field can be given as,

$$\Delta\tilde{\boldsymbol{u}}^{\alpha} = \sum b_e \boldsymbol{\beta}^{\alpha} = \boldsymbol{\tau}^{\alpha} \boldsymbol{R}^{\alpha} \tag{5.45}$$

where the residual is given as:

$$R^{\alpha} = \mathrm{DIV}\left[\boldsymbol{P}^{\alpha}\right] + \rho_R^{\alpha} \boldsymbol{b}^{\alpha} + J^{\alpha} \boldsymbol{I}^{\alpha} \tag{5.46}$$

The stabilization tensor of the constituent in this formulation is not a square matrix of dimension 3, but a rectangular matrix of dimension of $3n \times 3$, where n is the number of bubble functions employed.

5.4.1 Variational embedding into coarse scales

Consider the coarse-scale probem (5.39) which is a function of both coarse scale and fine scale displacement. In order to solve this equation, the coarse scale problem is first linearized with respect to the fine scale field and given as,

$$\begin{aligned} \bar{R}^{\alpha}\left(\bar{\boldsymbol{\eta}}^{\alpha}; \boldsymbol{u}^{\alpha}\right) \equiv & \int_{\Omega} \nabla_X \bar{\boldsymbol{\eta}}^{\alpha} : \boldsymbol{P}^{\alpha} \mathrm{d}\Omega - \int_{\Omega} \bar{\boldsymbol{\eta}}^{\alpha} \cdot \rho_R^{\alpha} \boldsymbol{b}^{\alpha} \mathrm{d}\Omega - \int_{\Omega} \bar{\boldsymbol{\eta}}^{\alpha} \cdot J^{\alpha} \boldsymbol{I}^{\alpha} \mathrm{d}\Omega \\ & \int_{\Omega} \left[\nabla_X \left(\Delta\tilde{\boldsymbol{u}}^{\alpha}\right) \phi^{\alpha} \boldsymbol{S}^{\alpha}\right] : \nabla_X \bar{\boldsymbol{\eta}}^{\alpha} \mathrm{d}\Omega \\ & + \int_{\Omega} \Delta\boldsymbol{E}\left(\bar{\boldsymbol{\eta}}^{\alpha}\right) : \left[\phi^{\alpha} \boldsymbol{C}^{\alpha} : \Delta\boldsymbol{E}\left(\Delta\tilde{\boldsymbol{u}}^{\alpha}\right)\right] \mathrm{d}\Omega \qquad = 0 \\ & - \int_{\Omega} \bar{\boldsymbol{\eta}}^{\alpha} \cdot \mathrm{D}\left[J^{\alpha} \boldsymbol{I}^{\alpha}\right] \cdot \Delta\tilde{\boldsymbol{u}}^{\alpha} \mathrm{d}\Omega \end{aligned} \tag{5.47}$$

where the first three terms are the standard Galerkin terms and the last three terms are the terms that arise due to linearization with respect to the fine scales that enhances the stabilization of the formulation. To keep the formulation simple, the contribution of the interactive force terms to the stabilization is ignored, i.e. the last term in (5.47).

5.4.2 Multiscale and stabilized formulation for mixture theory

By substituting the incremental fine scale field (5.45) into (5.47), we obtain the multiscale form of the matrix governing equations:

$$\begin{aligned}&\bar{R}^{\alpha}\left(\bar{\boldsymbol{\eta}}^{\alpha};\boldsymbol{u}^{\alpha}\right)\equiv\int_{\Omega}\nabla_{X}\bar{\boldsymbol{\eta}}^{\alpha}:\boldsymbol{P}^{\alpha}\mathrm{d}\Omega-\int_{\Omega}\bar{\boldsymbol{\eta}}^{\alpha}\cdot\rho_{R}^{\alpha}\boldsymbol{b}^{\alpha}\mathrm{d}\Omega-\int_{\Omega}\bar{\boldsymbol{\eta}}^{\alpha}\cdot J^{\alpha}\boldsymbol{I}^{\alpha}\mathrm{d}\Omega\\&\int_{\Omega}\left[\nabla_{X}\left(\boldsymbol{\tau}^{\alpha}\boldsymbol{R}^{\alpha}\right)\phi^{\alpha}\boldsymbol{S}^{\alpha}\right]:\nabla_{X}\bar{\boldsymbol{\eta}}^{\alpha}\mathrm{d}\Omega+\int_{\Omega}\Delta\boldsymbol{E}\left(\bar{\boldsymbol{\eta}}^{\alpha}\right):\left[\phi^{\alpha}\boldsymbol{C}^{\alpha}:\Delta\boldsymbol{E}\left(\boldsymbol{\tau}^{\alpha}\boldsymbol{R}^{\alpha}\right)\right]\mathrm{d}\Omega=0\end{aligned}\tag{5.48}$$

where ϕ^{α} is the volume fraction of the α^{th} constituent. The interactive force terms in equation (5.48) is a higher order term which is the second order derivative of the displacement field. In this formulation, the incremental fine scale field is tracked and total final scales are allowed evolve as a function of the total residual. This fine scale field along with the coarse scale field is employed in evaluating the interactive force. To keep the computations simple and achieve quadratic convergence rate in the Newton-Raphson scheme, the fine scales field are updated only for the first three iterations.

5.5 Employing Inherent Post-erriori Error Estimation of VMS method for spatial distribution of error

A hallmark feature of the Variational Multiscale method is that it naturally gives rise to an error estimation procedure which quantifies numerical solution accuracy. This procedure was described in the context of linear elasticity by Masud and coworkers in [39] and [42] and other techniques are referenced therein. In this chapter we extend these arguments to the finite deformation problem in the context of the higher order mixture theory.

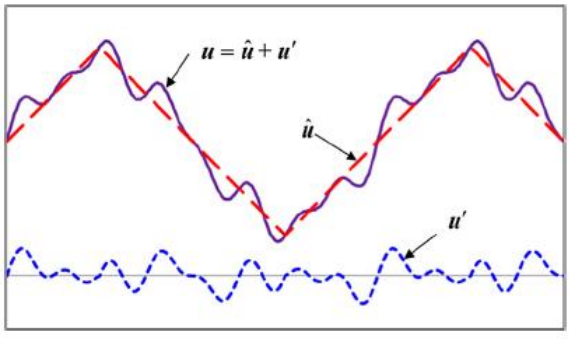

Figure 5.4. Multiscale decomposition of the total solution into coarse and fine scales.

In the context of residual based stabilized methods, the total error $\boldsymbol{e} = \boldsymbol{u} - \boldsymbol{u}^k$ is due to the difference between the exact solution $\boldsymbol{u}$ and the discrete solution $\boldsymbol{u}^h$. As shown in Figure 5.4, we split our total solution into the coarse solution $\bar{\boldsymbol{u}}$ and fine solution $\tilde{\boldsymbol{u}}$. As we use bubble function to represent the fine scale solution, our modeling of the fine scale may not capture all the unsolved features. Thus, there exists some localized error $\tilde{\boldsymbol{e}}_L = \tilde{\boldsymbol{u}} - \hat{\boldsymbol{u}}$ between the true fine scales and the modeled fine scales $\hat{\boldsymbol{u}}$. In additional, when we plug back the fine solution to find the coarse scale solution, i.e. $\boldsymbol{u}^h \cong \bar{\boldsymbol{u}}(\hat{\boldsymbol{u}})$. Therefore, we represent the difference between the true coarse scale solution $\hat{u}$ and the modeled discrete solution $\boldsymbol{u}^h$ as the global error $\boldsymbol{e}_G = \bar{\boldsymbol{u}} - \boldsymbol{u}^h$. Thus we can get the total error in the following expression:

$$\boldsymbol{e} = \boldsymbol{u} - \boldsymbol{u}^h = \boldsymbol{e}_G + \tilde{\boldsymbol{e}}_L + \hat{\boldsymbol{u}} = \boldsymbol{e}_G + \boldsymbol{e}_L \tag{5.49}$$

Where $\boldsymbol{e}_L = \tilde{\boldsymbol{e}}_L + \hat{\boldsymbol{u}}$ is the total local errors, which represent the local errors below the level of the mesh ($\hat{u}$) arising from modeled fine scales $\hat{u}$ and the inaccuracies in these models $\tilde{\boldsymbol{e}}_L$. Referring back to Figure 5.4 $\boldsymbol{e}_G$ represents how far off the red (long-dashed) curve $\hat{u}$ is from interpolation the purple (solid) curve $\boldsymbol{u}$, and $\tilde{\boldsymbol{e}}_L$ measures the inaccuracy in the blue (short-dashed) curve $\tilde{\boldsymbol{u}}$.

Due to the nonlinearity of the multiscale problem under consideration, the equation for these error components are also nonlinear. To ensure the economy of the error estimation method, we seek a linearized approximation that incrementally improves the computed multiscale solution. Thus, we focus on the linearized system of fine-scale equation and the coarse-scale equation.

5.5.1 Local Error

Within the context of the present version of residual based multiscale method, the very first calculation of the fine scale in any time step is in fact driven by the computed total solution from the last converged step. As such, as one goes to the next load level and computes the fine-scale via (5.28), it provides a first order estimate of the local error. As stated, the total local error is comprised of localized error $\tilde{\boldsymbol{e}}_L = \tilde{\boldsymbol{u}} - \hat{\boldsymbol{u}}$ between the true fine scales and the modeled fine scales $\hat{u}$, as well as of the assumption inherent in the use of bubble functions that consider the error to be zero at the inter-element boundaries. Consequently, this computed value via (5.28) is only a

part of the local error. However, based on our earlier experience, it is a good indicator for use in case if adaptive mesh refinement strategies are to be employed.

From Section 5, the local error has two components as $\hat{\boldsymbol{u}}$ and $\tilde{\boldsymbol{e}}_L$. For simplicity, we ignore $\tilde{\boldsymbol{e}}_L$ and take $\boldsymbol{e}_L = \hat{\boldsymbol{u}}$ as an assumption. Since $\hat{\boldsymbol{u}}$ is the modeled fine scale solution, we get the following expression for the incremental fine scale solution:

$$\boldsymbol{e}_L = \Delta \boldsymbol{u}' = \boldsymbol{\tau} \bar{\boldsymbol{R}}(\bar{\boldsymbol{u}}) \tag{5.50}$$

where the residual and the proportionality tensor is given as $\bar{\boldsymbol{R}}(\bar{\boldsymbol{u}}) = \mathrm{DIV}\left[\bar{\boldsymbol{F}}\boldsymbol{S}(\bar{\boldsymbol{u}})\right] + \rho_o \boldsymbol{b}$. As can be seen, the last converged solution is fully represented in this residual, and therefore (5.50) is a measure of the local error. This idea will be exploited in the numerical test cases presented in Section 9.

5.5.2 Global Error

With the fine scales computed, we get the total finite element solution to current point in time as:

$$\boldsymbol{u}_h^{\alpha} = \hat{\boldsymbol{u}}^{\alpha} + \boldsymbol{u}'^{\alpha} \tag{5.51}$$

As mentioned, we seek incremental improvements to allow for a linear approximation and thus give the following representations of the coarse scale:

$$\hat{\boldsymbol{u}} = \boldsymbol{u}_h^{\alpha} + \tilde{\boldsymbol{e}}_G^{\alpha} \tag{5.52}$$

To obtain equations for this quantity, we generalize the derivation of the global error equations performed in [150] to the current system of nonlinear equations. We start by returning to the coarse-scale problem linearized about the fine scales, given by (5.35). Expression for the fine scales $u' = e_L$ is substituted in place of $\Delta \boldsymbol{u}'$, and then integration by parts is applied along with the formula for the local-explicit error (5.50) to arrive at equations analogous to (56) but containing additional terms involving e_L. Next, we linearize these equations about the coarse scale in the same manner as in Section 5.1. Finally, noting that $R_u\left(\boldsymbol{\eta}_o^h; \boldsymbol{u}^h\right) = 0$ because $\boldsymbol{u}^h$ is the converged solution from the Newton-Raphson algorithm, the contributions from $\boldsymbol{u}^h$ and e_L

vanish identically. Thus, we obtain a reduced system of equations to be solved for the global error components.

$$a^{\alpha}\left(\boldsymbol{\eta}^{h},\tilde{\boldsymbol{e}}_{G,\alpha}\right)=-\int_{\Omega^{\alpha}}\nabla\boldsymbol{\eta}^{h}:\left(\nabla\tilde{\boldsymbol{e}}_{L}\cdot\boldsymbol{\sigma}\right)+\nabla^{s}\boldsymbol{\eta}^{h}:\left(\boldsymbol{c}:\nabla^{s}\tilde{\boldsymbol{e}}_{L}\right)\mathrm{d}\Omega^{\alpha}-\int_{\Omega^{\alpha}}\boldsymbol{\eta}^{h\alpha}\cdot\boldsymbol{I}^{\alpha}J^{\alpha}\ \mathrm{d}\Omega^{\alpha} \tag{5.53}$$

Remark: *We highlight that the left-hand side of the system attained above is completely identical to the left-hand side from the last iteration of the Newton-Raphson algorithm applied to the linearized coarse-scale system* (56). *Therefore, if this stiffness matrix was previously factorized and stored, then the calculation of* $\tilde{\boldsymbol{e}}_{G,\boldsymbol{u}}$ *involves only a back-substitution with an updated right-hand side evaluated according to* (81).

5.5.3 Multiscale and stabilized formulation for mixture theory

The estimated error components presented in the preceding sections can be combined into a total estimate for the discretization error. As proposed in [41], an algorithmic simplification can be obtained by dropping the local-implicit component that corresponds to the assumption that fine-scales are nodally exact, to obtain an explicit error estimate, thereby saving on the computational cost of solving the local problems:

$$e^{\alpha}=\overline{e}_{L}^{\alpha}+\overline{e}_{G}^{\alpha} \tag{5.54}$$

Remark: *The key conclusion from the preceding discussion is that the error estimation method contained in the VMS approach carries over from linear to nonlinear problems. Other remarks on these error estimation techniques are contained in* [41] and [42].

5.6 Material Model for the Matrix and the Fiber

Following material model are employed for the constituents, where the matrix is considered to be isotropic and the fiber to be transversely isotropic.

$$\psi^{m}\left[x,t\right]=\frac{1}{\rho_{T}^{m}}\left\{\frac{1}{2}\lambda^{m}\left(tr\boldsymbol{\varepsilon}^{m}\right)^{2}+\mu^{m}tr\left[\left(\boldsymbol{\varepsilon}^{m}\right)^{2}\right]\right\} \tag{5.55}$$

$$\psi^r\left[\boldsymbol{x},t\right]=\frac{1}{\rho_T^r}\left\{\begin{array}{l}\frac{1}{2}\lambda^r\left(tr\left[\boldsymbol{\varepsilon}^r\right]\right)^2+\mu_T^r tr\left[\left(\boldsymbol{\varepsilon}^r\right)^2\right]+\alpha^r\left(\boldsymbol{m}^0\bullet\boldsymbol{\varepsilon}^r\boldsymbol{m}^0\right)tr\left[\boldsymbol{\varepsilon}^r\right]\\ \quad+2\left(\mu_L^r-\mu_T^r\right)\left(\boldsymbol{m}^0\bullet\left(\boldsymbol{\varepsilon}^r\right)^2\boldsymbol{m}^0\right)+\frac{1}{2}\beta^r\left(\boldsymbol{m}^0\bullet\boldsymbol{\varepsilon}^r\boldsymbol{m}^0\right)^2\end{array}\right\} \tag{5.56}$$

In mixture theory, as each constituent is homogenized, the fiber material property is to be modeled such that it can represent the effective composite behavior. Let us consider a glass epoxy composite, whose properties are provided in Table 5.1. For the single continuum effective composite material, the material properties are obtained using self-consistent field (SCF) model. For mixture theory, the homogenized fiber properties are obtained using the eq. (5.57), where $\boldsymbol{C}^c$ represents the effective material moduli of the composite obtained from SCF model, $\boldsymbol{C}^m$ is the material moduli of the matrix material and $\boldsymbol{C}^r$ is the material moduli of the fiber material.

$$\boldsymbol{C}^r=\frac{\boldsymbol{C}^c-V^m\boldsymbol{C}^m}{V^r} \tag{5.57}$$

This is shown schematically in Figure 5. First, the underlying discrete fibers and matrix materials are segregated. Then their material effects are homogenized across the entire domain; the anisotropic character of the fiber preform is still maintained, as is shown in the blue hatched subdomain. Then these two distributed materials are combined in an overlapping sense into a single mixture across the entire domain, and the anisotropy induced by the oriented fiber subdomain is inherited by the resulting material. Each material particle can be viewed as containing a portion of each underlying constituent material, apportioned according to the volume fraction of each constituent. The discrete interactions between the constituents are then accounted for through the interaction force terms in the governing equation of balance of linear momentum.

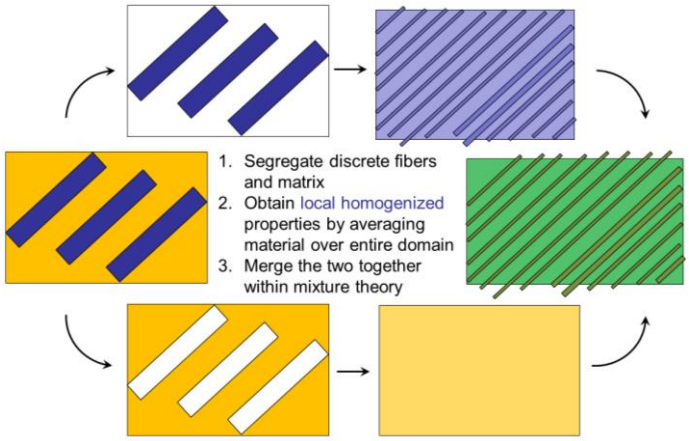

Figure 5.5. Mixture theory homogenization

Table 5.1: Glass-epoxy composite properties

$V_f = 0.5$	E_1 (GPa)	E_2 (GPa)	ν_{12}	G_{12} (GPa)	G_{23} (GPa)
Matrix (Epoxy)	3.45		0.3		
Fiber (Glass)	73		0.22		
Composite (SCF)	38.23	8.62	0.251	3.565	3.131

In the current implementation of the model, the fiber-matrix volume fraction is assumed to be constant all over the domain. As such, the respective volume fractions are constants. This restriction can however be removed for cases where a non-uniform distribution of reinforcing fibers is encountered. In that case the V^r will be a function, varying as a function of the spatial coordinates. Accordingly, V^m would also vary smoothly and therefore the resulting composite would inherit anisotropy and material heterogeneity. This aspect of functional form of V^r will be pursed in future extensions of this work, and it will account for the uncertainty in the designed microstructure of the material. It is important to note that the underlying framework would allow for a rapid variation in the value of V^r and this would indicate a local defect in the material. However, rapid variation in V^r will lead to rough coefficients in the discrete nonlinear coupled system of equations.

In the current framework, once the value of $\boldsymbol{C}^m$ is obtained at time zero, then material properties evolve as the Helmholtz functional for the fiber-matrix system evolve. Furthermore, it is important to realize that from a discrete constituents viewpoint, $\boldsymbol{C}^r$ does not evolve because we have assumed that the reaction takes place in the matrix material and not in the fiber. Consequently, it is the matrix material at the fiber-matrix interface that evolves and makes the interphase, and thereby $\boldsymbol{C}^m$ continuously evolves. As a consequence, $\boldsymbol{C}^m$ evolves continuously and provides us the provision to be able to track the evolution of the mechanical material properties of the resulting material.

5.7 Numerical Results

In this section, the performance of the variational multiscale method presented in section 5.3.1 and section5.4 is analyzed through 1D and 3D numerical examples. In section 5.7.1, a one dimensionsal curing of the composite is considered, where the interactive forces modeled through standard linear, quadratic Lagrange element is compared with 8 VMS Lagrange element. In section 5.7.2, matrix and fiber constituents are modeled individually as a three dimensional block where the interactive force modeled through the VMS element is highlighted. In section 5.7.3, we present a holistic numerical problem of process modeling and performance modeling of a composite plate with hole.

5.7.1 Curing of composite

In this section, we present the numerical results for curing of composites using Ruiz model [54] with quadratic elements, linear elements and linear-VMS elements. This problem was introduced in Section 3.4.1, where we had employed quadratic/cubic Lagrange functions to show the features of the mixture model. The results for the Linear VMS Lagrange elements are presented, where for the coarse scale fields, linear Lagrange functions are employed and for fine scales, quadratic bubble functions are employed. The matrix stress and interactive force between these elements are compared and the capability of the variational multiscale framework to capture the interactive force higher order effect with linear elements, which otherwise could be modeled only using quadratic or higher order elements, are highlighted.

The one-dimensional problem with a prescribed displacement of 0.1 was run for 600 seconds with a time step size of 5 seconds. The temperature was assumed to be uniform and constant and assigned a value of 393 K. Figure 5.6 shows the degree of cure as a function of time with Linear-VMS elements. Figure 5.7 shows the interactive force along the rod at 600 seconds obtained using quadratic, linear and linear-VMS elements. From equation (5.12) it can be seen that the interactive force is a function of the spatial gradient of the Helmholtz free energy function. As seen in Figure 5.7, under the standard Galerkin method, linear elements are unable to model the evolution of the interactive force due to chemical curing, and the computed value is zero in the domain. The quadratic elements can however provide a piecewise linear representation of the interactive force due to interphase evolution and is around 120 N along the domain. This requirement for the use of higher order functions arises due to the spatial gradient of the deformation-gradient present in the interactive force term. The Variational multiscale framework with locally defined higher order bubble functions is shown to capture almost 90% of the physical value via the fine scale modeling terms. The computed value with Linear-VMS elements is 109 N.

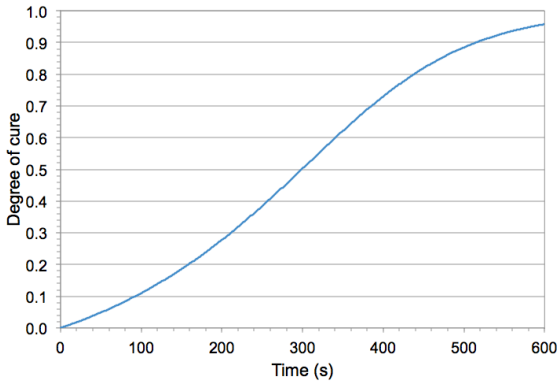

Figure 5.6. Degree of cure as a function of time with Linear-VMS elements

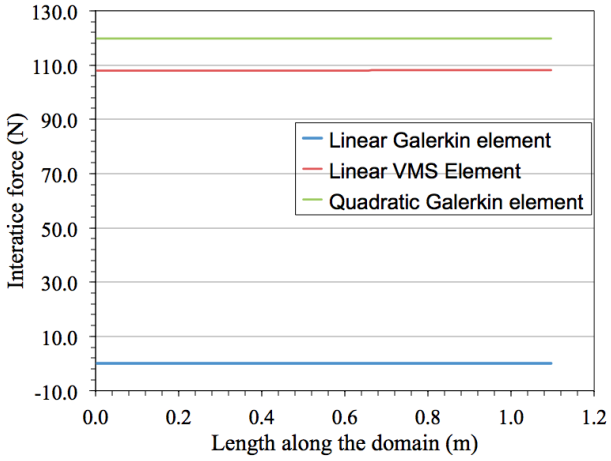

Figure 5.7. Comparison of Interactive force along the rod using Quadratic-Galerkin, Linear-Galerkin, and Linear-VMS elements

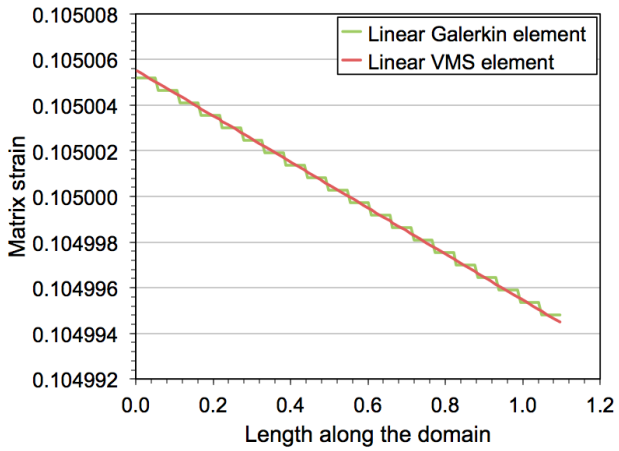

Figure 5.8. Comparison of matrix stress along the rod using Quadratic-Galerkin and Linear-Galerkin elements

Figure 5.8 shows the comparison of the matrix strain along the rod at 600 seconds obtained from linear-Galerkin and linear-VMS elements. While linear-Galerkin elements only provide a first-order approximation to the strain field, the linear-VMS can model the uniform strain field in the domain. We show in Figure 5.9 that the matrix stress response of linear-VMS elements that employ quadratic bubble functions in the modeling of fine-scales is similar to that from the quadratic Lagrange elements. As stated earlier, the major advantage of using linear-VMS element is the reduced computational cost in comparison to quadratic element. Through

additional local element calculations, the interactive force is modeled to a reasonable accuracy, which is impossible with the standard linear Lagrange elements.

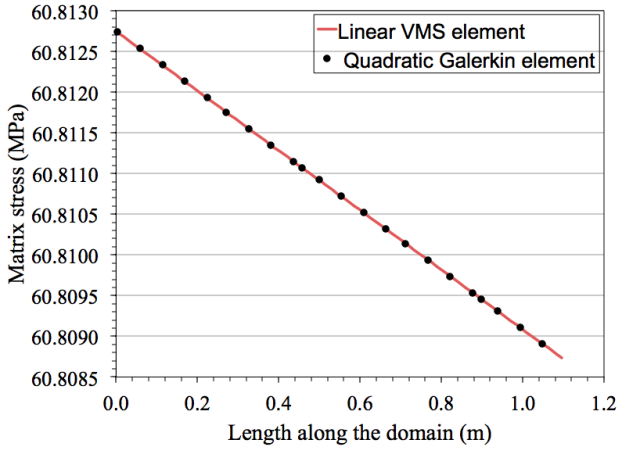

Figure 5.9. Comparison of matrix stress along the rod using Quadratic-Galerkin and Linear-VMS elements

5.7.2 Fine scale evolution 3D

In this section, a 3D block of dimension 1.0x0.1x0.1 mm is considered. The domain is discretized using 8-noded Lagrange elements, 8-noded VMS Lagrange elements and 27-noded Lagrange elements. The x=0, y=0, z=0 face is constrained in u, v, w directon respectively. The x=1.0, y=0.1 and z=0.1 plane is subjected to u, v and w displacement of -0.001 respectively. Similar to section 5.7.1, the axial stress and interactive force in x and y direction are compared with all three elements as mentioned above. The results are presented first for matrix material and then for fiber material. The matrix material is subjected to a gravity of 9810000 mm/s^2 in x, y and z direction and the results are presented Figure 5.10-Figure 5.13. Figure 5.10 shows the matrix axial stress for 8-noded Lagrange element, 27-noded Lagrange element and 8-noded VMS Lagrange element. It can be observed that the matrix axial stress profile for all three elements are similar. Figure and Figure 5.12 shows the interactive force contour in the domain in X and Y direction respectively. The interactive force in X direction for 8-noded Lagrange element varies between -0.00255 and 0.00211 N/mm^3 while for the quadratic Lagrange element varies between -0.897 to 0.151 N/mm^3. By allowing the fine scales to evolve, the 8-noded VMS Lagrange element is able to capture the interactive force similar to the quadratic Lagrange

element and achieves a minimum and maximum of -0.909 and 0.13 N/mm^3. A similar trend is observed for the interactive force in Y direction as shown in Figure 5.12. The interactive force in X and Y direction are plotted along the length of the domain at the center of the block in Figure 5.13. The line plot clearly shows the advantage of the proposed variational multiscale method in comparison to the linear Lagrange and quadratic Lagrange element.

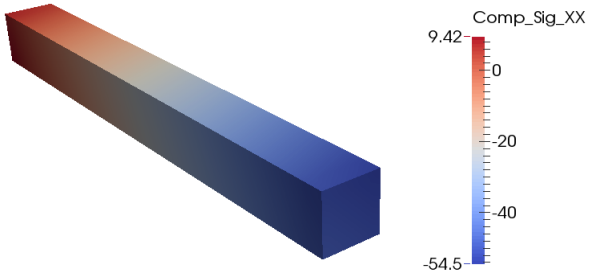

(a) B8 element

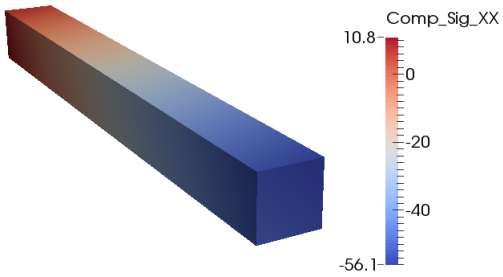

(b) B27 element

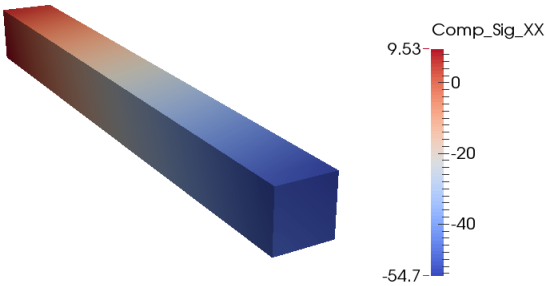

(c) B8-VMS element

Figure 5.10. Matrix axial stress

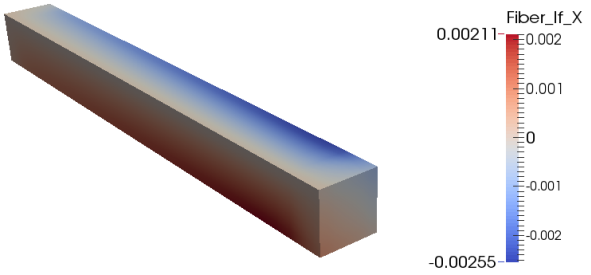

(a) B8 element

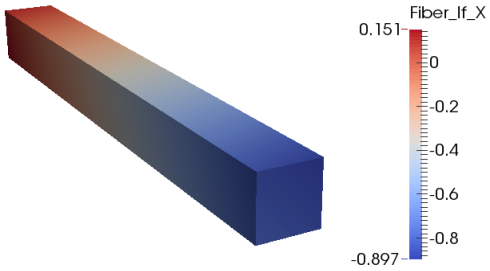

(b) B27 element

Figure 5.11. Matrix Interactive force in X direction

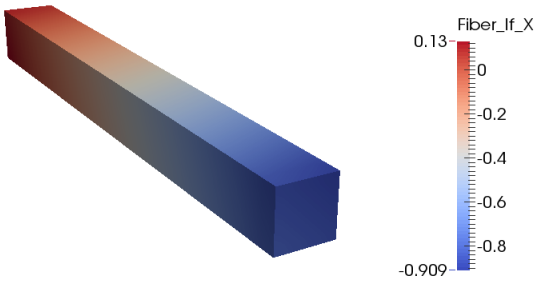

(c) B8-VMS element

Figure 5.11 (cont.). Matrix Interactive force in X direction

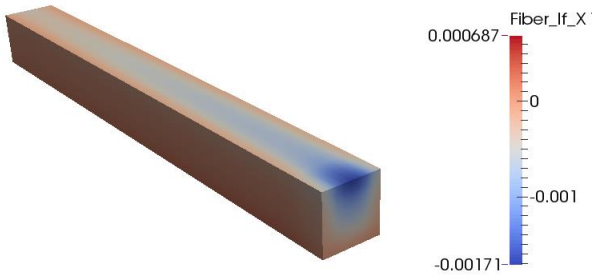

(a) B8 element

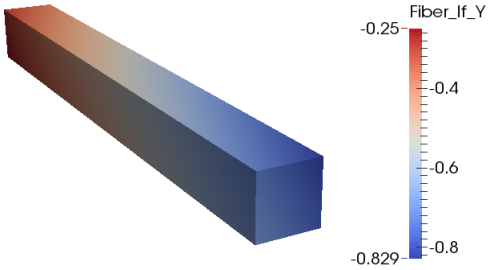

(b) B27 element

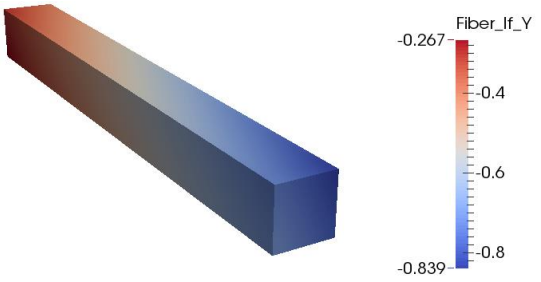

(c) B8-VMS element

Figure 5.12. Matrix Interactive force in Y direction

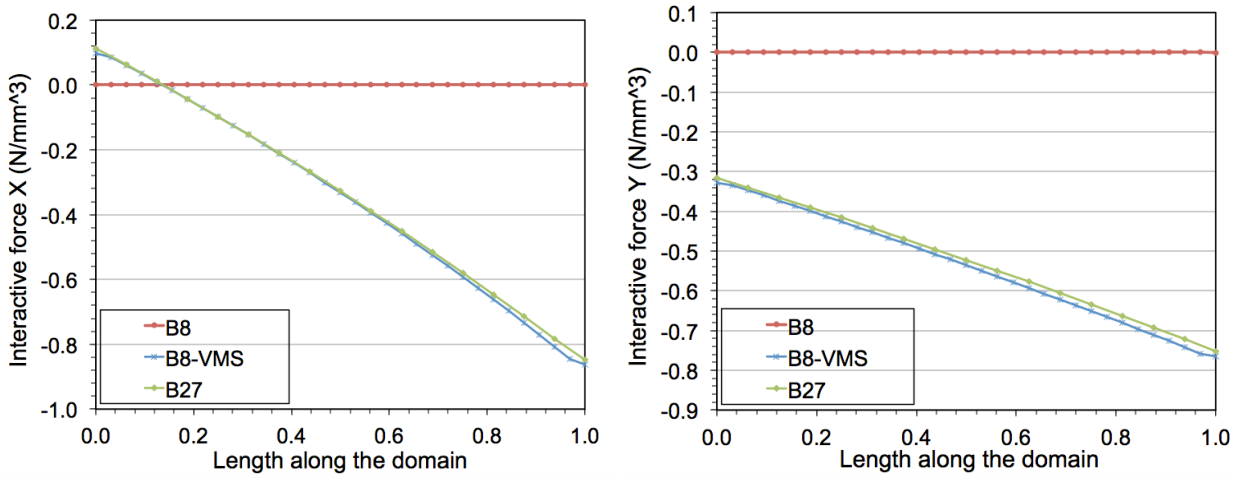

(a) Interactive force in X direction (b) Interactive force in Y direction

Figure 5.13. Interactive force along the length of the domain

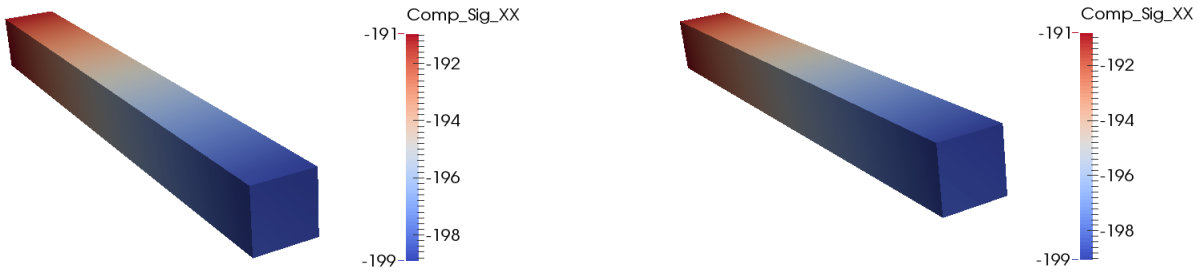

(a) B8 element (b) B27 element

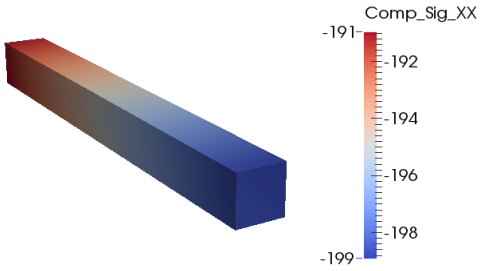

(c) B8-VMS element

Figure 5.14. Fiber axial stress

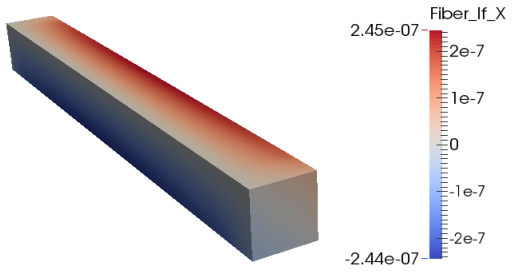

(a) B8 element

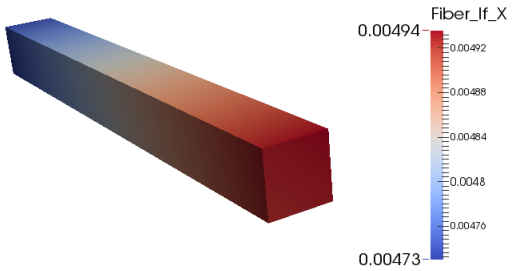

(b) B27 element

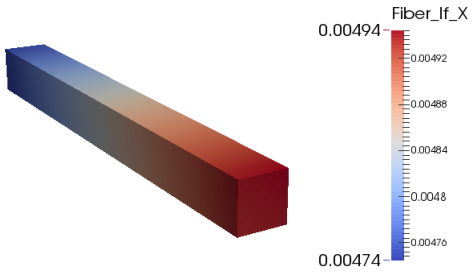

(c) B8-VMS element

Figure 5.15. Fiber Interactive force in X direction

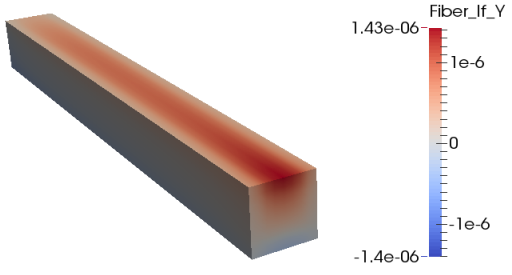

(a) B8 element

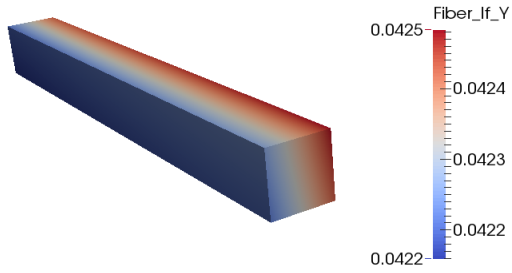

(b) B27 element

Figure 5.16. Fiber Interactive force in Y direction

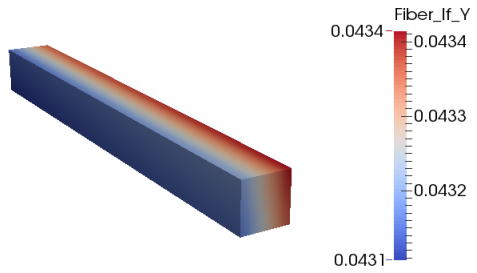

(c) B8-VMS element

Figure 5.16 (cont.). Fiber Interactive force in Y direction

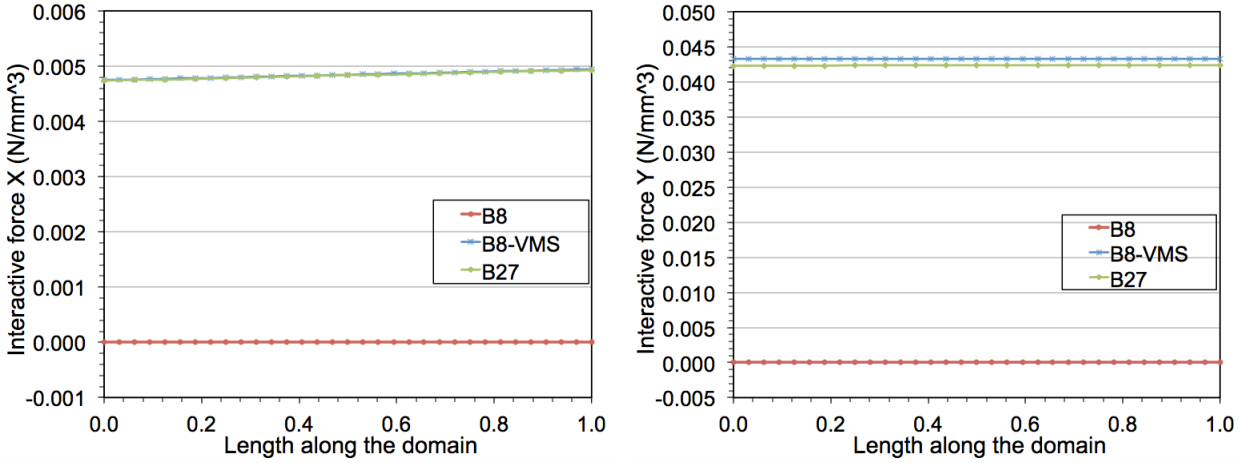

(a) Interactive force in X direction (b) Interactive force in Y direction

Figure 5.17. Interactive force along the length of the domain

Next, the same problem is solved for the fiber material which is transversely isotropic and is subjected to a gravity force of 98100000 mm/s^2. This problem is solved to showcase the proposed method's capability to capture the interactive force in X and Y direction due to material directionality. From Figure 5.17, it can be inferred that the 8-noded VMS Lagrange element models the interactice force in X and Y direction similar to the quadratic Lagrange element.

5.7.3 Plate with a hole

The objective of this section is to showcase the proposed method's capability to model both process modeling and performance modeling of the composite. Most available methods in

literature, perform process modeling independent of the performance modeling of the material. Homogenized idealized material models are employed in determining the load carrying capacity of the material involved. In this process, the inhomogeneity in the material property distribution, residual stresses due to differential cooling of the constituents are neglected and hence, the design of structures with these mateials requires a certain amount of factor of safety to ensure robustness. In this section, we consider a rectangular prismatic domain of dimensions $60 \times 20 \times 2.5$ mm with a circular hole of radius of 1.0 mm. This pre-impregnated composite with a fiber orientation of zero degrees has a epoxy resin with properties as shown in Table 5.2. Initially, the resin is assumed to have a very low Youngs modulus. This pre-impregnated composite is then allowed to cure until the matrix reaches a fully cured state of 0.99. In this problem, a temperature field as shown in Figure 5.18a is specified to model the thermal field variation in the actual curing process. The temperature is assumed to have a maximum value of 413 K at x=+/-30 plane and reaches a minimum of 393K at x=0 plane. The lamina is subjected to an axial pressure of 2 MPa at x=+/-30 plane in the axial direction until the matrix reaches a cure value of 0.99. The nodes are appropriately constrained at $x = 0$ plane to avoid rigid body motion. Once the matix is fully cured, the laminate is unloaded. To study the performance modeling aspect due to the variation in material properties after curing, an axial pressure of 200 MPa is applied at x=+/- 30 plane. The hoop stress vs applied pressure ratio along the circumference of the hole is compared with the exact solution provided in [51].

Table 5.2. Material properties of the lamina

	λ (MPa)	α (MPa)	β (MPa)	μ_L (MPa)	μ_T (MPa)	ρ (kg/mm^3)	Volume Fraction
Fiber	1.314E+03	-3.86E+03	2.252E+05	9.674E+03	3.531E+03	1550E-09	0.7
Matrix	3.4315	-	-	2.2877	-	1200E-09	0.3

Figure 5.18 presents the temperature profile, degree of cure and Youngs modulus variation at 300 seconds of the cure cycle. It can be observed from Figure 5.18b that the matrix material

cures faster in the region close to the boundary in comparison to the middle region of the lamina. This is due to the temperature distribution as shown in Figure 5.18a, where the temperature is higher close to the boundaries and hence faster cure rate. Figure 5.18c shows the Youngs modulus distribution of the matrix material at 300 seconds. The matrix Youngs modulus peaks at x=+/- 15 plane, while it has a lower Youngs modulus at the fully cured boundary region. Though the curing rate is faster near boundaries, this distribution is due to the fact that the fully cured matrix Youngs modulus at higher tmperature is lower than the middle region where the temperature is cooler by 20K. Figure 5.19 shows the composite axial stress profile across the domain at 300 seconds. It can be seen that the axial stress is higher in the region around the hole, where the tensile stress is 13.6 MPa for an applied pressure of 2 MPa.

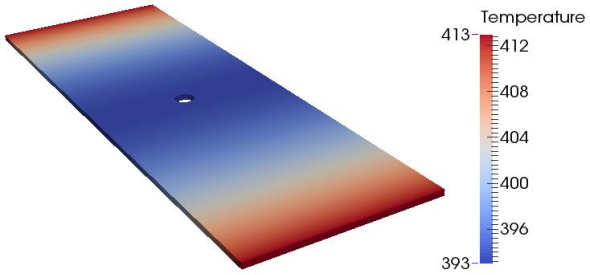

(a) Temperature profile across the domain

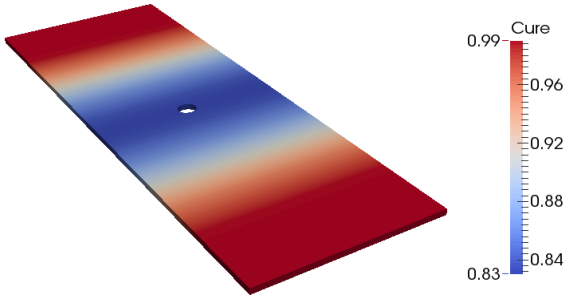

(b) Degreee of cure

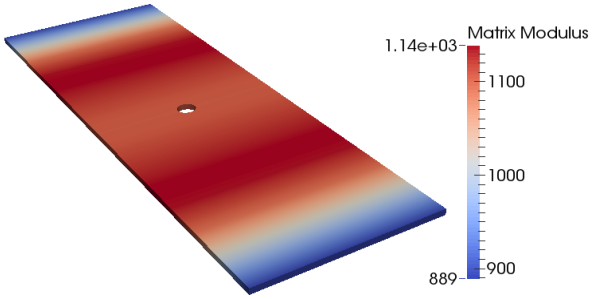

(c) Matrix modulus

Figure 5.18. Temperature, Cure, Matrix modulus variation at 300 seconds

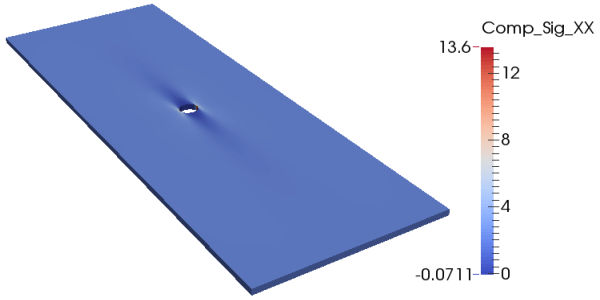

Figure 5.19. Composite axial stress at 300 seconds cure cycle

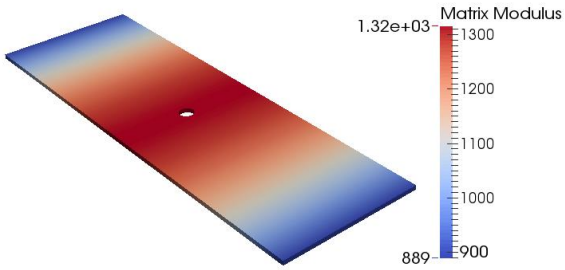

Figure 5.20. Matrix modulus of a fully cured matrix, cure = 0.99

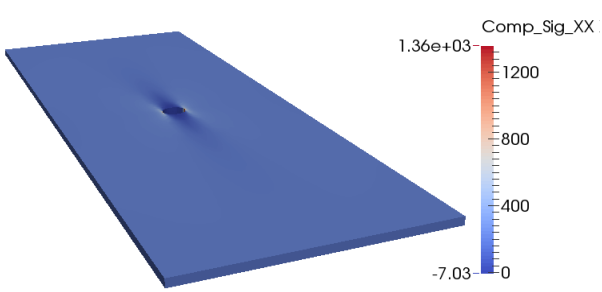

(a) Composite axial stress

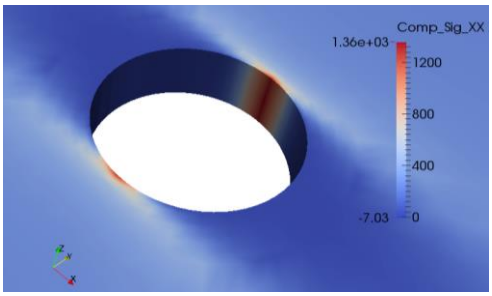

(b) Composite axial stress – Zoomed view

Figure 5.21. Composite axial stress of a fully cured composite at 200MPa loading

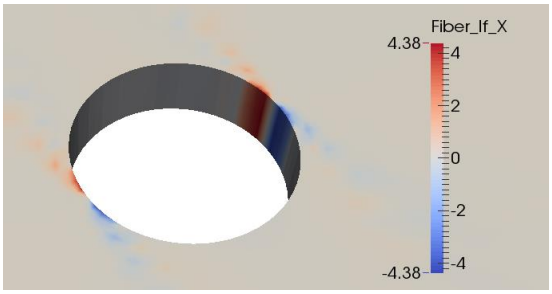

(a) Interactive force in X direction

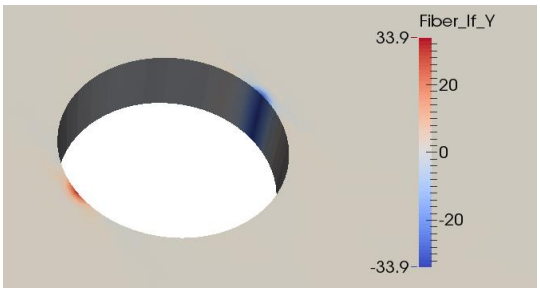

(b) Interactive force in Y direction

Figure 5.22. Interactive force of a fully cured composite at 200 MPa loading

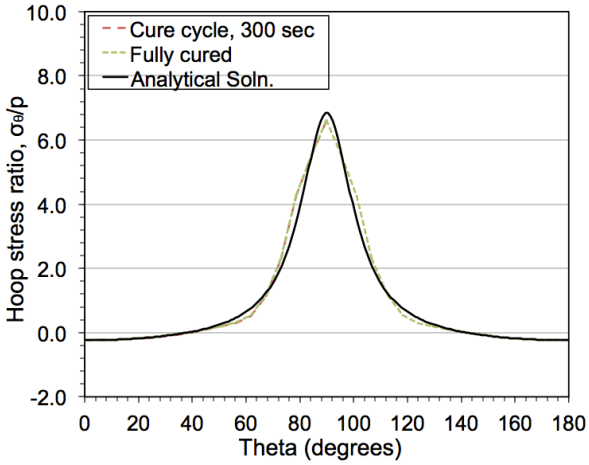

(a) Hoop stress vs applied pressure

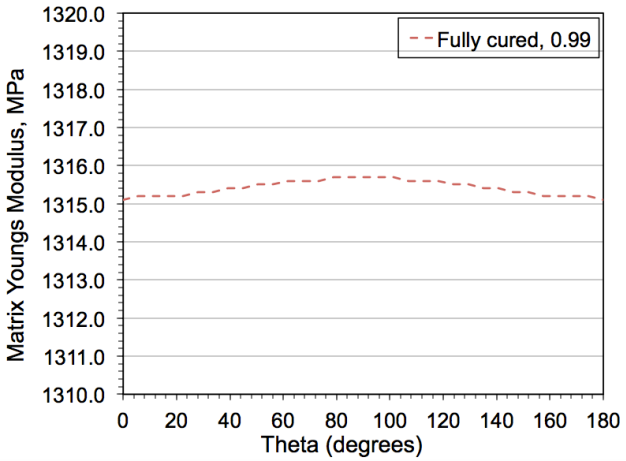

(b) Matrix Youngs Modulus

Figure 5.23. Variation of the hoop stress and matrix modulus along the circumference of the hole

Figure 5.20 show the matrix modulus variation once the matrix is fully cured, where the degree of cure reaches a value of 0.99 at every spatial point in the domain. As mentioned earlier, due to the specified temperature variation, the matrix Youngs modulus is higher in the middle region in comparison to the regions near the boundaries. This is a representative simulation of how curing can affect the distribution of the resin properties in the manufactured composite due to heat treatment. This composite is subjected to an axial loading of 200 MPa at x=+/- 30 plane. Figure 5.21 shows the composite axial stress contour in the lamina, where the maximum axial stress of 1.36e3 MPa occurs at 90^0 position along the circumference of the hole with respect to the axial direction. Figure 5.22a and Figure 5.22b shows the interactive force profile in X and Y direction

respectively. Both these plots shows that the interactive force in X and Y direction achieves a maximum at 90^0 position along the circumference of the hole, suggesting the failure initiation location. Figure 5.23a shows the distribution of the hoop stress vs applied pressure along the circumference of the hole for fiber orientation of 0^0 degree. The hoop stress vs applied pressure is plotted for two cases: (i) At 300 seconds of cure cycle, where a pressure of 2 MPa is applied, (ii) For a fully cured material, where a pressure of 200 MPa is applied. As the material model employed in this work is nonlinear elastic and as shown in Figure 5.23b, the temperature variation along the circumference of the hole is almost constant, the hoop stress vs applied pressure for both the materials overlap over each other and compares well with the exact solution.

5.8 Conclusions

In this chapter we have presented a numerical scheme that is based on a new variational formulation that possesses enhanced stability properties as well as an ability to account for multiple spatial scales in the solution. Specifically, it is shown that linear Lagrange functions with VMS based fine-scale modeling leads to an enriched method that can capture the physics that is otherwise captured only via quadratic or higher order Lagrange interpolation functions. A capstone problem which starts with process modeling of composite followed by the performance modeling of the cured material under one framework is presented. The variation in the material properties due to the thermal field and degree of cure is highlighted and its impact of stress distribution is studied.

Chapter 6

Concluding Remarks and Future Work

6.1 Concluding Remarks

An objective of this research was to develop a unified theoretical and computational framework for process modeling and performance modeling in fibrous composite materials. A literature review reveals that laminated composites made of directionally oriented fibrous materials are of prime interest for application in military and commercial planes, as well as in a variety of products of commercial interest. Although there are many theoretical and computational models that are available in the literature that can be used for performance modeling of laminated composite materials and structures, robust theoretical frameworks along with computationally efficient algorithms that can result in scalable codes which can be used for process modeling of fibrous composite materials are still under development. Another prime objective of this research was to be able to employ the same framework for modeling of interface and interphase evolution in fibrous composite materials. To this end we employed a thermodynamically consistent mixture theory that formed the theoretical basis of developments presented here, and we employed and further developed the Discontinuous Galerkin Variational Multiscale (DGVMS) method for application to multi-constituent materials in a coupled chemo-mechanical environment.

We started our developments in Chapter 2 with the presentation of a new stabilized finite element method [23-25] for the fluid-solid mixture theory model of Hall and Rajagopal [13] that is based on the constituent equations of motion and mass balance. The model addresses the energy and entropy production equations through an equation for Lagrange multiplier that results from consideration of the full set of balance equations as a constraint during the process of maximization of entropy production. The resulting system of equations is applied to isothermal processes in the one-dimensional context. Employing VMS ideas, a multiscale decomposition of

the fluid density field into coarse and fine scales and a-priori unique decomposition of the admissible spaces of functions leads to two coupled nonlinear problems termed as the coarse-scale and the fine-scale sub-problems. The fine-scale solution is extracted from the nonlinear fine-scale sub-problem which is then variationally projected onto the coarse-scale space, leading to a formulation that is expressed entirely in terms of the coarse-scales. Although the final formulation does not depend explicitly on the fine-scale density field for the fluid, the effects of fine-scales are consistently represented via the additional residual based terms, and they add to the stability of the numerical method. The resulting stabilized method for the mixture model is applied to hyperbolic propagation while recovering Fickian diffusion, anisotropic oxidation in composite materials recovering the data of Tandon et al. [14], and mass deposition. Results of the oxidation modeling of Tandon et al. [14] are recovered by employing the reaction kinetics model and properties assumed therein; the only additional assumed properties are two constants describing coupled chemo-mechanical and purely chemical dissipation. In all of these cases the mixture provides rich detail concerning the kinematic and kinetic behaviors of the constituents, in contrast to standard effective media approaches.

In Chapter 3 we presented a model for interphase formation during the curing process of composite materials in the context of mixture theory and cast in a finite strain framework. The model is based on the maximization of the rate of entropy production constraint and accommodates anisotropic effective reaction rates accompanied with an anisotropic tensor that provides coupling of chemical reaction and mechanical stresses. In this multi-continuum theory for composites, the material particles of different constituents are grouped together at reference configuration to define a composite particle. Though these constituent particles occupy different spatial points as the material deforms, the interactions between constituents are evaluated in the reference configuration using the composite particle. A significant feature of the mixture model is the interactive force field that is generated due to the interplay of the constituents. Even though in the homogenized mixture element an explicit discrete representation of the constituents is suppressed, the interplay of the constituents is fully accounted for via interactive force fields and the corresponding coupling terms that emanate from the mixture modeling ideas. It is important to realize that the standard single continuum homogenization theories do not possess this feature and while they can model kinematics of deformation, they cannot provide an insight into the interplay of the constituents. As such they are not able to identify the regions in the composite

where interactive force fields can exceed the load transfer capability between fiber and matrix which can lead to the initiation of localized damage.

In Chapter 4 we presented a mixture based model for multi-constituent solids where constituents are governed by their individual balance laws and are cognizant of the presence of other coexisting constituents via the interactive forces that emanate from maximizing the entropy production. The model is locally homogeneous while the structural layout of the fiber component introduces directionality as well as heterogeneity at the mesoscale. The coexisting constituents are represented independently inside the domain, weighted by their volume fractions and coupled via the interactive force field. To model the damage-free boundaries of the composite, a method is presented to tie the constituents at the Neumann boundaries. The boundary constraint equations find roots in the interface mechanics literature and they are modified to account for the non-zero applied tractions. The resulting computational method draws from the stabilized Discontinuous Galerkin method for finite strain kinematics where VMS based multiscale decomposition of the deformation map at the Neumann boundary and subsequent elimination of the underlying Lagrange multiplier via local modeling of the edge fine scales via edge bubble functions results in terms that self-consistently tie the multiple constituents. The resulting terms that enable the condensation of the multiplier field from the formulation also provide an edge based stabilization of the method. Closed-form expressions are derived for a generalized penalty tensor and a weighted numerical flux that are free from any tunable stability parameters. Numerical tests verify that the consistently derived constituent coupling parameters automatically evolve with evolving material and geometric nonlinearity at the boundaries. Several three-dimensional test cases are presented to validate the method via comparison with experimental, numerical and analytical data published in the literature. In all the cases the representative volume element consists of overlapping and coexisting matrix and fiber domains where matrix constituent is considered to be homogenous and isotropic and the fiber constituent is considered to be a transversely isotropic material. The interactive force field plots for the various test cases highlight the region that are susceptible to peeling and debonding of the laminates and this insight can help in developing methods for delamination in composites that is one of the most dominant modes of failure of laminated material systems. A large deformation bending of a composite beam problem is presented that has an analytical solution. Rate of

convergence study in terms of H1 seminorm is presented that highlights the variational convergence of the method.

6.2 Future Work

The theoretical and computational framework developed in this work can be extended for a variety of problem classes in computational material science and engineering. One extension is to combine the mixture theory model with the DGVMS ideas employed at the laminate interfaces to model delamination of the compistes as shown in Figure 6.1. Since DG functions are employed between the lamina, the fields may or may not be continuous. The continuity of the fields can be weakly enforced via interface coupling terms [43,45,60].

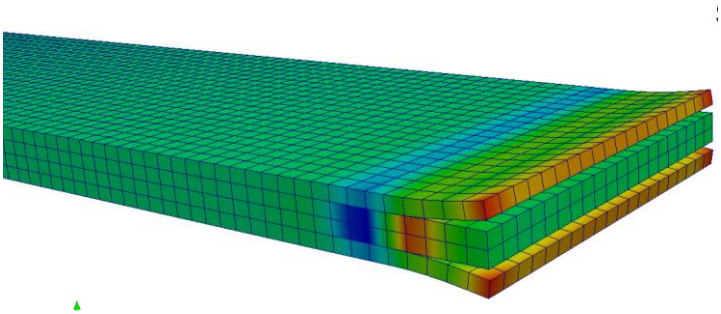

Figure 6.1. Delamination of the lamina

Another class of problem that can be considered is the modeling of laminates for macro-scale applications. As discrete modeling of the laminate for real world applications will be computationally intensive, the regions where the response will be homogenous can be modeled using mixture theory while the tow regions can be modeled in a discrete sense. These two class of PDE's can be combined at the interface using the heterogeneous multiscale method [60].

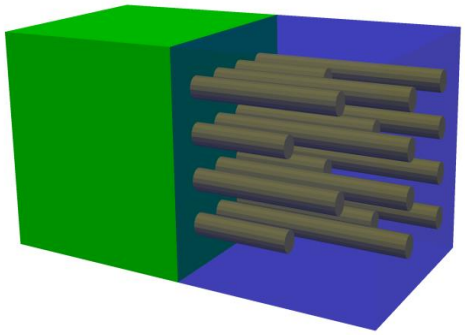

Figure 6.2. Heterogeneous modeling of composite

References

1. Truesdell C, Noll W. The non-linear field theories of mechanics. Springer Berlin Heidelberg; 2004.
2. Atkin R, Craine R. Continuum theories of mixtures: basic theory and historical development. The Quarterly Journal of Mechanics and Applied Mathematics 1976;29(2):209-244.
3. Green AE, Naghdi PM. On basic equations for mixtures. The Quarterly Journal of Mechanics and Applied Mathematics 1969;22(4):427-438.
4. Green AE, Naghdi PM. A theory of mixtures. Archive for Rational Mechanics and Analysis 1967;24(4):243-263.
5. Rajagopal K, Tao L. Mechanics of Mixtures. World Scientific Publishing Company, Incorporated; 1995.
6. Rajagopal K, Srinivasa A. On the thermomechanics of materials that have multiple natural configurations Part I: Viscoelasticity and classical plasticity. Zeitschrift für angewandte Mathematik und Physik ZAMP 2004;55(5):861-893.
7. Rajagopal K. Diffusion through polymeric solids undergoing large deformations. Materials science and technology 2003;19(9):1175-1180.
8. Karra S. Diffusion of a fluid through a viscoelastic solid. arXiv preprint arXiv:1010.3488 2010.
9. Karra S, Rajagopal K. A model for the thermo-oxidative degradation of polyimides. Mechanics of Time-Dependent Materials 2012;16(3):329-342.
10. Humphrey J, Rajagopal K. A constrained mixture model for growth and remodeling of soft tissues. Mathematical models and methods in applied sciences 2002;12(03):407-430.
11. Rao I, Rajagopal K. A thermodynamic framework for the study of crystallization in polymers. Zeitschrift für angewandte Mathematik und Physik ZAMP 2002;53(3):365-406.
12. Malek J, Rajagopal K. A thermodynamic framework for a mixture of two liquids. Nonlinear Analysis: Real World Applications 2008;9(4):1649-1660.
13. Hall R, Rajagopal K. Diffusion of a fluid through an anisotropically chemically reacting thermoelastic body within the context of mixture theory. Mathematics and Mechanics of Solids 2012;17(2):131-164.
14. Tandon G, Pochiraju K, Schoeppner G. Modeling of oxidative development in PMR-15 resin. Polym Degrad Stab 2006;91(8):1861-1869.
15. Schoeppner G, Tandon G, Pochiraju K. Predicting thermooxidative degradation and performance of high-temperature polymer matrix composites. Multiscale modeling and simulation of composite materials and structures: Springer; 2008. p. 359-462.
16. Varghese J, Owens BC, Whitcomb JD. Simulation of oxidation in textile composites. J Composite Mater 2011;45(17):1771-1782.

17. Varghese J, Whitcomb J. Micromechanics of oxidation in composites with impermeable fibers. J Composite Mater 2009;43(19):2011-2043.

18. Hughes TJ, Liu WK, Zimmermann TK. Lagrangian-Eulerian finite element formulation for incompressible viscous flows. Comput Methods Appl Mech Eng 1981;29(3):329-349.

19. Khurram RA, Masud A. A multiscale/stabilized formulation of the incompressible Navier–Stokes equations for moving boundary flows and fluid–structure interaction. Comput Mech 2006;38(4-5):403-416.

20. Calderer R, Masud A. A multiscale stabilized ALE formulation for incompressible flows with moving boundaries. Comput Mech 2010;46(1):185-197.

21. Simo JC, Hughes TJ. Computational Inelasticity. Illustrated ed.: Springer; 2000.

22. Hughes TJR. Multiscale phenomena: Green's functions, the Dirichlet-to-Neumann formulation, subgrid scale models, bubbles and the origins of stabilized methods. Comput Methods Appl Mech Eng 1995;127(1):387-401.

23. Masud A, Hughes TJR, A space-time Galerkin/least-squares finite element formulation of the Navier-Stokes equations for moving domain problems, Comput Methods Appl Mech Eng 1997;146(1):91-126.

24. Masud A, Khurram R. A multiscale/stabilized finite element method for the advection–diffusion equation. Comput Methods Appl Mech Eng 2004;193(21):1997-2018.

25. Masud A, Kwack J. A stabilized mixed finite element method for the first‐order form of advection–diffusion equation. Int J Numer Methods Fluids 2008;57(9):1321-1348.

26. Bowen R. Porous Elasticity: Lectures on the Elasticity of Porous Materials as an Application of the Theory of Mixtures. Available electronically from http://hdl.handle.net/1969.1/91297. 2010.

27. Bansal NP, Boccaccini AR. Ceramics and composites processing methods. : Wiley. com; 2012.

28. Civan F. Porous media transport phenomena. : John Wiley & Sons; 2011.

29. Bowen RM, Wiese JC. Diffusion in mixtures of elastic materials. International Journal of Engineering Science. 1969 Jul 1;7(7):689-722.

30. Bedford A, Stern M. Toward a diffusing continuum theory of composite materials. Journal of Applied Mechanics. 1971 Mar 1;38(1):8-14.

31. Hall, RB. A theory of coupled anisothermal chemomechanical degradation for finitely-deforming composite materials with Eshelbian interactive forces. Proceedings of 46 XIII International Congress and Exposition on Experimental and Applied Mechanics, Society for Experimental Mechanics; 2016 Jun 6–9, Orlando, FL, Springer.

32. Brezzi F, Fortin M. Mixed and hybrid finite element methods. Springer Science & Business Media; 2012 Dec 6.

33. Nitsche J. Über ein Variationsprinzip zur Lösung von Dirichlet-Problemen bei Verwendung von Teilräumen, die keinen Randbedingungen unterworfen sind. InAbhandlungen aus dem mathematischen Seminar der Universität Hamburg 1971 Jul 1 (Vol. 36, No. 1, pp. 9-15). Springer Berlin/Heidelberg.

34. Hansbo A, Hansbo P. An unfitted finite element method, based on Nitsche's method, for elliptic interface problems. Computer methods in applied mechanics and engineering. 2002 Nov 22;191(47):5537-52.

35. Dolbow J, Harari I. An efficient finite element method for embedded interface problems. International journal for numerical methods in engineering. 2009 Apr 9;78(2):229-52.

36. Sanders JD, Dolbow JE, Laursen TA. On methods for stabilizing constraints over enriched interfaces in elasticity. International Journal for Numerical Methods in Engineering. 2009 May 28;78(9):1009.

37. Embar A, Dolbow J, Harari I. Imposing Dirichlet boundary conditions with Nitsche's method and spline- based finite elements. International Journal for Numerical Methods in Engineering. 2010 Aug 13;83(7):877-98.

38. Annavarapu C, Hautefeuille M, Dolbow JE. A robust Nitsche's formulation for interface problems. Computer Methods in Applied Mechanics and Engineering. 2012 Jun 15;225:44-54.

39. Masud A, Truster TJ, Bergman LA. A variational multiscale a posteriori error estimation method for mixed form of nearly incompressible elasticity. Computer Methods in Applied Mechanics and Engineering. 2011 Nov 1;200(47):3453-81

40. Masud A, Scovazzi G. A heterogeneous multiscale modeling framework for hierarchical systems of partial differential equations. International Journal for Numerical Methods in Fluids. 2011 Jan 10;65(1-3):28-42.

41. Masud A, Truster TJ, Bergman LA. A unified formulation for interface coupling and frictional contact modeling with embedded error estimation. International Journal for Numerical Methods in Engineering. 2012 Oct 1;92(2):141-77.

42. Masud A, Truster TJ. A framework for residual-based stabilization of incompressible finite elasticity: stabilized formulations and methods for linear triangles and tetrahedra. Computer Methods in Applied Mechanics and Engineering. 2013 Dec 1;267:359-99.

43. Truster TJ, Masud A. Primal interface formulation for coupling multiple PDEs: A consistent derivation via the Variational Multiscale method. Computer Methods in Applied Mechanics and Engineering. 2014 Jan 1;268:194-224.

44. Truster TJ, Masud A. A Discontinuous/continuous Galerkin method for modeling of interphase damage in fibrous composite systems. Computational Mechanics. 2013 Sep 1;52(3):499-514.

45. Truster TJ, Chen P, Masud A. Finite strain primal interface formulation with consistently evolving stabilization. International Journal for Numerical Methods in Engineering. 2015 Apr 20;102(3-4):278-315.

46. Masud A, Tham CL, Liu WK. A stabilized 3-D co-rotational formulation for geometrically nonlinear analysis of multi-layered composite shells. Computational Mechanics. 2000 Jul 1;26(1):1-2.

47. Tham CL, Zhang Z, Masud A. An elasto-plastic damage model cast in a co-rotational kinematic framework for large deformation analysis of laminated composite shells. Computer methods in applied mechanics and engineering. 2005 Jun 10;194(21):2641-60.

48. Masud A, Panahandeh M. Finite-element formulation for analysis of laminated composites. Journal of engineering mechanics. 1999 Oct;125(10):1115-24.

49. Pipes RB, Pagano NJ. Interlaminar stresses in composite laminates under uniform axial extension. Journal of Composite Materials. 1970 Oct 1;4(4):538-48.

50. Reddy JN. An evaluation of equivalent-single-layer and layerwise theories of composite laminates. Composite Structures. 1993 Jan 1;25(1-4):21-35.

51. Leknitskii SG. Theory of elasticity of an anisotropic elastic body. Holden-Day; 1963.

52. Reddy JN. Mechanics of laminated composite plates and shells: theory and analysis. CRC press; 2004 Jun 1.

53. Ogden RW. Non-linear elastic deformations. Courier Corporation; 1997

54. Ruiz E, Trochu F. Thermomechanical properties during cure of glass-polyester RTM composites: elastic and viscoelastic modeling. Journal of Composite Materials. 2005 May 1;39(10):881-916.

55. Ruiz E, Trochu F. Numerical analysis of cure temperature and internal stresses in thin and thick RTM parts. Composites Part A: Applied Science and Manufacturing. 2005 Jun 30;36(6):806-26.

56. Yang F, Pitchumani R. Effects of interphase formation on the modulus and stress concentration factor of fiber-reinforced thermosetting-matrix composites. Composites Science and Technology. 2004 Aug 31;64(10):1437-52.

57. Yang F, Pitchumani R. A kinetics model for interphase formation in thermosetting matrix composites. Journal of applied polymer science. 2003 Sep 19;89(12):3220-36.

58. Yang F, Pitchumani R. Modeling of interphase formation on unsized fibers in thermosetting composites. ASME-PUBLICATIONS-HTD. 2000 Dec 31;366:329-38.

59. Vanlandingham MR, Eduljee RF, Gillespie Jr JW. Relationships between stoichiometry, microstructure, and properties for amine-cured epoxies. Journal of Applied Polymer Science. 1999 Jan 31;71(5):699-712.

60. Masud A, Scovazzi G. A heterogeneous multiscale modeling framework for hierarchical systems of partial differential equations. International Journal for Numerical Methods in Fluids. 2011 Jan 10;65(1-3):28-42.

61. Simo JC, Hughes TJ. Computational inelasticity. Springer Science & Business Media; 2006 May 7.

62. Bonet J, Wood RD. Nonlinear continuum mechanics for finite element analysis. Cambridge university press; 1997 Sep 28.

63. S. Reese, P. Wriggers, B.D. Reddy, New locking-free brick element technique for large deformation problems in elasticity, Computers and Structures. 75 (2000) 291-304.

64. J. Korelc, U. Šolinc, P. Wriggers, An improved EAS brick element for finite deformation, Computational Mechanics. 46 (2010) 641-659.

Appendix A

Relation between Solid Diffusivity and Drag Coefficient

In section 2.5, we have presented a reduced order mixture problem, oxidation of PMR-15 resin and slurry infiltration problem. A literature review reveals that the reduced order mixture problem and the oxidation problem is in general modeled via diffusion reaction equation, while the slurry infiltration problem is typically modeled via Darcy equation. In the context of the mixture theory model, the fluid solid interaction is accounted for via the interactive force field, which requires the specification of drag coefficient A^{v}. The relation between the drag coefficient A^{v} and the diffusivity of the solid D can be obtained by comparing the mixture theory equations and the Fick's diffusion reaction equation. Similarly, the relation between the drag coefficient A^{v} and the permeability of the solid K can be obtained by comparing the mixture theory equations and the Darcy equations for the slurry infiltration problem.

A.1 Fick's Diffusion Reaction Equation

The Fick's diffusion reaction equation is written as follows:

$$\frac{\partial \rho^{f}}{\partial t} = D\frac{\partial^{2} \rho^{f}}{\partial x^{2}} + m^{f} \tag{A.1}$$

where, D is the solid diffusivity. Consider a semi-infinite domain, where the initial concentration in the domain at time $t = 0$ is ρ_{R}^{f} and ρ_{0}^{f} is the specificed concentration at left end of the domain. For the case, where there is no chemical reaction, the exact solution for concentration ρ^{f} and it gradient is given as,

$$\rho^{f} = \rho_{R}^{f} + \left(\rho_{0}^{f} - \rho_{R}^{f}\right)\left(1 - erf\left(\frac{x}{2\sqrt{Dt}}\right)\right) \tag{A.2}$$

$$\frac{\partial \rho^f}{\partial x} = -\frac{1}{\sqrt{D\,t}}\left(\rho_0^f - \rho_R^f\right)\exp\left(-\left(\frac{x}{2\sqrt{D\,t}}\right)^2\right)\frac{1}{\sqrt{22/7}} \tag{A.3}$$

A.2 Darcy Equation

The fluid balance of mass and the Darcy's law are given as follows:

$$u_1^f = -\frac{K}{A^L}\frac{\partial p}{\partial x} \tag{A.4}$$

$$\frac{\partial \rho^f}{\partial t} + \frac{\partial(\rho^f v_1^f)}{\partial x} = m^f \tag{A.5}$$

where u_1^f is the filtration velocity, K is the permeability of the solid, and A^L is the viscosity of the fluid. Assuming that the pressure of the fluid follows ideal gas law, $p = \rho^f \bar{R}\theta$, eqs. (A.4) and (A.5) can be combined as follows,

$$\frac{\partial \rho^f}{\partial t} - \frac{K\bar{R}\theta}{A^L\phi^s}\frac{\partial}{\partial x}(\rho^f\frac{\partial \rho^f}{\partial x}) = m^f \tag{A.6}$$

where ϕ^s is the solid porosity. Equation (A.6) can be written in an expanded form as:

$$\frac{\partial \rho^f}{\partial t} - \frac{K\bar{R}\theta\rho^f}{A^L\phi^s}\frac{\partial^2 \rho^f}{\partial x^2} - \frac{K\bar{R}\theta}{A^L\phi^s}(\frac{\partial \rho^f}{\partial x})^2 = m^f \tag{A.7}$$

A.3 Mixture Theory

The fluid balance of mass and linear momentum are given as,

$$\frac{\partial \rho^f}{\partial t} + \frac{\partial(\rho^f v_1^f)}{\partial x} = m^f \tag{A.8}$$

$$\frac{\partial T_{11}^{f}}{\partial x} + I_1^f = 0 \tag{A.9}$$

where, the fluid body force and inertial effects are neglected.

A3.1 Reduced order mixture problem

Consider the constitutive relations for the fluid stress and interactive force as given in eqs. (2.57) and (2.58). Substituting these constitutive relations in eq. (A.9), the fluid velocity can be written as,

$$v_1^f = -\frac{\bar{R}\theta}{\rho^f A^v}\frac{\partial \rho^f}{\partial x} \tag{A.10}$$

Equations (A.6) and (A.8) can be combined to give,

$$\frac{\partial \rho^f}{\partial t} - \frac{\bar{R}\theta}{A^v}\frac{\partial^2 \rho^f}{\partial x^2} = m^f \tag{A.11}$$

Comparing eqs. (A.1) and (A.11), the drag coefficient can be written in terms of solid diffusivity as:

$$D = \frac{\bar{R}\theta}{A^v} \tag{A.12}$$

A3.2 Oxidation and slurry infiltration problem

Consider a simplified form of the constitutive relations for the fluid given in eqs. (2.31) and (2.32), as given below,

$$T_{11}^f \approx -\rho^f \rho \frac{\partial \psi}{\partial \rho^f} \approx -\frac{\rho^f \rho}{\rho_T}\bar{R}\theta \tag{A.13}$$

$$I_1^f \approx -\mu A^v v_1^f \tag{A.14}$$

Substituting the above eqs. (A.13) and (A.14) in eq. (A.8), the fluid velocity can be written as,

$$v_1^f \approx -\frac{\bar{R}\theta}{\mu A^v}\frac{\partial}{\partial x}\left(\frac{\rho^f \rho}{\rho_T}\right) \tag{A.15}$$

Fluid velocity given in the above expression is substituted in the fluid balance of mass, eq. (A.8) and is written as follows,

$$\frac{\partial \rho^f}{\partial t} - \frac{\bar{R}\theta}{\mu A^v}\frac{\partial}{\partial x}\left(\rho^f \frac{\partial}{\partial x}\left(\frac{\rho^f \rho}{\rho_T}\right)\right) = m^f \tag{A.16}$$

$$\frac{\partial \rho^f}{\partial t} - \frac{\bar{R}\theta\rho^f}{\mu A^v \rho_T}(\rho + \rho^f)\frac{\partial^2 \rho^f}{\partial x^2} + \cdots = m^f \tag{A.17}$$

Comparing eq. (A.17) and eq. (A.1), we can obtain the following relation for solid diffusivity and drag coefficient for the oxidation problem as,

$$D = \frac{\bar{R}\theta\rho^f}{\mu A^v \rho_T}(\rho + \rho^f) \tag{A.18}$$

Comparing eq. (A.17) and eq. (A.7), we can obtain the relation between the drag coefficient and the permeability of the solid for the slurry infiltration problem as,

$$A^v = \frac{A^L \phi^s}{K\mu\rho_T}(\rho + \rho^f) \tag{A.19}$$

In the section 2.5.3, we have presented numerical results for a simplified form of the above relation, $A^v \approx \frac{A^L}{K}$.

Appendix B

Consistent Linearization

B.1 Stiffness Contribution from the Interactive force

This section presents the expressions for the variational derivative of the interactive force with respect to the fine scale fields.

$$
\begin{aligned}
\mathrm{D}\left[J^m \boldsymbol{I}^m \right] \cdot \Delta\tilde{\boldsymbol{u}}^m = & -V^r J^r \frac{\rho_R^m \rho^m}{\rho^2} \left(\left(\boldsymbol{F}^r \cdot \boldsymbol{S}^r \right) : \nabla \boldsymbol{F}^r \right) \left(\nabla \cdot \Delta\tilde{\boldsymbol{u}}^m \right) \\
& + V^m \frac{\rho^r \rho^m}{\rho^2} \left(\left(\boldsymbol{F}^m \cdot \boldsymbol{S}^m \right) : \nabla \boldsymbol{F}^m \right) \left(\nabla \cdot \Delta\tilde{\boldsymbol{u}}^m \right) \\
& + V^m \frac{\rho^r}{\rho} \left(\mathrm{C} : \left(\boldsymbol{F}^{m^T} \cdot \nabla \left(\Delta\tilde{\boldsymbol{u}}^m \right) \cdot \boldsymbol{F}^m \right) \right) : \left(\boldsymbol{F}^{m^T} \cdot \nabla \boldsymbol{F}^m \right) \\
& + V^m \frac{\rho^r}{\rho} \nabla \left(\Delta\tilde{\boldsymbol{u}}^m \right) \cdot \left(\left(\boldsymbol{F}^m \cdot \boldsymbol{S}^m \right) : \nabla \boldsymbol{F}^m \right) \\
& + V^m \frac{\rho^r}{\rho} \left(\boldsymbol{F}^m \cdot \boldsymbol{S}^m \right) : \left(\nabla_X \nabla_X \left(\Delta\tilde{\boldsymbol{u}}^m \right) \right) \cdot \boldsymbol{F}^{m^{-1}} \\
& - V^m \frac{\rho^r}{\rho} \left(\left(\boldsymbol{F}^m \cdot \boldsymbol{S}^m \right) : \nabla \boldsymbol{F}^m \right) \left(\nabla \cdot \Delta\tilde{\boldsymbol{u}}^m \right)
\end{aligned}
\tag{B.1}
$$

$$
\begin{aligned}
\mathrm{D}\left[J^m \boldsymbol{I}^m \right] \cdot \Delta\tilde{\boldsymbol{u}}^r = {} & V^r \frac{1}{J^r} \frac{\rho_R^m \rho^m}{\rho^2} \left(\left(\boldsymbol{F}^r \cdot \boldsymbol{S}^r \right) : \nabla \boldsymbol{F}^r \right) \left(\nabla \cdot \Delta\tilde{\boldsymbol{u}}^r \right) \\
& - V^m \frac{\rho^r \rho^m}{\rho^2} \left(\left(\boldsymbol{F}^m \cdot \boldsymbol{S}^m \right) : \nabla \boldsymbol{F}^m \right) \left(\nabla \cdot \Delta\tilde{\boldsymbol{u}}^r \right) \\
& - V^r \frac{1}{J^r} \frac{\rho_R^m}{\rho} \left(\mathrm{C} : \left(\boldsymbol{F}^{r^T} \cdot \nabla \left(\Delta\tilde{\boldsymbol{u}}^r \right) \cdot \boldsymbol{F}^r \right) \right) : \left(\boldsymbol{F}^r \cdot \nabla \boldsymbol{F}^{r^T} \right) \\
& - V^r \frac{1}{J^r} \frac{\rho_R^m}{\rho} \left(\nabla \left(\Delta\tilde{\boldsymbol{u}}^r \right) \cdot \left(\boldsymbol{F}^r \cdot \boldsymbol{S}^r \right) : \nabla \boldsymbol{F}^m \right) \\
& - V^r \frac{1}{J^r} \frac{\rho_R^m}{\rho} \left(\boldsymbol{F}^r \cdot \boldsymbol{S}^r \right) : \left(\nabla_X \nabla_X \left(\Delta\tilde{\boldsymbol{u}}^r \right) \right) \cdot \boldsymbol{F}^{r^{-1}} \\
& + V^r \frac{1}{J^r} \frac{\rho_R^m}{\rho} \left(\left(\boldsymbol{F}^r \cdot \boldsymbol{S}^r \right) : \nabla \boldsymbol{F}^r \right) \cdot \left(\nabla \cdot \Delta\tilde{\boldsymbol{u}}^r \right)
\end{aligned}
\tag{B.2}
$$

The variation of the fiber interactive force with respect to the matrix fine scale displacement field is obtained by interchanging *m* and *r* indices in (B1) and (B2).

B.2 Consistent Linearization

This subsection provides consistent linearization of the final multiscale weak form, equation (4.49). It can be observed that equation (4.49) is a function of both matrix and fiber displacement fields. To solve this problem in a fully coupled fashion using Newton-Raphson scheme, we linearize the stabilized primal formulation with respect to both the constituents. The tangent stiffness matrix of the final multiscale weak form given in (4.49) can be written in symbolic form as,

$$
K\left(\bar{\boldsymbol{\varphi}}^r, \bar{\boldsymbol{\varphi}}^m, \boldsymbol{\lambda}; \tilde{\boldsymbol{\eta}}_o^r, \tilde{\boldsymbol{\eta}}_o^m \right) = \mathrm{D}\bar{R}_{\boldsymbol{\varphi}} \left(\bar{\boldsymbol{\varphi}}^r, \bar{\boldsymbol{\varphi}}^m, \boldsymbol{\lambda}; \tilde{\boldsymbol{\eta}}_o^r, \tilde{\boldsymbol{\eta}}_o^m \right) \bullet \Delta\bar{\boldsymbol{u}}^r + \mathrm{D}\bar{R}_{\boldsymbol{\varphi}} \left(\bar{\boldsymbol{\varphi}}^r, \bar{\boldsymbol{\varphi}}^m, \boldsymbol{\lambda}; \tilde{\boldsymbol{\eta}}_o^r, \tilde{\boldsymbol{\eta}}_o^m \right) \bullet \Delta\bar{\boldsymbol{u}}^m \tag{B.3}
$$

The variational derivative of the coarse scale residual with respect to both the constituents in reference configuration is given as,

$$
\begin{aligned}
K\left(\bar{\boldsymbol{\varphi}}^{r},\bar{\boldsymbol{\varphi}}^{m},\boldsymbol{\lambda};\bar{\boldsymbol{\eta}}_{o}^{r},\bar{\boldsymbol{\eta}}_{o}^{m}\right) &= \sum_{\alpha=r,m}\left[\int_{\Omega^{\alpha}}\nabla_{X}\bar{\boldsymbol{\eta}}_{o}^{\alpha}:\mathbf{A}^{\alpha}:\nabla_{X}\Delta\bar{\boldsymbol{u}}^{\alpha}\,\mathrm{d}\Omega-\int_{\Omega^{\alpha}}\bar{\boldsymbol{\eta}}_{o}^{\alpha}\bullet\mathrm{D}\left[J^{\alpha}\boldsymbol{I}^{\alpha}\right]\bullet\Delta\bar{\boldsymbol{u}}^{\alpha}\,\mathrm{d}\Omega\right]\\
&-\sum_{\alpha=r,m}\left[\int_{\Gamma^{\alpha}}\left[\!\left[\bar{\boldsymbol{\eta}}_{o}^{r}-\bar{\boldsymbol{\eta}}_{o}^{m}\right]\!\right]\bullet\mathrm{D}\left[\left\{\boldsymbol{P}\;\boldsymbol{N}\right\}\right]\bullet\Delta\bar{\boldsymbol{u}}^{\alpha}\,\mathrm{d}\Gamma\right]\\
&+\int_{\Gamma^{\alpha}}\left[\!\left[\bar{\boldsymbol{\eta}}_{o}^{r}-\bar{\boldsymbol{\eta}}_{o}^{m}\right]\!\right]\bullet\tau_{s}\bullet\left[\!\left[\Delta\bar{\boldsymbol{u}}^{r}-\Delta\bar{\boldsymbol{u}}^{m}\right]\!\right]\mathrm{d}\Gamma\\
&-\int_{\Gamma^{r}_{\epsilon_{s2}}}\left\{\left(\nabla_{X}\bar{\boldsymbol{\eta}}_{o}:\mathbf{A}\right)\bullet\boldsymbol{N}\right\}\bullet\left[\!\left[\Delta\bar{\boldsymbol{u}}^{r}-\Delta\bar{\boldsymbol{u}}^{m}\right]\!\right]\mathrm{d}\Omega\\
&-\int_{\Gamma^{r}_{\epsilon_{s2}}}\mathrm{D}\left[\left\{\left(\nabla_{X}\bar{\boldsymbol{\eta}}_{o}:\mathbf{A}\right)\bullet\boldsymbol{N}\right\}\right]\bullet\Delta\bar{\boldsymbol{u}}^{\alpha}\bullet\left[\!\left[\boldsymbol{\varphi}^{r}-\boldsymbol{\varphi}^{m}\right]\!\right]\mathrm{d}\Omega
\end{aligned}
\tag{B.4}
$$

The weighted average of flux term in the above equation can be further simplified as,

$$
\begin{aligned}
\mathrm{D}\left[\left\{\boldsymbol{P}\;\boldsymbol{N}\right\}\right]\bullet\Delta\bar{\boldsymbol{u}}^{\alpha} &= \boldsymbol{\delta}_{s}^{r}\bullet\left(\mathrm{D}\left[\boldsymbol{P}^{r}\right]\bullet\Delta\bar{\boldsymbol{u}}^{r}\right)\boldsymbol{N}^{r}-\boldsymbol{\delta}_{s}^{m}\bullet\left(\mathrm{D}\left[\boldsymbol{P}^{m}\right]\bullet\Delta\bar{\boldsymbol{u}}^{m}\right)\boldsymbol{N}^{m}\\
&=\left\{\left(\mathbf{A}:\nabla_{X}\Delta\bar{\boldsymbol{u}}\right)\boldsymbol{N}\right\}
\end{aligned}
\tag{B.5}
$$

and the linearization of the acoustic tensor term is written as,

$$
\begin{aligned}
\mathrm{D}\left[\left\{\left(\nabla_{X}\bar{\boldsymbol{\eta}}_{o}:\mathbf{A}\right)\boldsymbol{N}\right\}\right]\Delta\bar{\boldsymbol{u}}^{\alpha} &= \left[\left(\nabla_{X}\bar{\boldsymbol{\eta}}_{o}^{r}:\Xi^{r}:\nabla_{X}\Delta\bar{\boldsymbol{u}}^{r}\right)\boldsymbol{N}^{r}\right]\left(\boldsymbol{\delta}_{s}^{r}\right)^{T}\\
&-\left[\left(\nabla_{X}\bar{\boldsymbol{\eta}}_{o}^{m}:\Xi^{m}:\nabla_{X}\Delta\bar{\boldsymbol{u}}^{m}\right)\boldsymbol{N}^{m}\right]\left(\boldsymbol{\delta}_{s}^{m}\right)^{T}\\
&=\left\{\left(\nabla_{X}\bar{\boldsymbol{\eta}}_{o}:\Xi:\nabla_{X}\Delta\bar{\boldsymbol{u}}\right)\boldsymbol{N}\right\}
\end{aligned}
\tag{B.6}
$$

Where, Ξ^{α} is the sixth order tensor of material moduli and is defined as,

$$
\mathsf{X}^{a}=\frac{\P^{3}y^{a}}{\P\boldsymbol{F}^{a}\,\P\boldsymbol{F}^{a}\,\P\boldsymbol{F}^{a}}
\tag{B.7}
$$

The final consistent tangent stiffness matrix contribution due to the constituent a can be written as,

$$
\begin{aligned}
&\mathrm{D}\bar{R}_{\boldsymbol{\varphi}}\left(\bar{\boldsymbol{\varphi}}^{\alpha},\bar{\boldsymbol{\varphi}}^{\bar{\alpha}},\boldsymbol{\lambda};\tilde{\boldsymbol{\eta}}_o^{\alpha}\right)\bullet\Delta\bar{\boldsymbol{u}}^{\alpha}=\sum_{\alpha=r,m}\left[\int_{\Omega^{\alpha}}\nabla_X\bar{\boldsymbol{\eta}}_o^{\alpha}:\mathbf{A}^{\alpha}:\nabla_X\Delta\bar{\boldsymbol{u}}^{\alpha}\,\mathrm{d}\Omega-\int_{\Omega^{\alpha}}\bar{\boldsymbol{\eta}}_o^{\alpha}\bullet\mathrm{D}\left[J^{\alpha}\boldsymbol{I}^{\alpha}\right]\bullet\Delta\bar{\boldsymbol{u}}^{\alpha}\,\mathrm{d}\Omega\right]\\
&-\int_{\Gamma^{\alpha}}\left[\!\left[\bar{\boldsymbol{\eta}}_o^{r}-\bar{\boldsymbol{\eta}}_o^{m}\right]\!\right]\bullet\left\{\left(\mathbf{A}:\nabla_X\Delta\bar{\boldsymbol{u}}\right)\boldsymbol{N}\right\}\mathrm{d}\Gamma\\
&+\int_{\Gamma^{\alpha}}\left[\!\left[\bar{\boldsymbol{\eta}}_o^{r}-\bar{\boldsymbol{\eta}}_o^{m}\right]\!\right]\bullet\tau_s\bullet\left[\!\left[\Delta\bar{\boldsymbol{u}}^{r}-\Delta\bar{\boldsymbol{u}}^{m}\right]\!\right]\mathrm{d}\Gamma\\
&-\int_{\Gamma^{r}_{e_{s2}}}\left\{\left(\nabla_X\bar{\boldsymbol{\eta}}_o:\mathbf{A}\right)\bullet\boldsymbol{N}\right\}\bullet\left[\!\left[\Delta\bar{\boldsymbol{u}}^{r}-\Delta\bar{\boldsymbol{u}}^{m}\right]\!\right]\mathrm{d}\Omega\\
&-\int_{\Gamma^{r}_{e_{s2}}}\left\{\left(\nabla_X\bar{\boldsymbol{\eta}}_o:\Xi:\nabla_X\Delta\bar{\boldsymbol{u}}\right)\bullet\boldsymbol{N}\right\}\bullet\left[\!\left[\boldsymbol{\varphi}^{r}-\boldsymbol{\varphi}^{m}\right]\!\right]\mathrm{d}\Omega
\end{aligned}
\tag{B.8}
$$

We now push forward the residual of the governing equations and the consistent tangent stiffness terms to the current configuration as follows.

Residual vector:

$$
\begin{aligned}
&\sum_{\alpha=r,m}\left[\int_{\Omega_{\varphi}^{\alpha}}\nabla\,\bar{\boldsymbol{\eta}}^{\alpha}\bullet\boldsymbol{\sigma}^{\alpha}\,\mathrm{d}\Omega_{\varphi}-\int_{\Omega_{\varphi}^{\alpha}}\bar{\boldsymbol{\eta}}^{\alpha}\bullet\rho^{\alpha}\boldsymbol{b}^{\alpha}\,\mathrm{d}\Omega_{\varphi}-\int_{\Omega_{\varphi}^{\alpha}}\bar{\boldsymbol{\eta}}^{\alpha}\bullet\boldsymbol{I}^{\alpha}\,\mathrm{d}\Omega_{\varphi}\right]-\int_{\Gamma_{\varphi}^{\alpha}}\left(V^{r}\bar{\boldsymbol{\eta}}^{r}+V^{m}\bar{\boldsymbol{\eta}}^{m}\right)\bullet\boldsymbol{h}^{c}\,\mathrm{d}\Gamma_{\varphi}\\
&-\int_{\Gamma_{\varphi}^{\alpha}}\left[\!\left[\bar{\boldsymbol{\eta}}^{r}-\bar{\boldsymbol{\eta}}^{m}\right]\!\right]\bullet\left[\boldsymbol{\delta}_s^{r}\bullet\left(\boldsymbol{\sigma}^{r}\boldsymbol{n}^{r}-V^{r}\boldsymbol{h}^{c}\right)-\boldsymbol{\delta}_s^{m}\bullet\left(\boldsymbol{\sigma}^{m}\boldsymbol{n}^{m}-V^{m}\boldsymbol{h}^{c}\right)\right]\mathrm{d}\Gamma_{\varphi}\\
&+\int_{\Gamma_{\varphi}^{\alpha}}\left[\!\left[\bar{\boldsymbol{\eta}}^{r}-\bar{\boldsymbol{\eta}}^{m}\right]\!\right]\bullet\tau_s\bullet\left[\!\left[\boldsymbol{\varphi}^{r}-\boldsymbol{\varphi}^{m}\right]\!\right]\upsilon_A\,\mathrm{d}\Gamma_{\varphi}\\
&-\int_{\Gamma_{\varphi}}\left\{\left[\left(\nabla\,\bar{\boldsymbol{\eta}}^{r}:\mathbf{a}^{r}\right)\bullet\boldsymbol{n}^{r}\right]\bullet\left(\boldsymbol{\delta}_s^{r}\right)^{T}-\left[\left(\nabla\,\bar{\boldsymbol{\eta}}^{m}:\mathbf{a}^{m}\right)\bullet\boldsymbol{n}^{m}\right]\bullet\left(\boldsymbol{\delta}_s^{m}\right)^{T}\right\}\bullet\left[\!\left[\boldsymbol{\varphi}^{r}-\boldsymbol{\varphi}^{m}\right]\!\right]\mathrm{d}\Gamma_{\varphi}=0
\end{aligned}
\tag{B.9}
$$

Stiffness matrix:

$$
\begin{aligned}
&\mathrm{D}\bar{R}_{\boldsymbol{\varphi}}\left(\bar{\boldsymbol{\varphi}}^{\alpha},\bar{\boldsymbol{\varphi}}^{\bar{\alpha}},\boldsymbol{\lambda};\tilde{\boldsymbol{\eta}}_o^{\alpha}\right)\bullet\Delta\bar{\boldsymbol{u}}^{\alpha}=\sum_{\alpha=r,m}\left[\int_{\Omega_{\varphi}^{\alpha}}\nabla\,\bar{\boldsymbol{\eta}}^{\alpha}:\mathbf{a}^{\alpha}:\nabla\,\Delta\bar{\boldsymbol{u}}^{\alpha}\,\mathrm{d}\Omega_{\varphi}-\int_{\Omega_{\varphi}^{\alpha}}\bar{\boldsymbol{\eta}}^{\alpha}\bullet\frac{1}{J^{\alpha}}\mathrm{D}\left[J^{\alpha}\boldsymbol{I}^{\alpha}\right]\bullet\Delta\bar{\boldsymbol{u}}^{\alpha}\,\mathrm{d}\Omega_{\varphi}\right]\\
&+\int_{\Gamma_{\varphi}^{\alpha}}\left[\!\left[\bar{\boldsymbol{\eta}}^{r}-\bar{\boldsymbol{\eta}}^{m}\right]\!\right]\bullet\tau_s\bullet\left[\!\left[\Delta\bar{\boldsymbol{u}}^{r}-\Delta\bar{\boldsymbol{u}}^{m}\right]\!\right]\upsilon_A\,\mathrm{d}\Gamma_{\varphi}-\int_{\Gamma_{\varphi}^{r}}\left\{\left(\nabla\,\bar{\boldsymbol{\eta}}\;:\mathbf{a}\right)\bullet\boldsymbol{n}\right\}\bullet\left[\!\left[\Delta\bar{\boldsymbol{u}}^{r}-\Delta\bar{\boldsymbol{u}}^{m}\right]\!\right]\mathrm{d}\Gamma_{\varphi}\\
&-\int_{\Gamma_{\varphi}^{\alpha}}\left[\!\left[\bar{\boldsymbol{\eta}}^{r}-\bar{\boldsymbol{\eta}}^{m}\right]\!\right]\bullet\left\{\left(\mathbf{a}:\nabla\,\Delta\bar{\boldsymbol{u}}\right)\bullet\boldsymbol{n}\right\}\mathrm{d}\Gamma_{\varphi}-\int_{\Gamma_{\varphi}^{r}}\left\{\left(\nabla\,\bar{\boldsymbol{\eta}}\;:\mathbf{d}:\nabla\,\Delta\bar{\boldsymbol{u}}\right)\bullet\boldsymbol{n}\right\}\bullet\left[\!\left[\boldsymbol{\varphi}^{r}-\boldsymbol{\varphi}^{m}\right]\!\right]\mathrm{d}\Gamma_{\varphi}
\end{aligned}
\tag{B.10}
$$

B.3 Body Force and Traction Field for Large Deformation Bending of the Composite Beam

For the case of fiber orientation along the axial direction, the first Piola-Kirchhoff stress and body force of the fiber are given as follows.

$$\boldsymbol{P}^r = V^r m_1^r \begin{bmatrix} \left(u^3 - u\right)\cos\theta & \left(t - t^3\right)\sin\theta & 0 \\ \left(u^3 - u\right)\sin\theta & \left(t^3 - t\right)\cos\theta & 0 \\ 0 & 0 & 0 \end{bmatrix} + \frac{1}{2}V^r a^r \begin{bmatrix} \left(t - u\right)\cos\theta & \left(t - t^3\right)\sin\theta & 0 \\ \left(t - u\right)\sin\theta & \left(t^3 - t\right)\cos\theta & 0 \\ 0 & 0 & \left(t^2 - 1\right) \end{bmatrix}$$
$$+ \frac{1}{2}V^r I^r \begin{bmatrix} \left(u^3 + t - 2u\right)\cos\theta & \left(2t - u - t^3\right)\sin\theta & 0 \\ \left(u^3 + t - 2u\right)\sin\theta & \left(u + t^3 - 2t\right)\cos\theta & 0 \\ 0 & 0 & \left(u^2 + t^2 - 2\right) \end{bmatrix} \tag{B.11}$$
$$+ \frac{1}{2}V^r a^r \begin{bmatrix} 0 & \left(-u - t^3 + 2t\right)\sin\theta & 0 \\ 0 & \left(u + t^3 - 2t\right)\cos\theta & 0 \\ 0 & 0 & 0 \end{bmatrix} + \frac{1}{2}V^r b^r \begin{bmatrix} 0 & \left(t - t^3\right)\sin\theta & 0 \\ 0 & \left(t^3 - t\right)\cos\theta & 0 \\ 0 & 0 & 0 \end{bmatrix}$$

Accordingly, the three components of the body force are given by,

$$r^r B_1^r = V^r m_1^r \cos\theta\left(\frac{3u^4}{r} - \frac{u^2}{r}\right) + \frac{1}{2}V^r I^r \cos\theta\left(\frac{3u^4}{r} - \frac{uy}{r} - \frac{2u^2}{r}\right) + \frac{1}{2}V^r a^r \cos\theta\left(-\frac{uy}{r} - \frac{u^2}{r}\right)$$
$$+ \left(V^r m_1^r + \frac{1}{2}V^r I^r + \frac{1}{2}V^r b^r\right)\left(t^3 - t\right)\cos\theta\frac{y}{L} \tag{B.12}$$
$$+ \frac{1}{2}V^r I^r\left(-2t + u + t^3\right)\cos\theta\frac{y}{L} + \frac{1}{2}V^r a^r\left(u + t^3 - 2t\right)\cos\theta\frac{y}{L}$$

$$r^r B_2^r = V^r m_1^r \sin q\left(\frac{3u^4}{r} - \frac{u^2}{r}\right) + \frac{1}{2}V^r l^r \sin q\left(\frac{3u^4}{r} - \frac{uy}{r} - \frac{2u^2}{r}\right) + \frac{1}{2}V^r a^r \sin q\left(-\frac{uy}{r} - \frac{u^2}{r}\right) \quad \text{(B.13)}$$
$$+\left(V^r m_1^r + \frac{1}{2}V^r a^r + \frac{1}{2}V^r b^r\right)\left(t^3 - t\right)\sin q\frac{y}{L}$$
$$+\frac{1}{2}V^r l^r\left(-2t + u + t^3\right)\sin q\frac{y}{L} + \frac{1}{2}V^r a^r\left(-2t + u + t^3\right)\sin q\frac{y}{L}$$

$$r^r B_3^r = 0 \quad \text{(B.14)}$$

where $u = \frac{L}{\psi r}$, $t = \frac{\psi r}{L}$.

B.4 Exact solution for plate with a hole problem

The exact solution for the hoop stress to applied pressure ratio based on two dimensional anisotropic elasticity is given as,

$$\frac{\sigma_\theta}{p} = \frac{A_{11}^{'}}{A_\theta}\begin{Bmatrix}\left[\cos^2\phi + \left(\mu_1\mu_2 - n\right)\sin^2\phi\right]\mu_1\mu_2\cos^2\theta \\ +\left[\left(1+n\right)\cos^2\phi + \mu_1\mu_2\sin^2\phi\right]\sin^2\theta \\ -n\left[1+n-\mu_1\mu_2\right]\sin\phi\cos\phi\sin\theta\cos\theta\end{Bmatrix} \quad \text{(B.15)}$$

$$A_\theta = A_{11}^{'}\sin^4\theta + \left(A_{66}^{'} + 2A_{12}^{'}\right)\sin^2\theta\cos^2\theta + A_{22}^{'}\cos^4\theta \quad \text{(B.16)}$$

$$\mu_1\mu_2 = -\sqrt{\frac{A_{22}^{'}}{A_{11}^{'}}} \quad \text{(B.17)}$$

$$n = \sqrt{\frac{A_{66}^{'}}{A_{11}^{'}} - 2\frac{A_{12}^{'}}{A_{11}^{'}} + 2\sqrt{\frac{A_{22}^{'}}{A_{11}^{'}}}} \quad \text{(B.18)}$$

$$\left(A_{ij}^{'}\right)^{-1} = A_{ij} = \sum_{k=1}^{n}\bar{Q}_{ij}^{k}\left(h_{k+1} - h_k\right) \quad \text{(B.19)}$$

where $\bar{Q}_{ij}^{k}$ is the stiffness coefficients of individual lamina, h_k is the plate thickness, ϕ is the angle between the fiber and applied pressure and θ is the angle around the hole.